Examination of Filamentous Fungi using FTIR and Raman Spectromicroscopy

by

Merrill Isenor

A Thesis submitted to the Faculty of Graduate Studies of

The University of Manitoba

in partial fulfilment of the requirements of the degree of

MASTER OF SCIENCE

Department of Chemistry

University of Manitoba

Winnipeg

Abstract

Several fungal endophytes (*C. protuberata, F. culmorum, and C. magna*) confer stress tolerance to plants in the presence of certain pressures. This relationship is known as habitat-adapted symbiosis; its mechanism is currently unknown. Here, sFTIR, FTIR coupled to an FPA detector, and Raman spectromicroscopy are used to examine whether any biochemical differences exist between different isolates of the same species: one that can confer stress tolerance to plants and the other that cannot.

No major differences have been observed in spectra that can differentiate between those endophytes that confer stress tolerance and those that do not. However, some hyphae from both isolates of *C. protuberata* have been found to contain mannitol; its presence may be more common in geothermal rather than non-geothermal isolates. Mannitol is a compound involved in providing stress tolerance to fungi. Any role that it may have in the mechanism of habitat-adapted symbiosis will need further investigation.

Acknowledgments

Dr. Kathy Gough

Dr. Susan Kaminskyj and her students, especially Xiaohui Bao

Dr. Rusty Rodriguez and Dr. Regina Redman

Committee Members:
Dr. John Sorensen
Dr. David Levin

Gough group members (current and recent):

Lsan Tzadu	Dr. Richard Wiens	Catherine Liao	Dave Stitt
Dr. Sivakumar Gajjeraman	Avid Khamenehfar	Kosta Jilkine	Alex Kuzyk
Dr. Marzena Kastyak	Fatemeh Faraz Khorasani		

Synchrotrons:
Dr. Bob Julian (SRC) for assistance and data collection
Dr. Luca Quaroni and Dr. Tim May (CLS) for assistance

Financial Support:

Manitoba Graduate Scholarship	Faculty of Graduate Studies
NSERC CGS M	Department of Chemistry
CIHR ITMHRT	

My family and friends

Contents

List of Tables

List of Figures

List of Presentations

Gough, K.M., Kaminskyj, S., **Isenor, M**., Bao, X., Rodriguez, R.J., Redman, R., Rak, M., El-Ganiny, A. (2009) Exploring fungal metabolism with Raman, SERS, synchrotron IR and XRF microscopy. Pittcon Conference & Expo 2009. Chicago, Illinois. March 8 – March 13.

Kaminskyj, S.G.W., **Isenor, M**., Jilkine, K., Liao, C., Rak, M., Gough, K.M. (2008) Correlative spectromicroscopy and conventional microscopy for exploring fungal metabolism. 35th Federation of Analytical Chemistry and Spectroscopy Societies Conference. Reno, NV. September 28 – October 2 (poster).

Isenor, M., Bao, X., Rodriguez, R., Redman, R., Kaminskyj, S., Gough, K. (2008) Spectromicroscopy of fungal endophytes using synchrotron FTIR. 54th International Conference on Analytical Sciences and Spectroscopy. Sainte-Anne-de-Bellevue, QC. August 3 – August 6.

Isenor, M., Rodriguez, R.J., Redman, R.S., Schmidt, R., Kaminskyj, S.G.W., Gough, K.M. (2008) Synchrotron FTIR examination of endophyte fungi conferring stress tolerance to plants. Canadian Light Source 11th Annual Users' Meeting. Saskatoon, SK. June 9 – June 10 (poster).

Isenor, M., Gough, K.M., Kaminskyj, S.G.W. (2008) Examination of fungal spores and hyphae using surface-enhanced Raman scattering. 91st CSC Canadian Chemistry Conference and Exhibition. Edmonton, AB. May 24 – May 29.

List of Abbreviations

ATCC …… American Type Culture Collection

ATP …….. adenosine triphosphate

ATR ……. attenuated total reflection

CCD …….. charge-coupled device

CLS ……... Canadian Light Source

CmPath ……... *Colletotrichum magna*, non-pathogenic mutant

Cp4666D …….. *Curvularia protuberata*, from geothermal plants

CpATCC ……... *Curvularia protuberata*, from culture collection

CThTV …… *Curvularia* thermal tolerance virus

DLATGS …….. deuterated l-alanine-doped triglycine sulphate

dsRNA ……... double-stranded ribonucleic acid

DTGS ……. deuterated triglycine sulphate

ESRF…….. European Synchrotron Radiation Facility

Fc18 …….. *Fusarium culmorum*, from non-coastal plants

FcRed1 …… *Fusarium culmorum*, from coastal plants

FPA …… focal-plane array

FT ……. Fourier transform

FTIR …… Fourier transform infrared

GC-MS …….. gas chromatography-mass spectrometry

GYE ……. glucose yeast extract

IR ……. infrared

L2.5 …….. *Colletotrichum magna*, wildtype pathogen

MCT ……... mercury cadmium telluride

N.A. ……. numerical aperture

PDA …….. potato dextrose agar

polyP …….. polyphosphate

PTFE …… polytetrafluoroethylene

SERS …… surface-enhanced Raman scattering

sFTIR ……... synchrotron Fourier transform infrared

S/N ……. signal-to-noise ratio

SRC ……... Synchrotron Radiation Center

U of M …… University of Manitoba

Chapter 1

Introduction

1.1 Overview

Fungi have a variety of roles in the environment that can range from beneficial (*e.g.* the production of important drugs) to detrimental (*e.g.* causing severe infections in animals and humans or destroying crops). It is essential to have a better understanding of how fungi interact with their surroundings in order to control their activities.

Mycologists employ a number of techniques for the examination of fungi. Cell ultrastructure can be studied with scanning electron microscopy, transmission electron microscopy, and atomic force microscopy (Kaminskyj & Dahms, 2008). Spatially resolved examinations of fungal composition can be performed using fluorescence techniques (*e.g.* immunofluorescence, epifluorescence) (Kaminskyj, 2000; Navratil *et al.*, 2006); however, with these approaches only one or a few chosen components are examined at a time. Chromatographic techniques (*e.g.* gas chromatography-mass spectrometry (GC-MS)) can also be used for fungal classification (Brondz *et al.*, 2004). While many different com-

pounds can be separated and identified with GC-MS, the technique is destructive and no information is gained with respect to location within the cell.

Fourier transform infrared (FTIR) spectroscopy has been used for the examination of fungi as far back as the 1960s (Michell & Scurfield, 1967). Several recent studies have evaluated FTIR as a tool for rapid clinical identification of infection-causing fungi (Erukhimovitch *et al.*, 2005; Essendoubi, *et al.*, 2005; Fischer *et al.*, 2006; Toubas *et al.*, 2007) including the identification of several *Candida* yeasts (Maquelin *et al.*, 2002a). FTIR has also been used for the detection of fungal deterioration in historic ceilings (Genestar & Palou, 2006), wood degradation caused by wood-rotting fungi (Fackler *et al.*, 2007), and fungal biodeterioration of historic papers (Zotti *et al.*, 2008). Yet, many studies have relied on the examination of bulk samples, typically ground to powder and pressed into a KCl (Michell & Scurfield, 1967) or KBr disc (Bahmed *et al.*, 2003; Fischer *et al.*, 2006; Nie *et al.*, 2007; Fackler *et al.*, 2007) or centrifuged to a pellet and placed on ZnSe crystals for transmission measurements (Erukhimovitch *et al.*, 2005; Fischer *et al.*, 2006), where all spatial resolution is lost. A few studies have employed moderate spatial resolution for the examination of fungal microcolonies. Apertures from 50 to 250 μm were used in order to correspond with colony size (Essendoubi *et al.*, 2005; Toubas *et al.*, 2007); the resulting spectra represent an average of many hyphae, over a large range of developmental stages.

Raman spectroscopy has also been used to study fungi, including examinations of biodegradation of paint binders (Cappitelli *et al.*, 2005), the detection of carotenoids within cells (Arcangeli & Cannistraro, 2000), and real-time studies of yeast cell mitosis (Huang *et al.*, 2003). Other studies have focused on the identification of single cells by

averaging high spatial resolution spectra (Rösch *et al.*, 2005; Rösch *et al.*, 2006) and the rapid identification of human pathogens with the goal of clinical applications (Maquelin *et al.*, 2002a; Maquelin *et al.*, 2002b; Maquelin *et al.*, 2003; Ibelings *et al.*, 2005). Raman has also been applied to the study and identification of individual fungal spores (De Gussem *et al.*, 2005; De Gussem *et al.*, 2007). While many of these studies have taken advantage of high resolution Raman microscopy, they are mainly focused on determining an average signal from a given species that can be used for clinical identification.

Fungal FTIR studies conducted by other groups do not offer the possibility to relate composition to location within the cell, nor can they offer insight into different developmental stages. The main goal of most Raman studies has been the identification of samples, rather than a study of cellular make-up. FTIR and Raman spectroscopy can give insight into the molecular composition of samples at defined locations and high spatial resolution (≤ 10 μm for IR, ≤ 2 μm for Raman). All compounds within the cell are examined simultaneously. FTIR and Raman do not damage samples so cultures can be examined with both techniques sequentially, providing they are on substrates suitable for both types of analyses (*vide infra*). No chemical treatments (*e.g.* staining) are performed prior to analysis.

Fungi can have a variety of ecological roles on the basis of habitat. For this thesis, filamentous fungi having different roles in the environment are examined at a molecular level with FTIR, synchrotron FTIR (sFTIR), and Raman microscopy. These spectroscopic techniques can provide spatially resolved sub-cellular details not obtainable with many other methods. Information gained has the potential to help reveal the mechanism(s) behind the different lifestyles of these samples.

1.2 Fungi

Fungi have a range of impacts on humans and the environment. Fungi produce many important compounds used in food and drug industries (*e.g.* citric acid, penicillin). Some are decomposers, playing a valuable role in woodland ecosystems; others are used in food production, from baking bread to brewing beer (Griffin, 1994; Carlile *et al.*, 2001). However, some fungi cause disease in plants and animals, either by host invasion or exuding toxic compounds (Griffin, 1994). Fungal plant pathogens are a risk to the global food supply and can damage a multitude of manufactured goods (Carlile *et al.*, 2001). Thus, it is essential to gain a better understanding of how fungi interact with their environment in order to direct their activities.

Fungi constitute good experimental models due to their short life cycles and rapid reproduction rates. Different species may have a similar genetic makeup and, therefore, knowledge gained for one species could apply to others (Galagan *et al.*, 2005). Although initially considered part of the plant kingdom due to their immobility and cell walls, fungi are now considered to be their own eukaryotic kingdom (Deacon, 1997).

Nutritional modes of living organisms are described by how energy is obtained. Heterotrophs ingest or absorb organic carbon while autotrophs synthesize it from simple molecules. Chemotrophs use inorganic molecules to power the reduction of carbon dioxide to organic carbon while phototrophs use light energy. Fungi are chemoheterotrophs, obtaining energy from absorbed organic materials (Deacon, 1997; Carlile *et al.*, 2001). Based on metabolism, fungi have a closer relation to humans (also chemoheterotrophs) than they do to plants (photoautotrophs) (Carlile *et al.*, 2001).

1.2.1 Fungal Structure

Filamentous fungi grow by extending hyphae (singular = hypha) in a search for nutrients. Hyphae are long tubular filamentous cells, shown in Figure 1. Hyphal growth occurs only at tips as the cell wall expands in the region termed the apical growth zone (Jennings & Lysek, 1999). This results in a younger region near the apex and mature region at the base. As hyphal extension occurs, there is a flow of cytoplasm to the tip (Gow & Gadd, 1995). The overall structure of a branched fungal system is called the mycelium and is formed by hyphal branching (see Figure 1) in sub-apical regions (Griffin, 1994).

Figure 1. Filamentous *Aspergillus nidulans* grown on a BaF_2 substrate. Vertical arrows point to selected hyphal tips. The horizontal arrow shows the position of a hyphal branch. Scale bar = 200 µm.

Many fungal species have hyphae separated into cells or compartments by cross-walls, called septa (singular = septum), shown in Figure 2. Pores in the septa allow for movement of cytoplasm and organelles as the hypha grows (Griffin, 1994). In the case of hyphal damage, Woronin bodies (small, round, and dense organelles) act as plugs to block the pore. This prevents loss of cellular components from other sections of the hypha (Deacon, 1997; Jennings & Lysek, 1999).

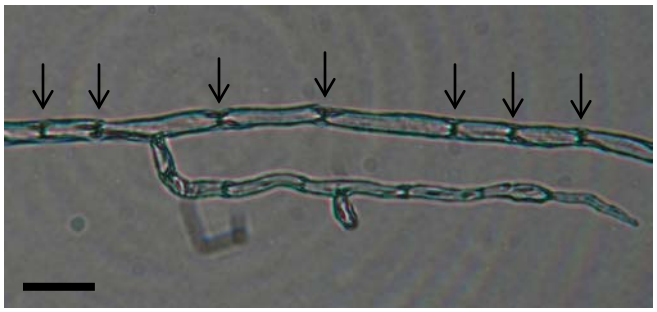

Figure 2. *Curvularia protuberata* grown on a MirrIR slide. The hypha is divided into sections by septa, indicated by arrows. Scale bar = 20 µm.

Vegetative hyphae lack reproductive structures (Jennings & Lysek, 1999). Typically, fungi grow in a vegetative manner as long as there are nutrients available. If conditions become unfavourable, spores may be produced. Spores serve to initiate new fungal colonies and to provide survival in the presence of adverse growth conditions (Carlile *et al.*, 2001). Spores may germinate upon exposure to appropriate conditions (typically a proper substrate, light, water, and nutrient source). This first emergence of a hypha from a spore is known as a germ tube.

1.2.2 Fungal Cell Structure

Fungal cells have an organization typical of many eukaryotic cells. The cell membrane defines the cell and contains the cytoplasm and organelles. The membrane consists of a phospholipid bilayer with sterols (mainly ergosterol) and membrane bound proteins (Deacon, 1997). Organelles found within the cytoplasm include nuclei, mitochondria, vacuoles, endoplasmic reticulum, and Golgi apparatus (Jennings & Lysek, 1999). However, in fungi, a cell wall composed of polysaccharides (mainly chitin, chitosan, glucans) with lesser amounts of proteins and lipids, surrounds cells and supports the cell membrane (Deacon, 1997). Cell walls are not typical of eukaryotic cells.

Fungal nuclei are around 1-5 µm in diameter and are the main gene location within cells (Griffin, 1994). There may be more than one nucleus per hyphal compartment (Carlile *et al.*, 2003). Mitochondria are another gene location within cells but mainly function to produce the cell's energy, adenosine triphosphate (ATP). Vacuoles act as storage sites within cells and are mainly located in basal hyphal regions. Calcium and nitrogen are the main storage components (Griffin, 1994; Carlile *et al.*, 2001); however, fungi may also accumulate polyphosphate in vacuoles (Deacon, 1997). The fungal secretory system produces cell wall components as well as enzymes necessary for acquiring nutrients from the surroundings. It is composed of the endoplasmic reticulum, Golgi apparatus, and vesicles (Deacon, 1997).

1.2.3 Saprotrophic Fungi: Characteristics and Spectra

Saprotrophic fungi obtain nutrients by feeding on dead plant or animal material; hence they are major players in natural decay. Initial work in our lab was focused on the spatially-resolved examination of saptrotrophic fungi. Samples were selected for important environmental and biological impacts. The goals of these early studies were to characterize hyphae grown under optimal conditions and examine changes in cells caused by suboptimal growth conditions (pH, temperature). Three model fungal systems were chosen; all were well characterized in the biological community. *Aspergillus nidulans*, *Neurospora*, and *Rhizopus* were examined using sFTIR (Szeghalmi *et al.*, 2007a; Jilkine *et al.*, 2008; Kaminskyj *et al.*, 2008); *A. nidulans* was examined with Raman and surface-enhanced Raman scattering (SERS) (Szeghalmi *et al.*, 2007b).

The fungal kingdom is divided into different groups, called phyla. The phylum Ascomycota contains the ascomycetes, characterized by the sac structure (ascus) where spores are produced. Zygomycetes, characterized by the spherical spores produced at zygosporangia, belong to the phylum Zygomycota. *Aspergillus nidulans* and *Neurospora* are both ascomycetes and, therefore, are more closely related to each other than to *Rhizopus*, a zygomycete. *Rhizopus* had much more intense absorption bands in the sugar region than either *A. nidulans* or *Neurospora* while the spectra for the latter two samples contained intense protein bands (Szeghalmi *et al.*, 2007a; Kaminskyj *et al.*, 2008). For each of the three, there was an increased total quantity of biochemical compounds (proteins, sugars, lipids) in mature hyphal regions as compared to tips (Szeghalmi *et al.*, 2007a; Jilkine *et al.*, 2008; Kaminskyj *et al.*, 2008). It appears that these saprotrophs

conserve their resources in basal regions as they grow. Examinations of *Neurospora* hyphae that had committed to sporulation revealed an increase of sugar and protein at the sites of spore production compared to vegetative hyphae (Jilkine *et al.*, 2008). Germinated spores were found to contain more sugar than the germ tube and germ tubes appeared to reserve content in basal regions (Jilkine *et al.*, 2008).

Raman and SERS were used for the characterization of *A. nidulans* (Szeghalmi *et al.*, 2007b). Fungal hyphae, grown on commercially available SERS substrates, were mapped to acquire Raman and SERS spectra. Hyphae were found to exhibit a characteristic 1050 cm^{-1} peak in Raman spectra. The same peak was observed across the surface of the substrate in the area surrounding hyphae in SERS maps, attributed to the presence of a compound or compounds exuded by the hyphae as they grew. Identification of the compound(s) was not possible.

1.2.4 Fungal Endophytes

As the name implies, endophytes are organisms (*e.g.* bacteria, viruses, algae, nematodes or fungi) living entirely within plants (Giménez *et al.*, 2007). Fungal endophytes (hereafter, endophytes) are associated with many, if not all, plants (Petrini, 1986) and most likely aided in plant movement onto land (Pirozynski & Malloch, 1975). Endophytes are symbiotic with plants, where symbiosis describes a close association between two organisms. When both partners benefit from the association, it is a mutualistic relationship; if one of the partners is harmed, the relationship is parasitic.

Endophytes are different from mycorrhizal fungi, another plant symbiont. Mycorrhizae reside in plant roots with extensions into the rhizosphere (soil area surrounding

roots) and aid plant absorption of nutrients (*e.g.* phosphorus, nitrogen) (Deacon, 1997). Endophytes, however, are found in a wider variety of plant tissues, including stems and leaves (Stone *et al.*, 2004). Colonized plants may gain protection from pathogens and drought (Giménez *et al.*, 2007). It is possible for a single plant to be colonized by over 40 different endophyte species (Zhang *et al.*, 2006). Despite their prevalence in the environment and even after many years of work focused on plant/fungal interactions, endophyte symbiosis is not fully understood (Rodriguez *et al.*, 2009).

Four different endophyte classes exist. Assignments are based on criteria such as host range, tissues colonized, and benefits to plants (Rodriguez *et al.*, 2009). Class 1 endophytes belong to the Clavicipitaceae family of fungi. There are few Class 1 endophytes, which are found mainly in cool climate grasses. They were originally recognized due to their generation of compounds that protect plants from herbivory. The majority of endophyte studies have focused on Class 1 endophytes. Class 2, Class 3, and Class 4 endophytes are all nonclavicipitaceous. These endophytes have a much broader host range than Class 1 endophytes. Class 2 endophytes can be present the roots, stems, and leaves of plants while Class 3 endophytes are found almost exclusively in above-ground tissues and Class 4 endophytes are only in plant roots.

Many endophytes from each of these classes confer benefits to plants; the majority are not specific to a certain habitat. For example, tolerance to drought is not a habitat-specific benefit since many plants in different regions receive this protection from endophytes (Rodriguez *et al.*, 2009). Recent pioneering studies of Class 2 endophytes in stressful environments have shown that certain forms of stress tolerance are conferred to plants via habitat-adapted symbiosis (Rodriguez *et al.*, 2008). This means that the

mechanism of induced tolerance is habitat-specific and will result only in regions where specific stresses (*e.g.* extreme temperature, salinity) are present (Rodriguez *et al.*, 2009).

Currently, only Class 2 endophytes are known to confer habitat-adapted benefits to plants. Class 1 endophytes have not been found to offer any habitat-adapted stress tolerances and only a limited quantity of work has been conducted for Class 3 and Class 4 endophytes (Rodriguez *et al.*, 2009). The majority of studies on plant response to stress have overlooked possible symbiotic interactions with other organisms (Rodriguez & Redman, 2008). While a large number of papers have examined Class 2, Class 3, and Class 4 endophytes over the past four decades, most have focused on their variety in plants rather than their ecological significance (Rodriguez *et al.*, 2009).

1.2.5 Endophytes & Stress Tolerance in Plants: Current Work

In my thesis, I have focused on three different Class 2 endophyte species: *Curvularia protuberata*, *Fusarium culmorum*, and *Colletotrichum magna*. Each confers a specific stress tolerance to their host plant as outlined below.

Dichanthelium lanuginosum plants inhabiting geothermal soils at Yellowstone National Park in the United States receive tolerance to the high temperature soils (up to 65ºC) from the endophyte *C. protuberata* (Redman *et al.*, 1999a; Redman *et al.*, 2002; Rodriguez *et al.*, 2004; Rodriguez *et al.*, 2005; Henson *et al.*, 2005; Márquez *et al.*, 2007; Rodriguez *et al.*, 2008; Rodriguez & Redman, 2008; Rodriguez *et al.*, 2009). However, when the plant and fungus are grown separately, neither has the ability to withstand temperatures above 40ºC (Rodriguez *et al.*, 2009). It has been determined that there is a virus, named *Curvularia* thermal tolerance virus (CThTV), within the fungus; *C. protuber-*

ata samples without this virus do not confer any heat tolerance to plants (Márquez *et al.*, 2007). Similarly, an American Type Culture Collection (ATCC) *C. protuberata* sample acquired from non-geothermal plants does not protect plants from high soil temperatures (Rodriguez *et al.* 2008).

Coastal dunegrass (*Leymus mollis*) plants grow at Puget Sound beaches in Washington State. *Fusarium culmorum* endophytes live symbiotically with these plants and help them to tolerate the high salt concentrations in coastal soils (Rodriguez *et al.*, 2008; Rodriguez & Redman, 2008; Rodriguez *et al.*, 2009). When grown separately, neither the plant nor the fungus can endure high salt concentrations. When salt stress is not present, symbiotic and nonsymbiotic plants both appear to prosper (Rodriguez *et al.*, 2008). An ATCC sample of *F. culmorum* isolated from non-coastal plants does not have the ability to confer any salt protection to plants in coastal settings (Rodriguez *et al.*, 2008; Rodriguez & Redman, 2008).

Colletotrichum magna is a plant pathogen, causing disease in cucurbits (*e.g.* watermelons, squashes) (Freeman & Rodriguez, 1992; Freeman & Rodriguez, 1993; Redman *et al.*, 1999c; Rodriguez *et al.*, 2008). However, the same isolate has the ability to offer pathogen protection to tomato plants in agricultural habitats where there is a high prevalence of disease (Rodriguez *et al.*, 2008). A non-pathogenic mutant of *C. magna* has been generated by ultraviolet mutagenesis (Freeman & Rodriguez, 1992; Freeman & Rodriguez, 1993; Redman *et al.*, 1999c). This *C. magna* sample can also provide disease resistance to plants. Cucurbits colonized by the non-pathogenic mutant and later exposed to lethal amounts of several pathogenic fungi, including the original *C. magna* sample, do

not show disease symptoms (Freeman & Rodriguez 1993; Redman *et al.*, 1999b; Redman *et al.*, 1999c).

Each of these endophytes imparts a unique benefit (protection from heat, salt or pathogens) to their host plant. In addition, all three endophytes offer some degree of drought tolerance to colonized plants (Redman *et al.*, 2001; Rodriguez *et al.*, 2004; Rodriguez *et al.*, 2005; Márquez *et al.*, 2007; Rodriguez *et al.*, 2008; Rodriguez & Redman, 2008; Rodriguez *et al.*, 2009). Despite studies focusing on Class 2 endophytes over the past ten years (Redman *et al.*, 1999a; Redman *et al.*, 1999b; Redman *et al*., 2001; Redman *et al.*, 2002; Rodriguez *et al.*, 2004; Rodriguez *et al.*, 2005; Henson *et al.*, 2005; Márquez *et al.*, 2007; Rodriguez & Redman, 2008; Rodriguez *et al.*, 2008; Rodriguez *et al.*, 2009), the exact mechanism by which habitat-adapted symbiosis occurs has yet to be elucidated. The use of FTIR and Raman spectroscopy can provide insight into the biochemical composition of these endophytes with sub-cellular resolution. Differences in the spectra of the habitat-adapted and non habitat-adapted isolate of each sample could offer clues about the mechanism behind habitat-adapted symbiosis.

1.3 Principles of Vibrational Spectroscopy

1.3.1 Electromagnetic Radiation

Electromagnetic radiation is described by its wavelength (λ), frequency (ν), or wavenumber ($\tilde{\nu}$). Wavelength is the distance between adjacent wave crests, typically reported in nanometers (nm) for visible light or microns (μm) for infrared (IR) radiation. The frequency is the number of waves per unit time, given in Hertz (equivalent to s^{-1}). Wavenumbers describe the number of waves per distance, given in units of reciprocal centimetres (cm^{-1}). Wavelength, frequency, and wavenumber relate (in a vacuum) by

$$\lambda = \frac{c}{\nu} = \frac{1}{\tilde{\nu}} \tag{1}$$

where c is the speed of light. Wavelength is inversely proportional to energy; shorter wavelengths are higher in energy. Wavenumbers are directly proportional to energy.

1.3.2 Molecular Vibrations

The energy of a molecule includes vibrations, translations, rotations, and electronic transitions. All molecules have 3N degrees of freedom, where N is the number of atoms in the molecule. For non-linear molecules, three of these degrees of freedom refer to translations and three refer to rotations (for linear molecules, only two degrees of freedom are rotations). All the remaining degrees of freedom are vibrational motions, giving a non-linear molecule 3N-6 vibrational motions (linear molecules have 3N-5 vibrational motions).

The vibration of a diatomic molecule can be approximated by the harmonic oscillator model. In a simple macroscopic diatomic oscillator, two balls are connected by a spring, representing the atoms and the bond, respectively. Hooke's law describes this model by

$$F = -\frac{dV(x)}{x} = -kx \tag{2}$$

where F is the restoring force, V is the potential energy, k is the force constant, and x is the displacement of the atoms from their equilibrium bond length. Integration gives

$$V(x) = \tfrac{1}{2}kx^2 \tag{3}$$

which can be plotted as a harmonic potential, as shown in Figure 3. The energy of a given vibrational level is calculated by

$$E_{\mathrm{v}} = (\mathrm{v} + \tfrac{1}{2})h\nu \tag{4}$$

where h is Planck's constant and v is the vibrational quantum number, which must be an integer. The vibrational frequency (ν) for a molecule is dependent upon the force constant of the bond and the reduced mass (μ). It can be calculated from

$$\nu = \frac{1}{2\pi}\sqrt{\frac{k}{\mu}} \tag{5}$$

The reduced mass is dependent upon the atoms involved in the bond and, for a diatomic molecule, is determined from

$$\mu = \frac{m_A m_B}{m_A + m_B} \tag{6}$$

where m_A and m_B represent the masses of atoms A and B in the molecule.

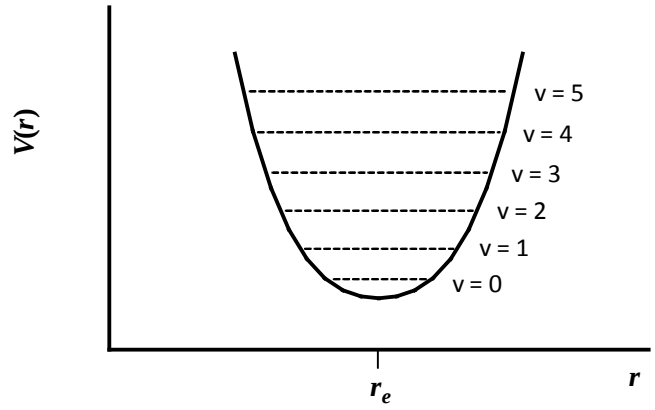

Figure 3. Harmonic potential for a diatomic molecule showing the relationship between potential energy and interatomic distance (r). The equilibrium bond length is marked by r_e. Dotted lines denote vibrational energy levels of quantum number v.

The difference in energy for two adjacent energy levels, E_{v}, and $E_{\mathrm{v}+1}$, corresponds to $h\nu$. The energy of vibrational energy level E_{v} is given by Equation 4. The energy of vibrational energy level $E_{\mathrm{v}+1}$ is therefore

$$E_{\mathrm{v}+1} = (\mathrm{v} + 1 + \tfrac{1}{2})h\nu \qquad (7)$$

The difference between these two adjacent vibrational energy levels can be expressed from the difference of Equation 4 and Equation 7

$$E_{\mathrm{v}+1} - E_{\mathrm{v}} = (\mathrm{v} + 1 + \tfrac{1}{2})h\nu - (\mathrm{v} + \tfrac{1}{2})h\nu = h\nu \qquad (8)$$

The IR region of the spectrum typically corresponds to the frequency of light required to change the vibrational energy of a molecule. For most chemical bonds, many of the characteristic modes will be between 400 and 4000 cm^{-1}.

The harmonic approximation is valid for low vibrational quantum numbers but does not give an accurate representation at higher vibrational quantum numbers; it fails to predict the dissociation energy. Vibration of a diatomic molecule is better represented by an anharmonic potential which predicts the energy of dissociation as the atoms move toward infinite separation, as seen in Figure 4.

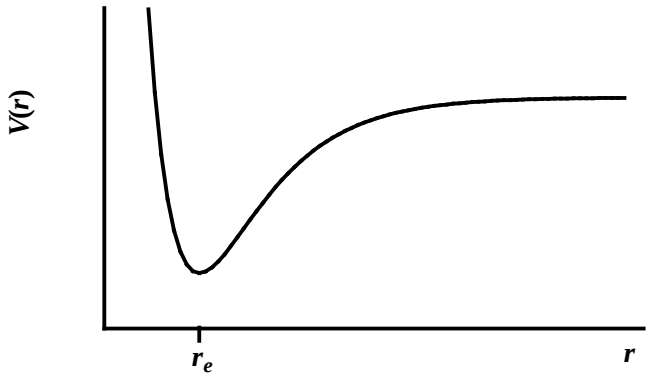

Figure 4. An anharmonic potential for a diatomic molecule showing the relationship between energy and atomic separation (r). The equilibrium bond length is marked by r_e.

Since the energy required to induce a vibration depends on the atoms in the bond and the bond strength, a given functional group (*e.g.* C=O) will always vibrate at approximately the same energy. Different bonds or functional groups vibrate at different energies (*e.g.* C-O vs. C=O, C-H vs. O-H). The exact energy of an absorption band will be influenced by the environment around the functional group (inter- and intramolecular interactions) and the composition of the normal mode. Therefore, a vibrational spectrum is unique to each molecule and can be used as a "fingerprint" for its identification.

1.4 Fourier Transform Infrared Spectroscopy

IR spectroscopy uses mid-IR radiation (2.5 μm to 25 μm) to induce molecular vibrations. Motions are IR active (absorb IR radiation) if a change in molecular dipole moment (μ) results during the vibration. The dipole moment describes an uneven allocation of electron density (*e.g.* for heteronuclear diatomic molecules, one atom has a partial positive charge and the other a partial negative charge). The condition of IR activity is

$$\left(\frac{\partial \mu}{\partial q}\right) \neq 0 \tag{9}$$

where q gives the normal coordinates of the atoms in a bond. Homonuclear diatomic molecules (*e.g.* N_2, H_2) are not IR active since their molecular dipole moments remain zero during stretching of the bond. The intensity of an absorbance band depends on the degree to which the dipole moment changes during a vibration and is proportional to

$$\left(\frac{\partial \mu}{\partial q}\right)^2 \tag{10}$$

1.4.1 Infrared Spectra

In IR spectra, values on the x-axis are given in wavenumbers since they are directly proportional to energy (see Equation 4). For the mid-IR region, the x-axis typically ranges from 4000–400 cm^{-1}, but can be extended or limited by the detector material.

IR spectra are often displayed with the y-axis in % Transmittance (T), calculated from

$$T = \frac{I}{I_0} \tag{11}$$

where I_0 is the radiant power of the light travelling to the sample and I is the radiant power of the light transmitted by the sample. In this format, quantitative analysis of IR spectra cannot be performed. Transmittance can be converted to absorbance (A) by

$$A = -\log T = -\log\left(\frac{I}{I_0}\right) \tag{12}$$

Figure 5 shows a spectrum displayed in % Transmittance and in absorbance. Absorbance is directly proportional to concentration (c), as summarized by Beer's Law

$$A = \varepsilon bc \tag{13}$$

where b is the pathlength and ε is the molar absorptivity of the sample. Spectra can be collected in transflectance mode for samples on IR reflective substrates, which also allows for quantitative analysis.

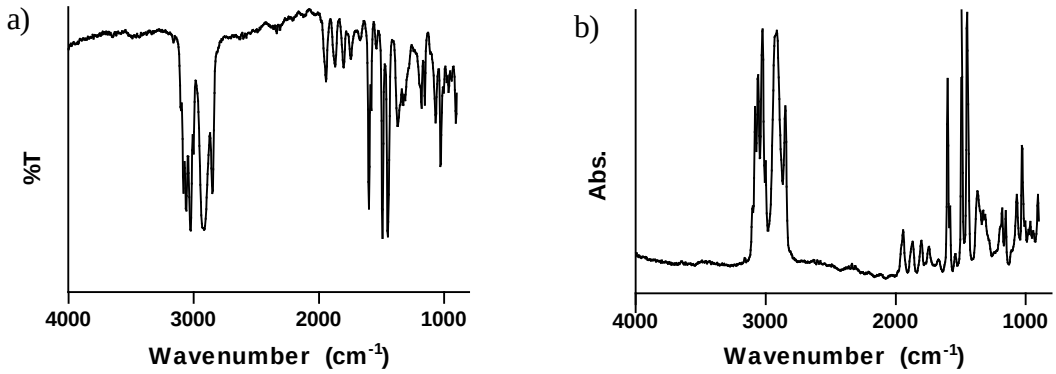

Figure 5. FTIR spectrum of polystyrene film displayed in a) %T and b) absorbance.

1.4.2 Dispersive IR

Early IR spectrometers were dispersive instruments. A prism or grating is used to separate the different wavelengths of radiation emanating from the source; typically, a slit is used to select a small wavelength range. The selected wavelength element then travels to the sample. The position of the dispersive element can be rotated to allow each wavelength element to pass through the slit. In dispersive instruments, there are typically two beam paths, one for the sample and one for a reference. These instruments have been replaced by Fourier transform (FT) spectrometers.

1.4.3 Michaelson Interferometer

The heart of an FTIR spectrometer is the interferometer. Figure 6 shows a diagram of a Michaelson interferometer. The key components are a light source, two mirrors (one moving, one stationary), and a beamsplitter (often KBr). IR radiation travels from the source to the beamsplitter, where about half is sent to each mirror. The IR radiation is reflected by the mirrors and travels back to the beamsplitter where it recombines, travels towards the sample, and to the detector. Since one mirror is moving while the other is stationary, light recombining at the beamsplitter may be out of phase (due to mis-matched path lengths) or in phase. Using monochromatic light as an example, the effect of different mirror positions (retardation, δ) can be examined. If both mirrors are equal distance from the beamsplitter, the light travels the same distance to each ($\delta = 0$). It is completely in phase when it recombines at the beamsplitter, giving constructive interference. A path difference of half the wavelength of light ($\delta = \lambda/2$), causes the waves to be out of phase

when they recombine, resulting in completely deconstructive interference. A path difference of one wavelength ($\delta = \lambda$) gives constructive interference again. In reality, all wavelengths of mid-IR radiation travel through the interferometer at the same time; the sum of all wavelengths in phase, slightly out of phase, or completely out of phase over the range of motions of the mirror produces the interferogram at the detector (see section 1.4.4).

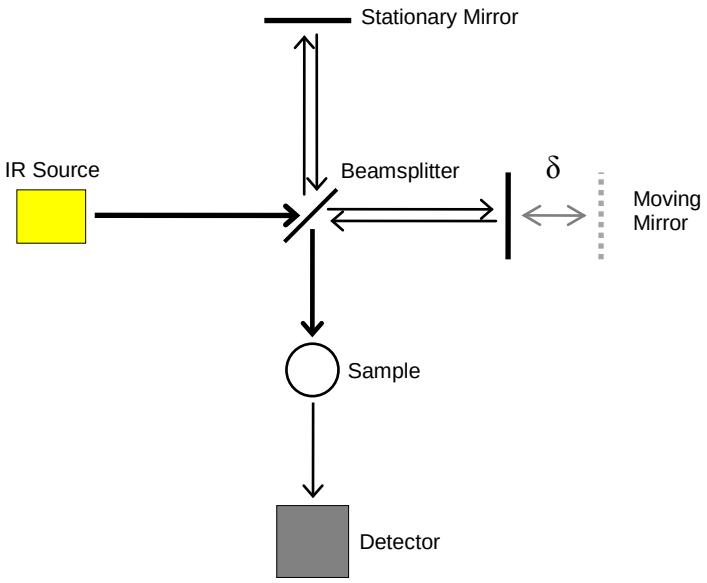

Figure 6. Schematic of a Michaelson Interferometer. Retardation (δ) represents the different path lengths for light travelling to the moving mirror versus the stationary mirror.

1.4.4 Mathematics of the Fourier Transform

The FT is a mathematical operation used to convert from the time domain (time to move the mirror) to the frequency domain and is described by two equations. One equation converts from the time domain to the frequency domain by

$$B(v) = \int_{-\infty}^{\infty} I(\delta)\cos(2\pi v\delta)d\delta \tag{14}$$

while the other converts from the frequency domain to the time domain by

$$I(\delta) = \int_{-\infty}^{\infty} B(v)\cos(2\pi v\delta)dv \tag{15}$$

In both equations, $I(\delta)$ is the intensity as a function of time (retardation) and $B(v)$ is the intensity as a function of frequency.

An FT conversion between the time and frequency domains for a single wavelength of light is shown in Figure 7. This monochromatic conversion is a simplified example. In reality, the detector sees an interferogram that results from all wavelengths of light in the detector range, as shown in Figure 8.

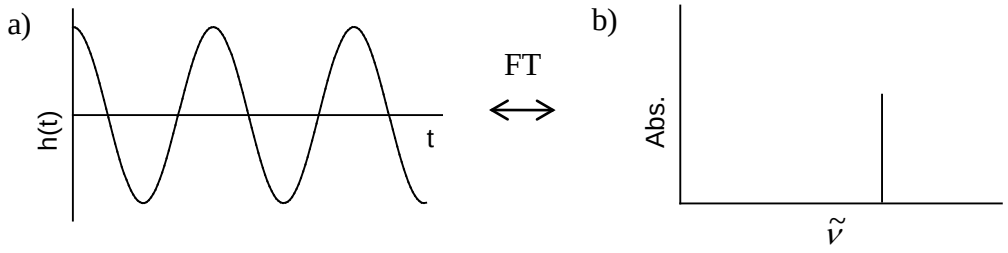

Figure 7. Conversion from a) time domain to b) frequency domain (monochromatic light) via FT.

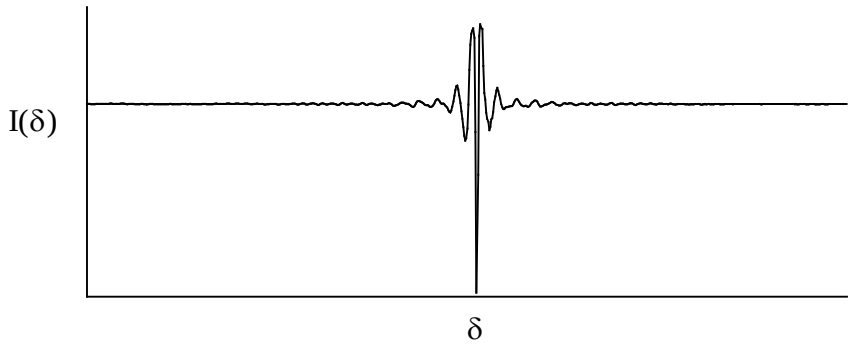

Figure 8. An interferogram. The intensity at the detector is plotted against mirror retardation (δ).

Prior to sample collection, a background is acquired. The background spectrum is recorded without a sample in place and only shows the output from the light source modified by the instrument response (and residual water vapour or carbon dioxide present in the system). The sample spectrum is obtained from a ratio of the sample scan to the background. Background and sample spectra are shown in Figure 9. At a synchrotron, the background also contains absorptions due to passage through the diamond window, shown in Figure 10.

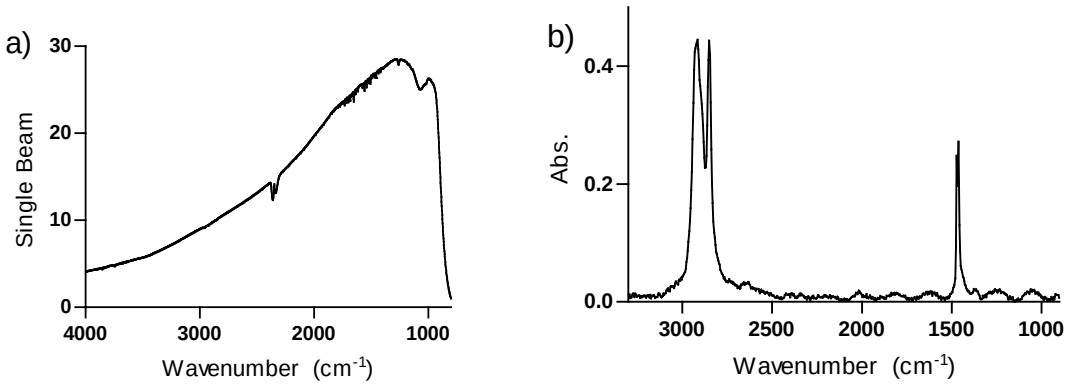

Figure 9. a) A typical background spectrum from an FTIR bench (single beam, response at detector) and b) a sample spectrum of polyethylene film that was ratioed to the background.

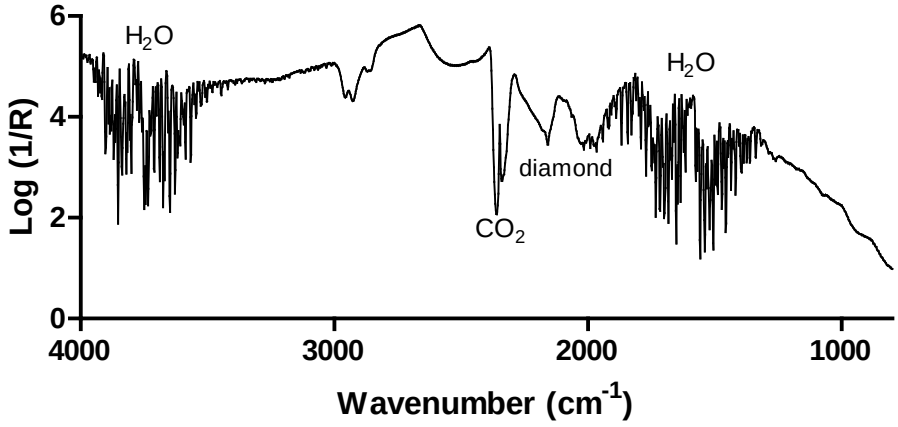

Figure 10. A synchrotron background spectrum. In addition to the usual water and carbon dioxide bands, absorptions by a diamond window are also present.

1.4.5 Advantages of the Fourier Transform

FT instruments have advantages over dispersive IR: the Jacquinot (or throughput) and the Fellgett (or multiplex) advantages. An FT instrument does not contain slits (see section 1.4.2) and therefore, more of the source radiation reaches the detector than in a dispersive IR spectrometer. This is the throughput advantage. Signal averaging with an FT spectrometer means that given the same amount of time (and collecting data at the same spectral resolution), an FT instrument gives a better signal-to-noise ratio (S/N) than a dispersive instrument. This is the multiplex advantage.

1.4.6 Infrared Sources

FTIR spectrometers typically employ a globar source (often a silicon carbide rod that emits IR radiation when heated). Another IR source is a synchrotron. A synchrotron is a particle accelerator; electrons are injected and travel around the ring at close to the speed of light. Bending magnets alter the path of the electrons as they circle the ring. As a result, they are slowed down (lose energy) and emit radiation from IR to X-ray (Dumas *et al.*, 2006). Beamlines devoted to certain types of analysis (*e.g.* X-ray absorbance, X-ray diffraction, mid-IR spectroscopy) are placed around the circumference of the ring and selected regions of the spectrum (*e.g.* X-ray, mid-IR) travel to their respective instruments. Synchrotron IR is often 1000 times brighter than globars (Miller & Smith, 2005; Reffner, 1998) due to the smaller emission area and angle (Dumas & Miller, 2003). This is especially useful when samples are small or contain little material (Duncan & Williams,

1983). The spatial resolution that can be achieved using a synchrotron is much greater than with a globar (see section 1.4.9).

1.4.7 Infrared Detectors

IR detectors are generally either thermal or quantum detectors. Thermal detectors sense a change in temperature while quantum detectors rely on the interaction between IR radiation and electrons within the detector, which are excited to a higher energy state (Griffiths & de Haseth, 2007). Common thermal detectors include deuterated triglycine sulphate (DTGS) and deuterated l-alanine-doped triglycine sulfate (DLATGS). A widely used quantum detector is the mercury cadmium telluride (MCT) detector. Tradeoffs exist between sensitivity and the wavelength range. The cut-off for MCT detectors varies, but the longer its wavelength range, the lower its sensitivity. MCT sensitivities are superior to DTGS; however DTGS detectors can detect longer wavelengths (lower wavenumbers) than MCT detectors (Griffiths & de Haseth, 2007).

The advent of linear array and focal plane array (FPA) detectors in IR microscopy has increased the ease and efficiency of microscopic examinations. Linear array detectors contain a number of detectors in a line. FPA detectors contain numerous individual detectors aligned in a grid. Both allow for the simultaneous collection of multiple spectra. The detection material for array detectors is typically MCT (Bhargava & Levin, 2005).

1.4.8 Infrared Microscopy

FTIR microscopy couples IR radiation to a microscope to gather spatially resolved (on the order of microns) spectra. An aperture is adjusted so that a small user-defined sample

area is exposed to the beam of IR light (with limitations, see section 1.4.9). IR microscopy produces 2-D chemical images of samples. Samples placed on a computer-controlled stage can be moved through the IR beam (raster scanning). Spectra are collected along a grid within a defined map area. Maps can be processed for spectral features (*e.g.* peak area, ratio of peaks) and displayed as a false-colour image to correlate composition with location in sample.

1.4.9 Spatial Resolution in IR Microscopy

Spatial resolution in FTIR microscopy is controlled by an aperture that limits the area of sample exposed to the radiation. As aperture size is reduced, the throughput decreases and, therefore, S/N decreases as well. Thus, the number of scans summed for a spectrum is increased to improve the S/N for smaller apertures. In order to maintain adequate S/N with a thermal source, the aperture size must be ≥ 20 μm (Smith, 2002; Dumas & Miller, 2003). Apertures with dimensions similar to the wavelengths of IR radiation cause a further decrease in throughput as a result of diffraction effects (Bhargava & Levin, 2005).

The use of a synchrotron IR source allows for analysis at cellular and sub-cellular resolution (Dumas *et al.*, 2006). The ability to use smaller apertures with synchrotron radiation results from the greater brightness of a synchrotron beam (Carr, 1999). At a synchrotron, spatial resolution is diffraction limited. The diffraction limit is dependent upon the wavelength of light and is given by

$$\Delta x \geq 0.61 \frac{\lambda}{n \sin \theta} \qquad (16)$$

where Δx represents the separation between two points. Numerical aperture (N.A.) of the objective is given by $n \sin\theta$ where n denotes the refractive index between the objective and sample and θ is the acceptance angle for the objective (Lasch & Naumann, 2006). As a result, spatial resolution is better at the shorter wavelength (larger wavenumber) region of the spectrum than at longer wavelengths (smaller wavenumber). In the mid-IR range (4000 – 400 cm^{-1}), the diffraction limit is around 10 μm (Reffner, 1998).

1.4.10 Infrared Band Assignments in Biological Tissues

Despite the large number of compounds in biological samples, their IR spectra appear to be simple, with only a few bands present. However, peaks seen in spectra are the summation of many underlying bands caused by all the different motions in all the molecules present within the sample. Therein lies the challenge of spectral interpretation. Some of the most important bands are described here.

A spectrum of biological tissue (mouse retina section) is shown in Figure 11. Transflectance spectra are displayed with values on the y-axis as log(1/R) by default in software, and this label is retained throughout this thesis. However, the y-axis should read transflectance.

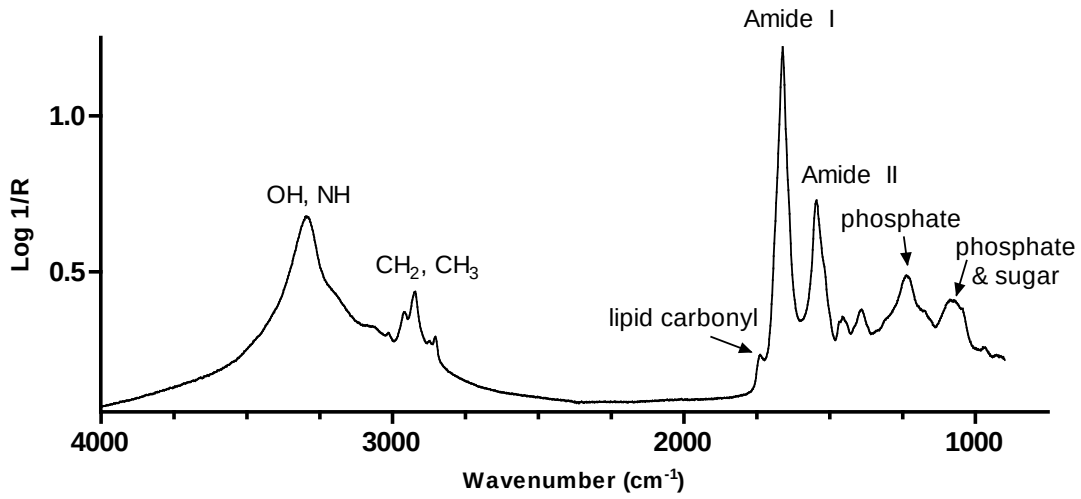

Figure 11. FTIR spectrum of mouse retina tissue (posterior segment of the retina, inner nuclear layer). The mouse was fed an omega-6 fatty acid enriched diet and sacrificed at 12 weeks. The spectrum shows many of the bands typically seen in biological tissues.

The broad band present between 3100 and 3200 cm^{-1} is caused by stretching of the OH bond in hydroxyl groups and NH groups in proteins. CH_2 and CH_3 stretching motions appear in spectra in the 2800 to 3000 cm^{-1} range. These functional groups are present in many molecules, in particular the long carbon chains of fatty acid esters that form the lipid bilayer membrane encasing cells and organelles. As a result, these peaks are often used to examine lipid content in biological tissues. The stretching of lipid carbonyl groups typically occurs between 1720 and 1750 cm^{-1}. The two strong bands between 1500 and 1700 cm^{-1} are known as the amide I and amide II bands. The amide I band is the higher energy band and is caused by stretching of the carbonyl groups in proteins. Due to the interactions involved in forming protein secondary structure (*e.g.* hydrogen bonding), protein carbonyl stretches are found at lower wavenumber than the carbonyl

stretch in lipids. The amide II band is lower in energy than the amide I band and is mainly a result of the CN stretch coupled to the NH bend in proteins. Bands present around 1230 cm^{-1} and 1075 cm^{-1} have been ascribed to phosphate groups in nucleic acids (DNA, RNA) and phospholipids. Finally, bands in the region of about 900 to 1200 cm^{-1} are the result of vibrations in carbohydrates (*e.g.* C-O-C ring vibrations) and other phosphate modes. A more detailed assignment of common IR bands arising from biological samples is given in Table 1; a more extensive assignment of IR bands has been assembled by Movasaghi *et al.* (2008).

Table 1. Assignment of IR bands common in the spectra of biological tissues (based on Maquelin *et al*., 2002a, Szeghalmi *et al.*, 2007a, Kaminskyj *et al.*, 2008).

Wavenumber (cm^{-1})	**Assignment**
3200-3100	υ OH, NH
2958-2953	$\upsilon_{asym}\, CH_3$
2930-2918	$\upsilon_{asym}\, CH_2$
2876-2870	$\upsilon_{sym}\, CH_3$
2854-2850	$\upsilon_{sym}\, CH_2$
1750-1720	υ C=O
1690-1620	υ C=O (amide I)
1550-1520	υ CN; δ CNH (amide II)
1250-1220	υ_{asym} P=O
1200-900	υ CO, CC; δ COH, COC
1090-1075	υ_{sym} P=O

υ = stretching, δ = deformation

1.4.11 Practical Considerations for Analysis with Infrared Spectroscopy

IR spectroscopy is a non-destructive technique; IR radiation causes only extremely minimal sample heating (about 0.5ºC) (Holman *et al.*, 2003). Samples can be analyzed multiple times with IR spectroscopy or subsequently analyzed by a number of other techniques. However, water and carbon dioxide have IR active vibrations and both gas-phase molecules are common in the atmosphere. Figure 12 shows a spectrum of the water and carbon dioxide bands that can interfere in spectra. Instruments are typically equipped with a dry nitrogen gas purge, while a background spectrum recorded prior to the sample spectrum accounts for any residual amounts of water vapour and carbon dioxide that may still be present in the system. This means that the analysis of aqueous samples by FTIR is not easy.

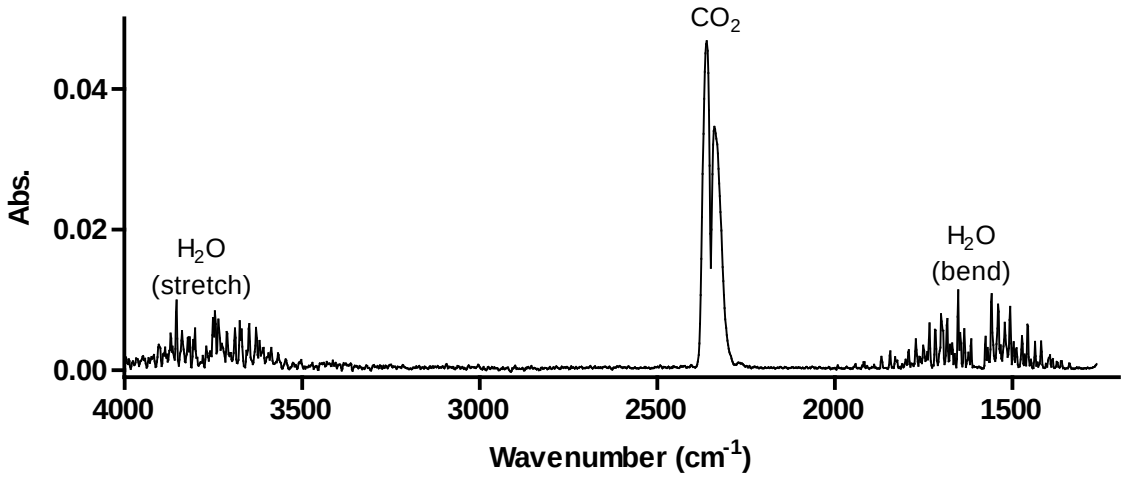

Figure 12. Spectrum of atmospheric gas-phase water and carbon dioxide. The narrow bands present between 1300 and 1900 cm^{-1} and 3500 and 4000 cm^{-1} are due to H_2O. The band envelope with two maxima between 2300 and 2400 cm^{-1} is caused by CO_2.

1.4.12 Scattering Artefacts in IR Spectra

Numerous challenges must be addressed in order to successfully carry out FTIR microscopic examinations of filamentous fungi. Both the size and shape of hyphae lead to scattering artefacts in spectra, as shown in Figure 13. Figure 11 offers a good example of a spectrum that does not contain scattering artefacts. Fungal hyphae are small and cylindrical. Hyphal dimensions (typically 2-10 μm in diameter) are on the same order as the wavelengths of IR radiation (2.5-25 μm). These physical features can be the source of some well known scattering artefacts: Mie, dispersion, and an apparent inversion of bands.

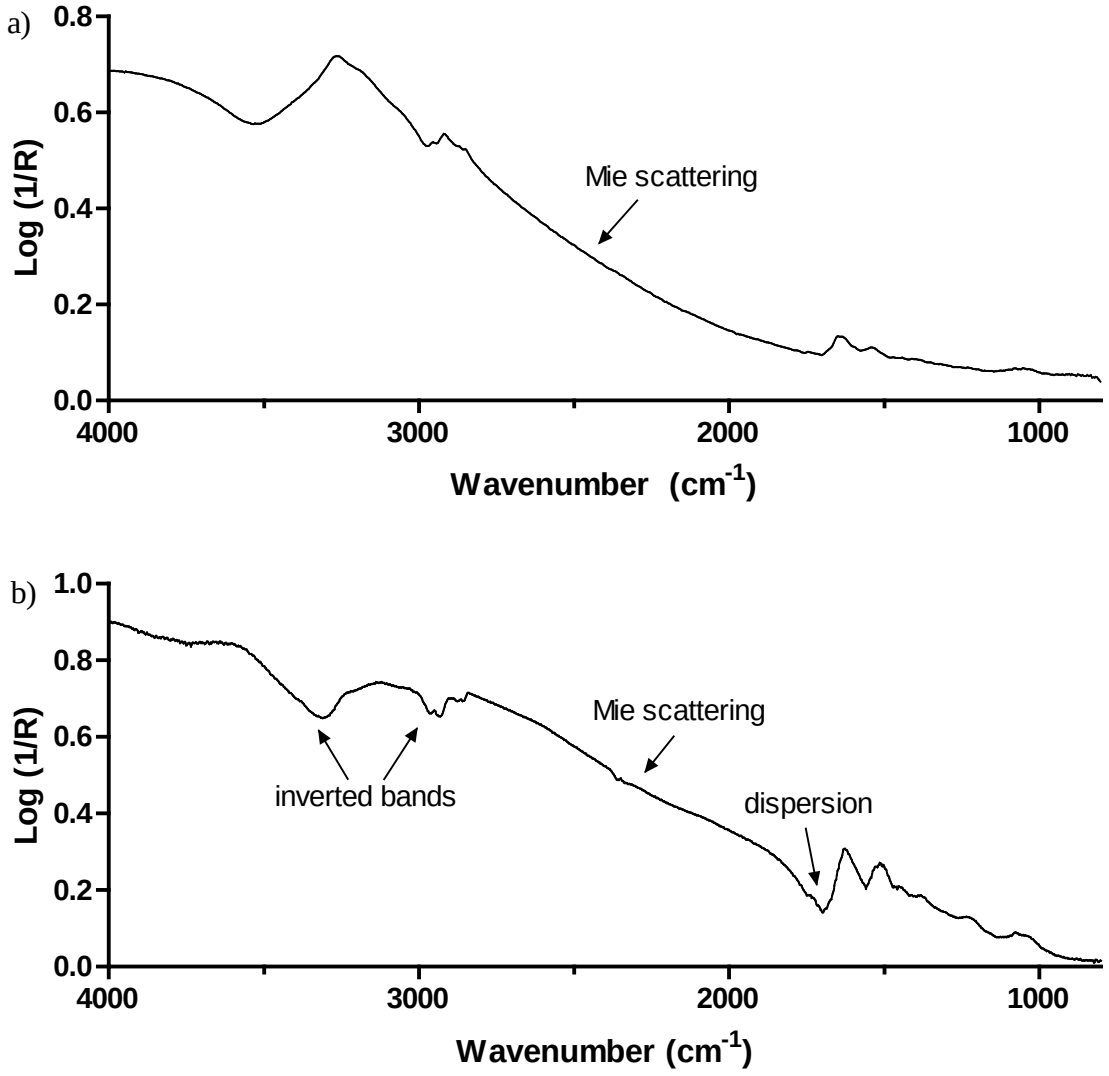

Figure 13. a) Spectrum collected 100 µm from the tip of an FcRed1 hypha. The sloping baseline is most likely caused by Mie scattering, a result of the size and cylindrical shape of hyphae. b) Spectrum collected at the tip of a Cp4666D hypha. The spectrum displays several artefacts: inverted OH and CH regions, dispersion, and Mie scattering. Both spectra were collected using a 10 x 10 µm aperture.

Origins of scattering artefacts in spectra

Mie scattering refers to the scattering of electromagnetic radiation by spherical particles when the wavelength of light has a similar dimension to that of the sphere (Bassan *et al.*, 2009). The diameters of fungal hyphae (2-10 μm) are similar to the wavelength of the IR radiation (2.5-25 μm) used for analysis. Nuclei are spherical and can also lead to scattering, the degree of which may be greater than that caused by whole cells (Pijanka *et al.*, 2009).

The dispersion artefact is a result of resonant Mie scattering (Bassan *et al.*, 2009; Bassan *et al.*, 2010). Mie scattering depends on a sample's refractive index, which should not change for a non-absorbing sphere. However, in the absorbing case, the refractive index changes on either side of the absorption band (where no IR radiation is absorbed), leading to resonant Mie scattering (Chalmers, 2002; Bassan *et al.*, 2009; Bassan *et al.*, 2010). A more thorough theoretical model of dispersion artefacts has been derived from Maxwell's equations (Davis *et al.*, 2010a; Davis *et al.*, 2010b).

Figure 14 shows the imaginary and real parts of the complex refractive index (absorption and dispersion lineshapes, respectively). The summation presented shows the familiar "dip" to the left of the absorption band and the change in position of the absorption band maximum.

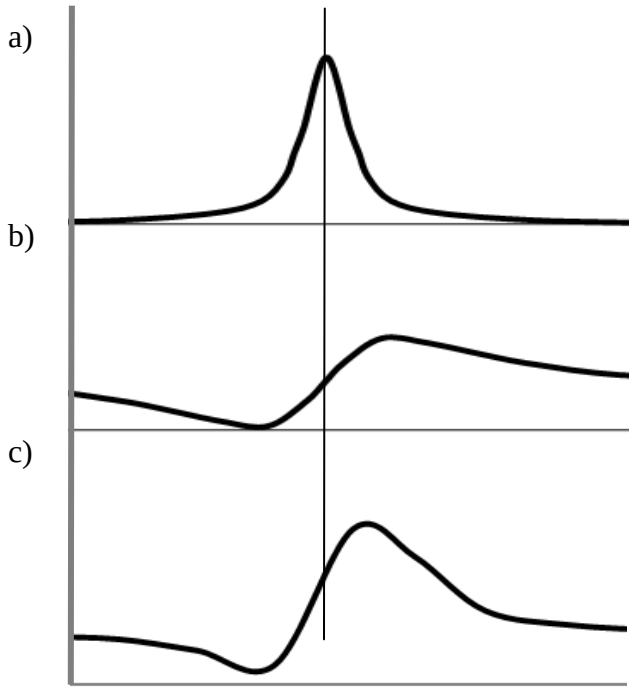

Figure 14. a) Absorption line shape due to the imaginary part of the refractive index and b) dispersion line shape due to the real part of the refractive index. c) Sum of (a) and (b). Note the dip to the left of the absorption band and the shift in the frequency of the peak maximum.

Another artefact common in spectra is the inversion of peaks (CH stretch, OH & NH stretch) in the region of 3500 to 2800 cm^{-1} (see Figure 13b). The origin of this artefact is likely due to reflection off the curved hypha.

Experimental observations

The sloped baseline present in hyphal spectra (see Figure 13) is likely caused by Mie scattering, an effect previously observed in IR spectra of cells (*e.g.* Mohlenhoff *et al.*,

2005; Romeo *et al.*, 2006; Lee *et al.*, 2007), including fungal cells (Szeghalmi *et al.*, 2007a; Kaminskyj *et al.*, 2008). This sloped baseline causes distortions of peak intensities and positions, mainly in the shorter wavelength regions (*e.g.* CH stretches) (Lee *et al.*, 2007).

A dispersion artefact may also be visible in spectra, as in Figure 13b. Dispersion results in the appearance of a "dip" in spectra at slightly higher energy to the amide I band; the amide I band maximum appears at a lower frequency in the spectrum and its intensity is artificially decreased, skewing the amide I to amide II ratio. Analysis of the amide I band, and therefore protein structure, becomes difficult since both the apparent position of band maximum and the intensity are altered. This artefact is common at the edges of tissues and cells or when there is an air-gap present between the sample and substrate, and is especially prominent for transflectance measurements (Romeo & Diem, 2005a; Davis *et al.*, 2010a). Since fungal hyphae and spores have diameters smaller than the apertures used for measurements, spectra are effectively always collected at the edge of cells and the appearance of the dispersion artefact in hyphal spectra is common.

The presence of inverted bands (see Figure 13b) in spectra appears to be related to the curved edge of the hypha present in the aperture. Additionally, inverted bands are often more common in spectra collected at the tips of hyphae.

Prevention and correction of scattering artefacts

Sample preparations can have an effect on the degree of scattering in spectra. Additionally, several theoretical models and correction methods for scattering in spectra have

been proposed; however, none of these correction methods have been applied in this thesis. The prevention and correction of scattering in spectra is outlined below.

One way to potentially avoid (or at least reduce) dispersion artefacts in spectra is to perform transmission measurements, rather than transflection measurements; however, chosen substrates must be transparent to IR radiation (*e.g.* KBr, BaF_2). These substrates are more expensive, often hygroscopic, or more fragile than gold or MirrIR substrates. Additionally, tissues measured on BaF_2 and ZnSe substrates have still been found to contain dispersion artefacts in spectra collected at the edge of tissues (Romeo & Diem, 2005a; Romeo & Diem, 2005b).

Recently, a rigorous theoretical model based on Maxwell's equations has been applied to FTIR microscopic measurements of homogeneous (Davis *et al.*, 2010a) and heterogeneous samples (Davis *et al.*, 2010b). The model focuses on both transmission and transflection measurements, takes into account effects such as focusing and sample geometry and predicts the artefacts observed in experimental data. This model is the most comprehensive prediction of scattering artefacts in spectra to date and correction methods are currently in development in the Bhargava lab at the University of Illinois at Urbana-Champaign (Davis *et al.*, 2010a; Davis *et al.*, 2010b).

Other scattering correction methods have been previously published. A correction for Mie scattering has been proposed, wherein the amount of Mie scatter in spectra is estimated from the distorted spectrum. A pseudo-fit to the Mie scattering is created and subtracted, giving a spectrum without a sloped baseline (Kohler *et al.*, 2008). A method to correct for dispersion has been proposed that involves separation of the absorptive and reflective components (Romeo & Diem, 2005b). Additionally, a recent extension of a Mie

scattering correction has been proposed to correct for both the sloped baselines and sharp dips in spectra (Bassan *et al.*, 2010). This method is the basis for a recently available software application and will be used in the future to correct for the sloped baselines and dips in spectra.

It has been determined that rotation of a hypha with respect to a rectangular aperture (displayed in Figure 15) can correct for inverted bands in synchrotron spectra. This artefact appears to be dependent on reflection off of the curved hypha.

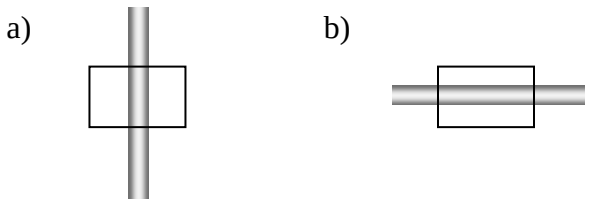

Figure 15. Orientation of a hypha with respect to a rectangular aperture. a) The orientation which led to inverted bands in the OH, NH and CH stretch regions of spectra. b) Rotation of the hypha by 90º removes the appearance of this artefact in spectra.

1.5 Raman Spectroscopy

Raman scattering is a weak process by which photons are inelastically scattered at different wavelengths after interacting with molecules and was first detected by C.V. Raman in 1928. Similar to IR spectroscopy, Raman is used to gain molecular information about a sample from its vibrational spectrum. Raman and IR spectroscopies are complementary techniques; some vibrational modes are only IR active, some are only Raman active, and some modes are both IR and Raman active.

Typically when a photon interacts with a molecule, it is elastically scattered at the same energy (same wavelength) as that of the incident photon. This process is known as Rayleigh scattering. However, a small number of photons will be inelastically scattered at either higher or lower energy than the incident photon. The change in energy (or wavelength shift) corresponds to the amount of energy required to cause a certain vibrational motion. Raman scattering is an inherently weak process, with an intensity on the order of about 10^{-5} the intensity of the incident radiation (Ferraro *et al.*, 2003).

Figure 16 shows the processes of Rayleigh and Raman scattering. When Rayleigh scattering occurs, a molecule is excited from a ground vibrational energy level to a virtual energy state (a non-stable energy level lower in energy than the first electronic excited state) and returns back to the ground vibrational energy level. This is the most probable occurrence. Stokes Raman scattering occurs when a molecule is excited from the ground vibrational level ($v = 0$) to a virtual energy state and then goes to an excited vibrational energy level ($v = 1$). This process involves a shift of the incident radiation to lower energy. Anti-Stokes scattering occurs when a molecule in an excited vibrational energy

level (v = 1) is excited to a virtual energy level, then returns to the ground vibrational energy level (v = 0). In this case, there is a shift of the incident radiation to higher energy. Stokes scattering is more probable than anti-Stokes scattering since the majority of molecules are in the ground vibrational energy level (v = 0) under ambient conditions.

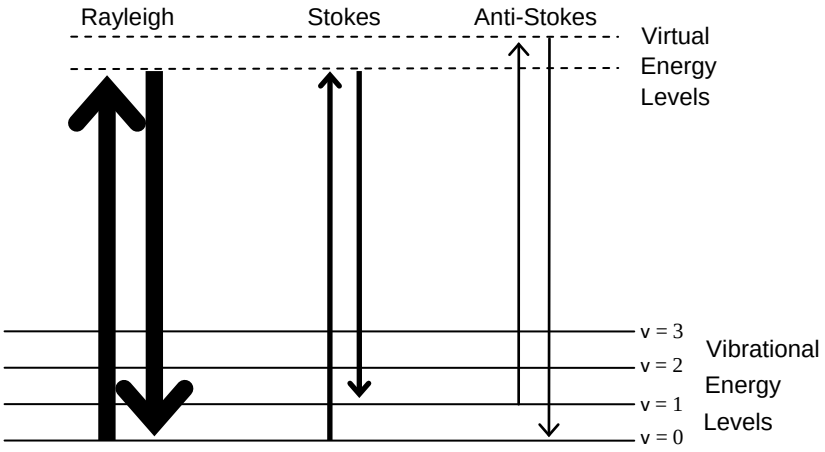

Figure 16. Energy diagram displaying the processes of Rayleigh scattering and Stokes and anti-Stokes Raman scattering. Line thickness gives a rough idea of transition probabilities.

When a molecule encounters an electric field, a dipole moment can be induced in the molecule. Polarizability (α) is related to the induced dipole moment (μ) by

$$\alpha = \frac{\mu}{E} \tag{17}$$

where E is the strength of the electric field. The polarizability of a molecule can be understood in terms of its electronic charge distribution. In order for a vibration to be Raman active, there must be a change in the polarizability of the molecule during the vibra-

tion. If there is a change in the electron cloud distribution during the course of a vibration (from one extreme to the other) then there is a change in polarizability. The requirement for Raman activity is shown by

$$\left(\frac{\partial \alpha}{\partial q}\right) \neq 0 \qquad (18)$$

where q represents the coordinates of the atoms involved in a bond. The intensity of a Raman band is dependent upon the magnitude of the change in polarizability of a molecule during a vibration and is proportional to

$$\left(\frac{\partial \alpha}{\partial q}\right)^2 \qquad (19)$$

1.5.1 Instrumentation

Raman spectrometers are often set up in a dispersive manner, relying on lasers as excitation sources. Lasers are ideal monochromatic sources due to their high power and small beam diameter (Ferraro *et al.*, 2003). Laser wavelengths can range from the UV to near-IR. The laser intensity can be controlled by adjusting the power at the source, by placing a neutral density filter (or combination of filters) in the beam path, or a combination of both. Notch filters built into the spectrometer reject the intense Rayleigh scattered light and allow only the Stokes scattered light to reach the detector.

A charge-coupled device (CCD) is a detector commonly used in Raman spectrometers. Raman scattered light is dispersed across the CCD. A CCD consists of pixels; each stores a charge in response to photons striking it (Ferraro *et al.*, 2003). CCD detectors are low noise and very sensitive, making them ideal for the detection of Raman signals

(Bhargava *et al.*, 2006). However, they can detect cosmic rays (extraterrestrial particles of very high energy). When one of these particles randomly hits the CCD, a charge is produced, resulting in the appearance of a very intense and narrow (width ≈ 2 cm^{-1}) band in the spectrum.

1.5.2 Raman Microscopy

Raman microscopy couples the instrumentation of Raman spectrometers to a standard microscope. The setup allows for Raman spectra to be collected from very small sample areas (≤ 2 μm, defined by the microscope objective). The use of a computer-controlled microscope stage allows for collection of maps by raster scanning across samples. Maps are then processed for a feature of interest.

1.5.3 Raman Spectra

As shown in Figure 17, the Stokes shift is more intense than the anti-Stokes Raman shift. However, for a given vibrational mode, the frequency shift is equivalent for both. The Stokes scattered light has been shifted to a lower energy, while the anti-Stokes scattered light is shifted to higher energy. Typically, a Raman spectrum displays the more intense Stokes shift; in most Raman spectrometers only the Stokes-shifted light is detected. Raman spectra are displayed as the number of photon counts against the Raman shift (the wavenumber shift from the incident laser wavelength). Figure 18 displays a sample Raman spectrum recorded from about 200 cm^{-1} to 1500 cm^{-1}. Many common Raman band assignments are contained in the review by Movasaghi *et al.* (2007).

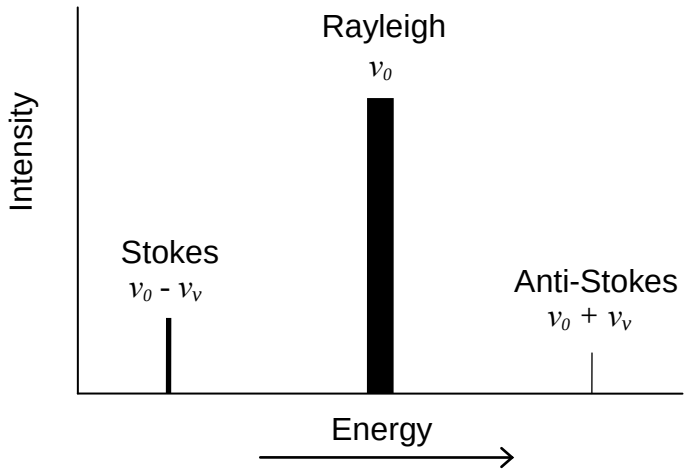

Figure 17. Rayleigh, Stokes, and anti-Stokes scattering and how they relate in energy. The incident frequency (Rayleigh line) is given by v_0, and the change in frequency is denoted as v_v.

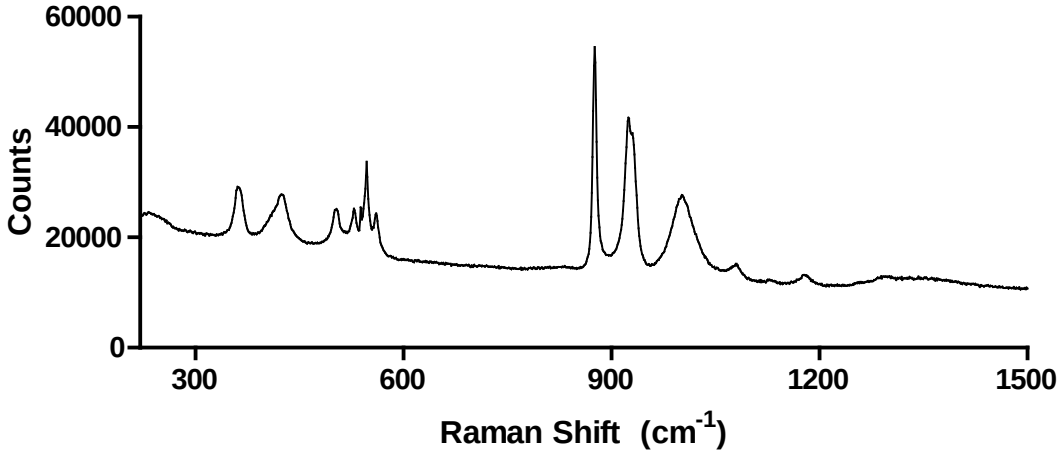

Figure 18. Raman spectrum of sodium monophosphate. The y-axis displays the number of photons that reach the detector; the x-axis displays the shift in energy from the Rayleigh line.

1.5.4 Practical Considerations for Analysis with Raman Spectroscopy

Water is a weak Raman scatterer and its presence does not conflict with the collection of Raman spectra. This makes sample preparations much simpler than in IR; it is not necessary to collect a background spectrum and aqueous samples can be easily examined. Under proper conditions, Raman is a non-destructive technique. However, it is important to keep laser power low to avoid burning samples. Using a laser power that is too high can result in a characteristic carbonaceous spectrum with two broad bands centered around 1324 cm^{-1} and 1589 cm^{-1} (see, for example, Szeghalmi *et al.*, 2007b). Similar to IR, samples can be analyzed multiple times with Raman or subsequently with other techniques.

Raman signals tend to be weak and can be over powered by fluorescence if the wavelength of the exciting line matches an electronic transition in the sample. Fluorescence can be reduced by switching to a longer wavelength, lower energy laser (*e.g.* a near-IR laser) to move away from the visible region that more typically matches electronic transitions.

Chapter 2

Methods

2.1 Sample Preparations

2.1.1 Filamentous Fungi

All fungal samples were grown in the Kaminskyj lab at the University of Saskatchewan by members of that group. Potato dextrose agar (PDA) was typically used as the growth medium. Four different PDA concentrations were prepared; 100% PDA was prepared as 39 g of dried PDA powder per litre of ultrapure water. 10%, 3%, and 1% PDA were prepared from 3.9 g, 1.2 g, and 0.39 g PDA powder per litre of ultrapure water, respectively. Agar was pH adjusted to 6.5 using NaOH, inoculated with spores, and placed on a suitable substrate (*vide infra*). Samples were incubated at 28°C in moist chambers to allow for sufficient growth of hyphae across the substrate (typically less than 24 hours). At this point, samples were frozen and lyophilized to dryness. Point IR spectra were generally

collected at hyphal tips and 30 µm, 50 µm and 100 µm back from tips, representing recent growth. Regions more than 100 µm back from tips are considered to be mature.

2.1.2 Standards

Some hyphal spectra contained unusual bands at 1078 and 1022 cm^{-1}. Phosphate and sugar motions occur in this region of spectra and therefore, such molecules were considered as the source of these bands. Fungi are known to accumulate polyphosphate (polyP) within cells and thus, polyP was isolated from cultures (described below) for spectroscopic analysis. Among the sugars considered, mannitol was identified in fungal hyphae. The preparation of mannitol for analysis is outlined below.

Polyphosphate

polyP was isolated from *C. magna* and *C. protuberata* samples by Dr. Rusty Rodriguez. Briefly (Rodriguez, 1993; Rodriguez, private communication), 100 mL cultures of fungal isolates were grown. The mycelia were freeze-dried in liquid N_2 and ground to a powder. Larger molecules were extracted in lysis buffer and polyP was precipitated with NH_4OAc. Further precipitations with NH_4OAc were performed to purify the polyP. PolyP derived from fungal samples was found to have a chain length of about 60 phosphate groups (Rodriguez, 1993). For IR analysis, 20 µL of the *C. magna* polyP isolate and 20 µL of the *C. protuberata* polyP isolate were pipetted onto individual polyethylene IR cards. 10 µL of each polyP isolate was pipetted onto individual polytetrafluoroethylene (PTFE) IR cards. Samples were allowed to dry prior to data collection (approxi-

mately 30 to 60 minutes). For Raman analysis, gold-coated silicon wafers were used as substrates.

Mannitol

To prepare a sample for analysis with IR spectroscopy, mannitol was dissolved in distilled water. 20 µL of the mannitol solution was pipette onto a gold-coated silicon wafer and allowed to dry overnight. Sample preparation for Raman analysis involved simply placing the mannitol onto a typical glass microscope slide.

2.2 FTIR

FTIR spectra were collected using either a bench (globar) or synchrotron source illumination. All fungal spectra were collected in transflectance mode. Choices for FTIR substrates were typically low-e MirrIR slides (Kevley Technologies, www.kevley.com) or, on occasion, gold-coated silicon wafers (U of M). MirrIR slides are 1x 3 inch glass slides that can be used for IR measurements in transflectance. The slides are coated in many thin layers, two of which are silver. The silver layers are reflective to IR radiation in the range of 4000 to 400 cm^{-1}. However, the slides are nearly transparent to visible light, allowing for easy visualization of samples with a standard light microscope. Anywhere from 256 to 2048 scans were co-added for each pixel and ratioed to a background spectrum collected on a clean area of the slide. All spectra were recorded at 4 cm^{-1} resolution in the mid-IR region from 4000 cm^{-1} to 900 or 800 cm^{-1} (depending on the detector's limit of sensitivity). Either the Happ-Genzel (SRC, CLS, FTIR bench) or Norton-Beer (FTIR microscope with FPA) apodization function was used. Spectra collected with the FTIR microscope and FPA detector contained some level of zero-filling (set to auto). When necessary, an appropriately scaled water spectrum was subtracted from spectra (see section 3.2.1). No other post-collection processes were performed.

2.2.1 Canadian Light Source

Spectra were collected on the 01B1-1 mid-IR beamline at the Canadian Light Source (CLS) in Saskatoon, Saskatchewan using a Bruker Optics IFS 66v/S bench with a Hyperion confocal microscope and mapping stage and a liquid nitrogen cooled MCT detector.

Data acquisition was performed using the Opus software package. The aperture was set to 10 x 10 μm for spectral acquisition at defined points along hyphae (in December 2008 many spectra were collected with a 15 x 15 μm aperture). Typically, spectra were collected at hyphal tips and 30 μm, 50 μm, and 100 μm from tips. Movement to subsequent positions was performed manually. Spectra were converted to SPC format (a file format that can be opened by many programs) and analyzed in the OMNIC software package.

2.2.2 Synchrotron Radiation Center

At the Synchrotron Radiation Center (SRC) in Madison, Wisconsin, spectra were collected on the 031 beamline with a Nicolet Magna 550 bench coupled to a Continuum microscope. The instrument is equipped with a liquid nitrogen cooled single element MCT detector (50 μm diameter). The OMNIC/Atlμs software was used for data collection and analysis. A 10 x 10 μm aperture was used for collection of spectra along hyphae at tips and 30 μm, 50 μm, and 100 μm from tips. Movement of the stage to the next position was performed manually.

2.2.3 FTIR Microscope with FPA Detector

Hyphal maps were collected using a Varian 670-IR FT-IR bench with a Varian 620-IR FT-IR imaging microscope at the University of Manitoba. Slides were placed on a computer-controlled Prior stage. This microscope has a single element MCT detector (not used for any of the work in this thesis) as well as a 64 x 64 element (nominal 5.5 μm spatial resolution; 350 x 350 μm sample area) focal plane array (FPA) detector, both cooled

with liquid nitrogen. All spectra were collected in transflectance mode. The Varian Resolutions Pro software was used for data acquisition and analysis. Individual spectra can be extracted from maps for individual analysis or the whole block of data can be analyzed for a feature of interest. Maps processed to show false colour displays in the Resolutions Pro software are blended, rather than a display of individual pixels.

2.2.4 FTIR Bench Spectrometer

Spectra of extracted polyP samples were collected on a Nicolet Nexus 870 FTIR E.S.P. spectrometer with a liquid nitrogen cooled MCT detector. Background spectra were collected using either a clean polyethylene or a clean PTFE card. Spectra were collected at 4 cm^{-1} resolution. For each spectrum, 64 scans were co-added and ratioed to an appropriate background collected on the respective blank substrate.

2.3 Raman

2.3.1 Fungal samples

Raman spectra were collected using a Renishaw inVia Raman microscope. For Raman spectra, gold-coated silicon substrates (U of M) or the smooth gold area of Klarite substrates (see section 2.3.4) were used. A 785 nm diode laser set at 10% power was used for excitation. The 1200 l/mm grating was used with the 785 nm laser. A 50x objective was used, giving laser spot sizes of about 2 µm. Spectra were collected by summing 256 static scans (centered at 700 cm^{-1} and 1000 cm^{-1}), each with an exposure of 4 s. Raman scattered light was collected with an electronically cooled CCD detector. Data acquisition was performed using the Renishaw proprietary WiRE software. Cosmic rays were removed from spectra using the "Zap" processing operation in the WiRE software (see section 3.3.1). Spectra were converted to Galactic SPC format and analyzed in OMNIC.

2.3.2 Polyphosphate

Two gold-coated silicon wafers (U of M) were mounted onto a standard microscope slide and the polyP samples were each pipetted onto a wafer (as described in section 2.1.2). Raman spectra were collected under a 50x objective with a 785 nm diode laser set to 10% power and a 1200 l/mm grating. For each spectrum, 4 scans of 60s exposure time each, were accumulated. Extended scans were collected over the range of 125 to 1700 cm^{-1}.

2.3.3 Mannitol

Mannitol was placed onto a glass microscope slide. A Raman spectrum was collected using a 785 nm diode laser set to 10% power, 1200 l/mm grating, and 20x objective. Spectra are the summation of 4 scans, each of 60s exposure, over an extended range of 125 to 1700 cm^{-1}.

2.3.4 Klarite Substrates

Klarite substrates (D3 Technologies, www.d3technologies.co.uk) are designed for SERS analysis. These substrates are made of a silicon base coated with a thin layer of gold. They are comprised of a 4 mm × 4 mm active area of gold-coated textured silicon, providing an enhancement of the Raman signal, and surrounded by a smooth gold surface for normal Raman measurements. Klarites have been used as substrates for one Cp4666D sample and one CPA sample in this thesis; however, spectra were only collected from hyphae on the smooth gold surface. No SERS analyses have been performed on any of the fungal endophytes.

Chapter 3

Results

3.1 Fungal Growth

Growth techniques have been refined by members of the Kaminskyj lab at the University of Saskatchewan over the past few years; all fungal samples in this study were grown by Kaminskyj group members. The following subsections outline the samples that were grown for analysis and the growth results.

3.1.1 Fungal Samples

Samples of *C. protuberata*, *F. culmorum*, and *C. magna* were grown at different times between November 2007 and October 2009. They are designated according to the names found in Rodriguez *et al.*, 2008. *Curvularia protuberata* samples acquired from a culture collection are named CpATCC while those isolated from geothermal plants and containing a virus are labelled Cp4666D. In addition to these two samples, a Cp4666D sample with the virus removed was examined, as well as a sample where the virus was removed

and later reintroduced. The former was labelled as Cp4666D no virus, the latter as CPA. *Fusarium culmorum* samples isolated from coastal and non-coastal plants are marked as FcRed1 and Fc18, respectively. The wildtype pathogenic *C. magna* sample is called L2.5; the non-pathogenic mutant is called CmPath. Table 2, Table 3, and Table 4 give details on growth (date, substrate, medium) of all examined *C. protuberata, F. culmorum,* and *C. magna* samples, respectively. Samples were subsequently analyzed with FTIR using a thermal source and FPA detector, sFTIR and/or Raman.

Table 2. *Curvularia protuberata* samples grown for spectroscopic analysis.

Slide	Growth Date	Substrate	Sample	Medium
34	November 2007	MirrIR	CpATCC	100% PDA
				10% PDA
37	November 2007	MirrIR	Cp4666D	100% PDA
				10% PDA
		Gold	Cp4666D	100% PDA
				10% PDA
39	June 2008	MirrIR	Cp4666D	100% PDA
				10% PDA
				3% PDA
				1% PDA
40	June 2008	MirrIR	CpATCC	100% PDA
				10% PDA
				3% PDA
				1% PDA
45	June 2008	MirrIR	CpATCC	100% PDA
				10% PDA
				3% PDA
				1% PDA
46	June 2008	MirrIR	Cp4666D	100% PDA
				10% PDA
				3% PDA
				1% PDA
63	December 2008	MirrIR	Cp4666D	1x GYE
				0.1x GYE
128	July 2009	MirrIR	Cp4666D no virus	100% PDA
129	July 2009	MirrIR	Cp4666D	100% PDA
133	July 2009	Klarite	Cp4666D no virus	100% PDA
134	July 2009	Klarite	Cp4666D	100% PDA
135	October 2009	MirrIR	Cp4666D	100% PDA
			CPA	100% PDA

Table 3. *Fusarium culmorum* samples grown for spectroscopic analysis.

Slide	Growth Date	Substrate	Sample	Medium
38	November 2007	MirrIR	FcRed1	100% PDA
				10% PDA
		Gold	FcRed1	100% PDA
				10% PDA
		MirrIR	Fc18	100% PDA
				10% PDA
		Gold	Fc18	100% PDA
				10% PDA
43	June 2008	MirrIR	FcRed1	100% PDA
				10% PDA
				3% PDA
				1% PDA
44	June 2008	MirrIR	Fc18	100% PDA
				10% PDA
				3% PDA
				1% PDA
47	June 2008	MirrIR	Fc18	100% PDA
				10% PDA
				3% PDA
				1% PDA
48	June 2008	MirrIR	FcRed1	100% PDA
				10% PDA
				3% PDA
				1% PDA

Table 4. *Colletotrichum magna* samples grown for spectroscopic analysis.

Slide	Growth Date	Substrate	Sample	Medium
34	November 2007	MirrIR	CmPath	100% PDA
				10% PDA
37	November 2007	MirrIR	L2.5	100% PDA
				10% PDA
		Gold	L2.5	100% PDA
				10% PDA
41	June 2008	MirrIR	L2.5	100% PDA
				10% PDA
				3% PDA
				1% PDA
49	June 2008	MirrIR	CmPath	100% PDA
				10% PDA
				3% PDA
				1% PDA
50	June 2008	MirrIR	L2.5	100% PDA
				10% PDA
				3% PDA
				1% PDA

3.1.2 Substrates

Substrate choice is governed by requirements for the type of spectroscopic analysis to be performed. In this work, MirrIR and gold-coated silicon were used for FTIR and sFTIR. Gold-coated silicon or the smooth gold surfaces of Klarites were used for Raman.

Most fungal samples were grown on MirrIR substrates. Due to the size of MirrIR slides (that of typical microscope slides), multiple samples, each grown from its own piece of potato dextrose agar (PDA), could be placed on the same slide and grown under the same conditions (temperature, humidity), as in Figure 19. Hyphae grew across the slide, away from agar. Figure 20 shows a magnified image of a *C. magna* sample grown

on MirrIR. Spectra are collected only from hyphae that have extended beyond the agar and out onto the slide; hyphae residing within agar are not examined since bands due to the agar would be present in spectra, obscuring bands from fungi. There was no apparent difference in growth of fungi on MirrIR compared to gold (Figure 21).

a) 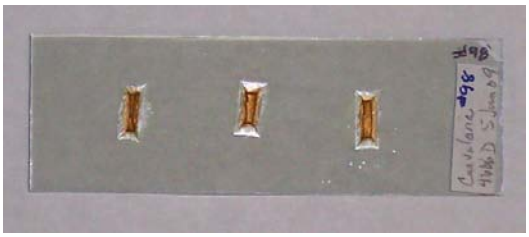 b) 

Figure 19. MirrIR slides with samples of Cp4666D. a) All samples were grown from 100% PDA which has not been removed from the slide after growth. b) Samples were grown from 100%, 10%, 3% and 1% PDA blocks (left to right), which has been removed after samples had grown out onto the slide. The agar block is often removed from slides after sufficient growth is achieved to allow for examination of samples with short working distance objectives.

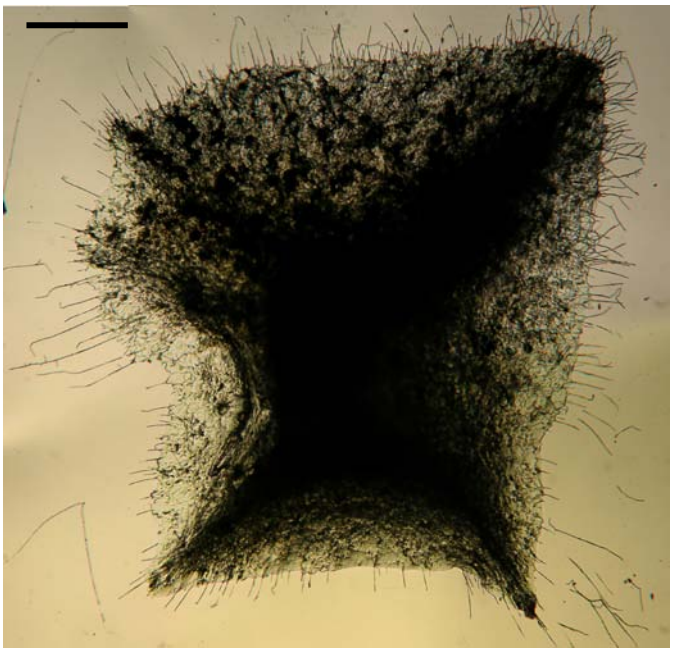

Figure 20. *Colletotrichum magna* grown on a MirrIR slide using 10% PDA as growth medium. Agar block was left intact on the slide after growth. Hyphae grew across the slide, away from the agar. Scale bar = 500 µm.

a) b)

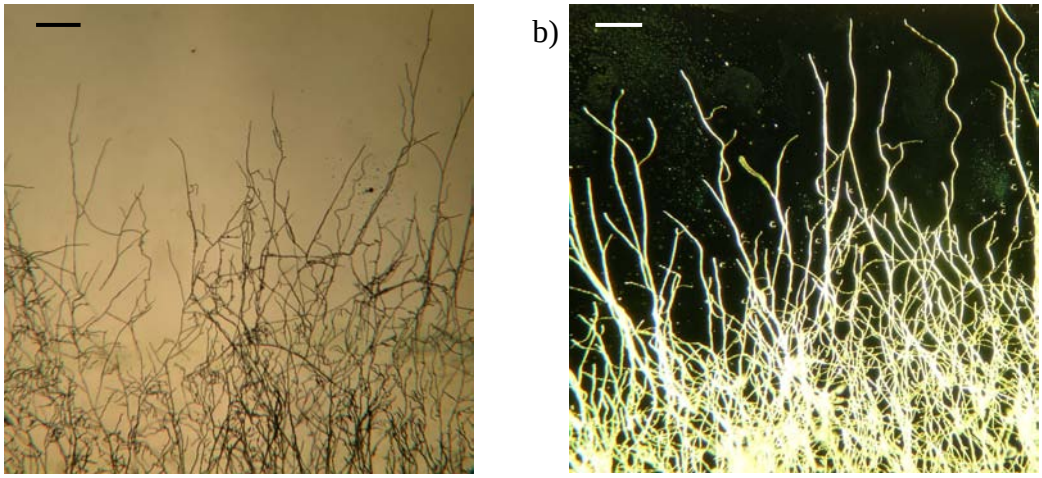

Figure 21. Cp4666D grown from 100% PDA on a) MirrIR and b) gold. The gold-coated silicon wafer (about 1 cm^2) was affixed to the MirrIR slide with double-sided tape. Both samples were grown under the same conditions. Scale bars = 200 µm.

3.1.3 Growth Media

PDA was the main growth medium used in this work. Samples were grown from different concentrations of PDA (100%, 10%, 3%, and 1%) to examine how the concentration of the growth medium (available nutrients) affected fungal growth and cell composition. Saprotrophs are generally grown from 100% PDA, however, the endophytes are able to grow under lower nutritional conditions. Typically, samples appeared to grow well from both 100% and 10% PDA. With the 3% and 1% PDA, some growth did occur, but typically much fewer hyphae were present compared to the 100% and 10% PDA samples grown under the same conditions (see Figure 22).

Glucose yeast extract (GYE) was also used as the growth medium for a few samples. Growth of samples from GYE was very similar to the growth of samples from PDA, as displayed in Figure 23. The sample grown from GYE has more hyphal branching; however, these samples were grown in a slightly different manner than samples grown from PDA. The growth with PDA involved placing the block of agar on the slide; growth with GYE involved placing a droplet of GYE onto the slide. The variables for these different growth methods were never evaluated. Samples grown from GYE are included here solely for completeness. Since GYE was only used for the growth of a very limited number of samples, the data presented in this thesis was restricted to samples grown from PDA.

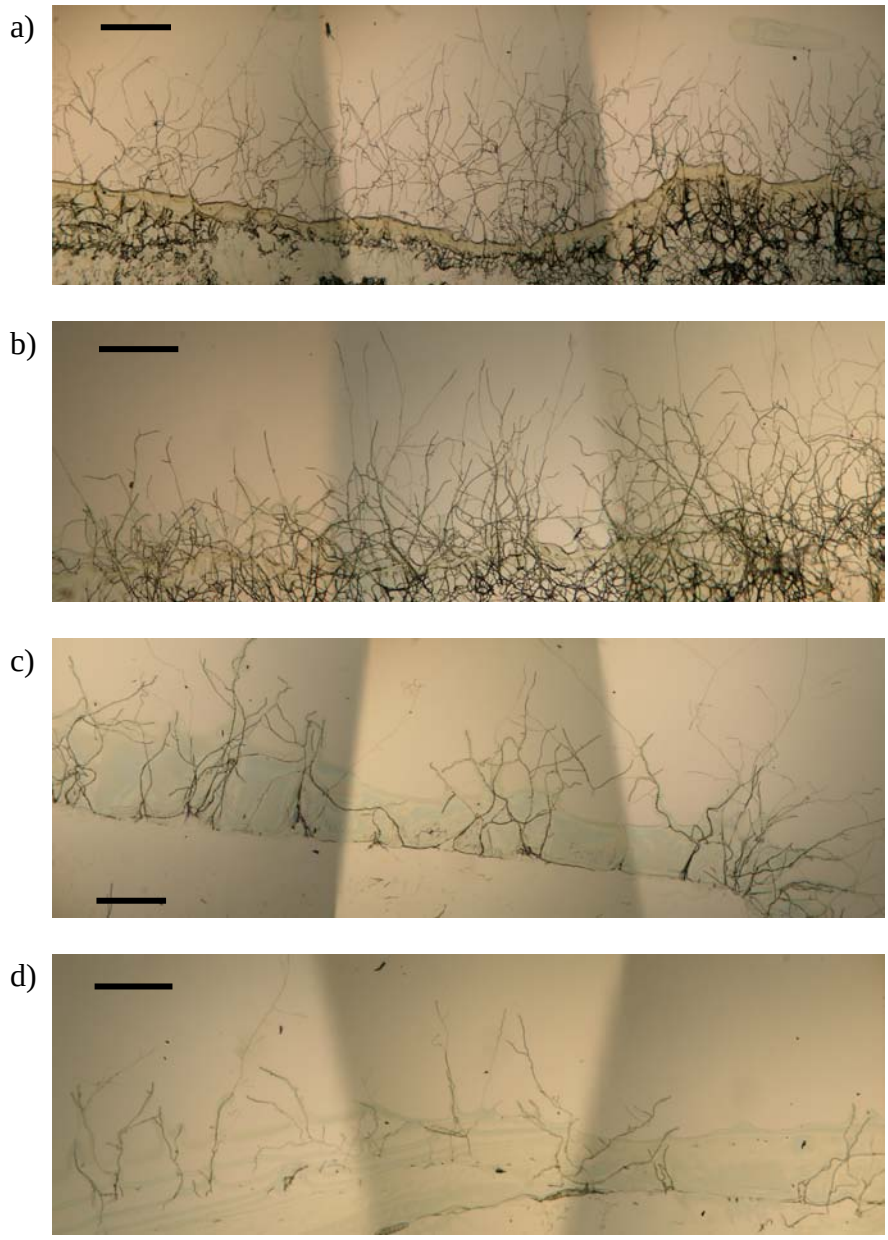

Figure 22. Photos of Cp4666D samples grown on MirrIR using a) 100% PDA b) 10% PDA c) 3% PDA and d) 1% PDA. Samples were grown on the same slide, ensuring that growth took place under uniform conditions. Scale bars = 500 µm.

a)

b)

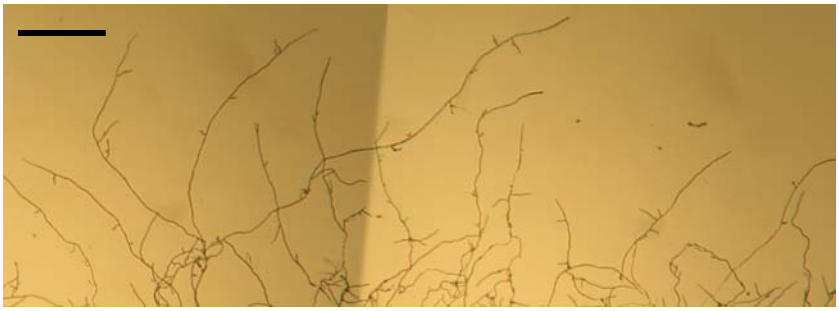

Figure 23. Cp4666D grown from a) 100% PDA and b) 1x GYE. Scale bars = 500 µm.

3.1.4 Sub-Optimal Growth

Not all growth attempts were successful. Slides 39 to 44 initially appeared to have adequate growth; however, when examined with sFTIR, low signal was often encountered. It was noted that segments of hyphae had an iridescent look when viewed through the FTIR microscope under white light illumination. Upon closer examination, it appeared that only a "shadow" of many hyphae remained on slides. This often only occurred along a section of the hypha, as shown in Figure 24. Figure 25 displays a similar issue, where hyphae appear to have missing segments that possibly broke or dried off of slides. *Aspergillus nidulans* samples (not examined in this thesis) grown on a Klarite substrate also had a similar appearance, as seen in Figure 26. The possible causes of these issues are explored in the Discussion.

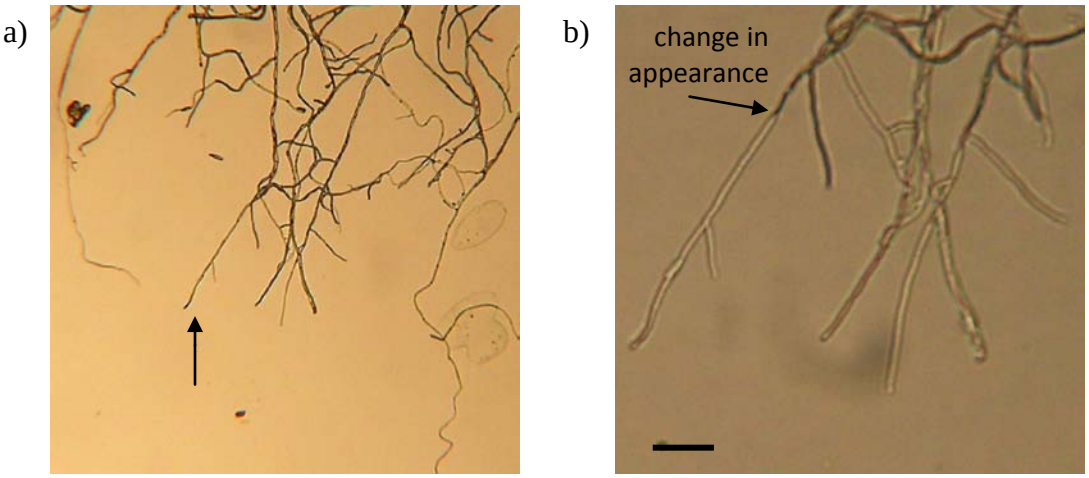

Figure 24. Images of Cp4666D grown on MirrIR from 100% PDA. Photos taken using a) a 4x objective and b) a 10x objective. At higher magnification, hypha's appearance changes at the position indicated by the arrow. Scale bar = 50 µm.

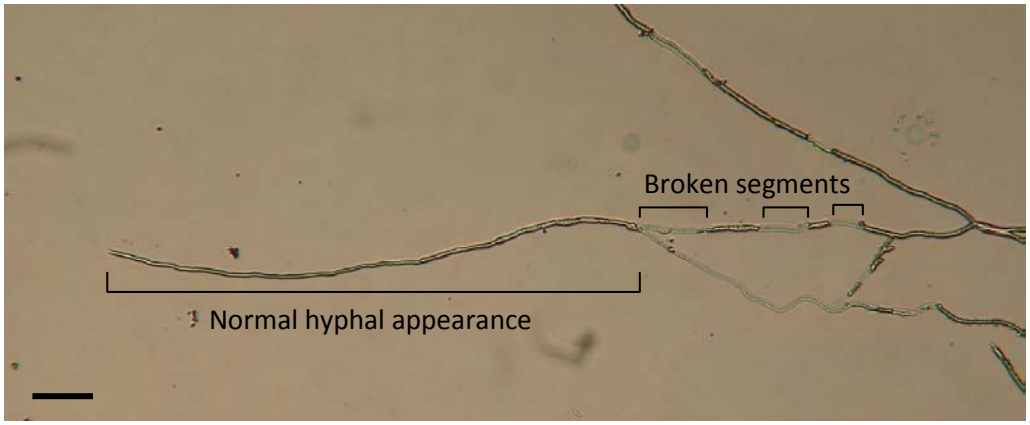

Figure 25. CpATCC grown from 10% PDA on MirrIR. At positions further back from tips, segments of hyphae appear to have broken off of the slide. Scale bar = 50 µm.

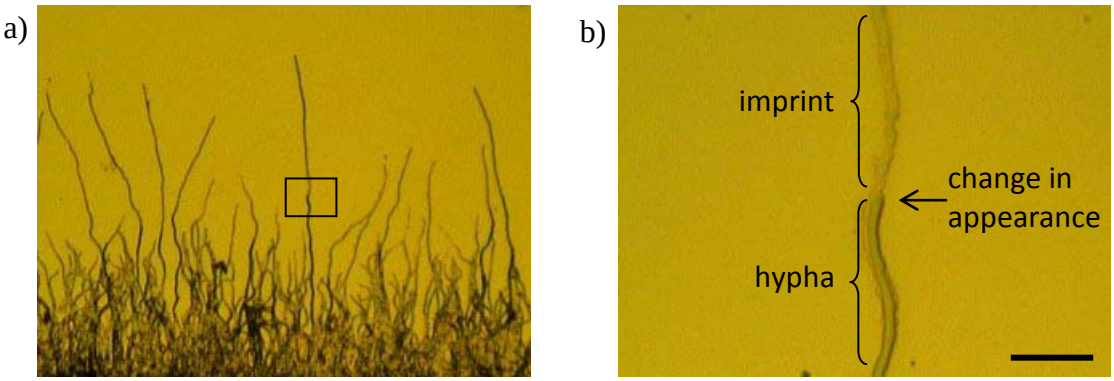

Figure 26. *Aspergillus nidulans* grown from 100% PDA onto the smooth gold area of a Klarite substrate. Photos taken with a) 5x objective and b) 50x objective. Box in photo (a) shows the area displayed in photo (b). Scale bar = 10 µm.

Typical sFTIR, FTIR, and Raman spectra are displayed in the following sections. FTIR data are presented first, starting with general information about the data and followed by specific results, which are separated by species (*C. protuberata, F. culmorum, C. magna*). Raman data are presented next, with general Raman results first followed by specific results for each species (*C. protuberata, F. culmorum*). The results are all discussed in further detail (band assignments, comparisons between samples, correlations between FTIR and Raman data, etc.) in the Discussion.

3.2 FTIR

sFTIR spectra from SRC and CLS are included in Appendix I. FTIR maps collected with a bench source and FPA detector are displayed in Appendix II. Typical spectra are presented here, displayed on the same scale and offset for clarity. Many spectra included in this thesis show only the amide and sugar regions (from 1800 to 900 cm^{-1}) due to the scattering in spectra. However, the full range of data collection (typically from 4000 to 900 or 800 cm^{-1}) is displayed for all dat in Appendix I. All sFTIR spectra were collected using a 10 x 10 μm aperture. Unless otherwise stated, samples are on MirrIR.

3.2.1 Water Subtraction from Spectra

Despite collecting a background spectrum (and having a purged enclosure around samples at CLS and SRC), water and carbon dioxide bands can still be noticeable in spectra. During the time between background acquisition and sample collection, there could be a small variation of water and carbon dioxide relative to the amount present when the

background was acquired. In addition, fungi are small and contain little material, resulting in low signal. Any water bands present in spectra are often prominent relative to the signal from fungi. The easiest way to deal with this issue is to collect "blank" spectra during the course of sample spectra acquisition. The blank spectrum, acquired on a clean slide area, should only contain bands due to water and carbon dioxide that are currently present in the atmosphere (differing from what was present when the background was acquired). In the case of FPA maps of fungi that contain water and carbon dioxide in spectra, there are many "blank" spectra already recorded within the map, since the majority of spectra are collected from blank areas of the slide. Figure 27 displays a hyphal spectrum that contained some water vapour bands, a blank spectrum, and the result after subtraction. Spectra presented in this work were corrected for water bands when needed.

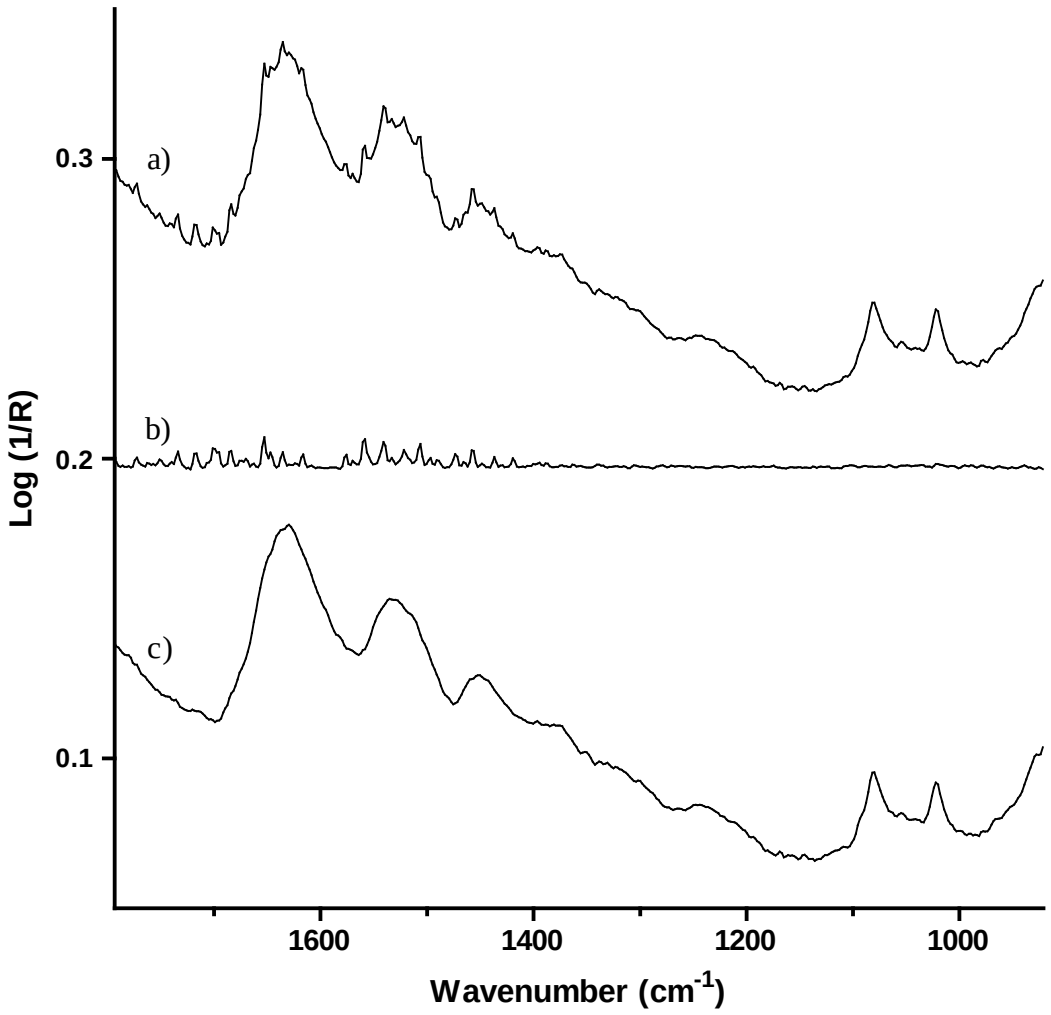

Figure 27. Water subtraction from spectra. a) Gas-phase water bands are present in the amide region of the Cp4666D sample spectrum. b) A blank spectrum recorded on a clean area of the slide shows water vapour bands. c) The sample spectrum after subtraction. The water bands are no longer visible in the spectrum and other bands have not been altered.

3.2.2 Quality of Synchrotron Data

sFTIR spectra were collected at CLS (November 2007, June 2008, December 2008) and SRC (April 2008, November 2008, August 2009). The typical appearance of the data obtained during each trip is shown in Figure 28 (CLS) and Figure 29 (SRC). The same slides were not examined at all locations/dates; however, all spectra in the figures were collected from Cp4666D hyphae grown from 100% PDA. Spectra are displayed for a comparison of the quality of data during each trip. Spectra collected at SRC were more consistently of better quality than those collected at CLS.

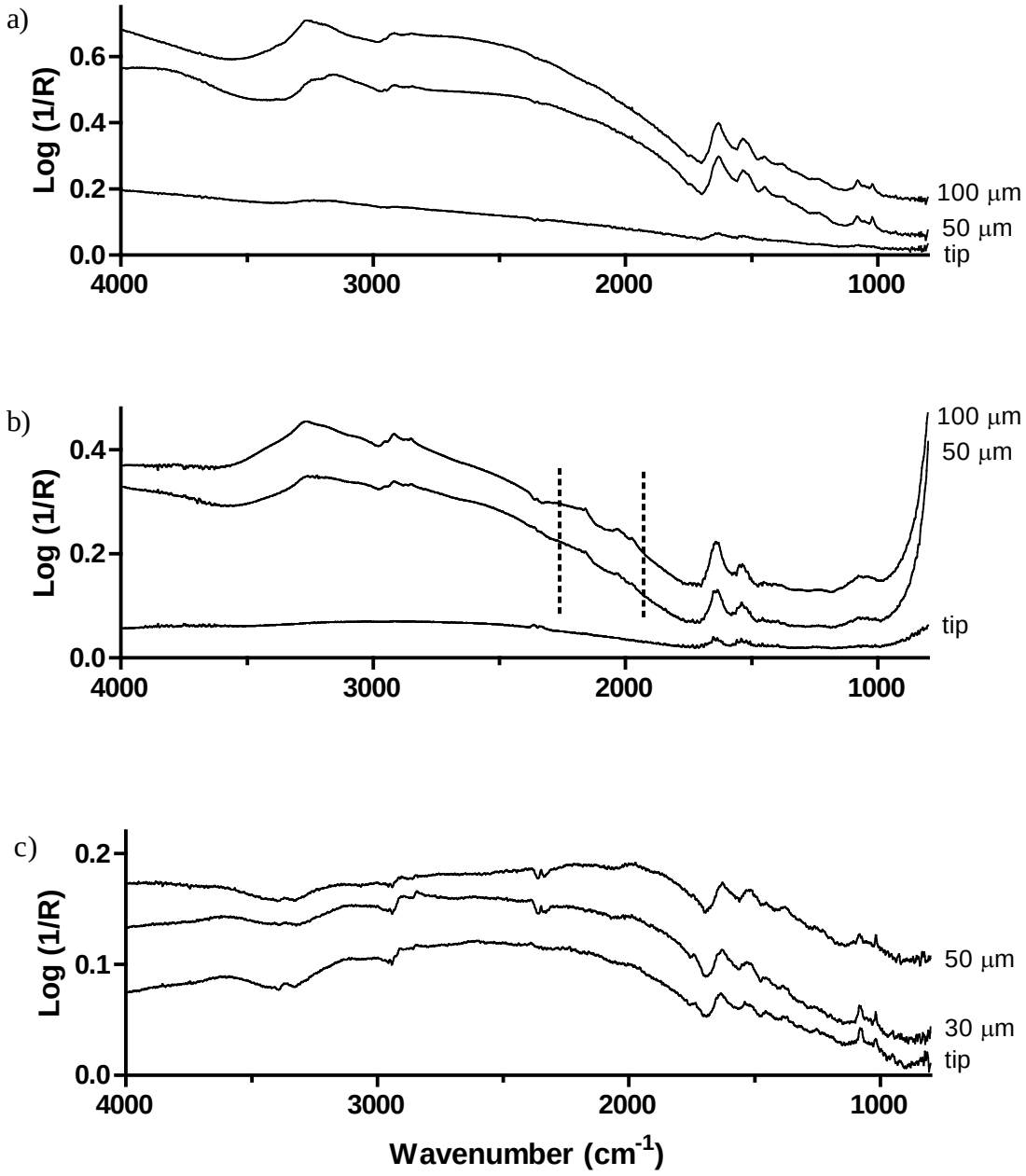

Figure 28. Spectra collected at CLS a) November 2007 (2048 scans), b) June 2008 (1024 scans), and c) December 2008 (1024 scans). Spectra were collected on Cp4666D hyphae grown from 100% PDA. Dotted lines outline where the diamond window absorptions can be seen in spectra.

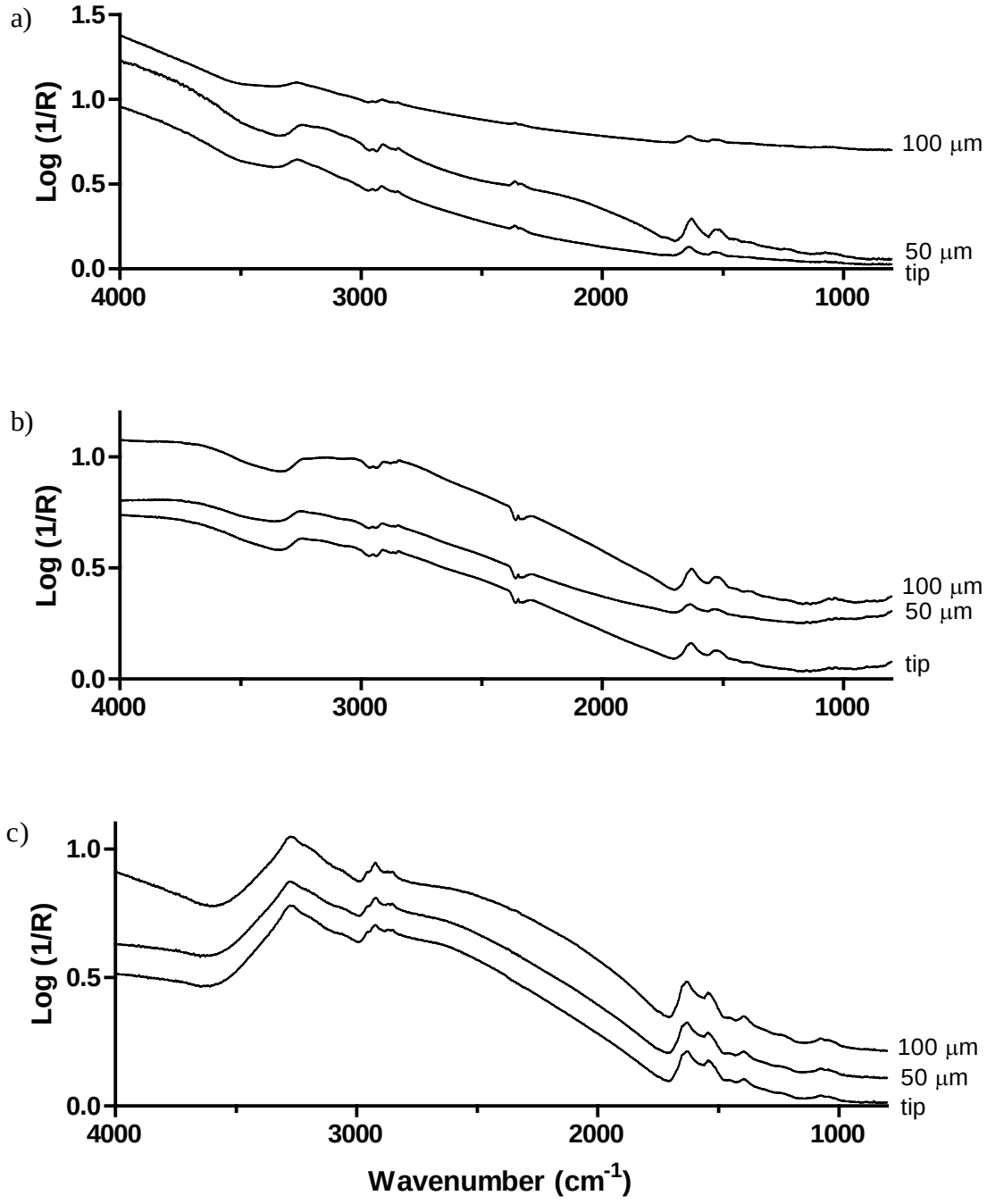

Figure 29. Spectra collected at SRC a) April 2008 (256 scans), b) November 2008 (1024 scans), and c) August 2009 (256 scans). All spectra were collected on Cp4666D hyphae grown from 100% PDA.

Figure 30 displays spectra collected at SRC (April 2008) and CLS (June 2008) on the same hypha and at the same positions. Figure 31 displays spectra collected at SRC (November 2008) and CLS (December 2008) from the same hypha. These figures further support the better quality of data attainable at SRC compared to CLS.

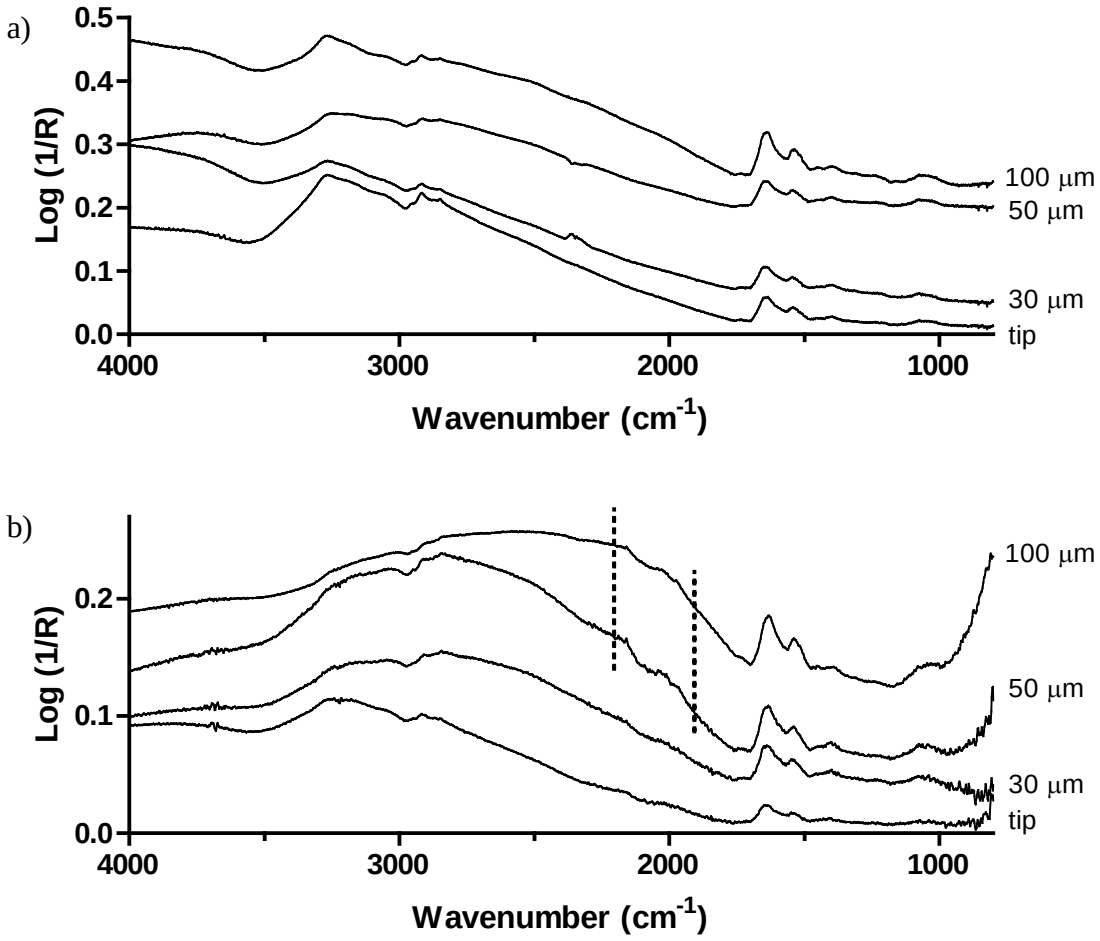

Figure 30. Spectra collected along a CpATCC hypha grown from 10% PDA at a) SRC (April 2008), summing 512 scans and b) CLS (June 2008), summing 1024 scans. Dotted lines outline the region where the diamond window absorptions are visible in spectra.

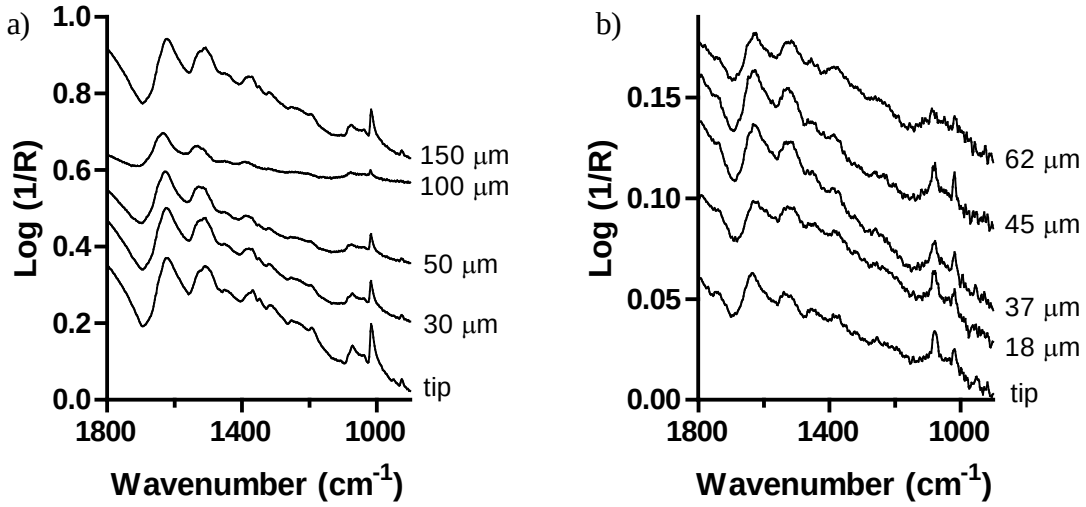

Figure 31. Spectra collected on a Cp4666D hypha grown from 100% PDA at a) SRC (November 2008) and b) CLS (December 2008). All spectra were collected by summing 1024 scans.

3.2.3 Media Contamination in Spectra

It is important to collect spectra from hyphae that have extended beyond the growth medium. Spectra collected from hyphae within the growth medium would be contaminated and the fungal signature would most likely be overpowered by that from the medium. Often on slides, there is a visible "high watermark" that extends beyond the agar, potentially containing components of the agar. Figure 32 illustrates the appearance of such a watermark. Many hyphae did not grow beyond this area because these fungi generally prefer to grow within liquid medium. Care was taken to select hyphae that extended beyond this point. Figure 33 shows spectra purposely collected from a hypha within the watermark along with a spectrum collected in an area adjacent to the hypha.

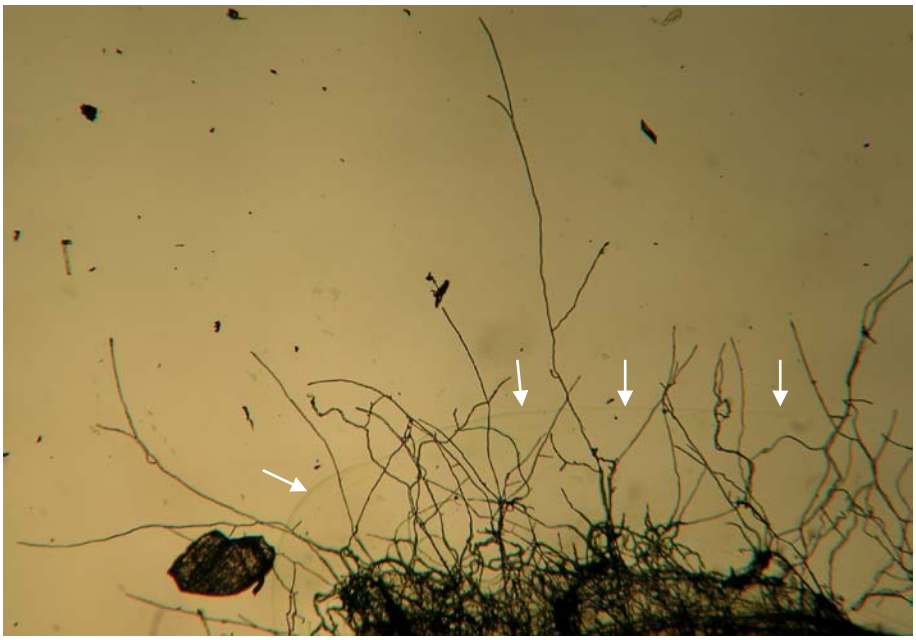

Figure 32. A CpATCC sample grown from 10% PDA. There is a "high watermark" present toward the base of hyphae. Arrows indicate the position of this faint line.

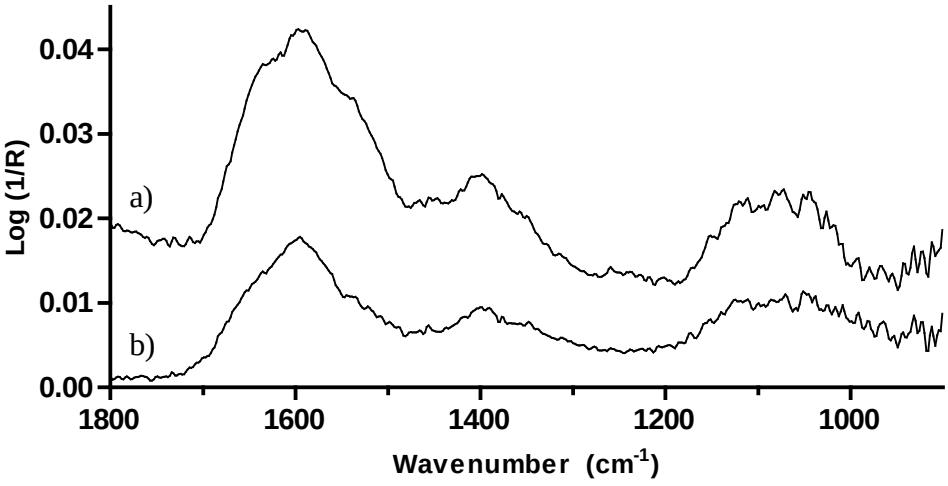

Figure 33. Spectra acquired a) 100 µm from the tip of a L2.5 hypha within the watermark and b) adjacent to the hypha and within the watermark (CLS, June 2008). Spectrum (a) is clearly the spectrum of growth medium.

3.2.4 *Curvularia protuberata*

In accordance with one of the primary goals of this thesis, culture collection (CpATCC) and geothermal (Cp4666D) *C. protuberata* were examined with sFTIR and FTIR to determine if there were differences in spectra that could be related to the mechanism of heat tolerance conferred by Cp4666D. Cp4666D samples contain a virus whose presence is necessary for thermal protection of plants (Márquez *et al.*, 2007); the CpATCC samples do not possess this virus.

Pairs of CpATCC and Cp4666D isolates were grown at the same times and under the same conditions. Figure 34 displays images of CpATCC and Cp4666D and shows no obvious growth differences (amount of growth or appearance of hyphae) between the samples. This was also observed for other pairs of CpATCC and Cp4666D. Hyphae were generally 3-4 µm in diameter. Samples were grown from 100%, 10%, 3% and 1% PDA and the amount of hyphal growth decreased as the PDA concentration decreased (Figure 22). This trend applied to both CpATCC and Cp4666D samples.

a) b)

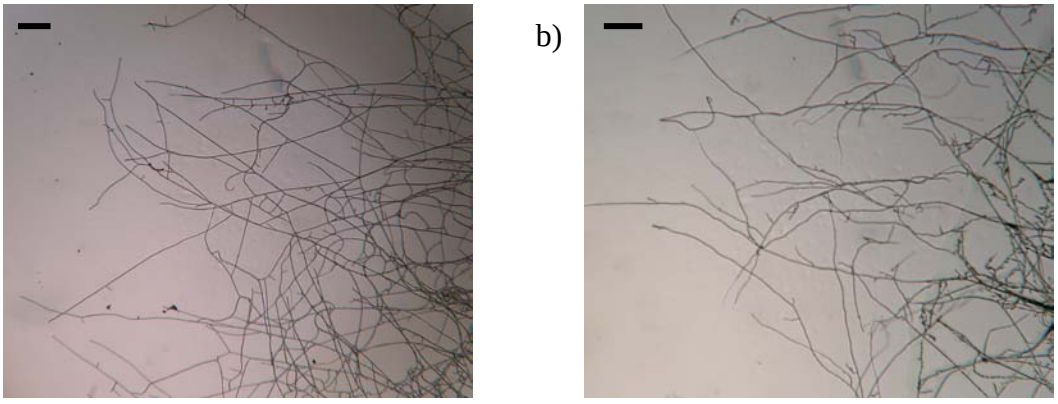

Figure 34. Images of a) CpATCC and b) Cp4666D hyphae. Both samples were grown on MirrIR from 100% PDA. Scale bars = 200 µm.

The number of hyphae examined from each sample is shown in Table 5 (CpATCC) and Table 6 (Cp4666D). Both tables include the locations(s) where samples have been analyzed (CLS, SRC, U of M), including the dates of analysis. Not all hyphae have been examined to the same extent. At synchrotrons, hyphae were typically examined at four positions (tip and distances of 30 μm, 50 μm, and 100 μm from the tip) with a 10 x 10 μm aperture. This method allowed for reasonable comparisons between hyphae. The IR microscope with an FPA detector at U of M allowed for examination of 350 x 350 μm areas of slides (at a pixel resolution of 5.5 μm). The FPA detector allows for collection of data along a hypha in a much shorter time frame (*vide infra*).

Table 5. Number of CpATCC hyphae examined with sFTIR and FTIR/FPA.

Slide	Substrate	Medium	Location	Date*	# of Hyphae
34	MirrIR	100% PDA	CLS	Nov. 2007	2
			SRC	Apr. 2008	4
			U of M FPA	2009	14
		10% PDA	CLS	Nov. 2007	6
			SRC	Apr. 2008	3
			CLS	Jun. 2008	1
			U of M FPA	2009	8
40	MirrIR	100% PDA	CLS	Jun. 2008	7
			U of M FPA	2009	2
		3% PDA	CLS	Jun. 2008	5
45	MirrIR	100% PDA	SRC	Nov. 2008	2
			CLS	Dec. 2008	1
			U of M FPA	2009	11
		10% PDA	U of M FPA	2009	6
		3% PDA	U of M FPA	2009	7

* An FTIR microscope with an FPA detector was installed at U of M in May 2009. Numerous images were acquired in May, June, September, October and November 2009.

Table 6. Number of Cp4666D hyphae examined with sFTIR and FTIR/FPA.

Slide	Substrate	Medium	Location	Date*	# of Hyphae
37	MirrIR	100% PDA	CLS	Nov. 2007	6
			SRC	Apr. 2008	3
			U of M FPA	2009	22
		10% PDA	CLS	Nov. 2007	6
			SRC	Apr. 2008	4
			U of M FPA	2009	12
	Gold	100% PDA	U of M FPA	2009	16
39	MirrIR	100% PDA	CLS	Jun. 2008	4
			U of M FPA	2009	14
		10% PDA	U of M FPA	2009	5
		1% PDA	CLS	Jun. 2008	5
46	MirrIR	100% PDA	SRC	Nov. 2008	3
			CLS	Dec. 2008	6
			U of M FPA	2009	8
		10% PDA	CLS	Dec. 2008	20
			U of M FPA	2009	6
		3% PDA	CLS	Jun. 2008	4
			U of M FPA	2009	7
		1% PDA	U of M FPA	2009	5
63	MirrIR	1x GYE	CLS	Dec. 2008	13
			U of M FPA	2009	2
		0.1x GYE	U of M FPA	2009	1
128[†]	MirrIR	100% PDA	SRC	Aug. 2009	7
129	MirrIR	100% PDA	SRC	Aug. 2009	6
135	MirrIR	100% PDA	U of M FPA	2009	11
135[‡]	MirrIR	100% PDA	U of M FPA	2009	5

* An FTIR microscope with an FPA detector was installed at U of M in May 2009. Numerous images were acquired in May, June, September, October and November 2009.
[†]Cp4666D no virus
[‡]CPA

Synchrotron Data

Initial work was carried out at synchrotrons (SRC & CLS) where spectra were collected at defined points along hyphae. sFTIR spectra were collected using a single pixel aperture. Collecting spectra at single points along hyphae is the most efficient method of data collection for these samples due to the size of hyphae. Choosing to raster scan across samples would be less productive since time would be spent on areas of slides without any sample. Additionally, the small amount of material within cells requires that a large number of scans (minimum of 256 but sometimes up to 2048) be summed in order to achieve adequate S/N. This means it would take hours to examine even the first 10 μm of a hypha. Choosing to acquire single pixel spectra at different positions along hyphae offers a greater view of the changes in cell composition while minimizing the time spent examining each hypha.

Spectra were collected from hyphae that had been grown from different concentrations of PDA (100%, 10%, 3%, and 1%) growth medium. For both the CpATCC and Cp4666D samples (grown from both 100% and 10% PDA), the intensity of absorbance observed at all examined positions along a given hypha was usually very similar, as seen in Figure 35. Figure 36 shows that there were, on the other hand, some hyphae with significant variations in signal intensity along their length.

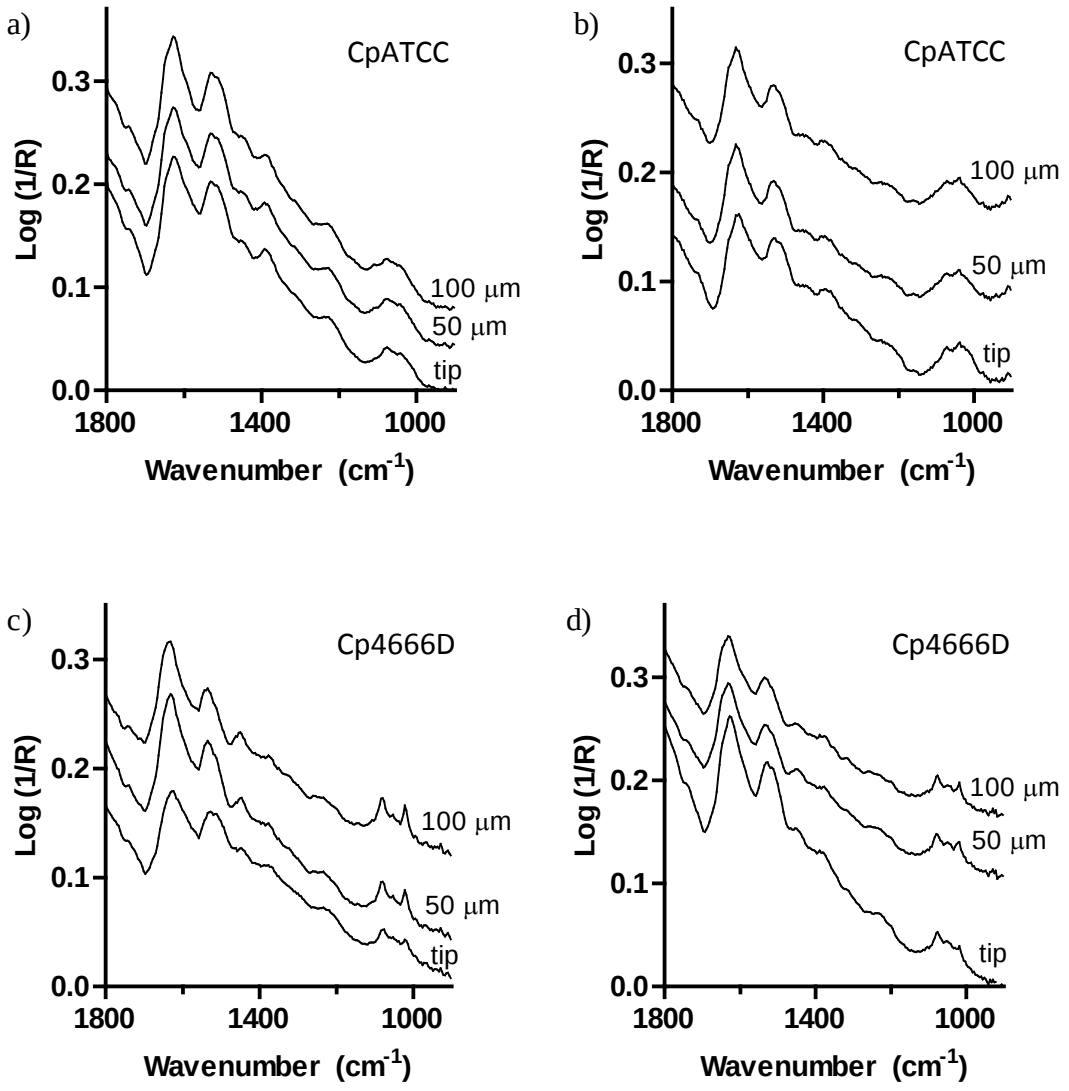

Figure 35. Hyphal spectra (CLS, Nov. 2007) collected from a) CpATCC (100% PDA) b) CpATCC (10% PDA) c) Cp4666D (100% PDA) d) Cp4666D (10% PDA). Spectra were collected at positions from tips, as indicated.

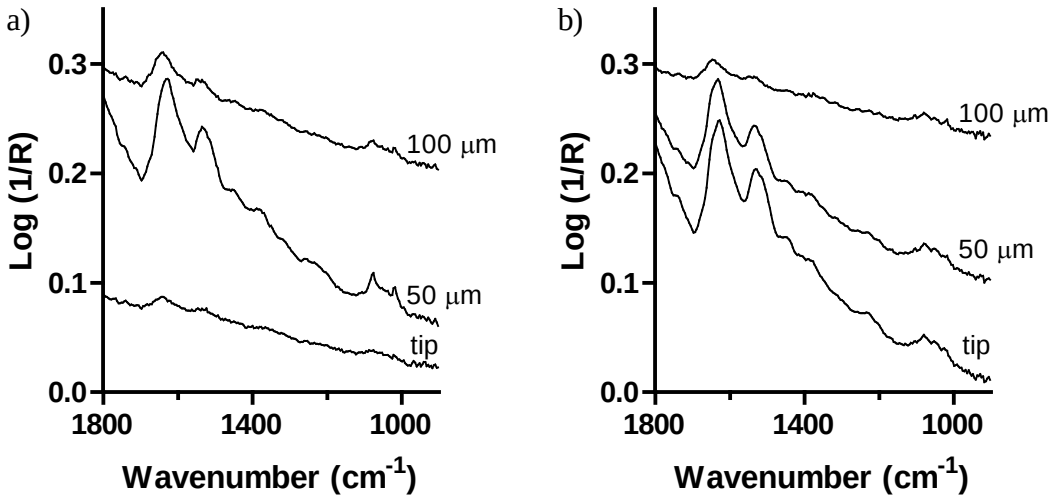

Figure 36. sFTIR (CLS Nov. 2007) spectra collected from Cp4666D hyphae grown from a) 100% and b) 10% PDA. Spectra were collected at positions as indicated relative to tip.

Samples grown from 3% and 1% PDA had less growth (fewer hyphae present) than those grown using higher concentrations of PDA; however, absorbance intensities in hyphal spectra are not necessarily decreased for these samples, as seen from the comparison of a hypha grown from 100% PDA and one grown from 1% PDA in Figure 37. Samples grown from 3% and 1% PDA have been examined more extensively with the FPA at the U of M than at synchrotrons (samples grown from 3% and 1% PDA were examined at CLS but not SRC). The FPA spectra, and therefore more detail about samples grown from 3% and 1% PDA, are presented later in this chapter.

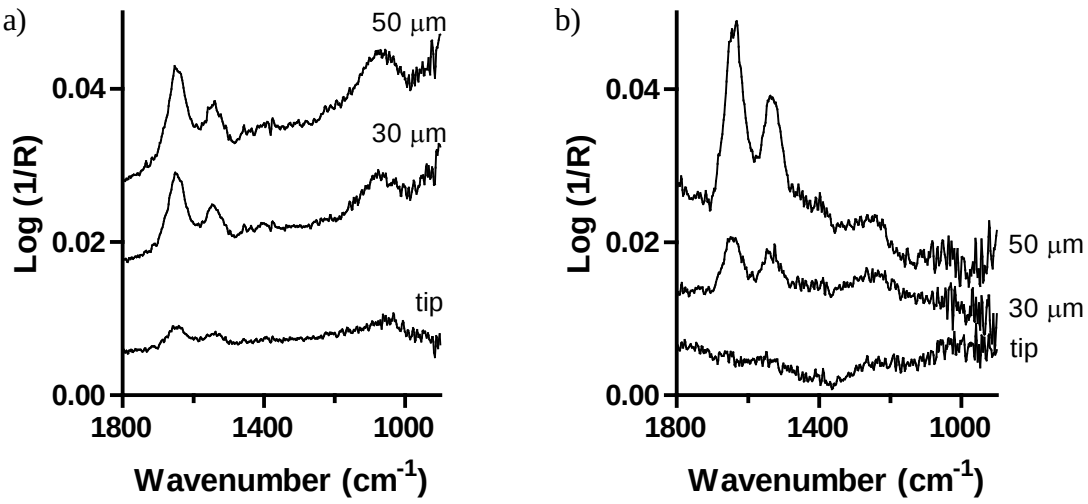

Figure 37. Cp4666D sFTIR spectra (CLS June 2008) collected from hyphae grown from a) 100% and b) 1% PDA. Spectra were collected at positions as indicated relative to tip. Again, the instability of the beam at CLS is apparent due to the low S/N in spectra, especially at lower wavenumbers.

Variations in sugar and amide absorption intensities were observed from one hypha to another within the same sample, as shown in Figure 38 for samples grown using 100% and 10% PDA. Spectra were collected 100 μm from tips on hyphae, all of which were grown at the same time and under the same conditions.

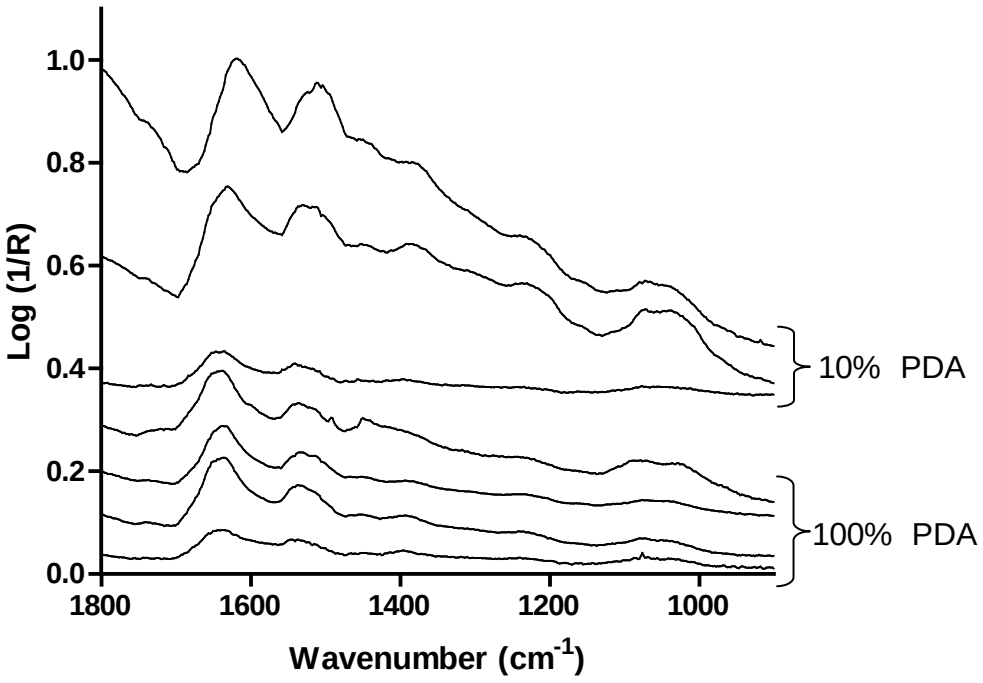

Figure 38. Variation in signal intensity observed in spectra collected 100 μm from tips on different CpATCC hyphae grown from 10% PDA (top three spectra) and 100% PDA (bottom four spectra). Both samples were grown on the same slide and under the same conditions. Spectra collected at SRC, April 2008.

Spectral Similarities and Differences between CpATCC & Cp4666D

The absorbance intensities of protein and sugar bands along the length of hyphae for both CpATCC and Cp4666D were often comparable to each other, as seen in Figure 39. The variations in absorbance intensity between the two samples are comparable to that seen along one hypha or between different hypha of the same sample (see Figure 38).

The clear difference initially observed between the geothermal and non-geothermal *C. protuberata* samples in synchrotron spectra was the presence of two sharp peaks at approximately 1078 and 1022 cm^{-1} in the spectra of geothermal samples, shown in Figure 40. These peaks were not present in spectra from every Cp4666D hypha (refer to Figure 39); however, they were never seen in the synchrotron spectra of any CpATCC hyphae. The peaks were present in spectra of Cp4666D hyphae for samples grown from both 100% and 10% PDA and the two peaks were always present together. Often, less intense peaks at 1050 and 930 cm^{-1} were also visible in spectra when the 1078 and 1022 cm^{-1} peaks were present, as illustrated in Figure 41.

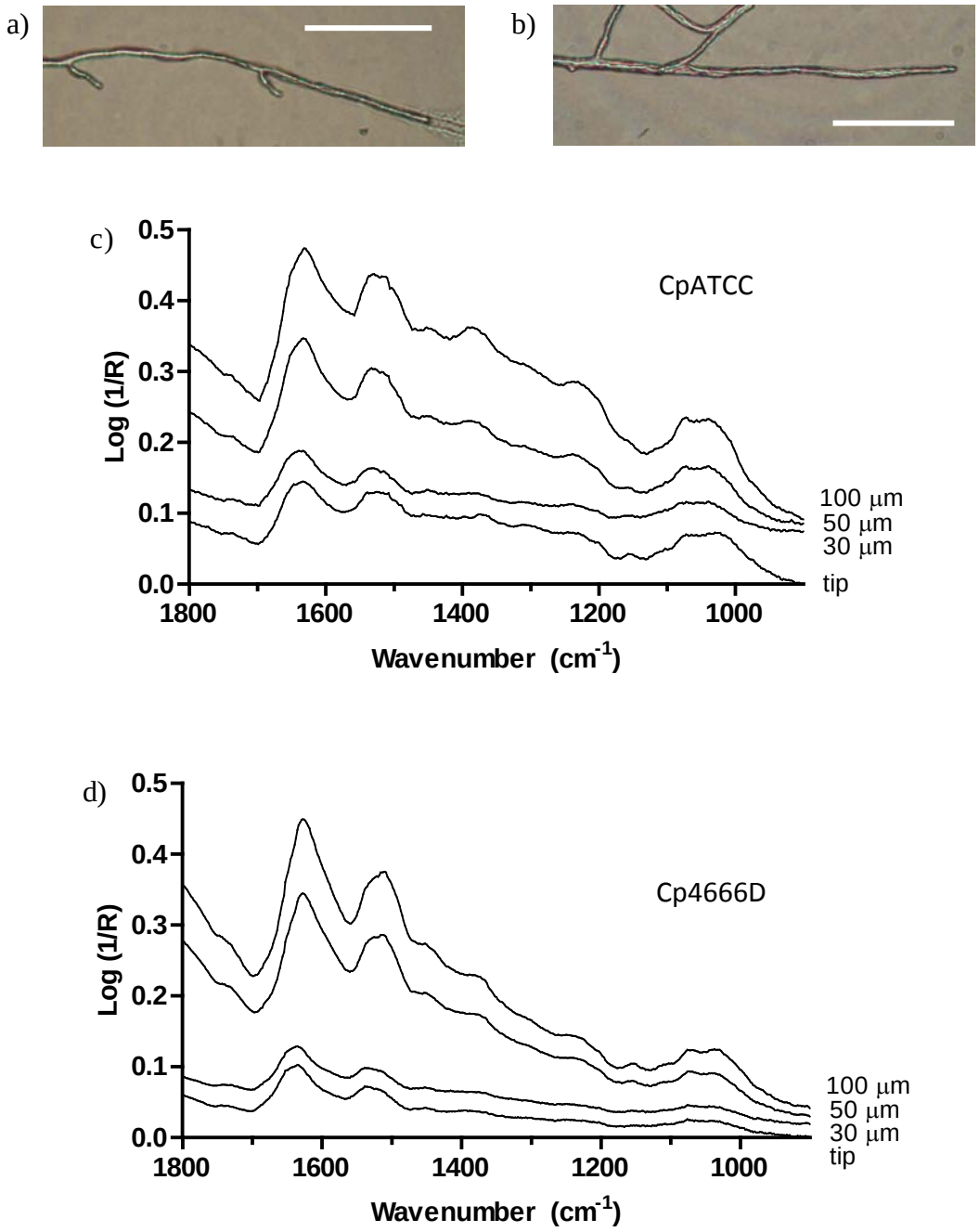

Figure 39. Photos of a) CpATCC and b) Cp4666D hyphae. sFTIR spectra (SRC April 2008) collected from c) CpATCC (256 scans) and d) Cp4666D (512 scans) hyphae at positions as indicated. Both samples were grown from 10% PDA. Scale bars = 50 μm.

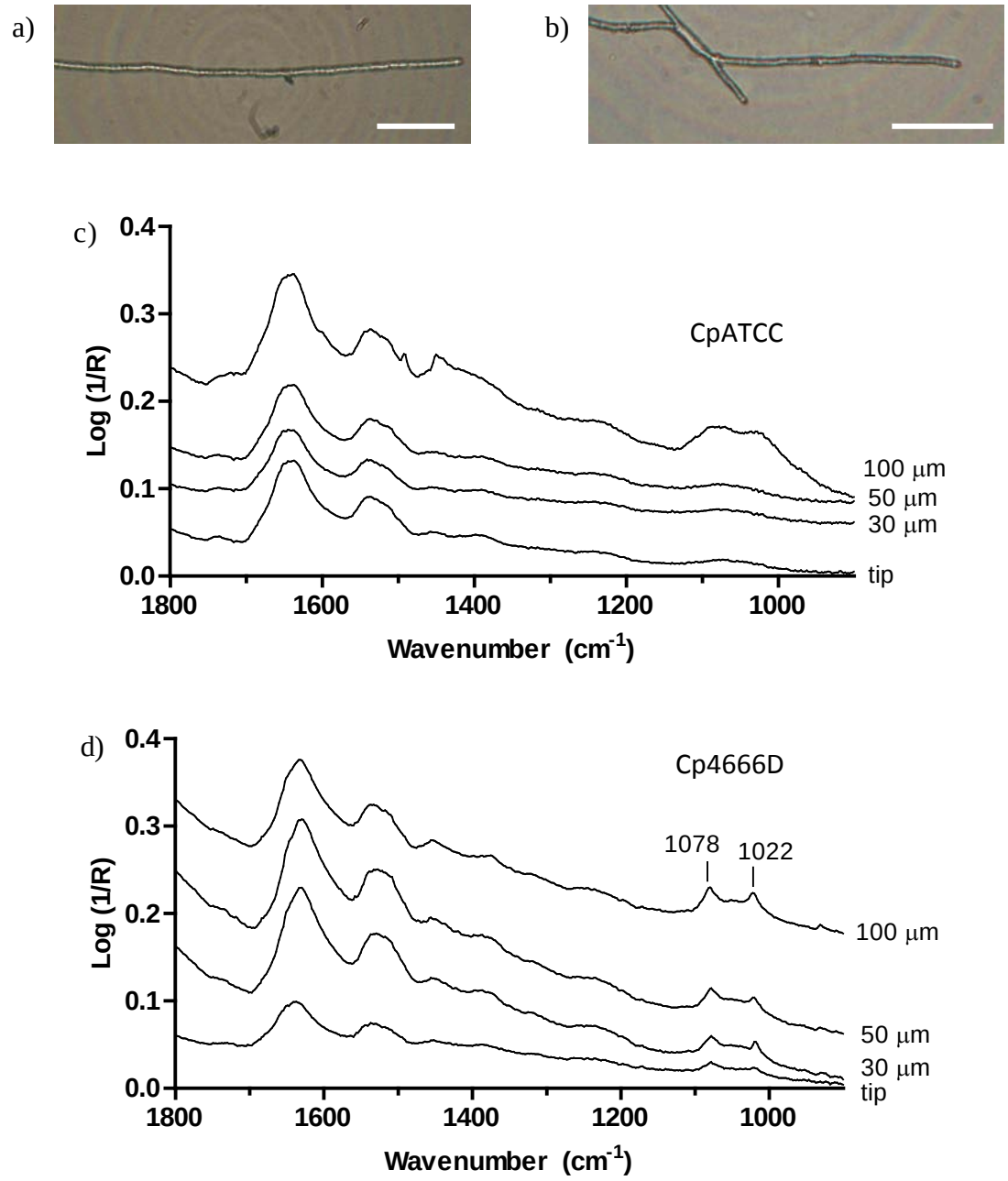

Figure 40. Photo of a) CpATCC and b) Cp4666D hyphae grown from 100% PDA and examined with sFTIR (SRC April 2008). Spectra (256 scans) collected from c) CpATCC and d) Cp4666D hyphae at positions as indicated. Scale bars = 50 μm.

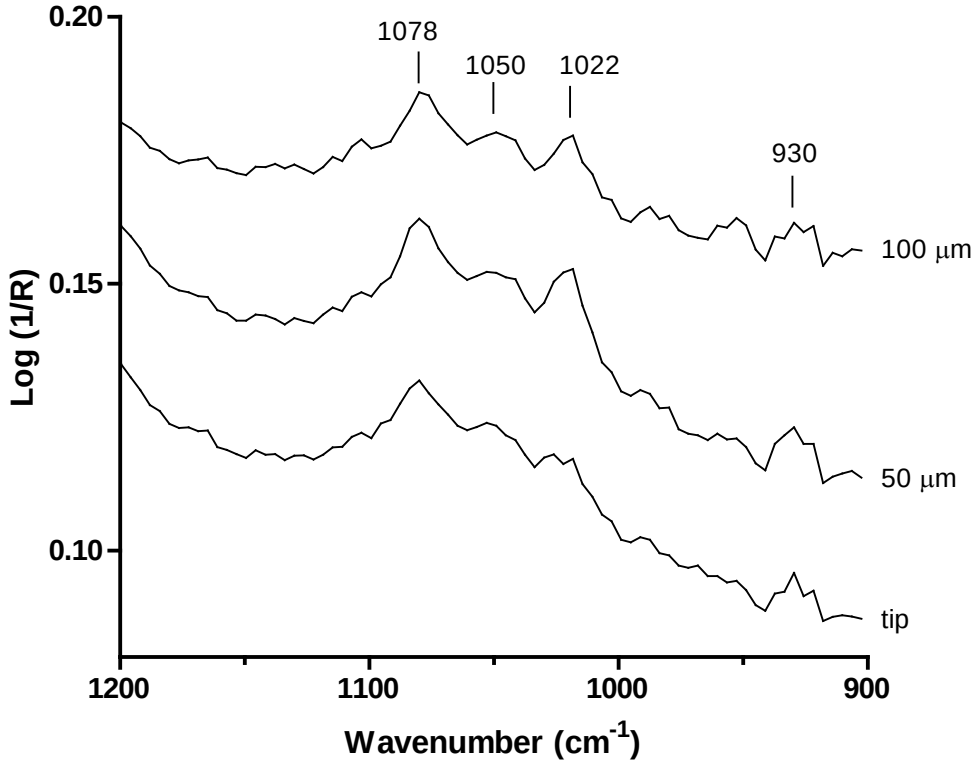

Figure 41. Spectra (CLS Nov. 2007) from a Cp4666D hypha grown from 10% PDA, expanded region showing the unusual bands at 1078, 1050, 1022, and 930 cm^{-1}.

A summary of the appearance of the 1078 and 1022 cm^{-1} peaks in spectra for all Cp4666D samples examined with sFTIR is given in Table 7. This table includes the number of hyphae examined from each sample along with the number of hyphae found to contain the two sharp peaks in spectra (for at least one position along the hypha). These peaks were never detected in sFTIR spectra from Cp4666D samples grown from 3% and 1% PDA; however, these samples were examined to a lesser extent than those grown from the higher concentrations of PDA.

Some spectra collected at CLS (June 2008 and December 2008) were very noisy, especially in the carbohydrate region (refer to Figure 31b). As a result, it was often difficult to determine whether any sharp peaks were present in this region. Unless the presence of these peaks was obvious (strong bands that could not be mistaken for noise), these hyphae were counted as not having the two peaks present. Therefore, Table 7 also contains a summary of data without the inclusion of CLS spectra from these two dates.

Table 7. Cp4666D hyphae containing peaks at 1078 and 1022 cm^{-1} in sFTIR spectra collected at SRC and CLS.

		All sFTIR Data		Without CLS June 2008 & December 2008 Data	
Slide	Medium	Total Hyphae	With Peaks	Total Hyphae	With Peaks
37	100% PDA	9	6	9	6
	10% PDA	10	5	10	5
39	100% PDA	4	0	-	-
	1% PDA	5	0	-	-
46	100% PDA	9	2	3	1
	10% PDA	20	3	-	-
	3% PDA	4	0	-	-
63	1x GYE	13	0	-	-
128[†]	100% PDA	7	0	7	0
129	100% PDA	6	0	6	0
	Total	**87**	**16**	**35**	**12**

[†]no virus

FPA Data

With the acquisition of a Varian FTIR spectrometer and Varian imaging microscope with a 64 x 64 element array detector at the U of M in May 2009, the number of hyphal positions that could be examined with respect to time was dramatically increased. Figure 42 displays FPA maps (processed for area under the amide I band) collected from different samples of Cp4666D grown on the same slide but from different concentrations of PDA (100%, 10%, 3%, 1%). Figure 43 displays spectra taken from within four other Cp4666D maps collected from samples grown from different PDA concentrations at comparable positions relative to hyphal tips. Both figures show a fairly consistent protein distribution along hyphae.

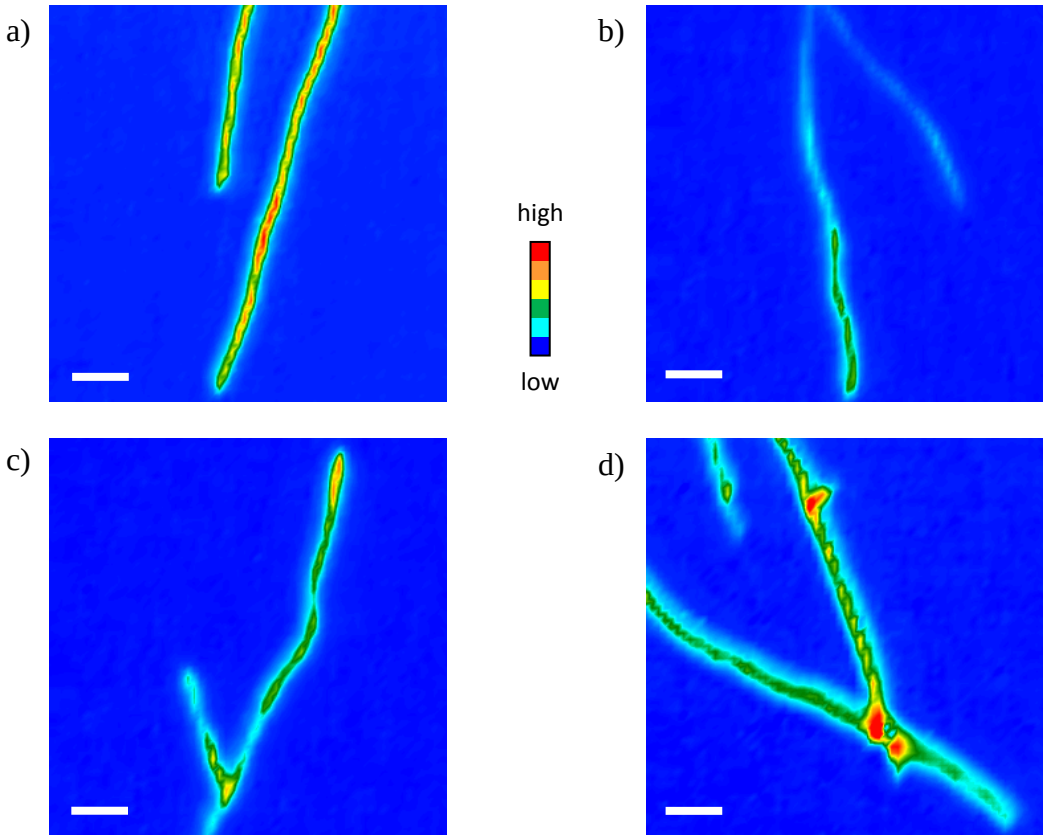

Figure 42. FPA maps of Cp4666D hyphae grown from a) 100% PDA, b) 10% PDA, c) 3% PDA, and d) 1% PDA. All samples were grown under the same conditions. False-colour maps show the area under the amide I band. All four maps are plotted with the same false-colour intensity scale. Scale bars = 50 µm. Each map took 52 minutes to acquire (4096 spectra each).

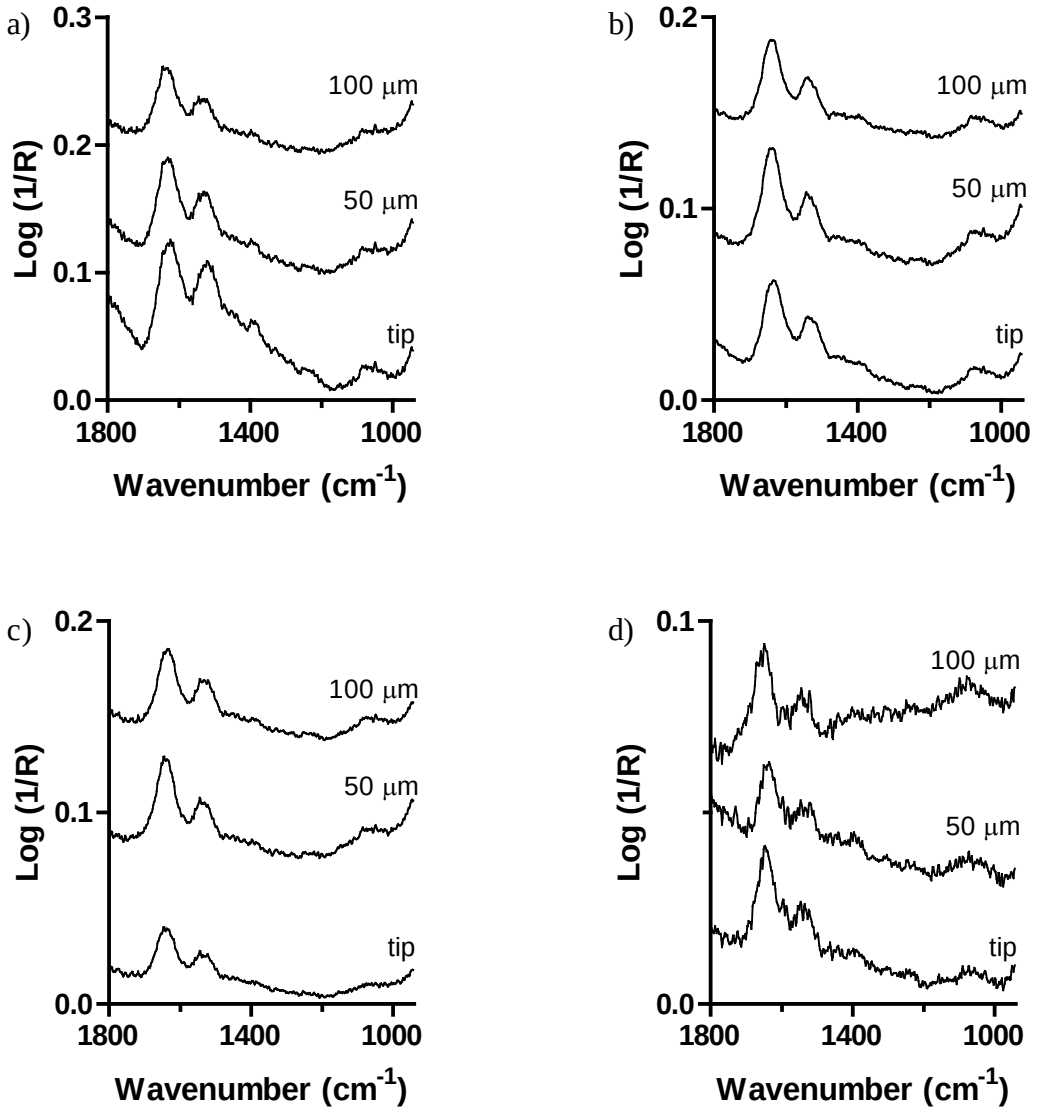

Figure 43. Spectra from FPA maps of Cp4666D hyphae grown from a) 100% PDA, b) 10% PDA, c) 3%PDA, and d) 1% PDA. Spectra were collected at hyphal positions as indicated.

Figure 44 (CpATCC) and Figure 45 (Cp4666D) each show sFTIR spectra collected at defined positions on a hypha and an FPA map collected with a globar source for the same hypha, along with spectra from the map at similar positions. The sFTIR spectra were collected using a 10 x 10 µm aperture and summing 512 scans for CpATCC spectra and 256 scans for Cp4666D spectra; the FPA maps (5.5 µm pixels) were collected by summing 1024 scans. Data collection for one hypha at SRC could take up to 90 minutes (background, four positions along hypha, and manually repositioning the sample between acquisition of each spectrum). Summing 1024 scans with the FPA detector takes 52 minutes. A background and sample map can be acquired in less than 2 hours, and the result is spectra along approximately 350 µm of the hypha or multiple hyphae (4096 spectra total, the majority of which are only on the blank slide surrounding hyphae).

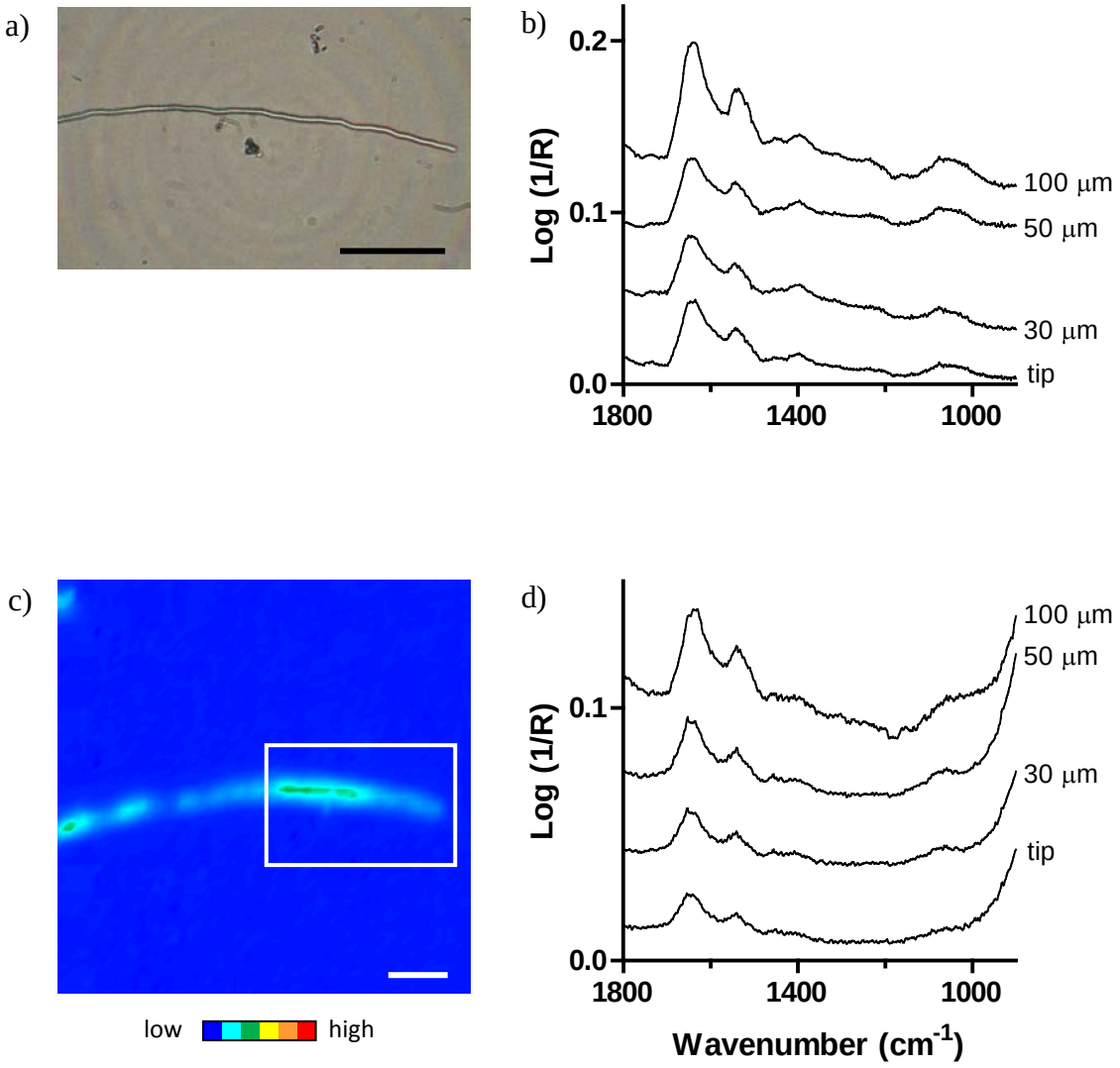

Figure 44. a) Photo of a CpATCC hypha grown from 10% PDA and b) spectra collected from the hypha at positions as indicated. c) FPA map of the same hypha processed for area under the amide I band. The box represents the area displayed in (a). d) Spectra from the FPA map from positions as indicated. Scale bars = 50 μm.

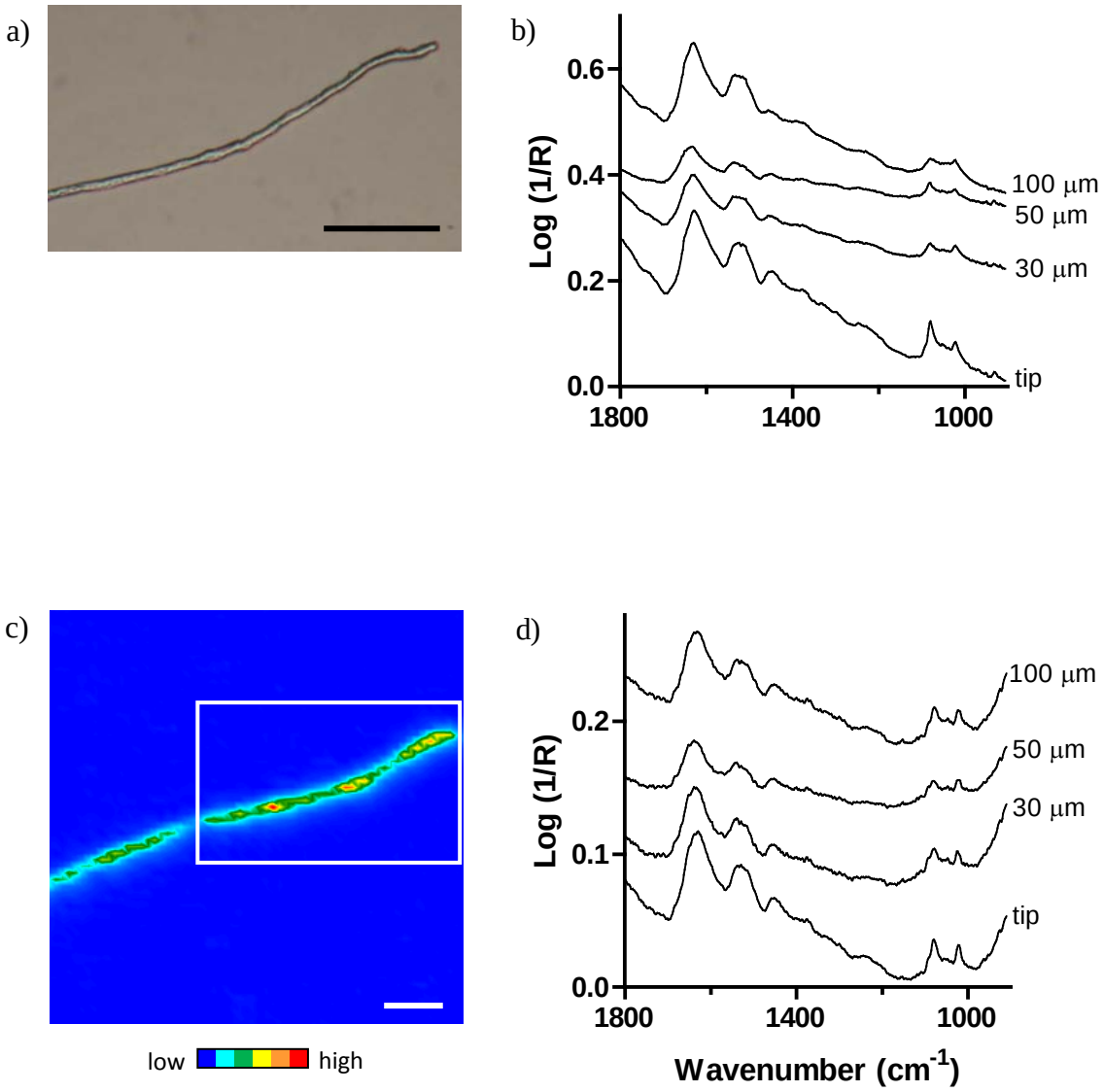

Figure 45. a) Photo of a Cp4666D hypha grown from 100% PDA and b) sFTIR spectra collected at positions indicated. c) FPA map of the same hypha processed for area under the amide I band. The box on the map represents the area shown in (a). d) Spectra from the FPA map at positions as indicated. Scale bars = 50 μm.

Figure 46 displays an FPA map of CpATCC hyphae processed for different bands of interest. It is clear from each of the displays that one hypha has an increased overall biochemical content (*e.g.* proteins, sugars) compared to the neighbouring hypha. The FPA detector is also useful for examining the biochemical distribution in cells along the length of hyphae, as shown in Figure 47. For the 1078 and 1022 cm^{-1} peaks in Cp4666D spectra, their distribution along the hypha is visualized with the FPA image and can be compared to the visible light image as well as to the protein allocation in the hypha.

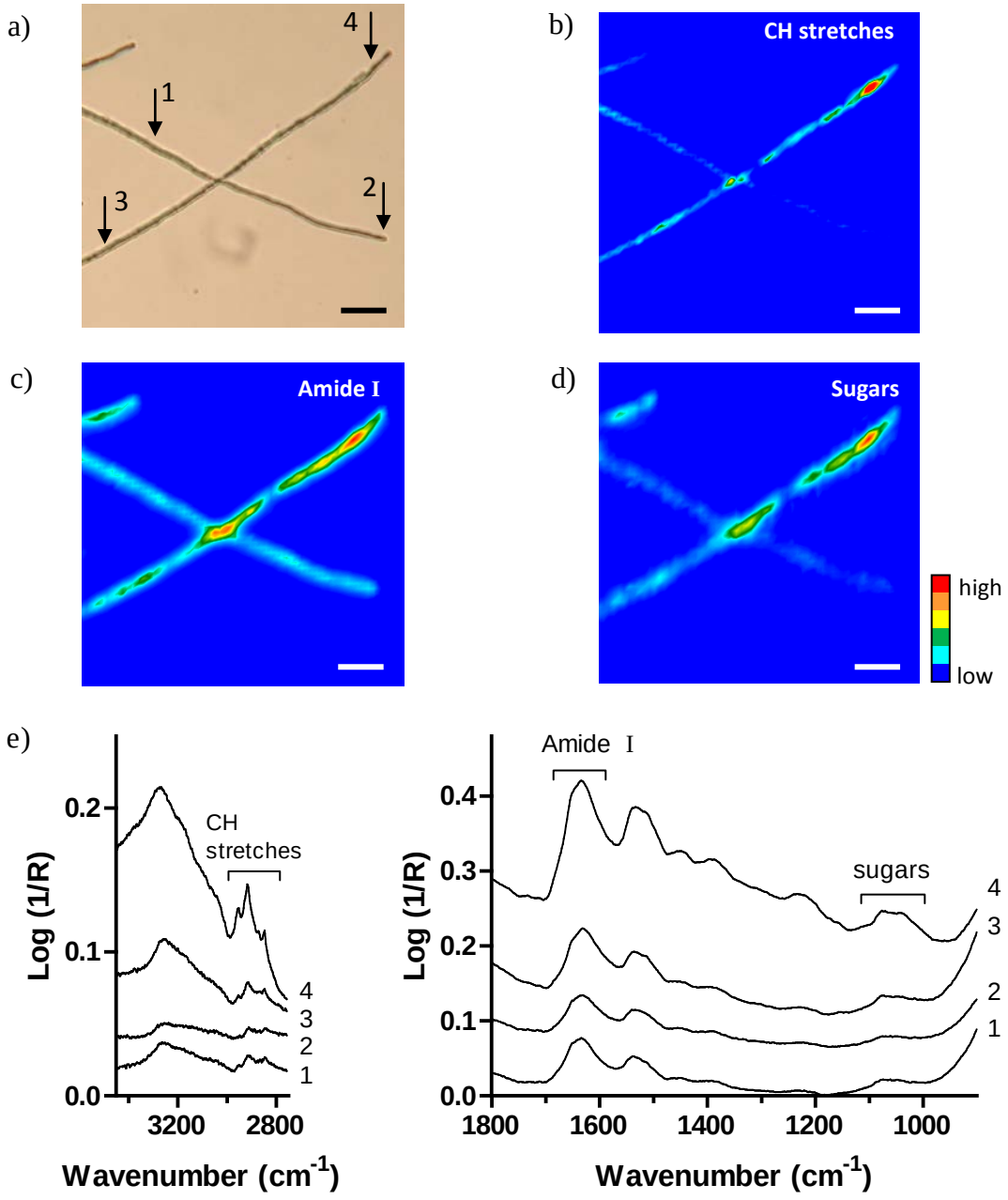

Figure 46. a) CpATCC hyphae grown from 100% PDA. FPA maps processed for area under b) CH stretch bands (2967-2840 cm^{-1}; baseline 2987-2831 cm^{-1}), c) amide I (1666-1610 cm^{-1}; baseline 1711-1480 cm^{-1}), and d) sugar region (1085-1022 cm^{-1}; baseline 1138-982 cm^{-1}). e) FPA spectra from hyphae, as marked in (a). Scale bars = 50 µm.

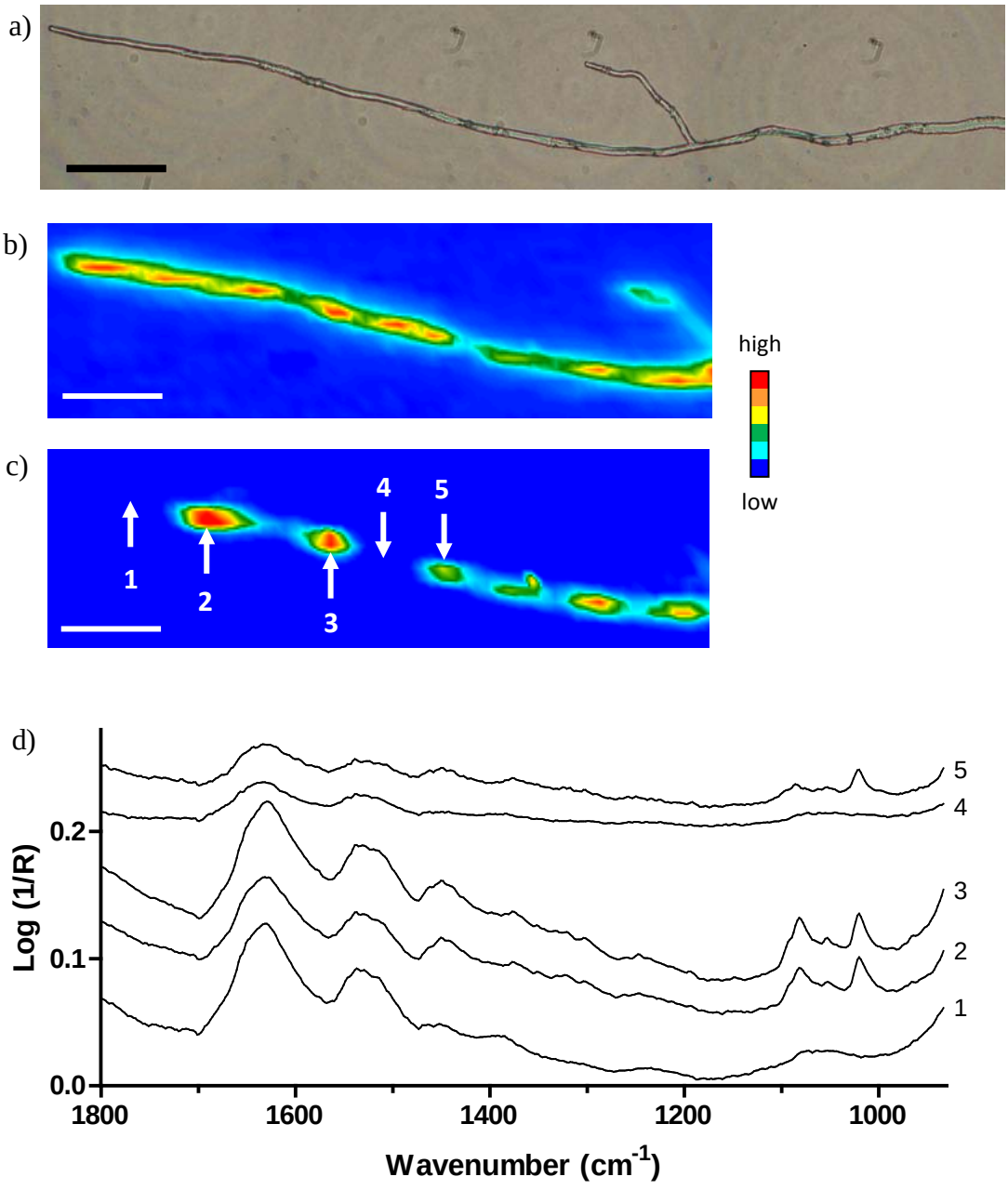

Figure 47. a) Image of a Cp4666D hypha grown from 100% PDA. FPA map of the hypha processed to show b) area under amide I and c) area under the 1021 cm^{-1} peak. d) Selected spectra from the map at positions as indicated on map (c). Scale bars = 50 µm.

As mentioned earlier, a few samples were grown on gold substrates. Figure 48 and Figure 49 display FPA maps collected from Cp4666D hyphae grown on gold. Spectra were similar to those collected along hyphae grown on MirrIR substrates. Several of these hyphae were also examined with Raman. These Raman spectra are displayed later in the Results section. The two sets of data are reviewed in the Discussion.

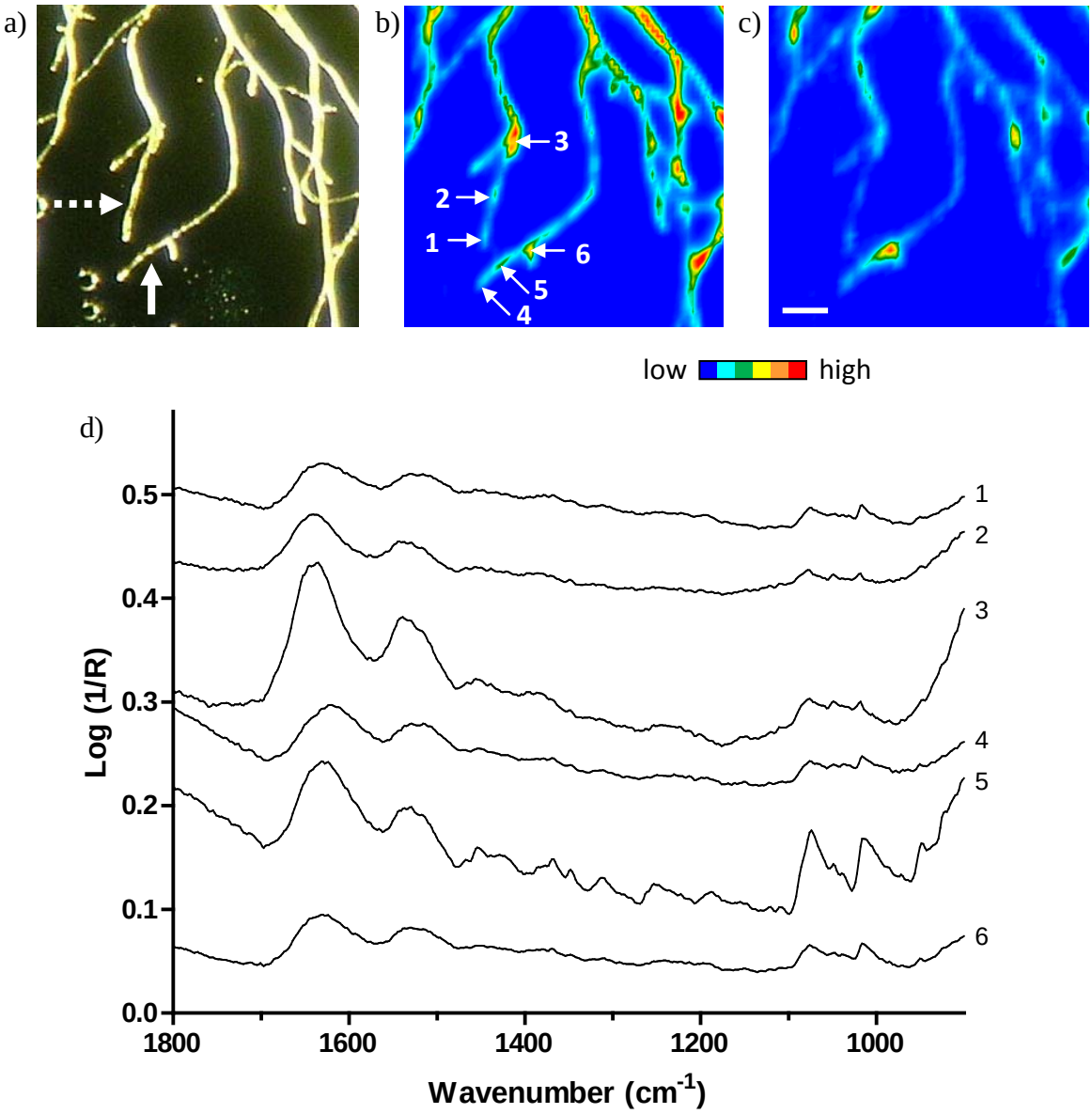

Figure 48. a) Photo of Cp4666D hyphae grown on gold from 100% PDA. Arrows point to hyphae also examined with Raman. FPA maps processed for area under b) amide I and c) the 1078 cm^{-1} band. d) Selected spectra from the map, as indicated in (b). Scale bar = 50 µm.

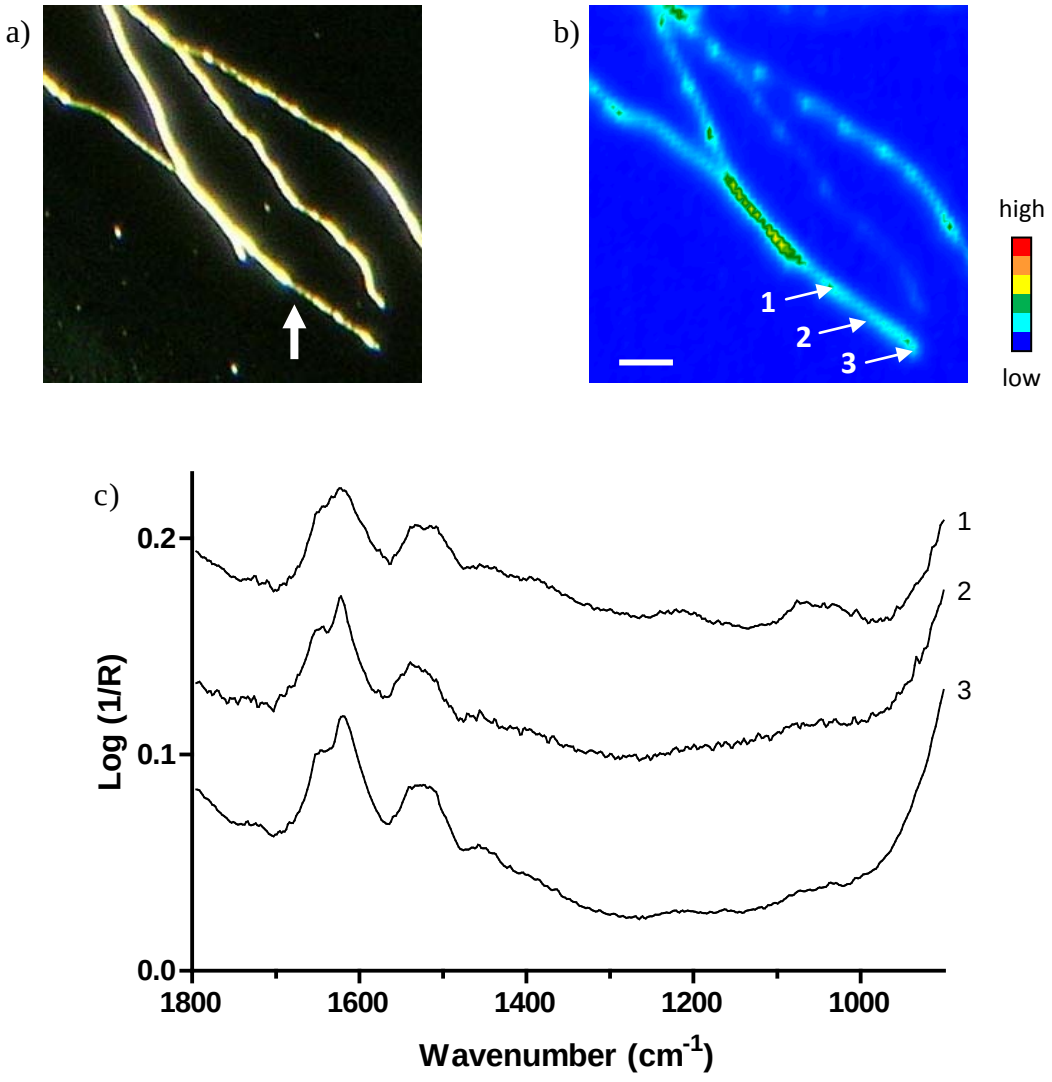

Figure 49. a) Photo of Cp4666D hyphae grown on gold from 100% PDA. Arrow points to a hypha that was also examined with Raman. b) FPA map processed for the area under the amide I band. c) Selected spectra as indicated on the FPA map. Scale bar = 50 µm.

Peaks at 1078 & 1022 cm^{-1} found in certain CpATCC FPA spectra

While collecting maps with the FPA detector at U of M, it was noted for the first time that some CpATCC hyphal spectra contained peaks at around 1078 and 1022 cm^{-1}, shown in Figure 50. These two peaks were not seen in any of the synchrotron spectra from CpATCC hyphae. The spectrum recorded 250 μm from tip of the hypha with the FPA detector (Figure 50f) contains very intense 1078 and 1022 cm^{-1} bands. sFTIR spectra (SRC, April 2008) were not collected this far from tips and therefore, bands at this position were not initially observed from the limited quantity of synchrotron data. Table 8 (CpATCC) and Table 9 (Cp4666D) outline the number of hyphae found to contain these peaks in spectra from FPA maps collected at the U of M.

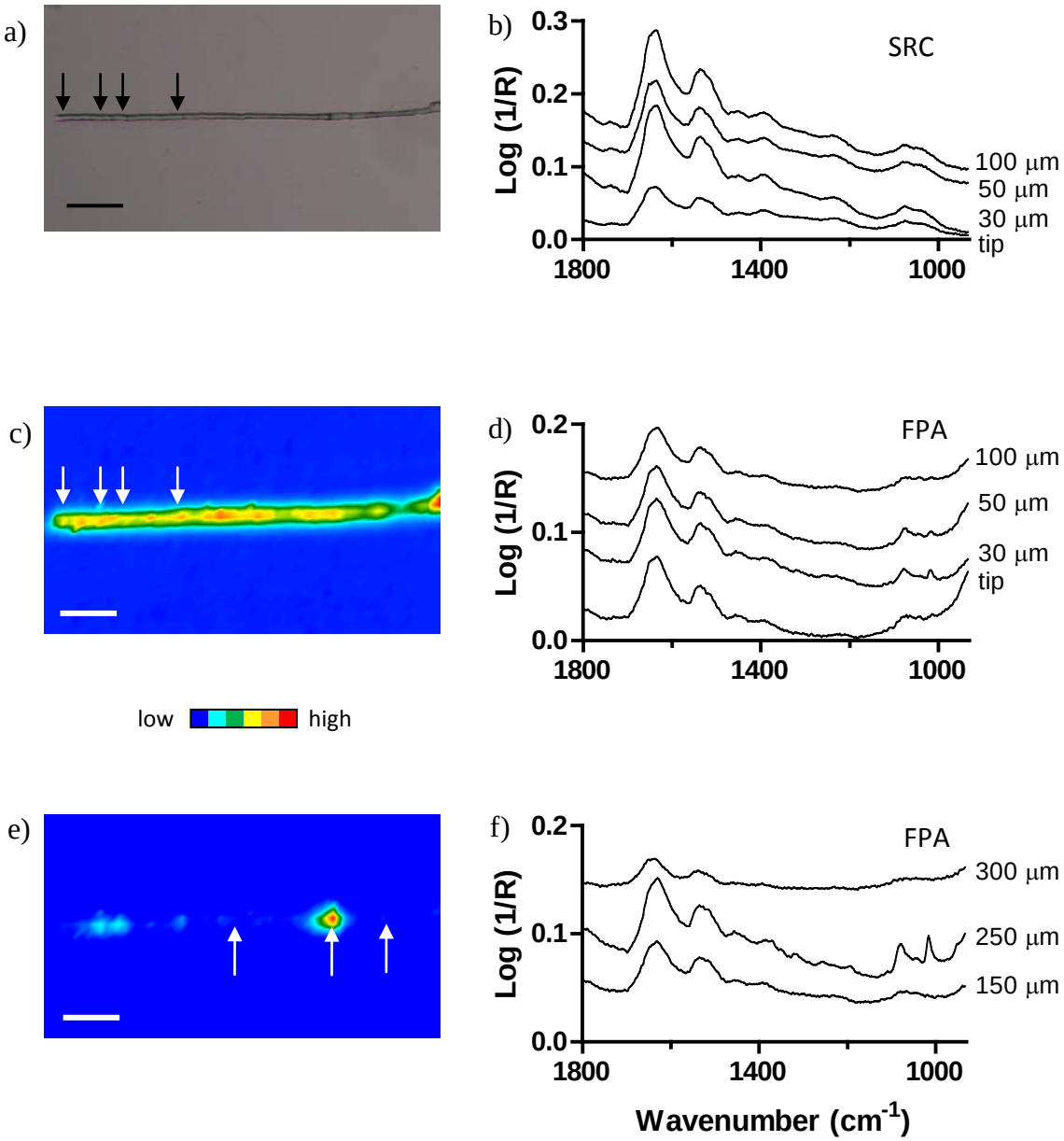

Figure 50. a) Photo of a CpATCC hypha grown from 100% PDA. b) sFTIR spectra collected at positions as indicated. c) FPA map processed for the area under the amide I curve. d) FTIR FPA spectra from positions as indicated. e) FPA map processed for the area under the 1076 cm^{-1} peak. f) FTIR spectra from the map at positions as indicated relative to the tip. Scale bars = 50 µm.

Table 8. CpATCC hyphae containing peaks at 1078 and 1022 cm^{-1} in FPA spectra.

			# of Hyphae	
Slide	Growth Date	Medium	Examined	With Peaks
34	November 2007	100% PDA	14	6
		10% PDA	8	0
40	June 2008	100% PDA	2	2
45	June 2008	100% PDA	11	1
		10% PDA	6	0
		3% PDA	7	0
		Total	**48**	**9**

Table 9. Cp4666D and CPA hyphae containing peaks at 1078 and 1022 cm^{-1} in FPA spectra.

			# of Hyphae	
Slide	Growth Date	Medium	Examined	With Peaks
37	November 2007	100% PDA	22	20
		10% PDA	12	9
37*	November 2007	100% PDA	16	9
39	June 2008	100% PDA	14	0
		10% PDA	5	0
46	June 2008	100% PDA	8	4
		10% PDA	6	1
		3% PDA	7	0
		1% PDA	5	0
63	December 2008	1x GYE	2	1
		0.1x GYE	1	1
135	October 2009	100% PDA	11	0
135 CPA	October 2009	100% PDA	5	0
		Total	**114**	**45**

*on gold

Spectra collected at positions where branches grow off a main hypha often contain bands at 1078 and 1022 cm^{-1}. Figure 51 displays two CpATCC hyphal branches growing out from a main hypha. One of the branches appears to be producing a spore at its tip. Figure 52 displays another instance of CpATCC hyphal branching; both branches may be producing spores at tips. An example of these bands in spectra collected at branch points for Cp4666D can be seen in Figure 48.

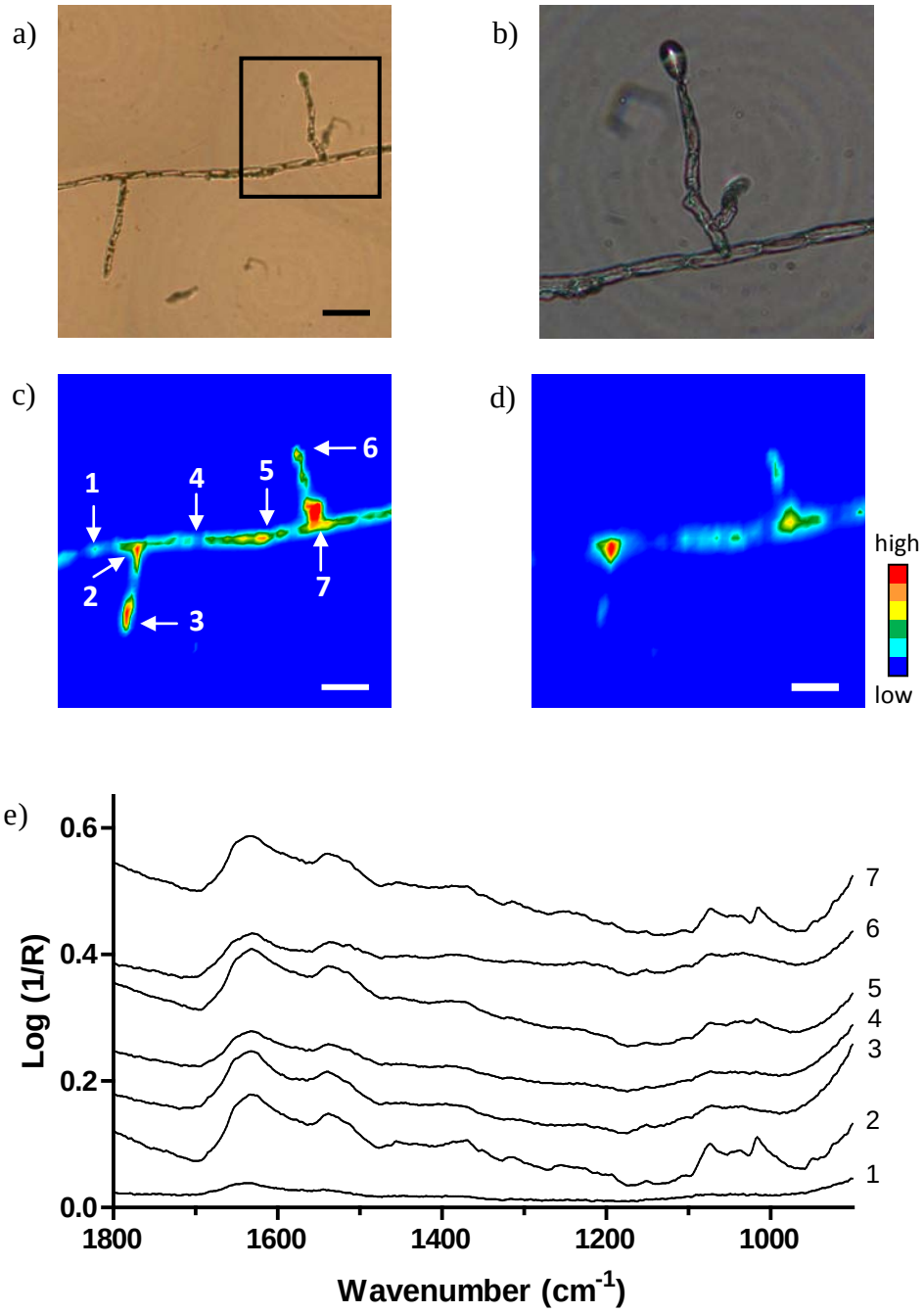

Figure 51. a) Photo of CpATCC branches grown from 100% PDA. The boxed area shows a branch that may be producing a spore at its tip and outlines the area displayed in (b). FPA maps processed for area under c) the amide I band and d) the band at 1016 cm^{-1}. e) Selected spectra from the map, at positions indicated in (c). Scale bars = 50 µm.

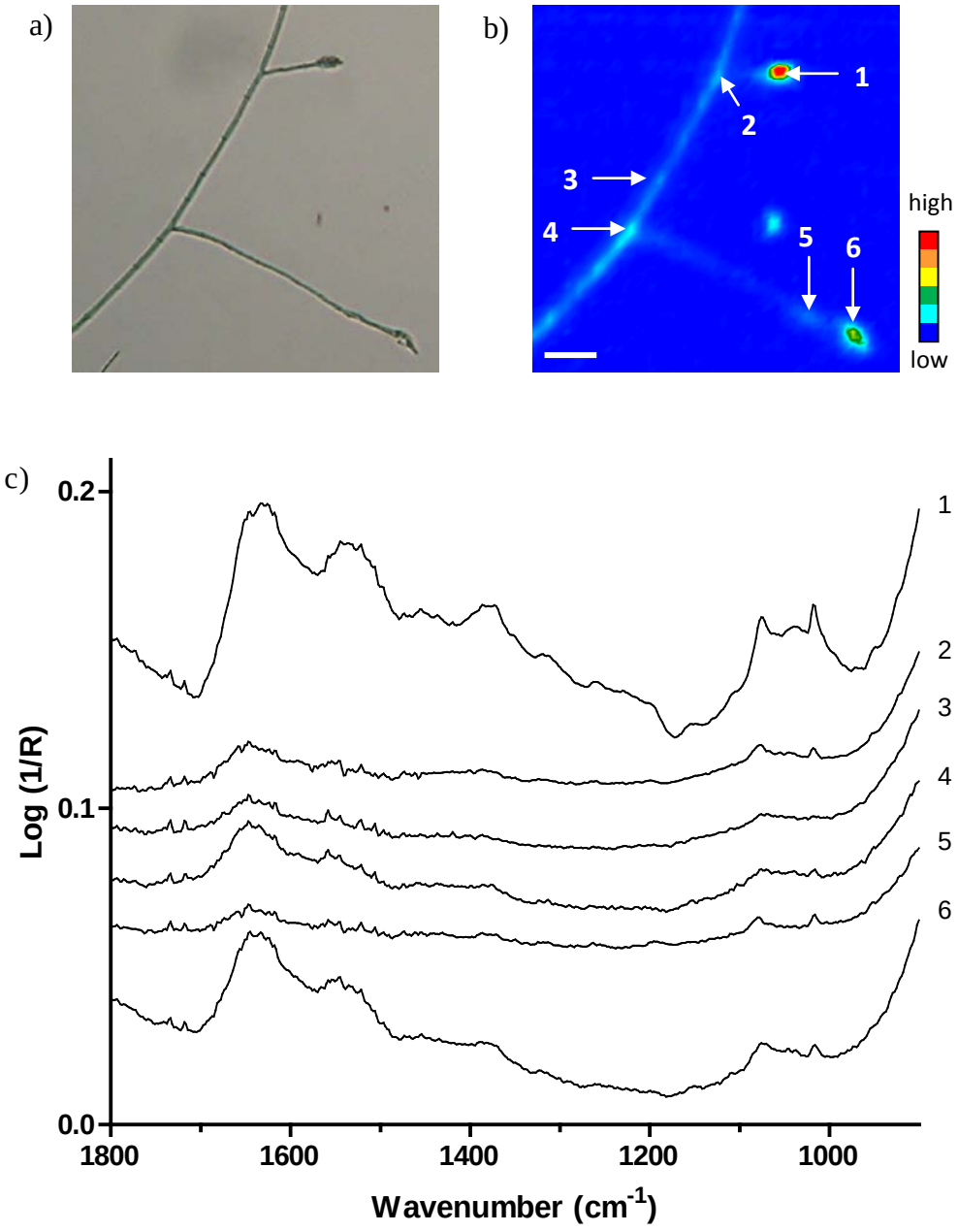

Figure 52. a) Photo of a CpATCC hypha with branches grown from 100% PDA and b) corresponding FPA map processed to show the area under the amide I band. This hypha was found to contain peaks at 1078 and 1022 cm^{-1} in spectra. c) Selected spectra, as indicated on the FPA map image, where the two peaks are present.

In order to determine the effect that the virus may have on spectra, geothermal *C. protuberata* with the virus removed (Cp4666D no virus) was grown at the same time as Cp4666D (containing the virus). Six Cp4666D hyphae and seven Cp4666D no virus hyphae were examined with sFTIR at SRC. Sample spectra are displayed in Figure 53. For a given hypha, there was comparable amide signal at positions of 30 µm, 50 µm and 100 µm from tips. For some hyphae, amide intensity was lower at tips, while for others the intensity was similar to that at other positions. The absorbance intensities in the carbohydrate region of spectra were generally low and neither Cp4666D nor Cp4666D no virus exhibited sharp peaks in spectra at 1078 and 1022 cm^{-1} at any positions. There were, however, certain Cp4666D hyphae that were found to contain greater amounts of sugar compared to Cp4666D no virus hyphae (*e.g.* spectra in Figure 53).

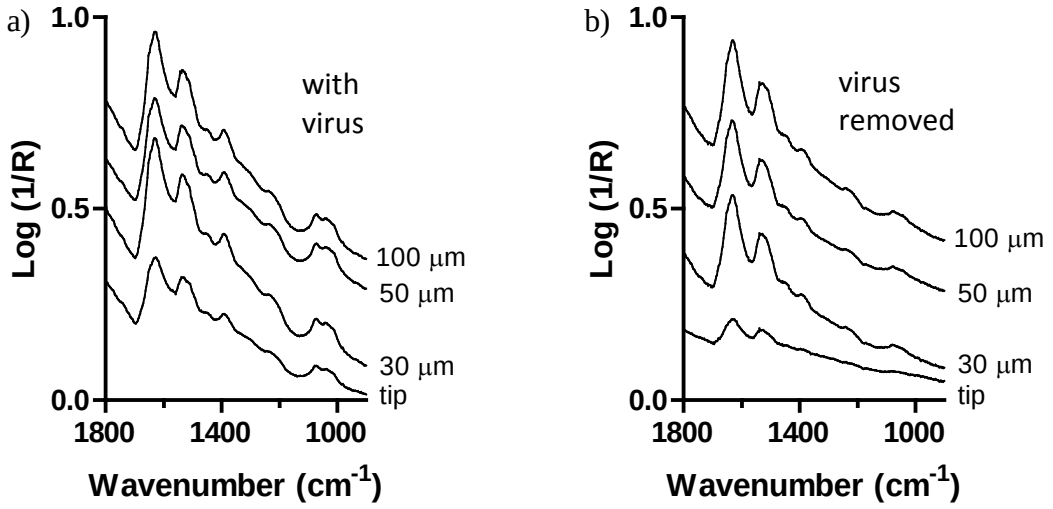

Figure 53. sFTIR spectra (SRC, Aug. 2009) collected from samples of Cp4666D a) containing the virus necessary to confer heat tolerance to plants and b) with the virus removed. Both samples were grown from 100% PDA.

A control Cp4666D sample (contains the virus) and CPA (virus removed and later reintroduced) were grown at the same time and examined with FTIR and the FPA detector at U of M. The CPA sample was prepared by freezing Cp4666D spores to -80ºC to remove the virus. Once revived, this sample was grown alongside Cp4666D (contained the virus) so that it could reacquire the virus. Figure 54 shows a map of two CPA hyphae along with selected spectra from within the map. Neither Cp4666D nor CPA hyphal spectra were found to contain peaks around 1078 and 1022 cm^{-1}.

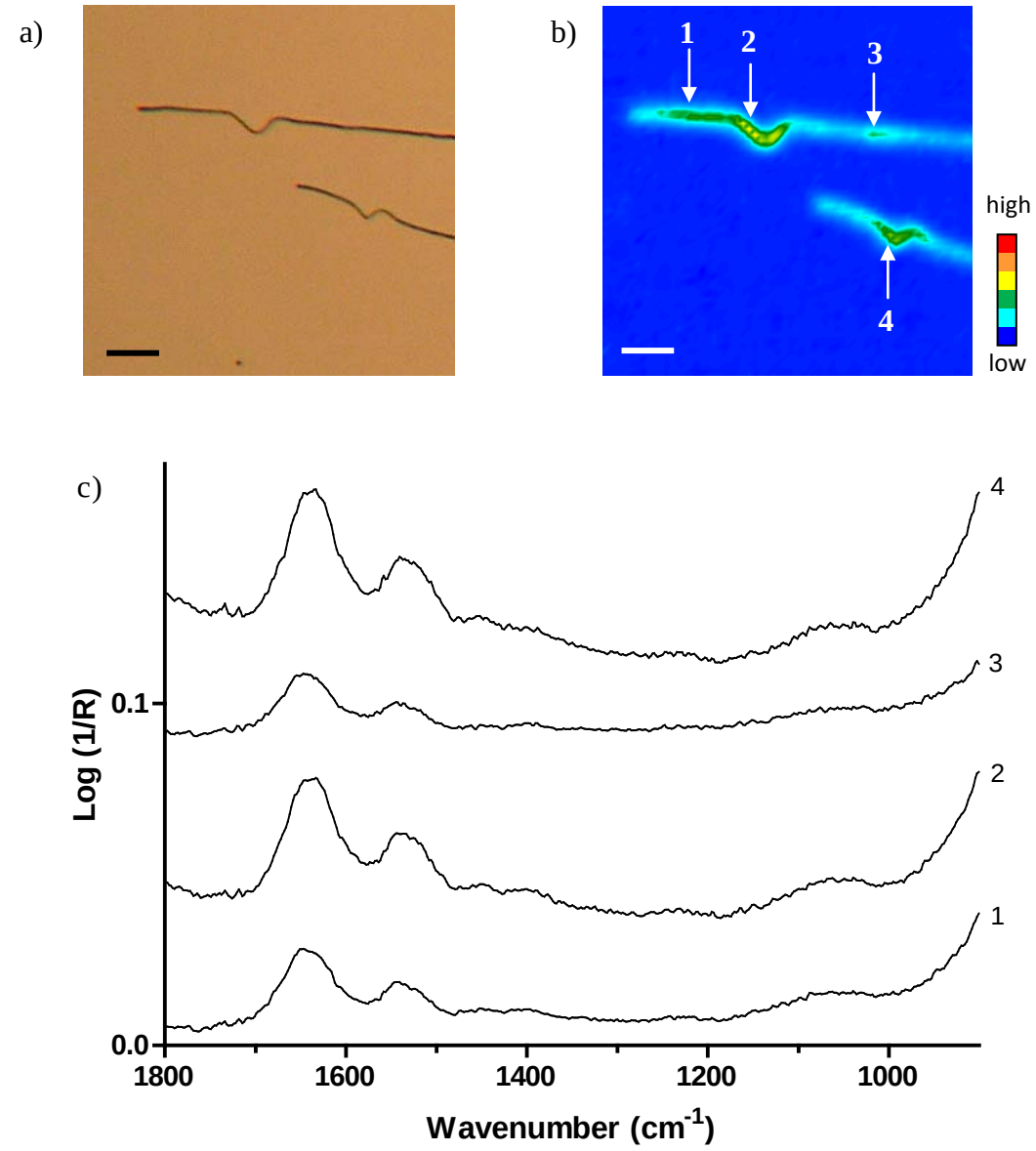

Figure 54. a) Image of two CPA hyphae grown on MirrIR from 100% PDA. b) FPA map of the hyphae. c) Selected spectra from the map from positions as indicated on the map. Scale bars = 50 µm. The curved hyphae suggest that these were growing aerially and collapsed onto the slide when frozen.

3.2.5 *Fusarium culmorum*

Fusarium culmorum samples isolated from non-coastal (Fc18) and coastal (FcRed1) plants were both examined using sFTIR to see whether spectra could offer insight into the mechanism of salt tolerance conferred by FcRed1 samples. Images of Fc18 and FcRed1 hyphae are displayed in Figure 55. No differences in growth were observed between the two samples; hyphae from both isolates were generally 2-3 µm in diameter. As with the *C. protuberata* samples (Figure 22), the concentration of PDA used as growth medium had an effect on *F. culmorum* growth. Both Fc18 and FcRed1 samples exhibited greater amounts of growth from 100% and 10% PDA as compared to the samples grown from 3% and 1% PDA.

a) b)

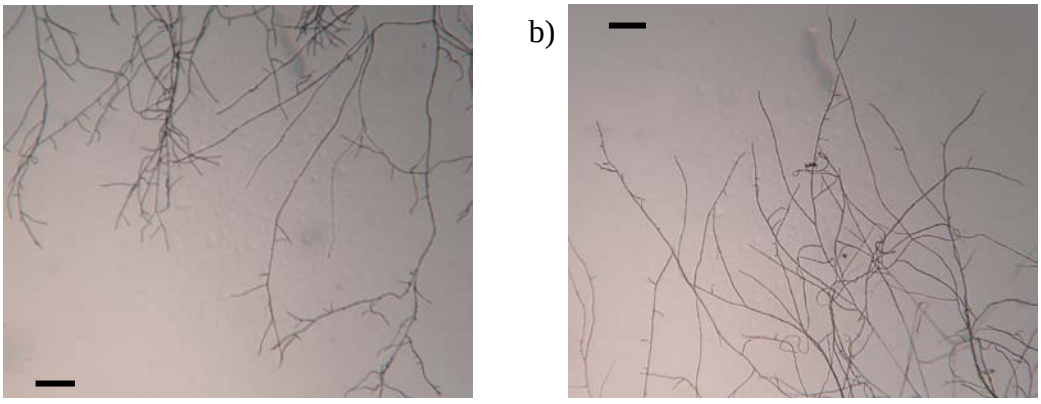

Figure 55. Photos of a) Fc18 and b) FcRed1. Both samples were grown from 100% PDA and on MirrIR. Scale bars = 200 µm.

Fusarium culmorum samples were only examined with sFTIR and not with thermal source FTIR plus an FPA detector. Table 10 (Fc18) and Table 11 (FcRed1) detail the number of hyphae from each sample that were examined and the locations (CLS, SRC) and dates of examination. Again, hyphae were generally examined at tips as well as 30 μm, 50 μm, and 100 μm from tips using 10 x 10 μm apertures.

Table 10. Number of Fc18 hyphae examined.

Slide	Substrate	Medium	Location	Date	# of hyphae
38	MirrIR	100% PDA	CLS	Nov. 2007	4
			SRC	Apr. 2008	3
		10% PDA	CLS	Nov. 2007	2
			SRC	Apr. 2008	3
44	MirrIR	1% PDA	CLS	Jun. 2008	2
47	MirrIR	100% PDA	SRC	Nov. 2008	2

Table 11. Number of FcRed1 hyphae examined.

Slide	Substrate	Medium	Location	Date	# of hyphae
38	MirrIR	100% PDA	CLS	Nov. 2007	5
			SRC	Apr. 2008	3
		10% PDA	CLS	Nov. 2007	4
			SRC	Apr. 2008	3
43	MirrIR	100% PDA	CLS	Jun. 2008	1
		3% PDA	CLS	Jun. 2008	5
48	MirrIR	100% PDA	SRC	Nov. 2008	3

For most hyphae, the overall signal intensity was very similar at all positions. The bands present in spectra collected along the length of hyphae were also similar (Figure 56). However, some hyphae did contain variations in signal intensities along their length, as seen in Figure 57. Samples grown from 10% PDA generally had absorbance intensities comparable to those grown from 100% PDA. No clear differences in the spectra of coastal and non-coastal *F. culmorum* samples have been observed, as shown in Figure 58. While some Fc18 spectra have higher protein and sugar absorption intensities than certain FcRed1 spectra, this does not necessarily apply to all hyphae.

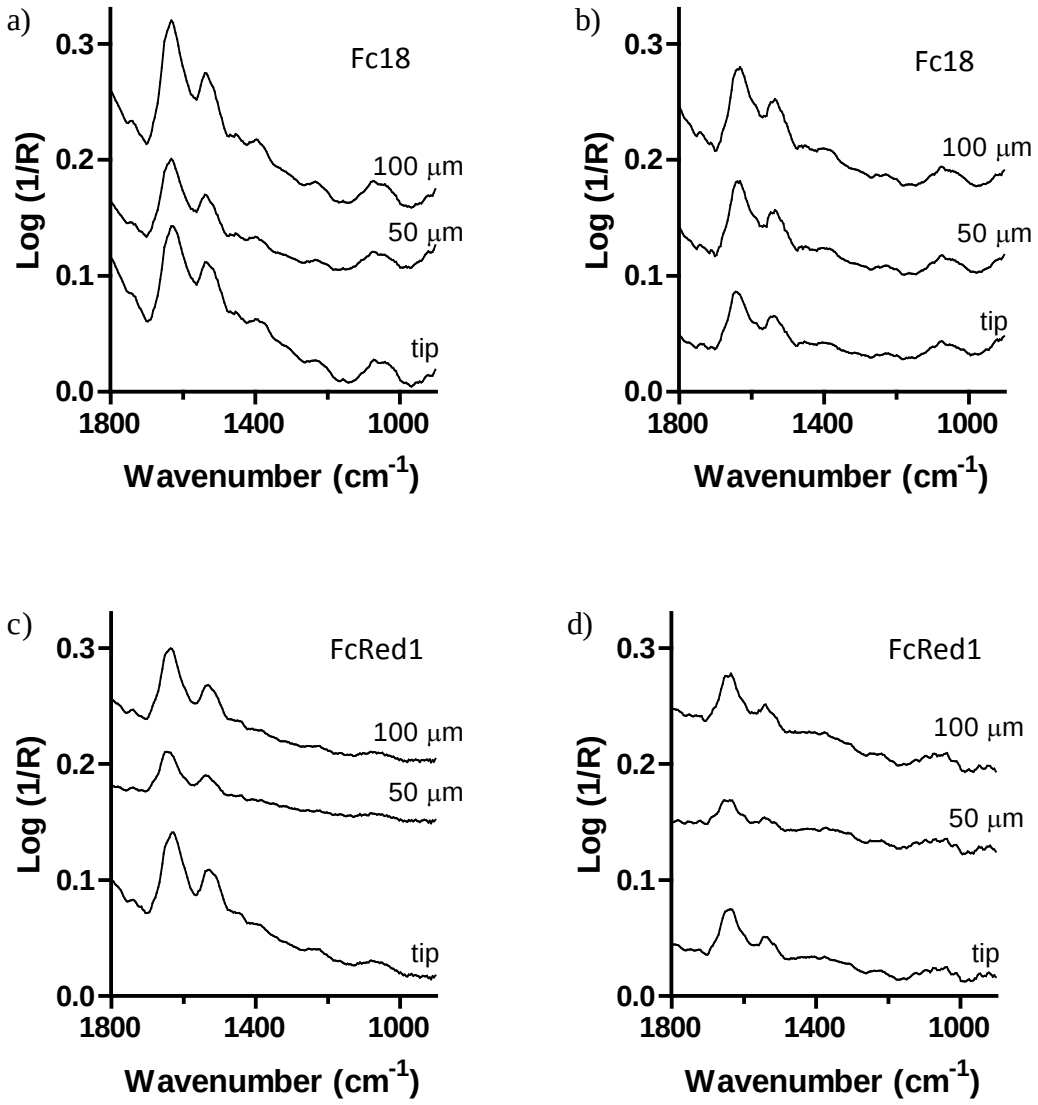

Figure 56. Hyphal spectra (CLS Nov. 2007) collected from a) Fc18 (100% PDA) b) Fc18 (10% PDA) c) FcRed1 (100% PDA) d) FcRed1 (10% PDA). Spectra were collected at positions as indicated.

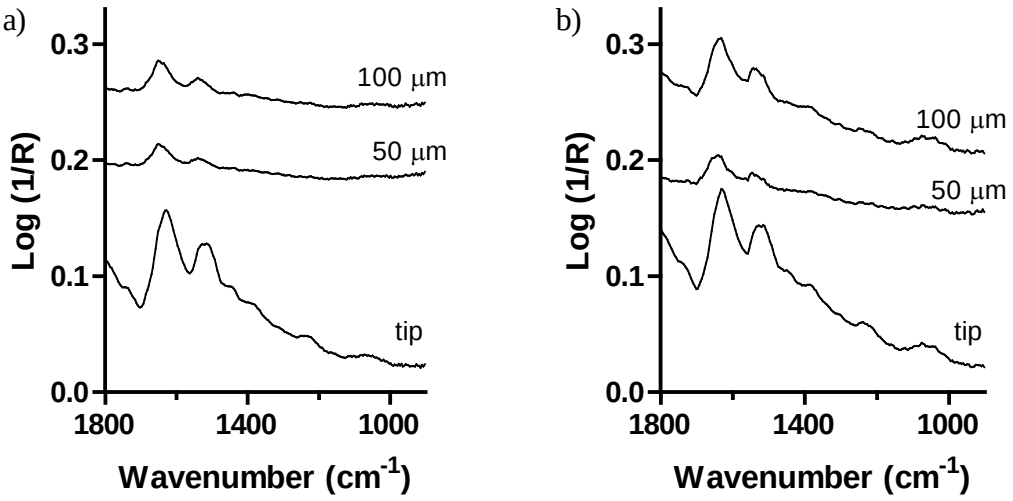

Figure 57. sFTIR spectra (CLS, Nov. 2007) collected along FcRed1 hyphae grown from a) 100% PDA FcRed1 b) 10% PDA FcRed1.

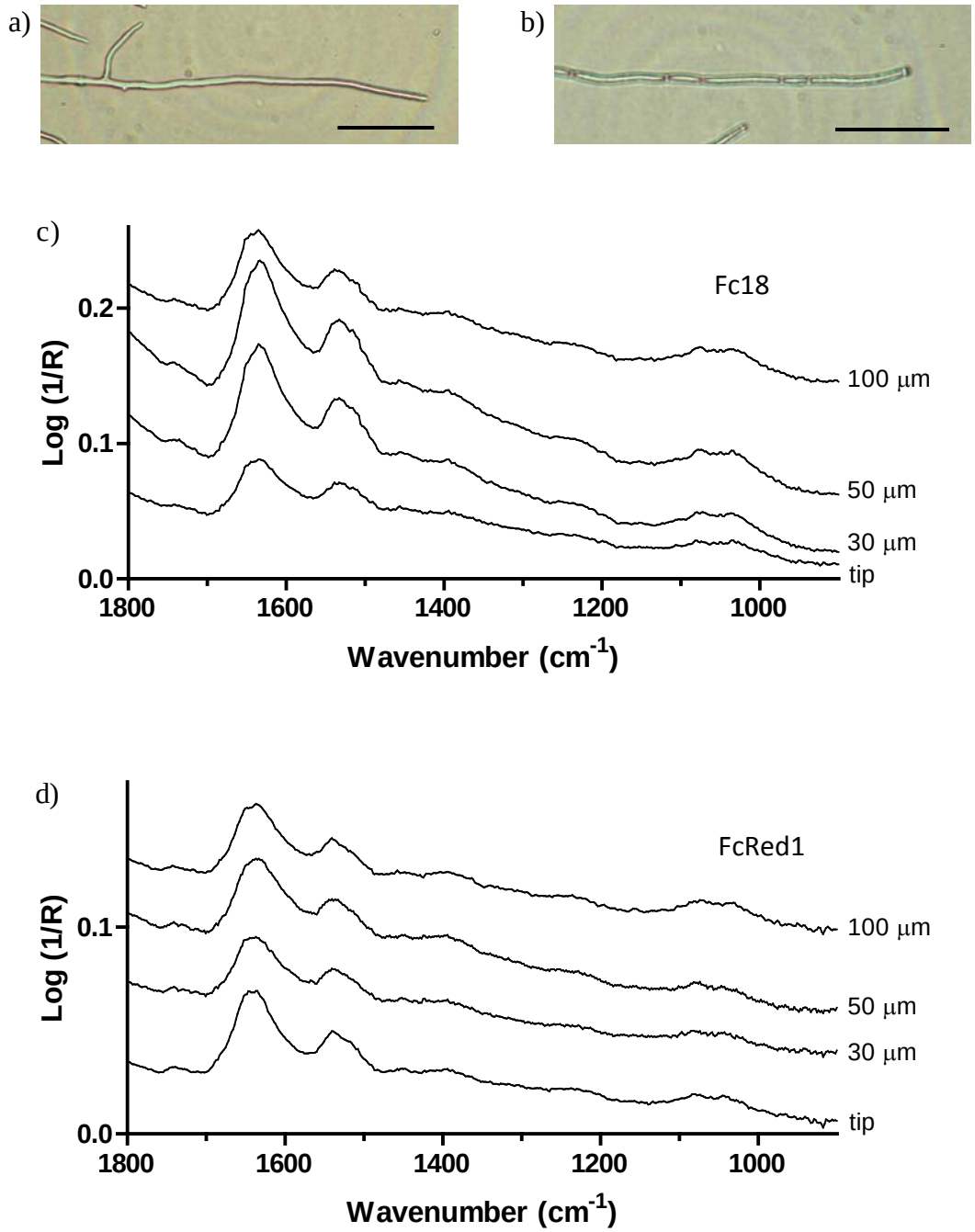

Figure 58. Photo of a) an Fc18 hypha and b) an FcRed1 hypha examined using sFTIR. Spectra (SRC, April 2008) of c) Fc18 and d) FcRed1 collected at positions as indicated. Both samples were grown from 100% PDA. Scale bars = 50 μm.

3.2.6 *Colletotrichum magna*

Pathogenic *C. magna* (L2.5) and a non-pathogenic mutant (CmPath) have been examined using sFTIR. Images of both samples are displayed in Figure 59. Figure 60 shows spectra recorded from each of the *C. magna* samples. *Colletotrichum magna* often proved to be a difficult species for the acquisition of good quality IR spectra despite the fact that the hyphae have similar diameters (usually 3-4 µm) to those of *C. protuberata* and *F. culmorum* hyphae. Many spectra had very low signal, especially in the carbohydrate region of spectra, and poor S/N. As a result, *C. magna* samples have been examined to only a limited extent. The number of *C. magna* hyphae analyzed is listed in Table 12 (L2.5) and Table 13 (CmPath). All *C. magna* spectra are displayed in Appendix I. Both the L2.5 and CmPath samples are discussed (to a limited degree) in the Discussion.

a) b)

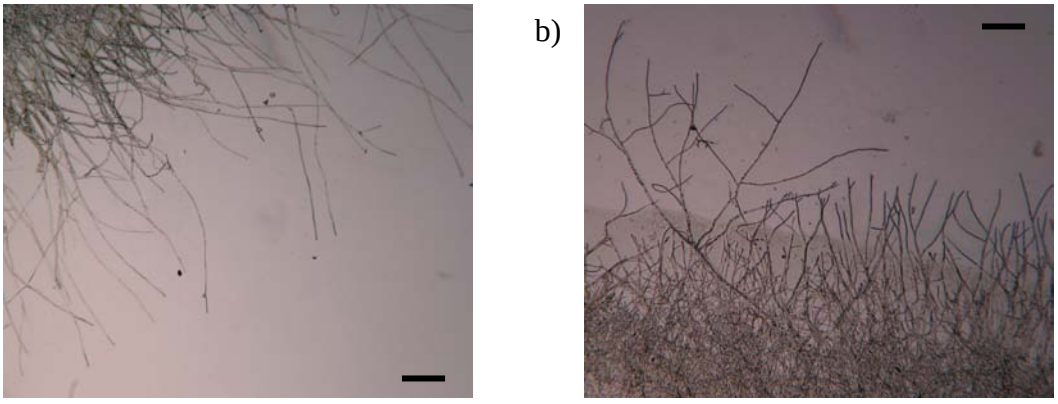

Figure 59. Photos of a) L2.5 and b) CmPath. Both samples were grown from 100% PDA and on MirrIR. Scale bars = 200 µm.

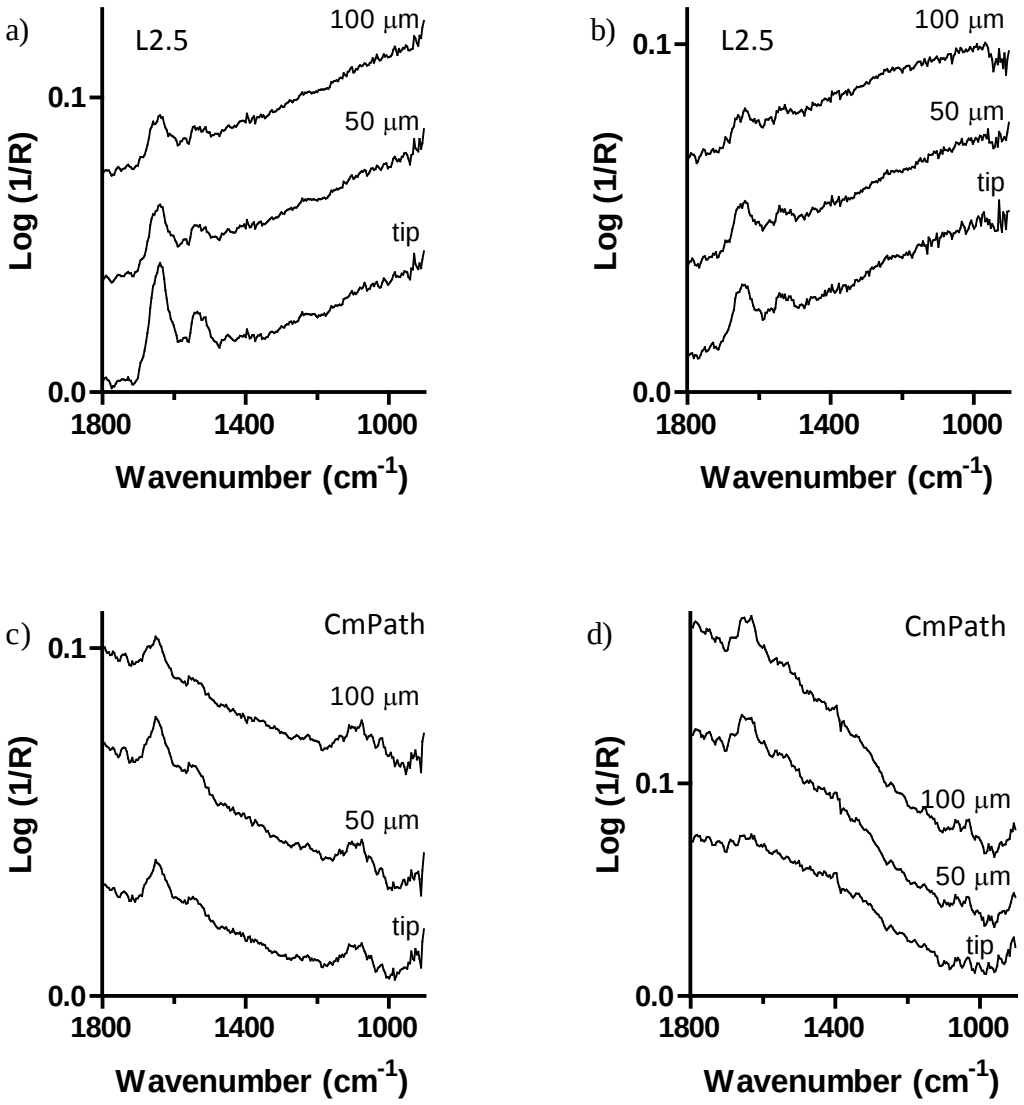

Figure 60. a) & b) sFTIR spectra acquired on two different L2.5 hyphae at positions as indicated. c) & d) Spectra acquired on two different CmPath hyphae at positions as indicated. Samples were each grown using 100% PDA (CLS, Nov. 2007). The displayed spectra are typical of each sample.

Table 12. Number of L2.5 hyphae examined.

Slide	Substrate	Medium	Location	Date	# of hyphae
37	MirrIR	100% PDA	CLS	Nov. 2007	7
			SRC	Apr. 2008	2
41	MirrIR	10% PDA	CLS	Jun. 2008	3
		1% PDA	CLS	Jun. 2008	1
50	MirrIR	100% PDA	CLS	Jun. 2008	3

Table 13. Number of CmPath hyphae examined.

Slide	Substrate	Medium	Location	Date	# of hyphae
34	MirrIR	100% PDA	CLS	Nov. 2007	6
			SRC	Apr. 2008	3
		10% PDA	SRC	Apr. 2008	4
49		100% PDA	CLS	Jun. 2008	4

3.2.7 Identification of Bands in *C. protuberata* IR Spectra

Fungi can produce long-chain polyphosphates (polyP) and phosphate is known to have an infrared absorption at 1080 cm^{-1}. Therefore, polyP was considered as candidate for the unusual sharp bands between 1100 and 1000 cm^{-1} in *C. protuberata* IR spectra. PolyP was isolated from Cp4666D and L2.5 by R. Rodriguez. Spectra from each polyP sample are displayed in Figure 61. Neither of the samples contained the two sharp peaks around 1078 and 1022 cm^{-1} in their spectra.

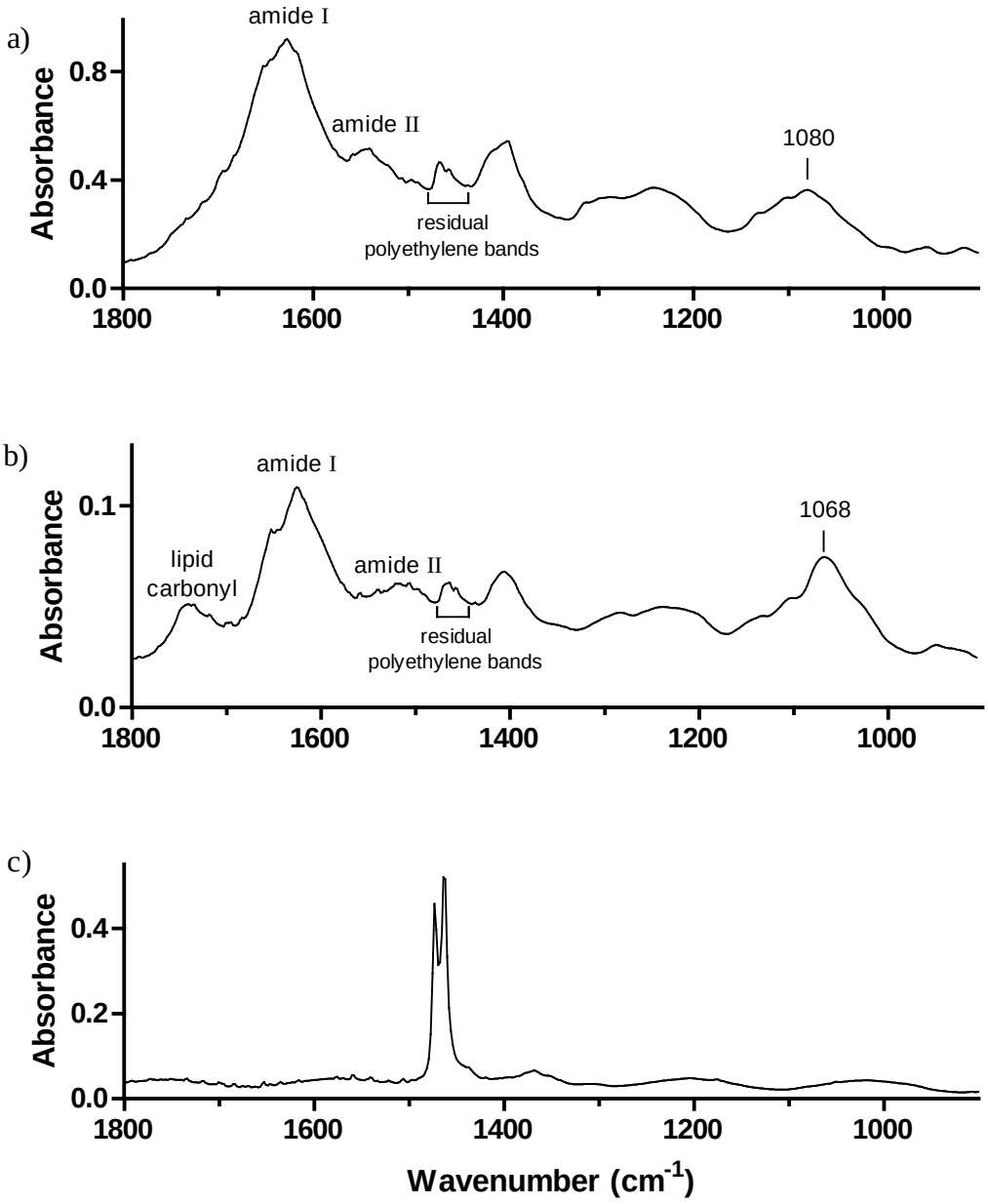

Figure 61. FTIR spectra of polyphosphate isolated from a) Cp4666D and b) L2.5. Both were recorded from a droplet dried onto polyethylene film; the background spectrum was recorded on polyethylene. c) FTIR spectrum of polyethylene. The film has few absorptions from 1800 to 900 cm^{-1}.

Many sugars were considered as a source of the bands at 1078 and 1022 cm^{-1} in spectra. Ultimately, mannitol was identified in hyphae. A spectrum of mannitol is displayed in Figure 62 along with a Cp4666D hyphal spectrum for comparison. The mannitol spectrum contains bands that would correspond to those seen at 1078, 1050, 1022, and 930 cm^{-1} in *C. protuberata* spectra.

Variations in the relative intensities of the bands at 1087, 1017 and 930 cm^{-1} in different mannitol spectra are shown in Figure 63. Variation between the relative intensities of the 1078 and 1022 cm^{-1} bands in hyphal spectra are observed as well upon rotation of the sample at a synchrotron.

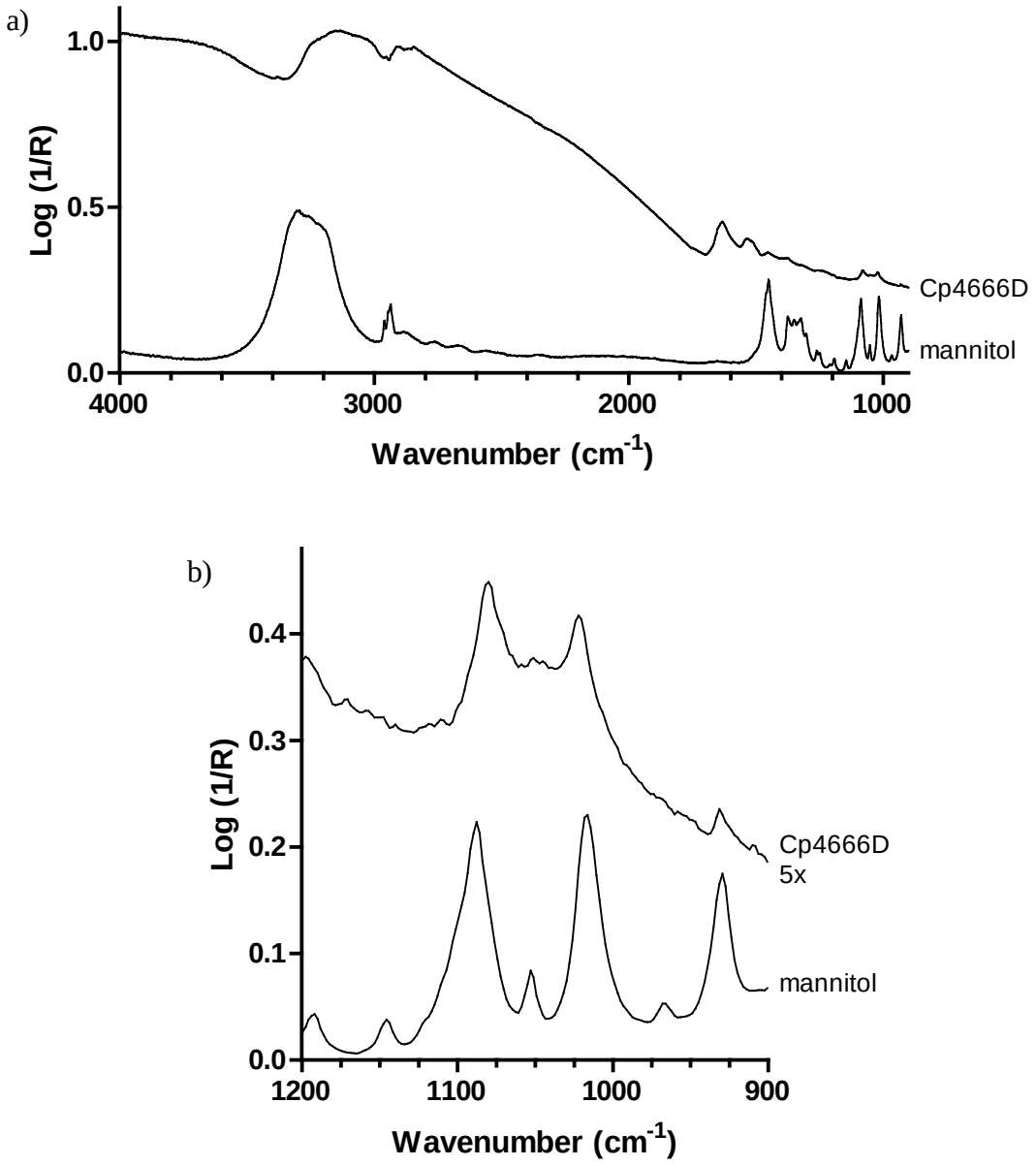

Figure 62. a) FTIR spectrum of mannitol and spectrum collected 100 μm from the tip of a Cp4666D hypha (grown from 100% PDA). b) Spectra from (a), displayed to highlight the region from 1200-900 cm^{-1}. The Cp4666D spectrum has been multiplied by a factor of 5.

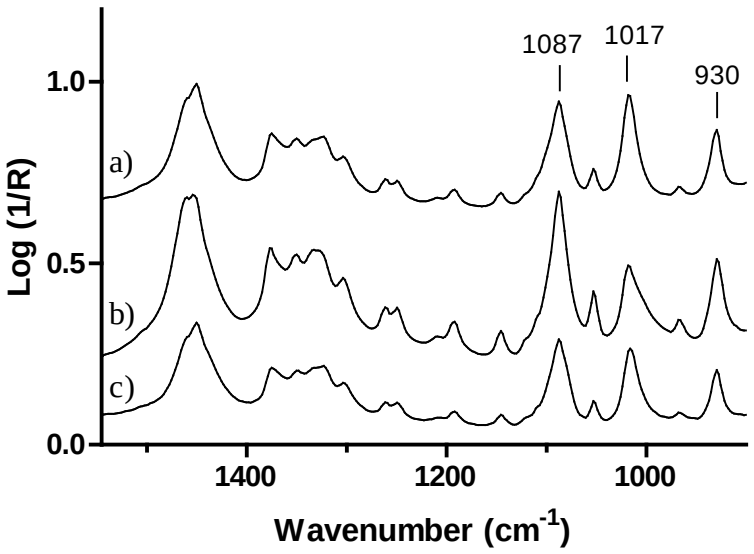

Figure 63. Spectra of mannitol showing the variation in relative intensities of the bands at 1087, 1017 and 930 cm^{-1} in spectra collected at different points in the film for the FPA image. a) Bands at 1087 and 1017 cm^{-1} have similar absorbance intensity, but the band at 1017 cm^{-1} is slightly more intense. b) The band at 1087 cm^{-1} has a higher absorbance intensity than the one at 1017 cm^{-1}. The band at 930 cm^{-1} is also more intense than the 1017 cm^{-1} band. c) The bands at 1087 and 1017 cm^{-1} have similar absorbance intensity, but the band at 1087 cm^{-1} is slightly more intense.

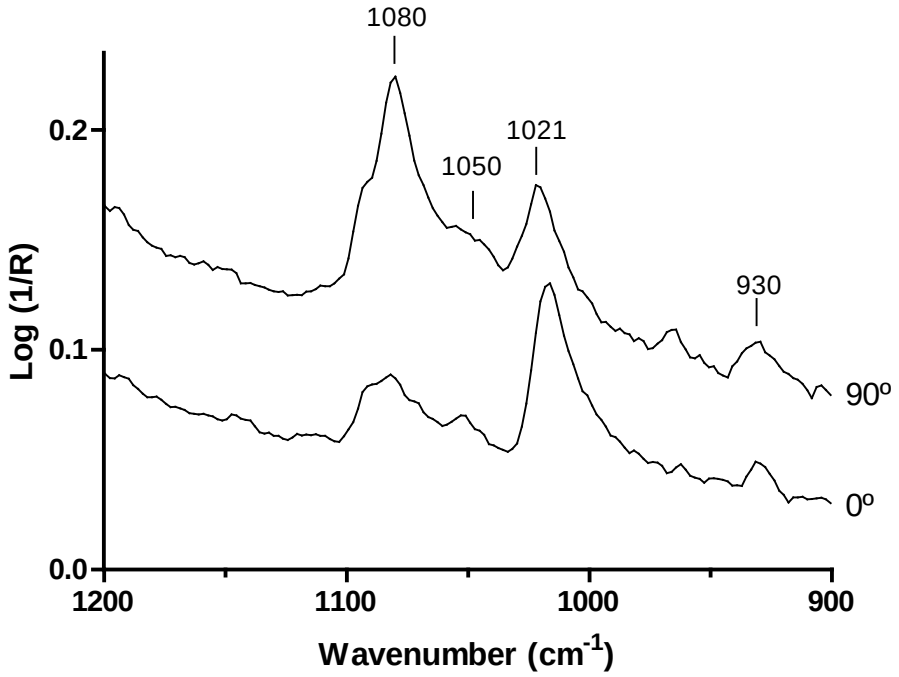

Figure 64. sFTIR spectra collected at the same position (approximately 70 µm from tip) on the Cp4666D hypha displayed in Figure 47. The hypha was rotated by 90º between acquisitions. Spectra were collected at SRC in April 2010. The aperture size was 18 x 14 µm.

3.3 Raman

Although the main focus of this project was the analysis of endophytes with FTIR spectromicroscopy, Raman has also been used to analyze a limited number of samples. Geothermal *C. protuberata* along with coastal and non-coastal *F. culmorum* samples have been examined with Raman microscopy. The typical data obtained from these samples are outlined here in the Results section and the complete collection of Raman data is included in Appendix III. Spectra are displayed on a common scale and offset for clarity. Raman spectra were possible only for hyphae grown across gold surfaces (see Methods chapter); this limited the number of samples available for analysis. The Raman results are compared with those from FTIR, when applicable, in the Discussion.

3.3.1 Anomalies

Cosmic Rays

Intense and narrow (typically no more than 3-4 cm^{-1} wide) bands can appear in spectra due to the sensitivity of CCD detectors to cosmic rays. If a cosmic ray line appears in a spectrum, it can be removed by using the "Zap" process in the WiRE software. This process zeroes the signal in a user-defined region. Figure 65 shows a Raman spectrum that contains three cosmic rays and the spectrum after their removal. Any cosmic rays present in spectra have been removed following this method, prior to further analysis.

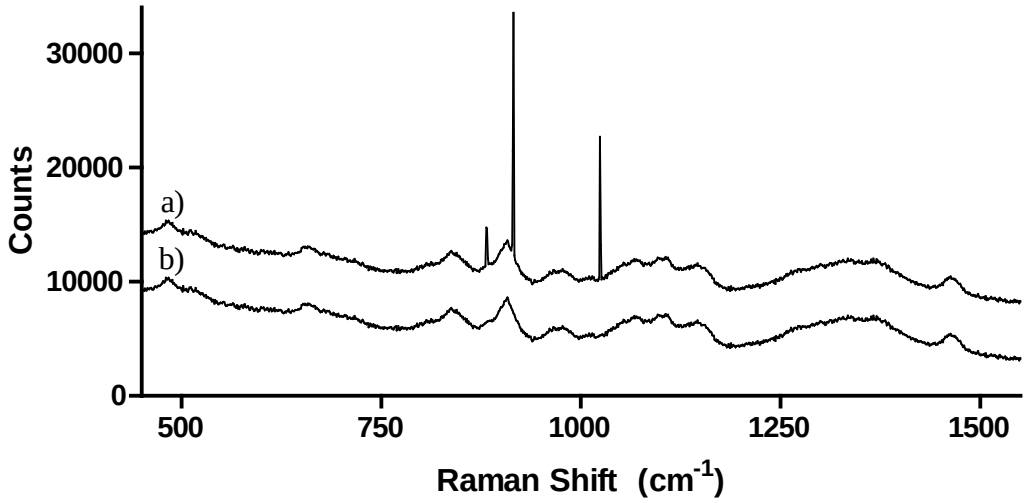

Figure 65. a) Raman spectrum of mannan. Three cosmic rays appeared in the spectrum. b) The mannan spectrum after cosmic ray removal.

Instability of the building housing the Raman microscope

The Raman microscope was located on the fifth floor of the Buller building at U of M when all spectra were acquired for this thesis. Often, samples could be seen to move around slightly while setting up spectra and on certain days, the floor could actually be felt shaking. It was not uncommon for samples to move 5 μm from their initial position during spectral acquisition. Since samples cannot be seen while collecting spectra (visible illumination is not on), it was only apparent that samples had moved after spectral acquisition. Spectra were re-collected whenever a sample moved out of the laser illumination during spectral acquisition.

3.3.2 *Curvularia protuberata*

The *C. protuberata* samples analyzed with Raman spectroscopy and the number of hyphae examined from each is outlined in Table 14. Slide 37, which is a MirrIR substrate, also holds samples of Cp4666D grown from both 100% and 10% PDA on gold-coated silicon wafers. However, the agar blocks were placed very close to each other, as shown in Figure 66, resulting in some overlap of hyphae. Spectra were recorded only on hyphae in non-overlapping regions (circled regions in Figure 66).

Table 14. Number of Cp4666D hyphae examined with Raman.

Slide	Substrate	Sample	Medium	# of Hyphae
37	Gold	Cp4666D	100% PDA	13
			10% PDA	9
133	Klarite	Cp4666D[†]	100% PDA	8
134	Klarite	Cp4666D	100% PDA	3

[†]no virus

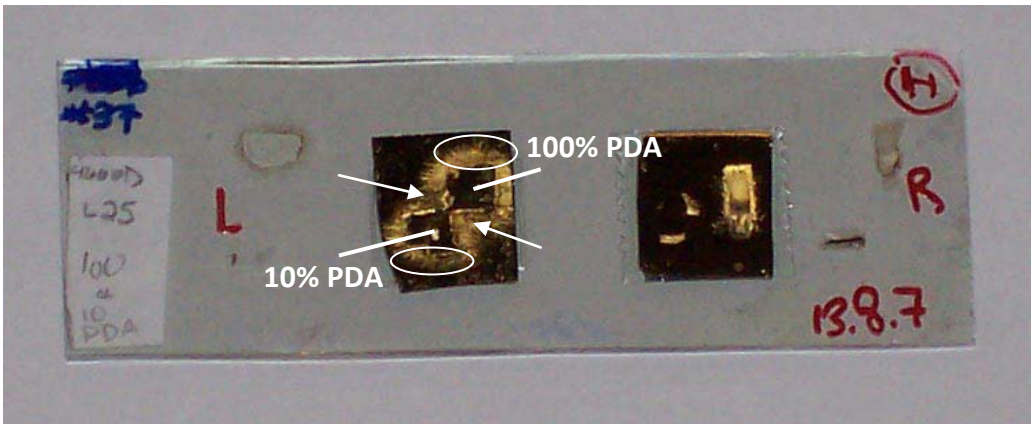

Figure 66. Photo of Slide 37 (MirrIR with two gold-coated silicon wafers). 100% and 10% PDA locations are indicated for the Cp4666D samples. Arrows point to the regions of overlapping hyphae from the two different PDA concentrations. Circled regions show the location of examined hyphae.

Raman spectra were collected at defined positions along hyphae. Spectra were collected at hyphal tips as well as 30 µm and 50 µm from tips. For several hyphae, spectra were also collected 100 µm from tips.

Static Raman scans offer the best spectral resolution but only give a limited range of the spectrum (about a 400 cm^{-1} range). To collect a "whole" spectrum, several acquisitions must be performed. For this thesis, spectra were collected centered at 700 cm^{-1} (with a range from approximately 500 to 900 cm^{-1}) and 1000 cm^{-1} (with a range from approximately 800 to 1200 cm^{-1}). Spectra were only acquired from these ranges due to the time to acquire each spectrum (about 18 minutes; summation of 256 scans and a 4 s exposure for each, necessary to obtain adequate S/N) and since these spectral regions were

found to contain the greatest number of bands. The time to acquire the data displayed in Figure 67 was approximately 2 hours.

Figure 67 displays typical Raman spectra collected from Cp4666D hyphae grown from 100% PDA. All spectra contain a strong band at 1003 cm^{-1} and a shoulder at 1010 cm^{-1}. The band at 1003 cm^{-1} is typically the most intense in spectra. The spectra in this figure are representative of spectra collected along many hyphae. Spectra resembling those in Figure 67 are hereafter referred to as Type 1. Figure 68 shows spectra acquired from another hypha (also grown from 100% PDA) that contains strong bands at 875 and 885 cm^{-1}. The spectra from a few hyphae resembled those in Figure 68. Spectra containing bands at 875 and 885 cm^{-1} are referred to as Type 2. The bands at 875 and 885 cm^{-1} always appear together in Type 2 spectra. The 885 cm^{-1} peak is generally more intense than the one at 875 cm^{-1}. When present, both peaks are more intense than the one at 1003 cm^{-1}.

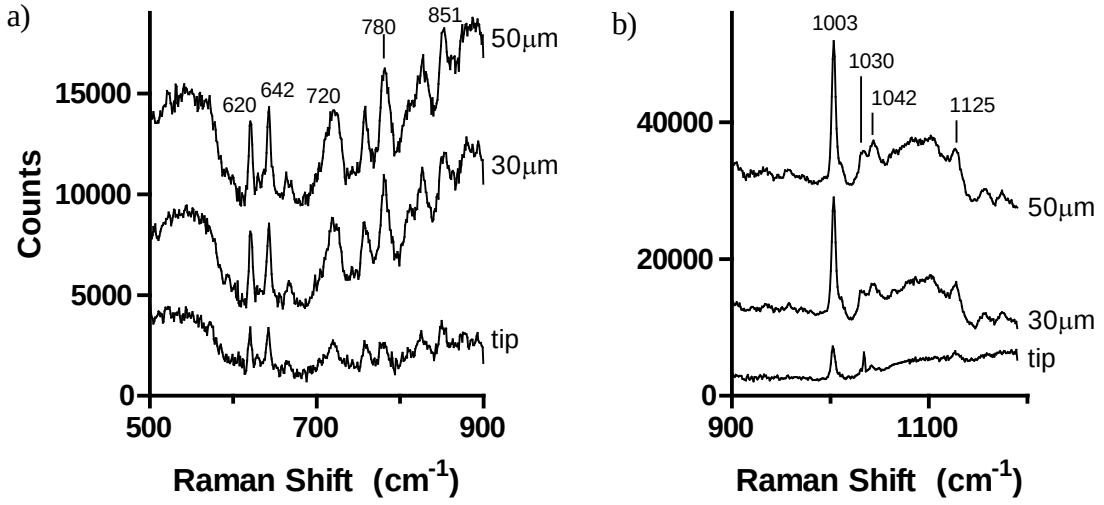

Figure 67. Raman spectra from a Cp4666D hypha (100% PDA). Data collection was centered at a) 700 cm^{-1} and b) 1000 cm^{-1}. Spectra collected at positions as indicated.

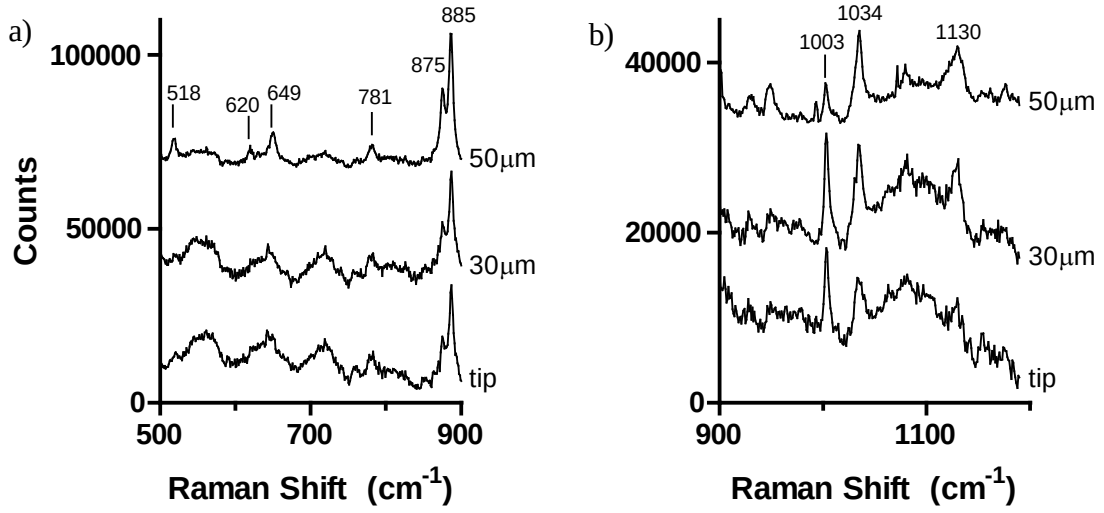

Figure 68. Raman spectra collected along a Cp4666D hypha (100% PDA). Data collection was centered at a) 700 cm^{-1} and b) 1000 cm^{-1}. Spectra were collected at positions as indicated. This hypha was also examined with FTIR, shown in Figure 48 (solid-line arrow).

It was found that for a given hypha, spectral profiles from all positions were either that of Type 1 or Type 2. This indicates that the composition along hyphae is consistent. Table 15 outlines the number of hyphae found to contain bands at 875 and 885 cm^{-1} in their spectra.

Table 15. Cp4666D hyphae containing bands at 875 and 885 cm^{-1} in Raman spectra.

Slide	Sample	Medium	Total Hyphae	With Peaks
37	Cp4666D	100% PDA	13	2
		10% PDA	9	4
133	Cp4666D†	100% PDA	8	0
134	Cp4666D	100% PDA	3	0

†no virus

Spectra collected from Cp4666D hyphae grown from 10% PDA generally produced similar spectra to those grown from 100% PDA. Both Type 1 and Type 2 spectra were collected from hyphae grown from 10% PDA. Again, each hypha contained either only Type 1 spectra or Type 2 spectra. Figure 69 displays spectra that do not contain any bands at 875 and 885 cm^{-1} while Figure 70 displays spectra containing these bands. Spectra displayed in Figure 69 and Figure 70 (10% PDA) are very similar to those displayed in Figure 67 and Figure 68 (100% PDA), respectively.

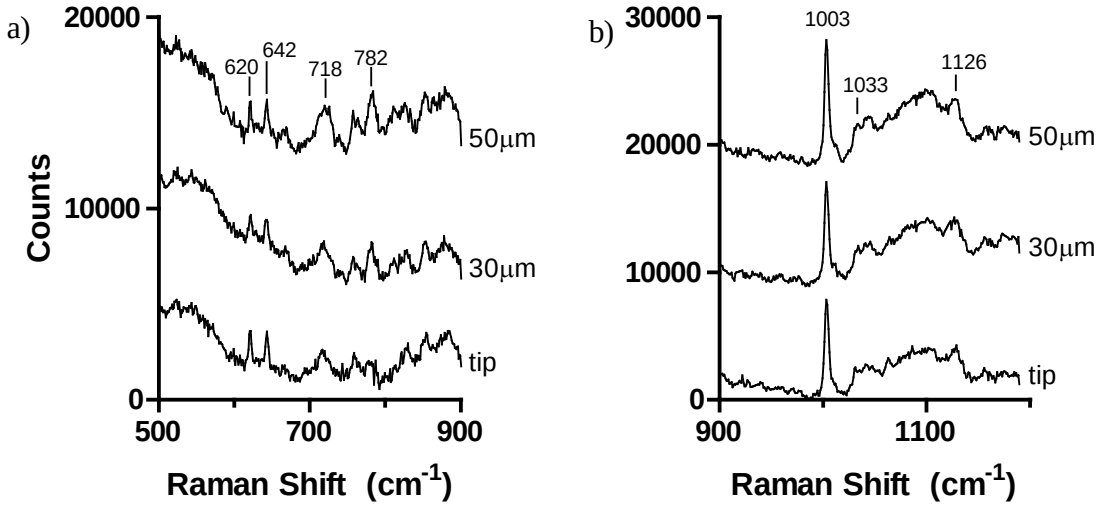

Figure 69. Raman spectra collected along a Cp4666D hypha grown from 10% PDA. Data collection was centered at a) 700 cm^{-1} and b) 1000 cm^{-1}. Spectra were collected at positions as indicated.

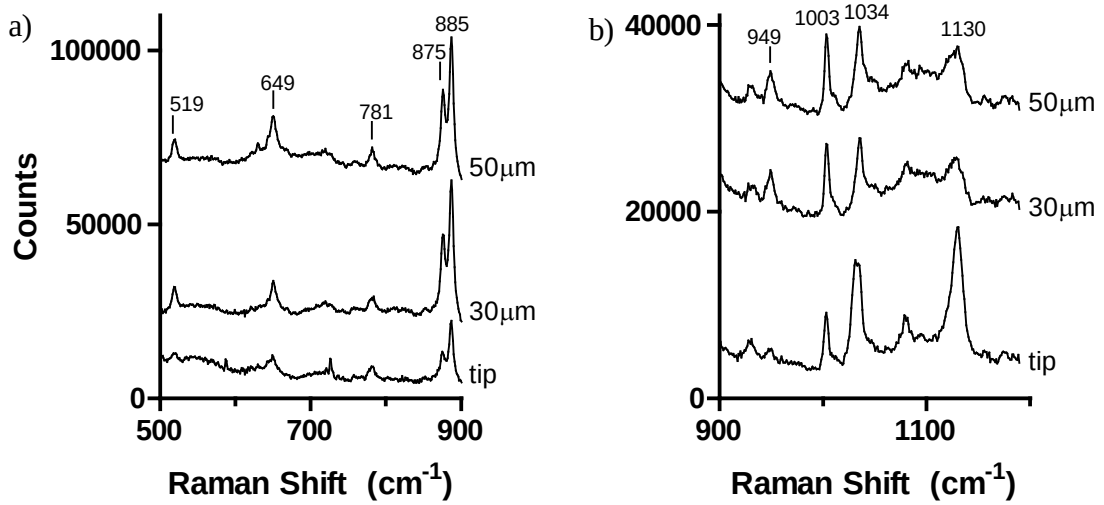

Figure 70. Raman spectra collected along a Cp4666D hypha grown from 10% PDA. Data collection was centered at a) 700 cm^{-1} and b) 1000 cm^{-1}. Spectra were collected at positions as indicated.

As noted earlier, the hypha examined in Figure 68 was also examined with FTIR. Figure 71 displays Raman spectra from another hypha shown in the FPA map in Figure 48 (marked with the dotted-line arrow). Figure 72 displays Raman spectra from a hypha that was examined with FTIR (FPA map is displayed in Figure 49).

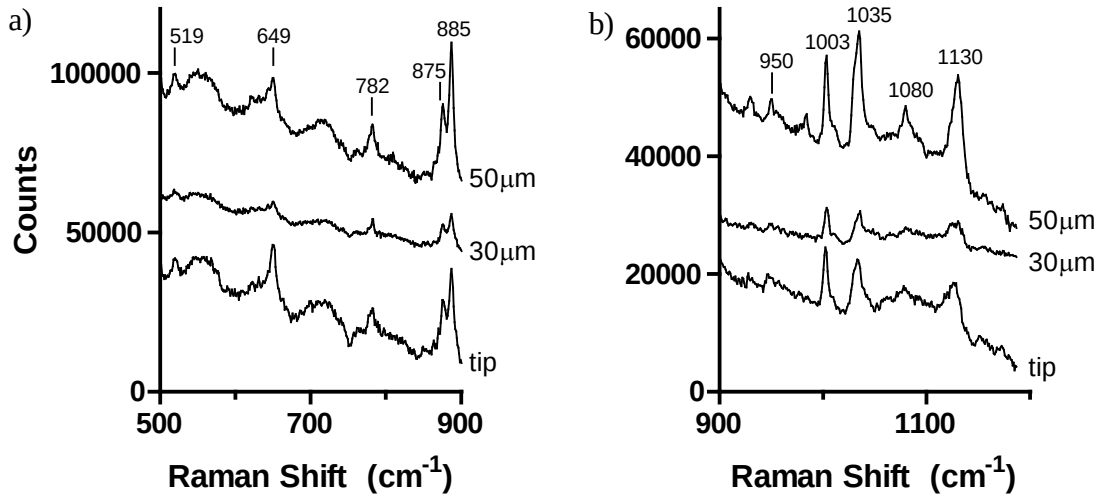

Figure 71. Raman spectra collected along a Cp4666D hypha grown from 100% PDA. Data collection was centered at a) 700 cm^{-1} and b) 1000 cm^{-1}. Spectra were collected at positions as indicated. This hypha was also examined with FTIR, shown in Figure 48 (dotted-line arrow).

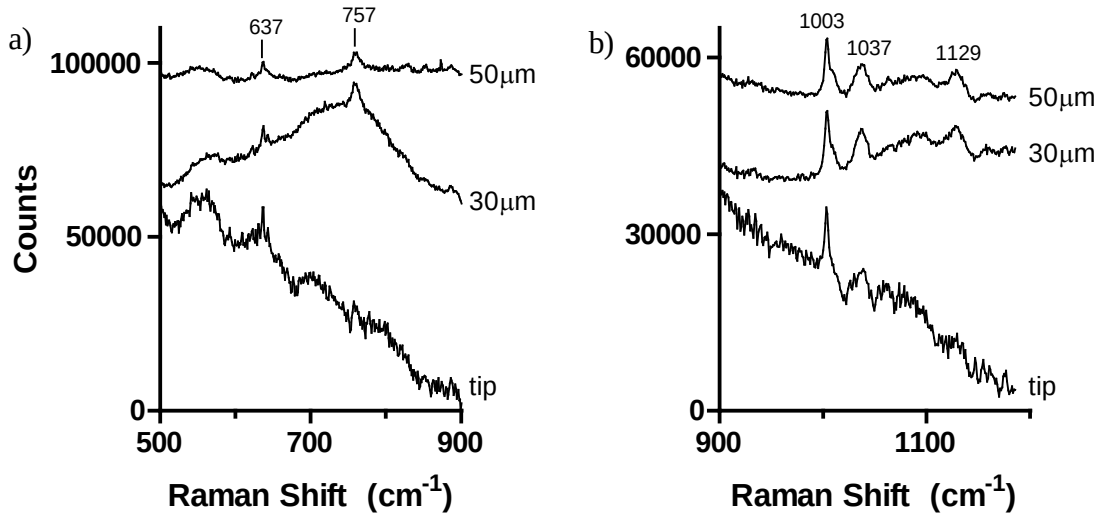

Figure 72. Raman spectra collected along a Cp4666D hypha grown from 100% PDA. Data collection was centered at a) 700 cm^{-1} and b) 1000 cm^{-1}. Spectra were collected at positions as indicated. This hypha was also examined with FTIR, shown in Figure 49 and indicated by the arrow.

Raman spectra of control Cp4666D (contains the virus) and Cp4666D no virus, both grown at the same time and under the same conditions, were also collected. Spectra for each are displayed in Figure 73 and Figure 74, respectively. Although these samples were grown on Klarite substrates, spectra were only collected from the smooth gold surface, which permits only normal Raman scattering. The profiles of these spectra are very similar to other Cp4666D Raman spectra and to each other. Neither of these samples was found to contain peaks at 885 and 875 cm^{-1} in spectra, as noted in Table 15.

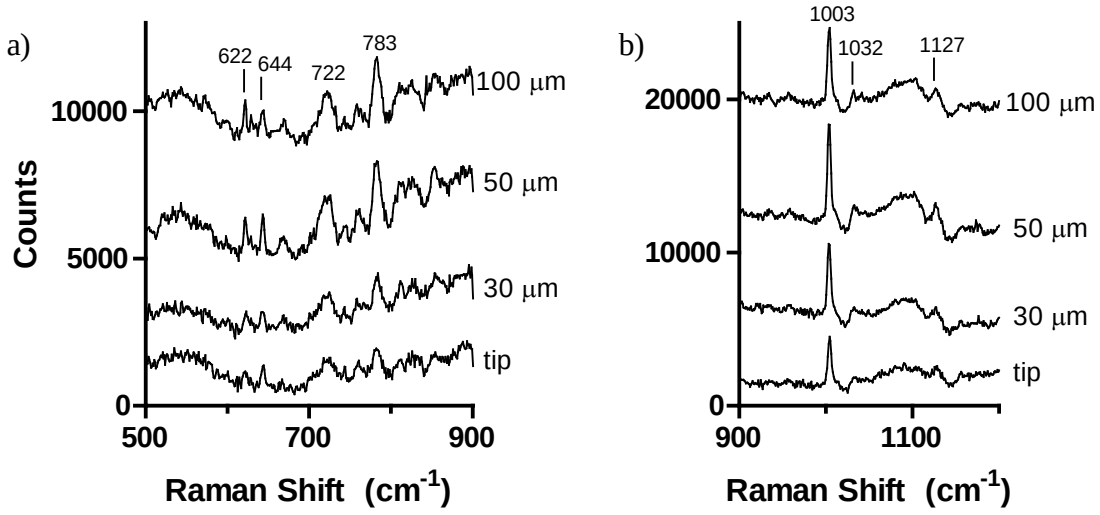

Figure 73. Raman spectra collected along a control Cp4666D hypha (grown from 100% PDA). Data collection was centered at a) 700 cm^{-1} and b) 1000 cm^{-1}. Spectra were collected at positions as indicated.

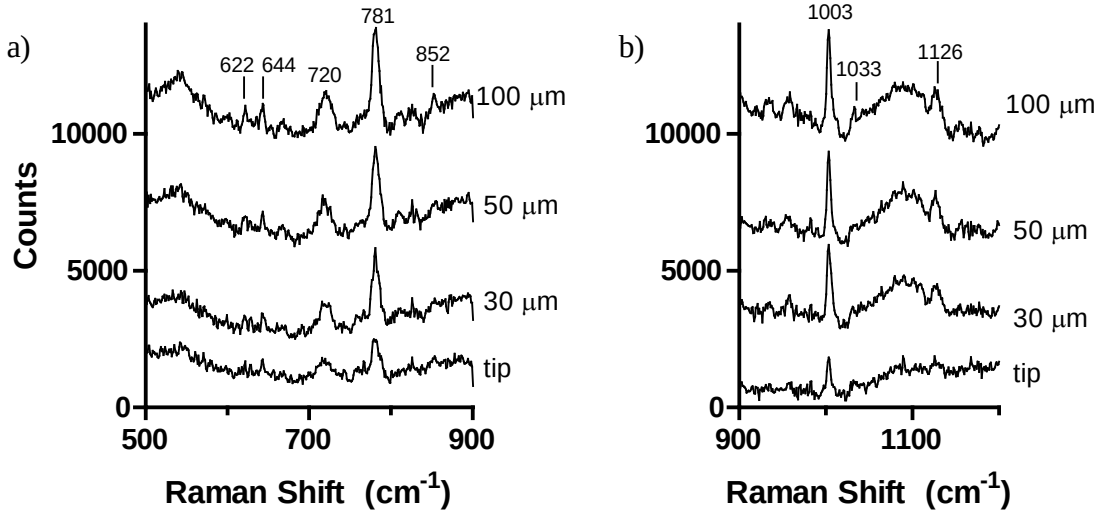

Figure 74. Raman spectra collected along a Cp4666D no virus hypha (grown from 100% PDA). Data collection was centered at a) 700 cm^{-1} and b) 1000 cm^{-1}. Spectra were collected at positions as indicated.

3.3.3 *Fusarium culmorum*

Raman spectra were collected for both the coastal and non-coastal *F. culmorum* isolates. Spectra were collected along *F. culmorum* hyphae as outlined for *C. protuberata* hyphae (refer to section 3.3.2). The number of Fc18 and FcRed1 hyphae analyzed with Raman microscopy is listed in Table 16.

Table 16. Number of Fc18 and FcRed1 hyphae examined with Raman.

Slide	Substrate	Sample	Medium	# of Hyphae
38	Gold	Fc18	100% PDA	7
			10% PDA	0
		FcRed1	100% PDA	10
			10% PDA	7

The typical Raman spectra from FcRed1 hyphae are displayed in Figure 75 and Figure 76 for hyphae grown from 100% PDA and 10% PDA, respectively. The spectra are very similar for hyphae grown from both concentrations of PDA. Spectra contain a strong band at 1003 cm^{-1} with a shoulder at 1010 cm^{-1}. The band at 1003 cm^{-1} is usually the most intense in spectra. Spectra from one FcRed1 hypha contain strong bands at 875 and 885 cm^{-1} (Figure 77). Spectra from all positions along a given hypha had similar profiles.

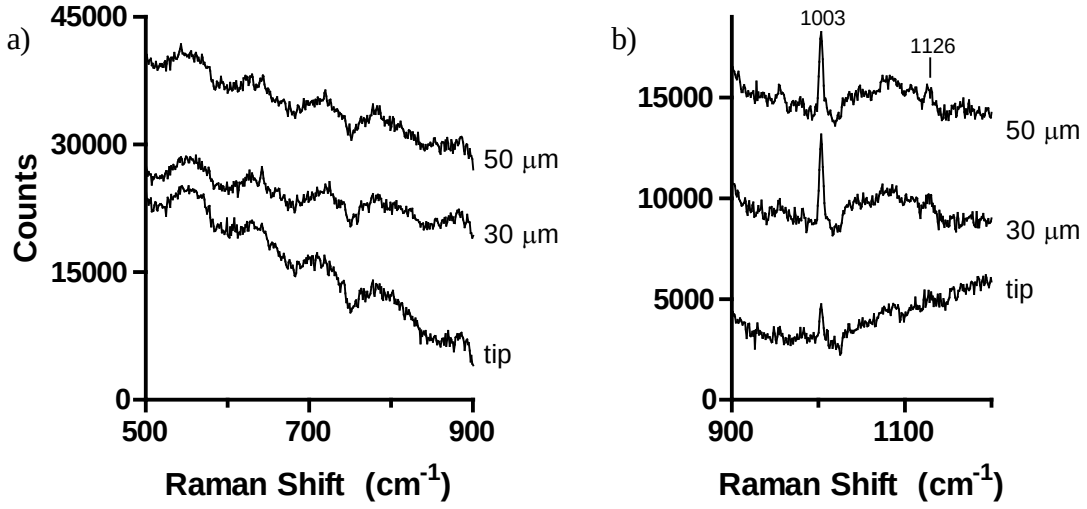

Figure 75. Raman spectra collected along an FcRed1 hypha grown from 100% PDA. Data collection was centered at a) 700 cm^{-1} and b) 1000 cm^{-1}. Spectra were collected at positions as indicated.

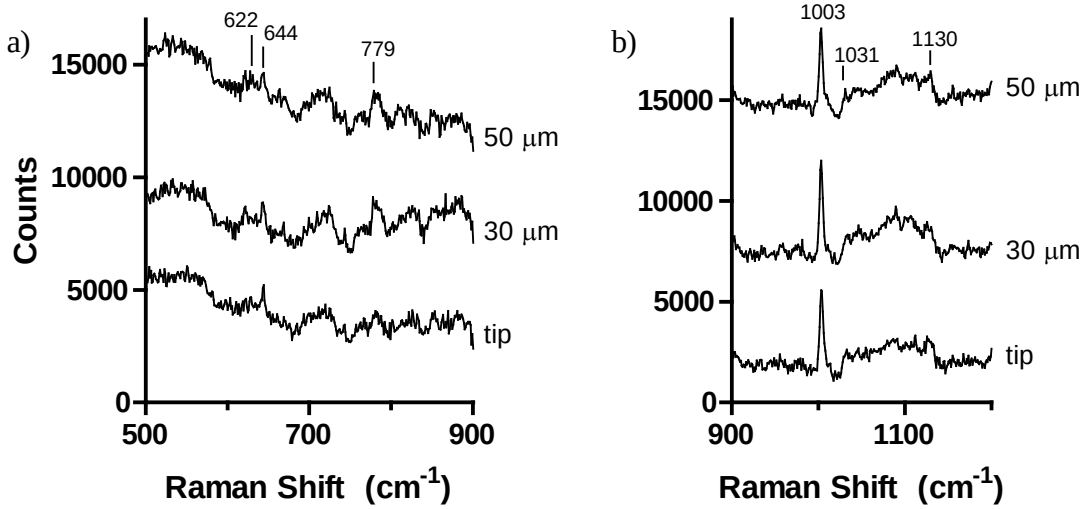

Figure 76. Raman spectra collected along an FcRed1 hypha grown from 10% PDA. Data collection was centered at a) 700 cm^{-1} and b) 1000 cm^{-1}. Spectra were collected at positions as indicated.

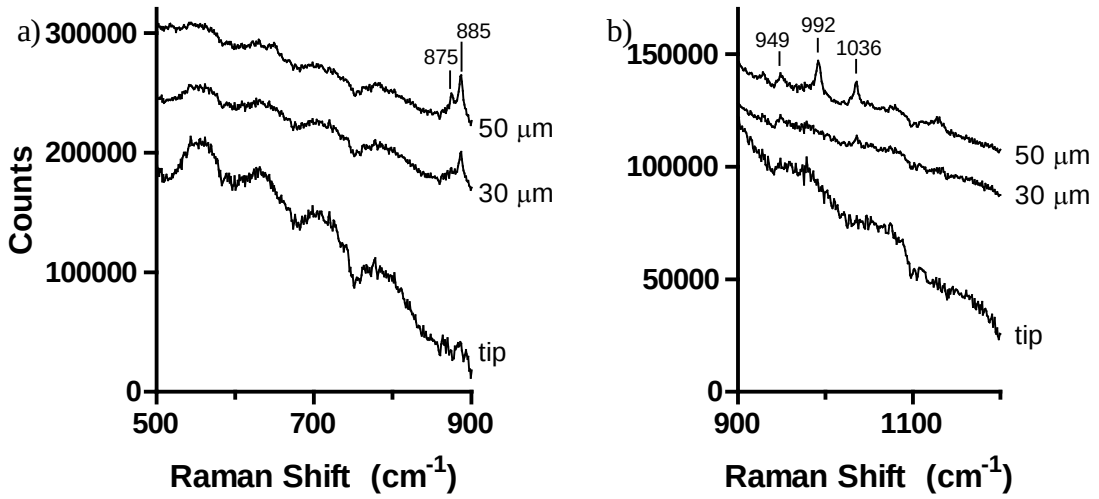

Figure 77. Raman spectra collected along an FcRed1 hypha grown from 100% PDA. Data collection was centered at a) 700 cm^{-1} and b) 1000 cm^{-1}. Spectra were collected at positions as indicated.

For Fc18, only hyphae grown from 100% PDA were analyzed with Raman microscopy. Raman analysis of Cp4666D and FcRed1 found that spectra from hyphae grown from 100% PDA and 10% PDA were very similar. Additionally, FTIR and sFTIR showed that PDA concentration did not appear to affect the composition of endophyte hyphae.

Spectra from an Fc18 hypha are displayed in Figure 78. The profiles of spectra are similar to those of FcRed1 hyphal spectra. The most intense band in spectra is located at 1003 cm^{-1}. Spectra from all positions along Fc18 hyphae are very similar to each other.

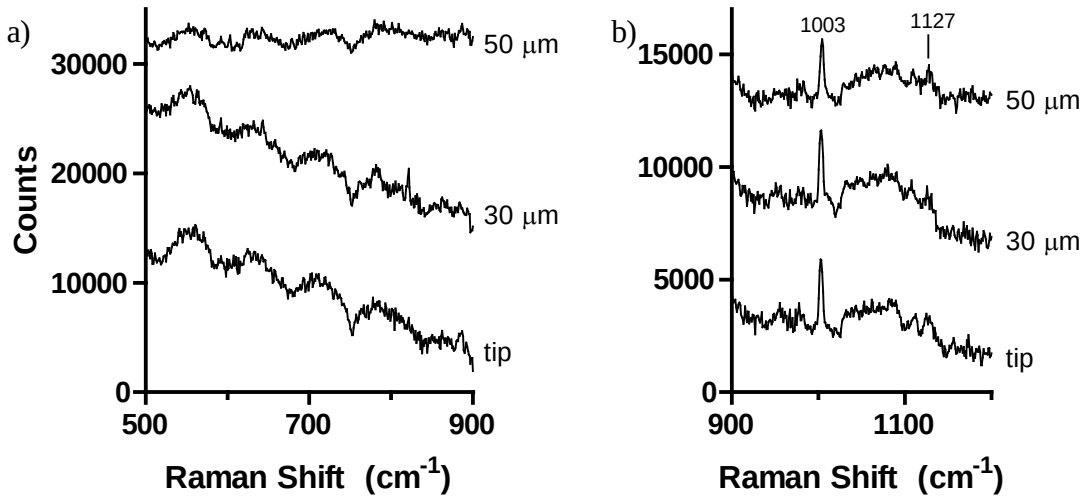

Figure 78. Raman spectra collected along an Fc18 hypha grown from 100% PDA. Data collection was centered at a) 700 cm^{-1} and b) 1000 cm^{-1}. Spectra were collected at positions as indicated.

3.3.4 Identification of Bands in Raman Spectra of Endophytes

Since polyP was considered for the 1078 and 1022 cm^{-1} bands in IR spectra, its Raman spectrum was also collected for comparison to the Raman spectra from *C. protuberata* and *F. culmorum* hyphae. PolyP isolated from both Cp4666D and L2.5 (by R. Rodriguez) was analyzed and spectra are displayed in Figure 79. There were no bands in these spectra that appeared to match bands in Raman spectra of the endophytes.

Raman spectra show that these samples are not pure polyP due to the band at 1003/1004 cm^{-1} in spectra. This band indicates the presence of phenylalanine and is a marker for proteins. IR spectra also indicated protein was present in samples due to the presence of amide I and amide II bands.

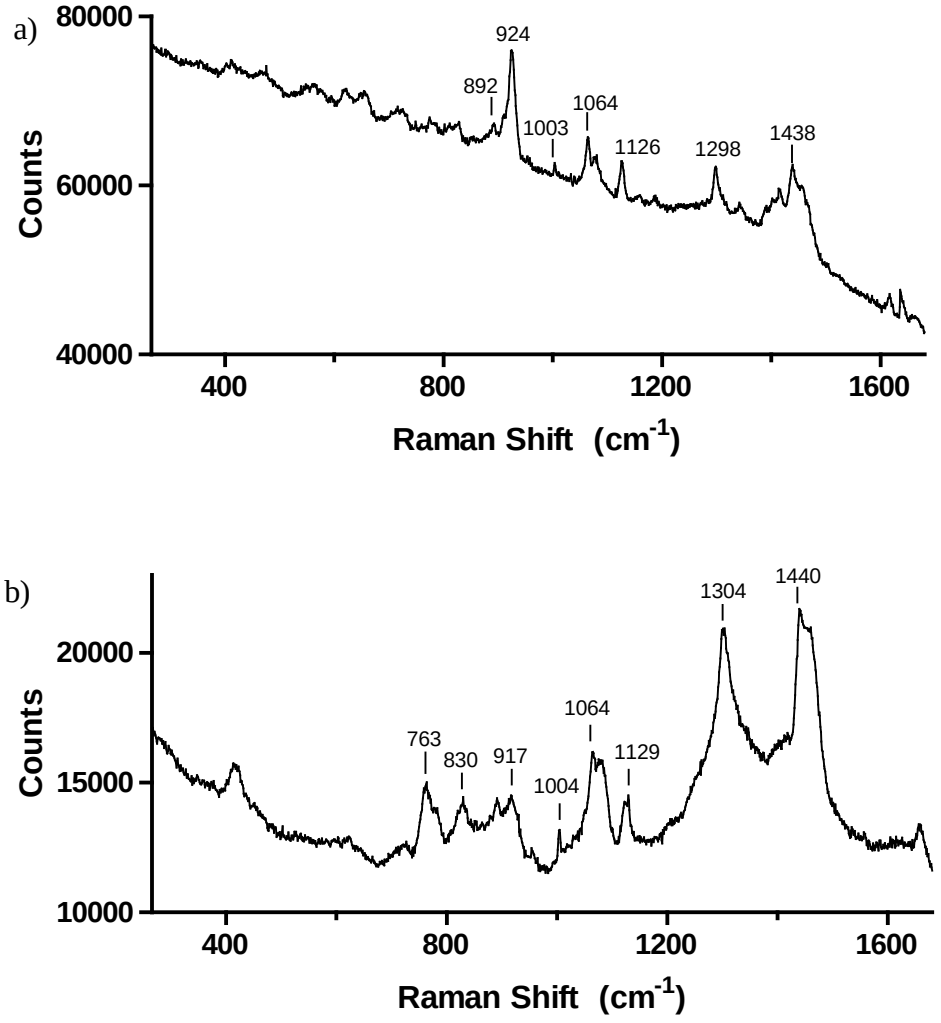

Figure 79. Raman spectra of polyphosphate isolated from a) Cp4666D and b) L2.5.

Mannitol was identified in *C. protuberata* hyphae from IR spectra (refer to section 3.2.7). Therefore, a Raman spectrum of mannitol was also collected for comparison to Raman spectra from the endophytes. Figure 80 displays a Raman spectrum of mannitol. The bands at 518, 649, 788, 876, 1038, and 1135 cm^{-1} are similar to bands present in the Type 2 Cp4666D spectra.

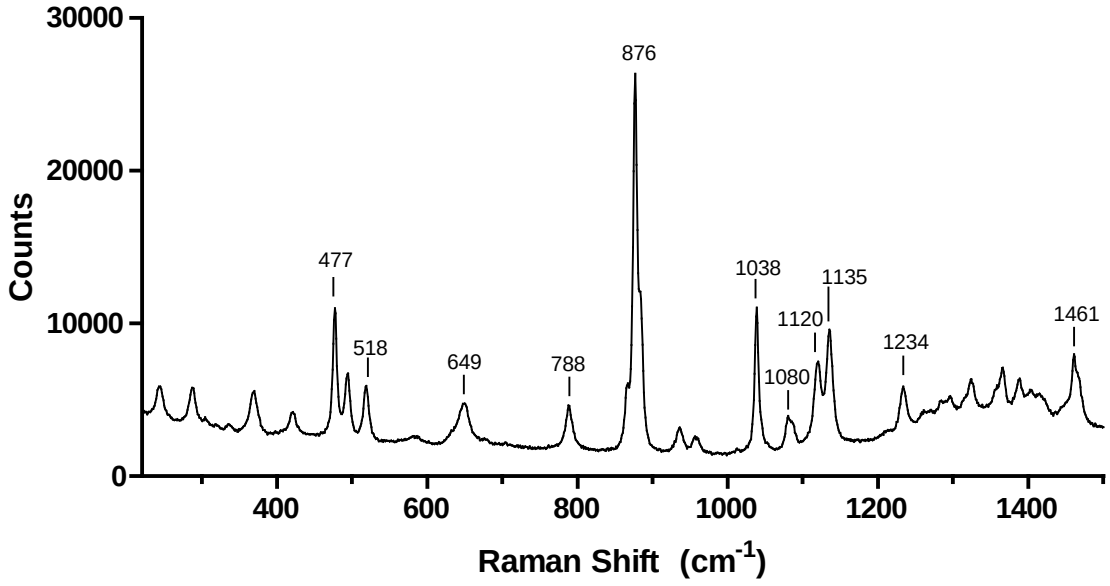

Figure 80. Raman spectrum of mannitol. Some of the most prominent band positions are marked.

Chapter 4

Discussion

4.1 Fungal Growth

4.1.1 Substrates

All endophyte species were grown on MirrIR slides. Cp4666D, Fc18 and FcRed1 samples were also prepared on gold-coated silicon wafers. L2.5 was also grown on gold; however, this sample was not analyzed. There did not appear to be any differences in growth of the endophytes on gold versus MirrIR (see the example of Cp4666D in Figure 21). Additionally, IR spectra from Cp4666D hyphae on each surface were comparable. It is possible that certain endophytes grow better on certain substrates; however, this has not been investigated. The MirrIR surface may not be optimal for growth of *C. magna* samples and could have resulted in low cell content and, therefore, low absorbance intensities in spectra. Use of a different substrate could lead to better growth and better quality spectra and is something to be examined in the future.

4.1.2 PDA Concentration

The concentration of PDA refers to the amount of nutrients available for growth. It is therefore not surprising that fewer spores germinate from 3% and 1% PDA, where fewer nutrients are available, compared to 100% and 10% PDA (see Figure 22). This trend applied to *C. protuberata*, *F. culmorum*, and *C. magna* species. However, sFTIR and FTIR spectra show that cell composition is typically comparable for hyphae grown from all PDA concentrations (*e.g.* Figure 42).

It is therefore concluded that PDA concentration affects the amount of fungal growth but not the composition of cells. Hyphae that grew from the 3% and 1% PDA appear to have acquired sufficient nutrients from the medium to allow for a similar composition to those hyphae grown from 100% and 10% PDA. Since 100% PDA allowed for development of the greatest number of hyphae, this concentration was typically chosen for growth of endophytes.

4.1.3 Hyphal Shadows on Slides

Less than adequate hyphal growth has been observed for some samples (shown in Figure 24, Figure 25, & Figure 26). A similar occurrence has been previously observed (Szeghalmi *et al.*, 2007a). *Rhizopus* hyphae grown at elevated pH appeared to have collapsed, leaving behind a "shadow" of cell contents.

There are several plausible explanations for this phenomenon. In the case of the *Rhizopus* hyphae (Szeghalmi *et al.*, 2007a), the stressed growth environment could have affected hyphal growth. For the endophytes as well as the *Rhizopus* sample, it is possible

that the freeze-dry process was too harsh, causing sections of hyphae to dry off the slide, leaving behind only remnants of hyphal material. Additionally, damage to samples during transport could cause segments of hyphae to become detached from slides. In either case, it is possible that hyphae did not adhere well to the substrate. This could have been in part a result of growth of endophytes at different times and by different people.

The slides that were mostly affected by this issue were Slides #39 to #44 (CpATCC, Cp4666D, Fc18, FcRed1, L2.5, CmPath; each of the samples were grown from 100%, 10%, 3%, and 1% PDA in June 2008). For the majority of samples, hyphae having this type of appearance were few and could be avoided.

4.2 FTIR

4.2.1 CLS versus SRC

With the exception of data collected in November 2007, spectra recorded at the CLS were relatively poor in comparison to SRC data. The quality of SRC data was much more consistent from one date to another (see Figure 28 & Figure 29). The spectra displayed in these figures are not from the same hypha (the same hyphae were not examined on all occasions) and are solely used as examples of typical data quality.

Spectra collected on a hypha at both SRC and CLS (the same positions were examined at each location) are displayed in Figure 30 in order to illustrate that the poorer data quality at CLS is not a result of samples. The SRC spectra were collected in April 2008 and CLS spectra were collected in June 2008. Spectra collected at SRC have better S/N despite summing fewer scans (512 at SRC vs. 1024 at CLS) and more well defined CH stretch regions. The spectra collected at CLS start to cut off within the sugar region and are especially noisy in this region while SRC spectra are generally better to lower wavenumbers. In addition, water bands were more common in spectra collected at CLS, leading to the need to frequently collect new backgrounds and many water blank spectra for correction by subtraction.

The poorer data quality at CLS versus SRC was not isolated to only one occasion. Figure 31 displays spectra collected on another hypha at both SRC (November 2008) and CLS (December 2008). While these spectra were not collected at all the same positions, it is still clear that CLS spectra were again noisier than SRC data, despite summing the

same number of scans (1024) for all spectra. Additionally, spectra collected at CLS have reduced overall absorbance intensities compared to SRC spectra at all positions. This results from more optics and a longer beam path at CLS, which leads to a loss of light.

Spectra in Figure 28b and Figure 30b contain absorptions due to the diamond window (separation between the storage ring and optical components), surrounded by dotted lines on spectra. Beam instability is the cause for these bands in spectra: a shift of the beam could cause the background to be invalid (a typical background recorded at a synchrotron can be viewed in Figure 10).

The weaker beam at CLS and its accompanying instability have resulted in poorer spectra from this synchrotron. Therefore, a preference for SRC data is evident in this work.

4.2.2 Synchrotron versus FPA Spectra

The bright synchrotron source offers greater S/N in spectra compared to thermal sources, which in turn allows for the summation of fewer scans. The use of the FPA detector at the U of M coupled to a globar source requires summation of a greater number of scans in order to achieve the same S/N as with a synchrotron source; however, data collection is greatly accelerated due to the large number of spectra collected simultaneously. For example, collecting a background, four spectra (tip, 30 µm, 50µm, and 100 µm), and a blank spectrum (if needed) at SRC typically took 90 minutes (summing 512 scans per spectrum). Part of this time is occupied by manually moving to the next position on samples. With the FPA detector, 4096 spectra are collected simultaneously, covering a 350 x 350 µm area of the sample. Collection of one map (summing 1024 scans per pixel)

takes 52 minutes; the collection of both a background and sample map can be done in less than 2 hours. Many blank spectra are included in the map since hyphae take up a relatively small amount of the FPA map area. Individual spectra can be extracted from the map for closer analysis or the entire block of data may be processed in a single step.

Figure 44 (CpATCC) and Figure 45 (Cp4666D) each display sFTIR spectra collected at SRC and the same hypha examined using the bench source and FPA detector at U of M. The signal is more intense in SRC spectra; however, at SRC a 10 x 10 μm aperture was used while each spectrum from the FPA map represents a pixel area of 5.5 x 5.5 μm. The greater S/N, despite summing fewer scans is also apparent in spectra collected using the synchrotron source (512 for CpATCC hypha, 256 for Cp4666D hypha) compared to the thermal source (1024 scans). This is a result of the synchrotron's greater brightness.

FPA maps give a more complete picture of hyphal compositions than a few select, single point sFTIR spectra. Figure 50 illustrates the importance of covering more area of the sample. When the CpATCC hypha was initially examined at SRC, it was found that none of the spectra contained peaks at 1078 and 1022 cm^{-1}. However, when mapped with the FPA, the same hypha was found to contain these peaks in spectra collected at a few, highly localized positions along the hypha. In the FPA map, spectra collected at approximately 30 μm and 50 μm from the tip contained these peaks while the same positions in sFTIR spectra did not. It is possible that for SRC data, there was a slight offset between the IR and visible light in the microscope or that a small error was made when measuring these positions and/or moving to them. This could have resulted in positions adjacent to 30 μm and 50 μm actually being examined, and therefore, the peaks were not seen. The FPA map (Figure 50c) also shows that the 1078 and 1022 cm^{-1} bands are the

most intense at a distance of 250 µm from the hyphal tip, a position overlooked when collecting sFTIR spectra.

The use of the FPA detector also allows for the collection of data from multiple hyphae within the same map area (*e.g.* Figure 46). This allows for an easy and direct comparison of the composition of neighbouring hyphae in addition to maximizing the number of analyzed hyphae with respect to time.

4.3 *Curvularia protuberata*

Curvularia protuberata samples confer heat tolerance to plants in high-stress regions when the thermal tolerance virus is present within the fungus (Márquez *et al.*, 2007). *Curvularia protuberata* samples from non-geothermal plants (and without the virus) do not have the ability to confer any heat protection to plants. CpATCC and Cp4666D samples have proven to be amenable fungal samples for examination with FTIR and sFTIR spectromicroscopies, and many spectra with good S/N were obtained from these samples. Some hyphae were also examined with Raman spectroscopy. The results of analysis with IR and Raman are discussed in the following sections and compared when appropriate.

4.3.1 Characterization of *C. protuberata* with FTIR

Spatially-resolved distribution of chemical signatures in C. protuberata hyphae

sFTIR spectra collected at defined positions on hyphae reveal that their composition is generally consistent over the first 100 μm. With the use of the FPA detector, many more points along hyphae can be examined in a short amount of time. Processed maps sometimes reveal more variations in signal intensity due to the greater number of positions examined. However, spectra collected along a hypha generally all have similar profiles. Comparisons between different hyphae show that the amount of material within cells is not necessarily the same for all hyphae (*e.g.* Figure 46).

Generally, regions of high protein absorptions in hyphae also correspond to regions of high carbohydrate absorptions (see Figure 46). Overall signal intensity is often increased at the position on a hypha where a branch point occurs (see Figure 51). This could be the

result of having a larger amount protein and/or sugar within cells at these branch points, perhaps necessary to fuel growth of the new branch, or simply that there is a greater amount of hyphal material contributing to the signal (within the aperture area for sFTIR or per pixel for FPA maps).

There were no large differences in spectra of hyphae grown from different concentrations of PDA. Thus, it is concluded that while the amount of nutrients available in the media affected the number of hyphae able to germinate from spores, it generally did not affect the composition of fungal cells of those hyphae that were able to grow.

Lipid content in hyphae

Curvularia protuberata hyphae do not contain large amounts of lipids. Analysis of lipid content is based on the fatty acid ester carbonyl band at around 1740 cm^{-1} and/or the CH stretch bands from the long carbon chains from 2850 to 2950 cm^{-1}. The absorbance intensities for carbonyl bands are very low in both CpATCC and Cp4666D spectra (*e.g.* Figure 35), indicating low lipid content. Additionally, when CH regions of spectra were not inverted, a band around 2930 cm^{-1} was often present in hyphal spectra. The CH profile for lipids generally contains two peaks at 2920 and 2850 cm^{-1} while the sugar CH profile has one intense peak at 2930 cm^{-1}. It is therefore concluded that the low lipid carbonyl absorptions in spectra and the profile of the CH stretch region indicate that CH stretch bands are likely the result of carbohydrate CH motions.

Protein content in hyphae

Proteins are a major component of fungal cells. Protein content is estimated from the absorption intensities of amide I and amide II bands (although dispersion may decrease amide I absorption intensities, see section 1.4.12). The absorbance intensities for amide I and amide II bands are typically very similar at all positions along a hypha (see Figure 35). FPA maps expose slightly larger variations in amide I and amide II intensities; however, they still show that the protein content along hyphae is generally constant (*e.g.* Figure 47 & Figure 50). Variations in protein absorption intensities have been observed between hyphae on the same sample (*e.g.* Figure 38 or FPA maps displayed in Figure 48 & Figure 49, both collected from the same sample and processed on the same false-colour scale). It has been determined that the absorbance intensities of amide bands for the CpATCC and Cp4666D samples were often comparable to each other (see Figure 39 & Figure 40).

Carbohydrate content in hyphae

Carbohydrates exhibit bands in the CH stretch region of spectra (2850-2950 cm^{-1}) and in the fingerprint region (1800-600 cm^{-1}). However, CH stretch bands in fungal spectra are difficult to analyze due to Mie scattering and occasional inversion of these bands (discussed in section 1.4.12). All analysis of the sugar content in fungal hyphae has been based on the absorptions in the 1200 to 900 cm^{-1} region of spectra.

Many carbohydrate motions (CO and CC stretches; C-O-H and C-O-C deformations) lie in the region from 1200-900 cm^{-1}. Strong absorptions in this region indicate greater amounts of sugar in hyphae. sFTIR point spectra reveal that carbohydrate content in hy-

phae is generally consistent from tips up to 100 µm from tips (Figure 35). Carbohydrate absorptions were typically more intense when protein content was also high (see Figure 38). Again, analysis using an FPA detector reveals slightly more variation in sugar composition along hyphae (Figure 46d); however, it was concluded that the amount of variation was similar to that seen for protein content.

Certain hyphae (from both Cp4666D and CpATCC) were found to contain two sharp bands (1078 and 1022 cm^{-1}) in the sugar region of spectra (e.g. Figure 45), ultimately identified as mannitol. These bands are discussed in a separate section (4.3.3), below.

4.3.2 Biochemical Distribution in Fungi: Saprotrophs versus Endophytes

Previous analyses of saprotrophic fungi (Szeghalmi *et al.*, 2007a; Jilkine *et al.*, 2008; Figure 81) showed that hyphal tips had less material (proteins, sugars, etc.) compared to mature regions. However, the first discovery during the examination of fungal endophytes was that absorbance intensities in all spectra were generally similar along the length of hyphae (*e.g.* Figure 35, Figure 40, Figure 56, Figure 58, & Figure 60) signifying a more continuous composition along hyphae.

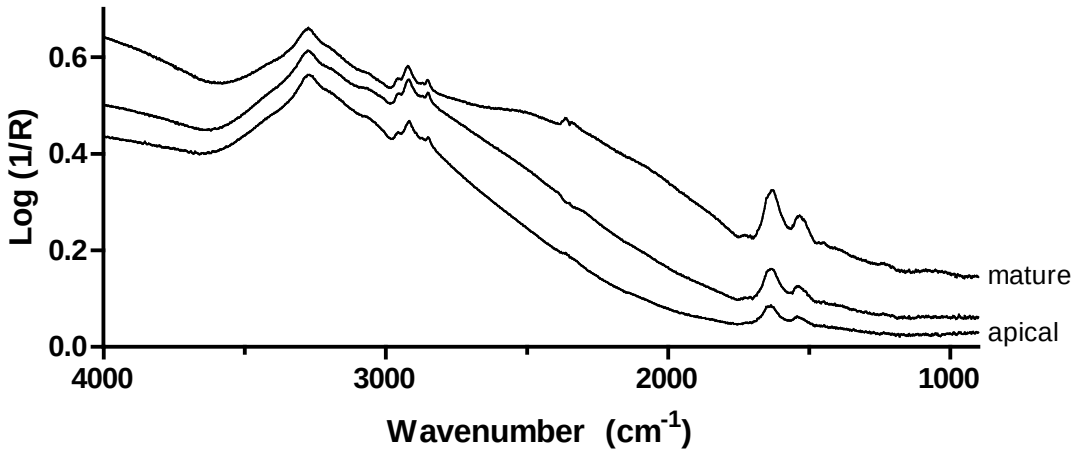

Figure 81. Spectra collected on a *Neurospora* hypha. Spectra were collected at the National Synchrotron Light Source, July 2005. Neurospora hyphae are wider than the endophytes examined in this work, thus absorbance intensities are higher.

This difference in how endophytes and saprotrophs appear to allocate their resources within hyphae could partially be a result of the different lifestyles lead by each group. Saprotrophs are decomposers and are always searching for a food source. Perhaps for these types of fungi, maintaining biochemical reserves in mature hyphal regions is necessary. If a hypha is not successful in finding nutrients, then the supply could be used to support growth of another branch in a new direction. On the other hand, endophytes live entirely within plants and can rely on the host plant as a nutrient source (Rodriguez *et al.*, 2008). It is concluded that endophytes may be able to move their resources to tips with little risk.

The time constraint at synchrotrons that permitted us to examine hyphae at only a few positions (typically four) along their length is not the most desirable method to explore

the distribution of biochemical compounds along hyphae. However, at synchrotrons (with 10 x 10 µm apertures used to examine only one point at a time), this is the most efficient way to gain representative information about samples. The use of an FPA detector to examine endophytes shows that there may be variations in absorbance intensities for certain bands along the length of hyphae (see Figure 42b for a variation in amide I absorption & Figure 47c for a variation in the intensity of the 1021 cm^{-1} band). Other FPA maps confirm the relatively even protein distribution along hyphae previously implied by synchrotron spectra (*e.g.* Figure 45 & Figure 50). Therefore, it can be concluded that, for the majority of endophyte hyphae, protein distribution is consistent along hyphae.

4.3.3 Mannitol identified in IR spectra of *C. protuberata*

Occurrence of 1078 and 1022 cm^{-1} bands in IR spectra

Initially, the major difference observed between ATCC and geothermal *C. protuberata* synchrotron spectra was the appearance of two peaks in the spectra from the geothermal sample at around 1078 and 1022 cm^{-1}, shown in Figure 40. The positions of the maxima range from 1081 to 1076 cm^{-1} and from 1024 to 1018 cm^{-1}, respectively; however, these variations are not considered to be significant since spectra are collected at 4 cm^{-1} resolution. These peaks were not observed in sFTIR point spectra from all Cp4666D hyphae; however, when present, they were in the spectra from all positions along that hypha (Figure 35c & d). In contrast, these two peaks were not seen in any CpATCC synchrotron spectra. Originally, the possibility that these peaks were related to the heat tolerance mechanism in geothermal samples was considered. However, once a spectrometer with an FPA detector was acquired, data collection was accelerated and a few ATCC samples

were found to exhibit the same two peaks in their spectra, as shown in Figure 50 (this is an example of the benefit of the FPA detector compared to collecting point spectra, an issue addressed earlier in section 4.2.2).

The peaks at 1078 and 1022 cm^{-1}, if present in a spectrum, are always together; the intensities of the two peaks are often very similar. When the 1078 and 1022 cm^{-1} peaks are present in spectra, less intense peaks at 1050 and 930 cm^{-1} are often also present (highlighted in Figure 41). This observation suggested that these four bands could be related to the same compound. Based on their frequencies, the most likely candidates are phosphates or sugars, which could also be markers for DNA.

Consideration of polyphosphate

Polyphosphate (polyP) was considered as a possible cause of the 1078 and 1022 cm^{-1} peaks in spectra. Fungi are known to accumulate polyP within cells (Deacon, 1997). Furthermore, IR absorptions from 1080-1078 cm^{-1} in the spectra of cells are the result of a phosphate (PO_2^-) symmetric stretch (examples of some recent studies observing this phosphate band in cell spectra include Wood *et al.,* 1998; Boydston-White *et al.,* 2005; Yang *et al.,* 2005; Chan & Lieu, 2009). PolyP was isolated from Cp4666D and L2.5 samples by R. Rodriguez. IR spectra of both polyP samples were collected and are displayed in Figure 61. Samples were not pure, as seen from the amide bands in spectra, signifying the presence of proteins. Neither of the polyP samples contained the sharp bands at 1078 and 1022 cm^{-1}. Therefore, the bands at 1078 and 1022 cm^{-1} in *C. protuberata* spectra are not the result of polyP in hyphae.

Consideration of sugars

Many sugars were considered as candidates for the bands at 1078 and 1022 cm^{-1} in spectra. IR spectra of common sugars in fungi were found in the literature and compared to the hyphal spectra. After a lengthy search, the bands at 1078 and 1022 cm^{-1} have been attributed to the presence of mannitol (Yoshinari *et al*., 2002; Sharma & Kalonia, 2004). Mannitol is a sugar alcohol known to be present in the majority of fungi (Solomon *et al.*, 2007). Figure 62 displays a spectrum from a Cp4666D hypha along with a spectrum of mannitol. The mannitol spectrum contains bands at 1088, 1053, 1017, and 930 cm^{-1} that correspond to the bands often present in *C. protuberata* spectra.

Figure 82 (below) shows an FTIR spectrum from a Cp4666D hypha without mannitol (a) and another from a hypha containing mannitol (b) for a comparison of the two types of spectra. A spectrum of mannitol (c) is also included for reference. There are clear differences in the spectra from each hypha in the region from 1100 to 1000 cm^{-1}. The differences correspond to the presence or absence of mannitol in hyphae.

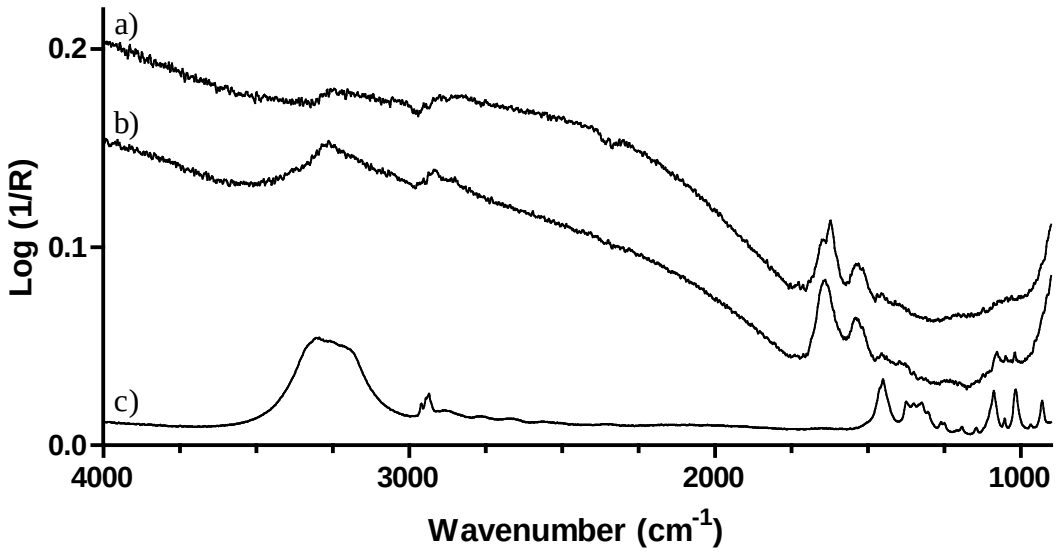

Figure 82. FTIR spectra from Cp4666D hyphae a) without mannitol and b) with mannitol. Spectra were collected 50 µm from hyphal tips. c) An FTIR spectrum of mannitol for comparison. Its intensity has been decreased by a factor of 10.

Possible roles of mannitol in fungi

Several roles of mannitol in fungi, including stress tolerance and carbohydrate storage, have been proposed (Solomon *et al.,* 2007 & references therein). For the fungus *Aspergillus niger*, the amount of mannitol within cells is known to vary with respect to growth stages and conditions of growth (Ruijter *et al.*, 2003). For certain *Aspergillus* species, the reproductive conidia are known to contain considerable amounts of mannitol (Ruijter *et al.*, 2003). The presences of mannitol in fungal spores can ensure viability of the spores under harsh or stressful conditions (*e.g.* extreme heat or high salt concentration) (Ruijter *et al.*, 2003; Pons *et al.*, 1986). However, the exact function of mannitol in fungal hyphae and spores is not fully understood.

Location of mannitol in hyphae

While the amide absorbance intensities along a hypha are often fairly evenly distributed, the occurrence of the bands at 1078 and 1022 cm^{-1} does not necessarily follow the same trend, as seen from FPA maps (see Figure 47). Point spectra indicated that the presence of mannitol was continuous along hyphae, but FPA maps reveal that mannitol is often "spotted" along hyphae.

Variation in the relative intensities of bands at 1088, 1017, and 930 cm^{-1} in pure mannitol spectra are shown in Figure 63. Rotation of hyphae by 90º at a synchrotron (polarized source) affects the relative intensities of the 1078 and 1022 cm^{-1} bands (Figure 64). The variations in peak intensities are a result of crystal orientation with respect to the incoming radiation and indicate that mannitol is present in the dried hyphae as a pure crystal. In living fungi, mannitol may be stored in either aqueous form or as a solid.

Mannitol has been commonly observed at branch points on hyphae and at tips that appear to be producing spores (Figure 51 & Figure 52). The appearance of mannitol in only certain spectra could indicate that it is related to different phases of the cell life cycle or different fungal structures. The fact that IR spectra show mannitol in reproductive structures of *C. protuberata* is consistent with increased mannitol content in the reproductive structures of other fungal species (Ruijter *et al.*, 2003). However, many *C. protuberata* vegetative hyphae also contain mannitol. Mannitol content and distribution, revealed by FTIR microspectroscopy, could potentially offer insight into the growth states of hyphae (vegetative vs. reproductive) at the time of death and later be extended to the examination of live growing samples. Hyphae are known to grow at different rates with respect to each other, and the growth rate of a hypha can change over time (Hubbard &

Kaminskyj, 2007; Sampson *et al.*, 2003). At the time of death, different hyphae were likely in different states of metabolic activity. This could explain why some hyphae contain mannitol while others do not. Again, the examination of living samples would offer more insight into any relationship of mannitol to growth rate and metabolic activity.

Effect of PDA concentration on the presence of mannitol

Mannitol has been observed in both CpATCC and Cp4666D samples grown from 100% and 10% PDA. However, no samples grown from 3% and 1% PDA have been found to contain mannitol. This is despite similar protein and overall sugar content in samples grown from all PDA concentrations.

Growth conditions (*e.g.* factors affecting osmotic pressure, such as NaCl concentration in growth medium) are known to affect mannitol concentrations in fungi (Witteveen & Visser, 1995; Ruijter *et al.*, 2003). The low concentration of nutrients from 3% and 1% PDA could explain the lack of mannitol in *C. protuberata* hyphae grown from these media concentrations. However, this observation could be solely due to the fact that these samples have been examined to a lesser extent than those grown from 100% and 10% PDA. Work is on-going to collect spectra from more hyphae grown from 3% and 1% PDA in order to confirm or refute this observation.

Comparison to A. nidulans spores

Curvularia protuberata is not the only fungal species found to contain sharp bands at 1078 and 1022 cm^{-1} in FTIR spectra. *Aspergillus nidulans* spores examined with sFTIR (Rak *et al.*, unpublished results) have also been found to exhibit these bands in spectra,

along with those around 1050 and 930 cm^{-1}. Spectra acquired from a Cp4666D vegetative hypha and from an *A. nidulans* spore are shown together in Figure 83. Both spectra exhibit the mannitol profile in the carbohydrate region of spectra. Mannitol has also been observed in spectra of *A. nidulans* conidiophores (reproductive structures that produce spores) but never in the spectra of vegetative *A. nidulans* hyphae (Rak *et al.*, unpublished results). This data demonstrates further that these bands may be associated with different fungal structures.

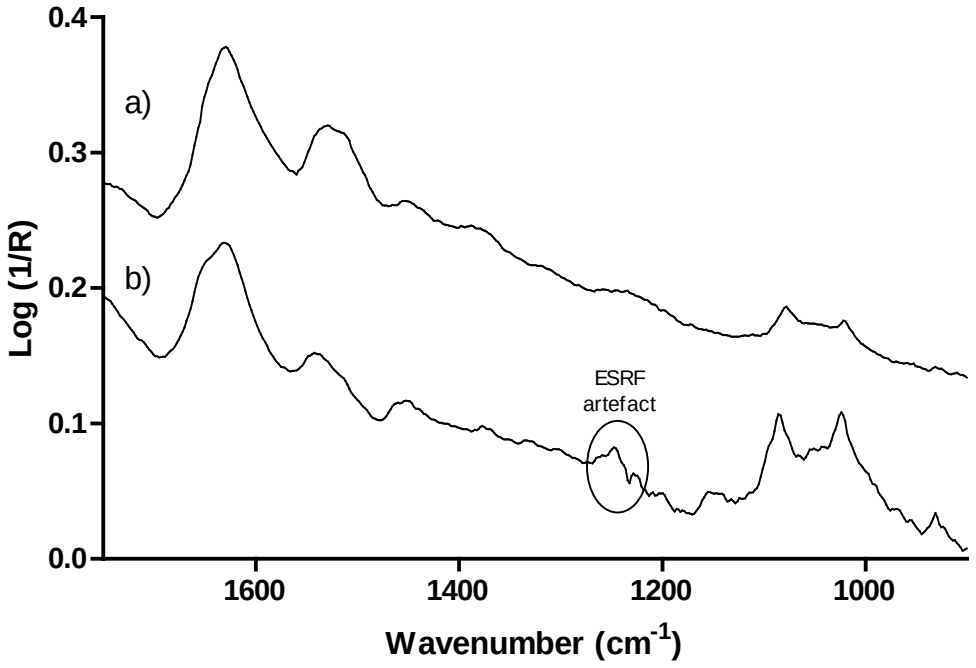

Figure 83. a) Spectrum recorded 50 µm from the tip of a Cp4666D hypha and b) spectrum of an *A. nidulans* spore (M Rak, SGW Kaminskyj, KM Gough; unpublished results. Spectra collected at the European Synchrotron Radiation Facility (ESRF), November 2007). The artefact in the ESRF spectrum is the result of an absorption by carbonaceous material present in the beam path.

Effect of the thermal tolerance virus on spectra

Further experiments were performed to determine whether any spectral differences existed between samples containing the thermal tolerance virus and those without the virus. Additionally, any relationship between the presence of the virus and the presence of mannitol in hyphae was examined.

The first of these experiments (August 2009) involved comparison of a sample of Cp4666D no virus with a control Cp4666D sample (contained the virus). Point sFTIR spectra were collected along hyphae. Neither the spectra from Cp4666D hyphae nor spectra from Cp4666D no virus hyphae were found to contain the sharp bands associated with mannitol (Figure 53). Cp4666D no virus spectra had very similar amide absorptions from one hypha to another and very weak carbohydrate absorption intensities at all positions. For some hyphae containing the virus, the absorption intensities from 1100 to 1000 cm^{-1} were more intense than for those without the virus (see Figure 53). Viruses that infect fungi contain double stranded ribonucleic acid (dsRNA). dsRNA is uncommon in fungi; its occurrence indicates the presence of a virus (Márquez *et al.*, 2007). Therefore, removal of the virus could potentially lower phosphate and sugar absorptions in spectra. However, many control Cp4666D hyphae had spectra with similar carbohydrate absorption intensities to Cp4666D no virus hyphae.

The second of these experiments involved the growth of CPA (Cp4666D sample with the virus removed then reintroduced) and unmodified Cp4666D. Both samples were examined with FTIR/FPA. Spectra from each sample were generally very similar to each other. Neither the control Cp4666D nor the CPA sample (seen in Figure 54) was found to contain any mannitol.

All samples were grown under the same conditions in the Kaminskyj lab; however, fresh media and spores were always required. No obvious deviations from growth protocols were recorded. We do not yet understand why none of the control Cp4666D samples (grown July 2009 & October 2009) were found to contain mannitol while mannitol was common in previous samples of Cp4666D (grown November 2007 & June 2008).

Mannitol has been observed in spectra from both CpATCC and Cp4666D hyphae but was not present in any of the spectra from Cp4666D no virus or CPA hyphae. Additionally, mannitol is not present in all Cp4666D hyphae or even all of the Cp4666D samples. From this, it seems unlikely that the presence of mannitol is associated with the thermal tolerance virus. However, hyphae were never grown at elevated temperatures, making it difficult to comment on any relationship between mannitol the mechanism of habitat-adapted symbiosis. Mannitol is known to be essential in protecting spores of certain species from high temperatures (Ruijter *et al.*, 2003), and therefore could potentially play a role in the mechanism of heat tolerance conferred to plants. Mannitol is considered an "enigmatic polyol" in filamentous fungi (Solomon *et al.*, 2007); its exact role in *C. protuberata* hyphae will require further exploration.

4.3.4 Characterization of *C. protuberata* with Raman

Effect of PDA concentration of spectra

Spectra of Cp4666D hyphae did not vary with concentration of growth medium. All prominent features in the spectral profiles from hyphae grown from 100% PDA (Figure 67 & Figure 68) were seen in spectra from 10% PDA samples (Figure 69 & Figure 70). Raman microscopy shows that the difference between the nutrients available in 100% and 10% PDA does not affect the contents of cells. The same conclusion was reached based on FTIR data.

Band Assignments

The spectral signatures at all points along a hypha were very similar. All spectra from a given hypha were of either Type 1 or Type 2. Type 2 spectra are defined as containing strong bands at 875 and 885 cm^{-1} in spectra (these bands are discussed in section 4.3.6). The most common bands present in Type 1 and Type 2 Cp4666D Raman spectra are listed with tentative assignments in Table 17.

Table 17. Major bands in Cp4666D Raman spectra with tentative assignments.

Peak Position (cm^{-1})	Tentative Assignment
620, 622	υ(CS), glutathione[1]; phenylalanine[2]
637	
642, 644	υ(CS), glutathione[1]; chitin, tyrosine[2]
718, 720, 722	
757	tryptophan[1]
780, 781, 782, 783	ring stretch, cytosine & uracil[3]
851, 852	υ(CC), υ(COC) 1,4-glycosidic link[2]
1003	ring breathing mode[1,2], phenylalanine[1]
1010	ring breathing mode[1,2], tryptophan[1]
1030, 1032, 1033	υ(CC), υ(CO)[2]
1042	glutathione[1]
1125, 1126, 1127, 1129	υ(CO), υ(CC) sugar, lipid[4]

[1]De Gelder *et al.*, 2007
[2]De Gussem *et al.*, 2007
[3]Chan & Lieu, 2009
[4]Szeghalmi *et al.*, 2007b

All hyphal spectra contain a strong, sharp band at 1003 cm^{-1} with a shoulder at 1010 cm^{-1}. The band at 1003 cm^{-1} can be attributed to phenylalanine (De Gelder *et al.*, 2007). The shoulder at 1010 cm^{-1} could be due to tryptophan, another amino acid (De Gelder *et al.*, 2007). Phenylalanine and tryptophan are general markers for proteins in hyphae. In Type 1 spectra, the 1003 cm^{-1} peak is usually the most intense.

Two common bands in spectra occur at about 620 and 642 cm^{-1}; both tend to have similar intensities in Raman spectra. These bands could indicate the presence of glutathione (a tripeptide) in hyphae. Bands at 625 and 643 cm^{-1} are the most intense in the spectrum of glutathione (De Gelder *et al.*, 2007) and are likely the result of C-S stretches. Another possibility for these bands could be skeletal motions of amino acids (phenylalanine and tyrosine) (De Gussem *et al.*, 2007).

4.3.5 Comparison of Raman Spectra from Cp4666D and Saprotrophs

Previous Raman/SERS studies of *A. nidulans* showed that spectra of this species contained an intense peak at 1050 cm^{-1}, tentatively assigned to C-O and C-C stretches in sugars and lipids and C-H deformations (Szeghalmi *et al.*, 2007b). The geothermal *C. protuberata* samples do not exhibit a peak at 1050 cm^{-1}, while the prominent 1003 cm^{-1} band in all *C. protuberata* spectra was not common in *A. nidulans* spectra. This offers information about the differing protein and sugar compositions of each species and could be useful in the identification and characterization of different fungal species.

4.3.6 Mannitol Identified in Raman Spectra of *C. protuberata*

Occurrence of 875 and 885 cm^{-1} bands in spectra

Raman spectra collected from geothermal *C. protuberata* hyphae could be categorized as one of two types, shown in Figure 67 (Type 1) and Figure 68 (Type 2). Type 2 spectra contain strong bands at 875 and 885 cm^{-1}; Type 1 spectra do not contain either of these bands. The spectra collected at all positions along a hypha were of one type only.

Consideration of polyphosphate

PolyP samples isolated from Cp4666D and L2.5 by R. Rodriguez were analyzed with Raman spectroscopy. Figure 79 displays spectra of polyP from Cp4666D and L2.5. However, as seen from both FTIR and Raman spectra of polyP, the isolated samples were not pure. Neither of these samples contains bands common in Raman spectra of *C. pro-*

tuberata samples. It was concluded that polyphosphate is not the source of the strong bands at 875 and 885 cm^{-1} in certain Raman spectra of hyphae.

Consideration of sugars

Mannitol was identified in *C. protuberata* hyphae from IR spectra. Therefore, a Raman spectrum of mannitol was collected for comparison to Cp4666D Raman spectra. Prior to the identification of mannitol in hyphae (on the basis of IR spectra), many sugars were considered as a source of the bands at 875 and 885 cm^{-1} in Raman spectra. Raman spectra of on-hand suspect sugars were collected at the U of M while the spectra of others were obtained from the literature.

A Raman spectrum of mannitol is displayed in Figure 80. Bands at 518, 649, 788, 876, 1038, and 1135 cm^{-1} in the mannitol spectrum are similar to bands present in Type 2 Cp4666D spectra. There is a shoulder on the 876 cm^{-1} band (at about 885 cm^{-1}) which likely corresponds to the band in Type 2 fungal spectra.

Figure 84 shows Raman spectra collected from a Cp4666D hypha without mannitol (a) and from a Cp4666D containing mannitol (b). A spectrum of mannitol is included for comparison (c). The mannitol bands at 518, 649, 781, and 875 cm^{-1} are present in (b) but not in (a). Although bands at 1034 and 1130 cm^{-1} are present in both spectra (a) and (b), they are much more intense in the hypha (b). The spectra displayed in this figure were collected on the same hyphae and at the same positions as the IR spectra displayed in Figure 82.

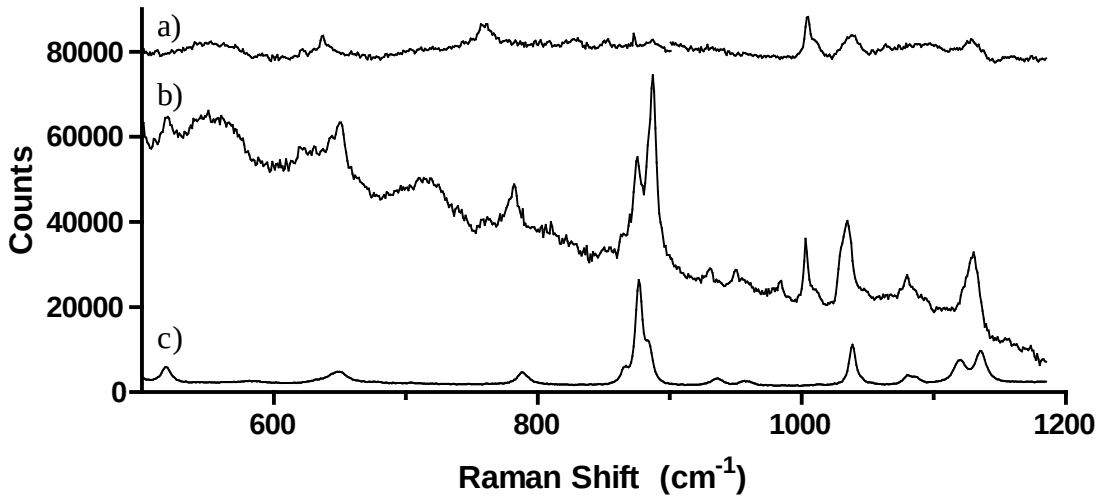

Figure 84. Raman spectra from Cp4666D hyphae a) without mannitol and b) with mannitol. Spectra were collected 50 µm from hyphal tips on the same hyphae displayed in Figure 82 (a and b, respectively). c) A Raman spectrum of mannitol for comparison.

Comparison to IR data

Several hyphae were analyzed with both Raman and FTIR microscopy. Figure 48 and Figure 49 show FPA maps of hyphae that were also examined with Raman. Raman spectra from these hyphae are shown in Figure 68, Figure 71 (corresponding to the hyphae in the FPA map displayed in Figure 48, indicated by arrows), and Figure 72 (corresponding to the hypha marked with an arrow in Figure 49). While spectra shown in Figure 68 and Figure 71 have strong bands at 875 and 885 cm^{-1}, spectra from Figure 72 do not contain these bands. One other hypha (data not shown in the Results chapter) was examined with both FTIR and Raman. This hypha was not found to contain 875 and 885 cm^{-1} bands in Raman spectra.

Comparison between the two sets of data shows hyphae that contain mannitol bands in IR spectra also contain mannitol bands in Raman spectra. Additionally, hyphae not containing mannitol bands in IR spectra also do not contain mannitol bands in Raman spectra. The identification of mannitol in both IR and Raman spectra confirms its presence in hyphae.

Effect of the thermal tolerance virus on spectra

Cp4666D no virus and a control Cp4666D sample were analyzed with Raman microscopy. These two samples were grown in the same month as those previously examined with IR (July 2009). The same bands were present in spectra collected from each sample, as shown in Figure 73 (Cp4666D) and Figure 74 (Cp4666D no virus). Spectra from both samples fell under the category of Type 1; no mannitol was found in any hyphae. This implies that mannitol is not related to the presence/absence of the virus necessary to confer thermal tolerance.

4.4 *Fusarium culmorum*

Fusarium culmorum samples living within coastal plants confer salt tolerance to their hosts while samples isolated from non-coastal plants do not possess this ability (Rodriguez *et al.*, 2008). Good quality sFTIR and Raman spectra were obtained from both Fc18 and FcRed1 hyphae. The results from both techniques are discussed below and data from *F. culmorum* samples are compared to data from the more extensively examined *C. protuberata* samples.

4.4.1 Characterization of *F. culmorum* with FTIR

As observed for *C. protuberata*, *F. culmorum* samples have been found to have a fairly consistent biochemical composition along hyphae. Absorption intensities for amide I, amide II, and sugar bands are generally comparable at all examined positions along a hypha (see Figure 56), with a few exceptions, as shown in Figure 57. This biochemical distribution along hyphae is comparable to what has been seen with *C. protuberata* samples. *F. culmorum* spectra are often less intense than spectra from *C. protuberata* hyphae. This could be explained by the slightly smaller diameters of *F. culmorum* hyphae (2-3 μm compared to 3-4 μm for *C. protuberata* samples) meaning a slightly smaller amount of material would be present in apertures (sFTIR) or per pixel (FTIR with FPA).

No strong differences between Fc18 and FcRed1 spectra have been noted. Certain FcRed1 hyphae have less intense protein and sugar absorptions than Fc18 hyphae (Figure 58), but this seems to depend on which hyphae are being compared. Both Fc18 and FcRed1 samples have been found to have very weak carbonyl absorbance bands at about

1740 cm^{-1}, indicating low quantities of lipids in cells. This is a characteristic also noted in *C. protuberata* spectra.

Fusarium culmorum hyphae have a very consistent composition (amount of protein, sugars) along the first 100 µm of hyphae. The same trend was also observed for *C. protuberata* hyphae and is in contrast to saprotrophic fungi that were previously examined (Szeghalmi *et al.*, 2007a; Jilkine *et al.*, 2008; see section 4.3.2).

Neither the Fc18 nor the FcRed1 samples have been found to contain bands around 1078 and 1022 cm^{-1} in their sFTIR spectra. This could indicate that these samples do not contain any mannitol or, if mannitol is present, its concentration is extremely low and is not detectable with sFTIR. However, for CpATCC samples, bands resulting from mannitol were only found once samples were examined with an FPA detector. *Fusarium culmorum* samples have been examined to a lesser extent than the *C. protuberata* samples (at synchrotrons only); collecting FPA maps of Fc18 and FcRed1 samples would offer more information about the contents of cells along the length of hyphae.

4.4.2 Characterization of *F. culmorum* with Raman

Both the coastal and non-coastal *F. culmorum* samples have been examined with Raman microscopy. Spectra from both were often very similar to each other. *Fusarium culmorum* spectra generally contained fewer bands than those from geothermal *C. protuberata*. However, bands present in *F. culmorum* spectra were often also present in Cp4666D spectra. Assignment of *F. culmorum* bands are the same as those for *C. protuberata*, located in section 4.3.4. No difference was found between spectra collected from FcRed1

hyphae grown from 100% PDA (Figure 75) versus hyphae grown from 10% PDA (Figure 76).

Only one FcRed1 hypha was found exhibit bands at 875 and 885 cm^{-1} in spectra (Figure 77); these bands indicate the presence of mannitol (see section 4.3.6). Further analysis of both Fc18 and FcRed1 hyphae is necessary to determine if any other hyphae contain mannitol. A survey could be performed with FTIR/FPA initially, followed by a more detailed analysis with Raman microscopy.

4.5 *Colletotrichum magna*

Colletotrichum magna is typically a plant pathogen; however, a mutant sample has been found to be non-pathogenic and confer pathogen protection to certain plants (Rodriguez *et al.*, 2008). *Colletotrichum magna* hyphae did not tend to provide nice sFTIR spectra compared to those obtained from *C. protuberata* and *F. culmorum*. As a result, the majority of this thesis focuses on *C. protuberata* and *F. culmorum*. Both L2.5 (a plant pathogen) and CmPath (a non-pathogenic mutant of L2.5) were examined with sFTIR. Only a limited amount of sFTIR spectra have been collected from these samples and, therefore, they are only discussed to a very limited extent. Neither L2.5 nor CmPath was analyzed with Raman microscopy.

Spectra collected from L2.5 and CmPath hyphae were often very noisy. L2.5 spectra often contained essentially no sugar absorptions, while those from CmPath samples were slightly more intense (Figure 60). However, biochemical signatures did appear to be consistent at all positions examined along a hypha, as observed for the other endophytes. Due to the low S/N, it is difficult to distinguish any potential carbonyl absorptions from the noise. The same is true in the sugar region. It does not appear that any of the *C. magna* spectra contain bands at 1078 and 1022 cm^{-1} in their spectra.

The low absorption intensities observed in synchrotron spectra could indicate that maps with a thermal source and FPA detector would require a large number of scans to be summed (and take a long time) to obtain decent S/N in spectra. Such experiments are feasible, but would require careful control of water vapour fluctuations during data col-

lection. Subtraction of water vapour post data collection would likely still be required (outlined in section 3.2.1).

Chapter 5

Conclusions and Future Work

5.1 Conclusions

This has been the first high-resolution spectroscopic study of fungal endophytes.

Endophytes were found to have a continuous biochemical composition along hyphae in contrast to saprotrophs that reserve material in mature hyphal regions. This could be a result of the different lifestyles lead by each of these groups of fungi.

The lowest concentrations of PDA (3% and 1%) allowed for fewer spores to germinate as compared to 100% and 10% PDA. However, the composition of hyphae was fairly similar for endophytes grown from all PDA concentrations.

No substantial differences have been observed between spectra of CpATCC compared to Cp4666D or of Fc18 compared to FcRed1. sFTIR, FTIR, and Raman have so far not provided the details for the mechanism behind habitat-adapted symbiosis. L2.5 and

CmPath hyphae typically provided only low quality (low S/N) spectra and, therefore, comparison between these isolates is not feasible.

A number of *C. protuberata* hyphae were found to contain mannitol (both CpATCC and Cp4666D isolates) on the basis of sFTIR, FTIR, and Raman analysis. It is currently not known if mannitol plays a role in the mechanism of habitat-adapted symbiosis.

No sFTIR spectra of *F. culmorum* hyphae showed the presence of mannitol; however, one FcRed1 hyphae was found to contain mannitol based on Raman analysis. The prevalence of mannitol in *F. culmorum* hyphae is currently not known.

5.2 Future Work

Future directions for this project are planned.

An extended analysis (FTIR/FPA) of *C. protuberata* will be performed in order to develop a better statistical evaluation of the occurrence and distribution of mannitol in hyphae. This in turn could lead to a better understanding of the role of mannitol.

Fusarium culmorum hyphae will be examined with FTIR/FPA to determine whether additional hyphae also contain mannitol.

The examination of *C. magna* hyphae with FTIR/FPA could find some hyphae that are better suited to spectroscopic analysis than those chosen at synchrotrons. L2.5 and CmPath isolates could then be compared to one another.

Growing samples on IR transparent material (*e.g.* BaF_2) would allow for data collection in transmission mode. This could potentially reduce the scattering artefacts (mainly the dispersion artefact) in spectra.

Staining samples post spectroscopic analysis would help to correlate spectra with organelles. No staining has been performed on any endophyte samples to this point because further spectroscopic analysis is desired.

Implementation of Mie scattering and dispersion corrections now being developed in the Bhargava lab, University of Illinois at Urbana-Champaign (Davis *et al.*, 2010a; Davis *et al.*, 2010b) could allow for better analysis of spectra (*e.g.* protein secondary structure, CH stretch region).

The IRENI beamline at SRC provides 0.54 μm pixel resolution in transmission mode. This beamline would offer much greater detail about septa and the distribution of mannitol in hyphae. Data collection has already commenced.

Imaging of live growing hyphae would provide detail about the composition of living cells. This could also offer information on the timing of mannitol appearance in hyphae and which structures it is associated with. Both these observations could lead to a better understanding of mannitol's role in hyphae.

References

Arcangeli C, Cannistraro S. (2000). In situ Raman microspectroscopic identification and localization of carotenoids: Approach to monitoring of UV-B irradiation stress on Antarctic fungus. *Biopolymers (Biospectroscopy)* 57: 179-186.

Bahmed K, Quillès F, Bonaly R, Coulon J. (2003). Fluorescence and infrared spectrometric study of cell walls from Candida, Kluyveromyces, Rhodotorula and Schizosaccharomyces yeasts in relation with their chemical composition. *Biomacromolecules* 4: 1763-1772.

Bassan P, Byrne HJ, Bonnier F, Lee J, Dumas P, Gardner P. (2009) Resonant Mie scattering in infrared spectroscopy of biological materials – understanding the 'dispersion artefact'. *Analyst* 134: 1586-1593.

Bassan P, Kohler A, Martens H, Lee J, Byrne HJ, Dumas P, Gazi E, Brown M, Clarke N, Gardner P. (2010). Resonant Mie scattering (RMieS) correction of infrared spectra from highly scattering biological samples. *Analyst* 135: 268-277.

Bhargava R, Levin IW. (2005) Fourier transform mid-infrared spectroscopic imaging: Microspectroscopy with multichannel detectors. In R Bhargava & I Levin (Eds.), *Spectrochemical analysis using infrared multichannel detectors* (pp. 1-24). Oxford, UK: Blackwell Publishing.

Bhargava R, Schaeberle MD, Levin IW. (2006). Raman and mid-infrared microspectroscopic imaging. In VG Gregoriou and MS Braiman (Eds.), *Vibrational Spectroscopy of Biological and Polymeric Materials*. (pp. 215-252). Boca Raton, USA: Taylor & Francis Group.

Boydston-White S, Chernenko T, Regina A, Miljoković M, Matthäus C, Diem M. (2005). Microspectroscopy of single proliferating HeLa cells. *Vibrational Spectroscopy* 38: 169-177.

Brondz I, Hoiland K, Ekeberg D. (2004). Multivariate analysis of fatty acids in spores of higher basidiomycetes: A new method for chemotaxonomical classification of fungi. *Journal of Chromatography B* 800: 303-307.

Cappitelli F, Vicini S, Piaggio P, Abbruscato P, Princi E, Casadevall A, Nosanchuk JD, Zanardini E. (2005). Investigation of fungal deterioration of synthetic paint binders using vibrational spectroscopic techniques. *Macromolecular Bioscience* 5: 49-57.

Carlile MJ, Watkinson SC, Gooday GW. (2001). *The Fungi.* San Diego, USA: Academic Press.

Carr GL. (1999). High-resolution microspectroscopy and sub-nanosecond time-resolved spectroscopy with the synchrotron infrared source. *Vibrational Spectroscopy* 19: 53-60.

Chalmers JM. (2002). Mid-infrared spectroscopy: anomalies, artifacts and common errors. In JM Chalmers & PR Griffiths (Eds.), *The Handbook of Vibrational Spectroscopy* (pp. 2327-2347). Chichester, UK: John Wiley & Sons Ltd.

Chan JW, Lieu, DK. (2009). Label-free biochemical characterization of stem cells using vibrational spectroscopy. *Journal of Biophotonics* 2: 656-668.

Davis BJ, Carney PS, Bhargava R. (2010a). Theory of midinfrared absorption microscpectroscopy: I. Homogeneous samples. *Analytical Chemistry* 82: 3474-3486.

Davis BJ, Carney PS, Bhargava R. (2010b). Theory of midinfrared absorption microscpectroscopy: II. Heterogeneous samples. *Analytical Chemistry* 82: 3487-3499.

De Gelder J, De Gussem K, Vandenabeele P, Moens L. (2007). Reference database of Raman spectra of biological molecules. *Journal of Raman Spectroscopy* 38: 1133-1147.

De Gussem K, Vandenabeele P, Verbeken A, Moens L. (2005). Raman spectroscopic study of *Lactarius* spores (Russulales, Fungi). *Spectrochimica Acta Part A* 61: 2896-2908.

De Gussem K, Vandenabeele P, Verbeken A, Moens L. (2007). Chemotaxonomical identification of spores of macrofungi: possibilities of Raman spectroscopy. *Analytical and Bioanalytical Chemistry* 387: 2823-2832.

Deacon JW. (1997). *Modern Mycology*. Oxford, UK: Blackwell Science.

Dumas P, Miller L. (2003). The use of synchrotron infrared microspectroscopy in biological and biomedical investigations. *Vibrational Spectroscopy* 32: 3-21.

Dumas P, Sockalingum GD, Sulé-Suso J. (2006). Adding synchrotron radiation to infrared microspectroscopy: What's new in biomedical applications? *TRENDS in Biotechnology* 25: 40-44.

Duncan WD, Williams GP. (1983). Infrared synchrotron radiation from electron storage rings. *Applied Optics* 22: 2914-2923.

Erukhimovitch V, Pavlov V, Talyshinsky M, Souprun Y, Huleihel M. (2005). FTIR microscopy as a method for identification of bacterial and fungal infections. *Journal of Pharmaceutical and Biomedical Analysis* 37: 1105-1108.

Essendoubi M, Toubas D, Bouzaggou M, Pinon JM, Manfait M, Sockalingum GD. (2005). Rapid identification of *Candida* species by FTIR microspectroscopy. *Biochimica et Biophysica Acta* 1724: 239-247.

Fackler K, Schwanninger M, Gradinger C, Hinterstoisser B, Messner K. (2007). Qualitative and quantitative changes of beech wood degraded by wood-rotting basidiomycetes monitored by Fourier transform infrared spectroscopic methods and multivariate data analysis. *FEMS Microbiology Letters* 271: 162-169.

Ferraro JR, Nakamoto K, Brown CW. (2003). *Introductory Raman Spectroscopy*. San Diego, USA: Academic Press.

Fischer G, Braun S, Thissen R, Dott W. (2006). FTIR spectroscopy as a tool for rapid identification and intra-species characterization of airborne filamentous fungi. *Journal of Microbiological Methods* 64: 63-77.

Freeman S, Rodriguez RJ. (1992). A rapid, reliable bioassay for pathogenicity of *Colletotrichum magna* on cucurbits and its use in screening for non-pathogenic mutants. *Plant Disease* 76: 901-905.

Freeman S, Rodriguez RJ. (1993). Genetic conversion of a fungal plant pathogen to a non-pathogenic, endophytic mutualist. *Science* 260: 75-78.

Galagan *et al.* (2005). Sequencing of *Aspergillus nidulans* and comparative analysis with *A. fumigatus* and *A. oryzae*. *Nature* 438: 1105-1115.

Genestar C, Palou J. (2006). SEM-FTIR spectroscopic evaluation of deterioration in an historic coffered ceiling. *Analytical and Bioanalytical Chemistry* 384: 987-993.

Giménez C, Cabrera R, Reina M, González-Coloma A. (2007). Fungal endophytes and their role in plant protection. *Current Organic Chemistry* 11: 707-720.

Gow NAR, Gadd GM. (1995). *The Growing Fungus*. London, England: Chapman & Hall.

Griffin DH. (1994). *Fungal Physiology*. New York, USA: Wiley-Liss.

Griffiths PR, de Haseth JA. (2007). *Fourier Transform Infrared Spectrometry*. New Jersey, USA: Wiley-Interscience.

Henson J, Redman R, Rodriguez R, Stout R. (2005). Fungi in Yellowstone's geothermal soils and plants. *Yellowstone Science* 13: 25-30.

Holman H-YN, Martin MC, McKinney WR. (2003). Tracking chemical changes in a living cell: Biomedical applications of SR-FTIR spectromicroscopy. *Spectroscopy* 17: 139-159.

Huang Y-S, Karashima T, Yamamoto M, Hamaguchi H. (2003). Molecular-level pursuit of yeast mitosis by time- and space-resolved Raman spectroscopy. *Journal of Raman Spectroscopy*. 34: 1-3.

Hubbard M, Kaminskyj S. (2007). Growth rate of *Aspergillus nidulans* hyphae is independent of a prominent array of microtubules. *Mycological Progress* 6: 179-189.

Ibelings MS, Maquelin K, Endtz HPh, Bruining HA, Puppels GJ. (2005). Rapid identification of *Candida* spp. in peritonitis patients by Raman spectroscopy. *Clinical Microbiology and Infection* 11: 353-358.

Jennings DH, Lysek G. (1999). *Fungal Biology: Understanding the Fungal Lifestyle.* New York, USA: Springer-Verlag.

Jilkine K, Gough KM, Julian R, Kaminskyj SGW. (2008). A sensitive method for examining whole-cell biochemical composition in single cells of filamentous fungi using synchrotron FTIR spectromicroscopy. *Journal of Inorganic Biochemistry* 102: 540-546.

Kaminskyj SGW. (2000). Septum position is marked at the tip of *Aspergillus nidulans* hyphae. *Fungal Genetics and Biology* 31:105-113.

Kaminskyj SGW, Dahms TES. (2008). High spatial resolution surface imaging and analysis of fungal cells using SEM and AFM. *Micron* 39: 349-361.

Kaminskyj S, Jilkine K, Szeghalmi A, Gough K. (2008). High spatial resolution analysis of fungal cell biochemistry-bridging the analytical gap using synchrotron FTIR spectromicroscopy. *FEMS Microbiology Letters* 284: 1-8.

Kohler A, Sulé-Suso J, Sockalingum GD, Tobin M, Bahrami F, Yang Y, Pijanka J, Dumas P, Cotte M, van Pittius DG, Parkes G, Martens H. (2008). Estimating and correcting Mie scattering in synchrotron-based microscopic Fourier transform infrared spectra by extended multiplicative signal correction. *Applied Spectroscopy* 62: 259-266.

Lasch P, Naumann D. (2006). Spatial resolution in infrared microspectroscopic imaging of tissues. *Biochimica et Biophysica Acta* 1758: 814-829.

Lee J, Gazi E, Dwyer J, Brown MD, Clarke NW, Nicholson JM, Gardner P. (2007). Optical artefacts in transflection mode FTIR microspectroscopic images of single cells on a biological support: the effect of back-scattering into collection optics. *Analyst* 132: 750-755.

Maquelin K, Dirschner C, Choo-Smith L-P, van den Braak N, Endtz HPh, Naumann D, Puppels GJ. (2002a). Identification of medically relevant microorganisms by vibrational spectroscopy. *Journal of Microbiological Methods* 51: 255-271.

Maquelin K, Choo-Smith L-P, Endtz HP, Bruining HA, Puppels GJ. (2002b). Rapid identification of *Candida* species by confocal Raman microspectroscopy. *Journal of Clinical Microbiology* 40: 594-600.

Maquelin K, Dirschner C, Choo-Smith L-P, Ngo-Thi NA, van Vreeswijk T, Stämmler M, Endtz HP, Bruining HA, Naumann D, Puppels GJ. (2003). Prospective study of the performance of vibrational spectroscopies for rapid identification of bacterial and fungal pathogens recovered from blood cultures. *Journal of Clinical Microbiology* 41: 324-329.

Márquez LM, Redman RS, Rodriguez RJ, Roossinck MJ. (2007). A virus in a fungus in a plant: Three-way symbiosis required for thermal tolerance. *Science* 315: 513-515.

Michell AJ, Scurfield G. (1967). Composition of extracted fungal cell walls as indicated by infrared spectroscopy. *Archives of Biochemistry and Biophysics* 120: 628-637.

Miller LM, Smith RJ. (2005). Synchrotrons versus globars, point-detectors versus focal plane arrays: Selecting the best source and detector for specific infrared microspectroscopy and imaging applications. *Vibrational Spectroscopy* 38: 237-240.

Mohlenhoff B, Romeo M, Diem M, Wood BR. (2005). Mie-type scattering and non-Beer-Lambert absorption behavior of human cells in infrared microspectroscopy. *Biophysical Journal* 88: 3635-3640.

Movasaghi Z, Rehman S, Rehman IU. (2007). Raman spectroscopy of biological tissues. *Applied Spectroscopy Reviews* 42: 493-541.

Movasaghi Z, Rehman S, Rehman IU. (2008). Fourier transform infrared (FTIR) spectroscopy of biological tissues. *Applied Spectroscopy Reviews* 43: 134-179.

Navratil M, Mabbott GA, Arriaga EA. (2006). Chemical microscopy applied to biological systems. *Analytical Chemistry* 78: 4005-4019.

Nie M, Luo J, Xiao M, Chen J, Bao K, Zhang W, Chen J, Li B. (2007). Structural differences between *Fusarium* strains investigated by FTIR spectroscopy. *Biochemistry (Moscow)* 72: 61-67.

Petrini O. (1986). Taxonomy of endophytic fungi of aerial plant tissues. In NJ Fokkema & J van den Huevel (Eds.). Microbiology of the phyllosphere (pp. 175-187). Cambridge, UK: Cambridge University Press.

Pijanka JK, Kohler A, Yang Y, Dumans P, Chio-Srichan S, Manfait M, Sockalingum GD, Sulé-Suso J. (2009). Spectroscopic signatures of single, isolated cancer cell nuclei using synchrotron infrared microscopy. *Analyst* 134: 1176-1181.

Pirozynski KA, Malloch DW. (1975). The origin of land plants: A matter of mycotrophism. *Biosystems* 6: 153-164.

Pons S, Mudge KW, Negm F. (1986). Effect of mannitol on the in vitro growth, temperature optimum, and subsequent ectomycorrhizal infectivity of *Pisolithus tinctorius*. *Canadian Journal of Botany* 64: 1812-1816.

Rak M, Kaminskyj SGW, Gough KM. (2007). Unpublished results.

Redman RS, Litvintseva A, Sheehan KB, Henson JM, Rodriguez RJ. (1999a). Fungi from geothermal soils in Yellowstone National Park. *Applied and Environmental Microbiology* 65: 5193-5197.

Redman RS, Freeman S, Clifton DR, Morrel J, Brown G, Rodriguez RJ. (1999b). Biochemical analysis of plant protection afforded by a non-pathogenic endophytic mutant of *Colletotrichum magna*. *Plant Physiology* 119: 795-804.

Redman RS, Ranson JC, Rodriguez RJ. (1999c). Conversion of the pathogenic fungus *Colletotrichum magna* to a non-pathogenic, endophytic mutualist by gene disruption. *Molecular Plant-Microbe Interactions* 12: 969-975.

Redman RS, Dunigan DD, Rodriguez RJ. (2001). Fungal symbiosis from mutualism to parasitism: who controls the outcome, host or invader? *New Phytologist* 151: 705-716.

Redman RS, Sheehan KB, Stout RG, Rodriguez RJ, Henson JM. (2002). Thermotolerance generates by plant/fungal symbiosis. *Science* 298: 1581.

Reffner JA. (1998). Instrumental factors in infrared microspectroscopy. *Cellular and Molecular Biology* 44: 1-7.

Rodriguez RJ. (1993). Polyphosphate present in DNA preparations from filamentous fungal species of Colletotrichum inhibits restriction endonucleases and other enzymes. *Analytical Biochemistry* 209: 291-297.

Rodriguez RJ, Redman RS, Henson JM. (2004). The role of fungal symbioses in the adaptation of plants to high stress environments. *Mitigation and Adaptation Strategies for Global Change* 9: 261-272.

Rodriguez RJ, Redman RS, Henson JM. (2005). Symbiotic lifestyle expression by fungal endophytes and the adaptation of plants to stress: Unraveling the complexities of intimacy. In J Dighton, JF White Jr., P Oudemans (Eds.), *The Fungal Community: Its Organization and Role in the Ecosystem* (pp. 683-695). Boca Raton, USA: Taylor and Francis Group.

Rodriguez RJ, Henson J, Van Volkenburgh E, Hoy M, Wright L, Beckwith F, Kim Y-O, Redman RS. (2008). Stress tolerance in plants via habitat-adapted symbiosis. *The ISME Journal* 2: 404-416.

Rodriguez R, Redman R. (2008). More than 400 million years of evolution and some plants still can't make it on their own: plant stress tolerance via fungal symbiosis. *Journal of Experimental Botany* 59: 1109-1114.

Rodriguez RJ, White JF, Arnold AE, Redman RS. (2009). Fungal endophytes: diversity and functional roles. *New Phytologist* 182: 314-330.

Rodriguez RJ. (2009). Private communication.

Romeo MJ, Diem M. (2005a). Infrared spectral imaging of lymph nodes: Strategies for analysis and artefact reduction. *Vibrational Spectroscopy* 38: 115-119.

Romeo M, Diem M. (2005b). Correction of dispersive line shape artefact observed in diffuse reflection infrared spectroscopy and absorption/reflection (transflection) infrared micro-spectroscopy. *Vibrational Spectroscopy* 38: 129-132.

Romeo M, Mohlenhoff B, Diem M. (2006). Infrared micro-spectroscopy of human cells: Causes for the spectral variance of oral mucosa (buccal) cells. *Vibrational Spectroscopy* 42: 9-14.

Rösch P, Harz M, Schmitt M, Popp J. (2005). Raman spectroscopic identification of single yeast cells. *Journal of Raman Spectroscopy* 36: 377-379.

Rösch P, Harz M, Peschke K-D, Ronneberger O, Burkhardt H, Popp J. (2006). Identification of single eukaryotic cells with micro-Raman spectroscopy. *Biopolymers* 82: 312-316.

Ruijter GJG, Bax M, P H, Flitter SJ, van de Vondervoort PJI, de Vries RP, vanKuyk PA, Visser J. (2003). Mannitol is required for stress tolerance in *Aspergillus niger* conidiospores. *Eukaryotic Cell* 2: 690-698.

Sampson K, Lew RR, Heath IB. (2003). Time series analysis demonstrates the absence of pulsatile hyphal growth. *Microbiology* 149: 3111-3119.

Sharma VK, Kalonia DS. (2004). Effect of vacuum drying on protein-mannitol interactions: The physical state of mannitol and protein structure in the dried state. *AAPS PharmSciTech* 5: 1-12.

Smith TI. (2002). The source issue in infrared microspectroscopy. *Nuclear Instruments and Methods in Physics Research A* 483: 565-570.

Solomon PS, Waters ODC, Oliver RP. (2007). Decoding the mannitol enigma in filamentous fungi. *TRENDS in Microbiology* 15: 257-262.

Stone JK, Polishook JD, White JRJ. (2004) Endophytic fungi. In G Mueller, GF Bills, MS Foster (Eds.), *Biodiversity of Fungi: Inventory and Monitoring Methods* (pp. 42-64). Amsterdam; Boston: Elsevier Academic Press.

Szeghalmi A, Kaminskyj S, Gough KM. (2007a). A synchrotron FTIR microspectroscopy investigation of fungal hyphae grown under optimal and stressed conditions. *Analytical and Bioanalytical Chemistry* 387: 1779-1789.

Szeghalmi A, Kaminskyj S, Rösch P, Popp J, Gough KM. (2007b). Time fluctuations and imaging in the SERS spectra of fungal hypha grown on nanostructured substrates. *Journal of Physical Chemistry B* 111: 12916-12924.

Toubas D, Essendoubi M, Adt I, Pinon JM, Manfait M, Sockalingum GD. (2007). FTIR spectroscopy in medical mycology: Applications to the differentiation and typing of Candida. *Analytical and Bioanalytical Chemistry* 387: 1729-1737.

Witteveen CFB, Visser J. (1995). Polyol pools in *Aspergillus niger*. *FEMS Microbiology Letters* 134: 57-62.

Wood BR, Quinn MA, Tait B, Ashdown M, Hislop T, Romeo M, McNaughton D. (1998). FTIR microspectroscopic study of cell types and potential confounding variables in screening for cervical malignancies. *Biospectroscopy* 4: 75-91.

Yang Y, Sulé-Suso J, Sockalingum GD, Kegelaer G, Manfait M, El Haj AJ. (2005). Study of tumor cell invasion by Fourier transform infrared microspectroscopy. *Biopolymers* 78: 311-317.

Yoshinari T, Forbes RT, York P, Kawashima Y. (2002). Moisture induced polymorphic transition of mannitol and its morphological transformation. *International Journal of Pharmaceutics* 247: 69-77.

Zhang HW, Song YC, Tan RX. (2006). Biology and chemistry of endophytes. *Natural Product Reports* 23: 753-771.

Zotti M, Ferroni A, Calvini P. (2008). Microfungal biodeterioration of historic paper: Preliminary FTIR and microbiological analyses. *International Biodeterioration & Biodegradation* 62: 186-194.

Appendix I: Synchrotron FTIR Spectra

Spectra are displayed in the following order (on the same scale and offset) unless otherwise indicated:

When 3 spectra present: tip, 50 μm, 100 μm (bottom to top)

When 4 spectra are present: tip, 30 μm, 50 μm, 100um (bottom to top)

When 5 spectra are present: tip, 30 μm, 50 μm, 100 μm, 150 μm (bottom to top)

CLS December 2007

Slide #34 CpATCC 100% PDA

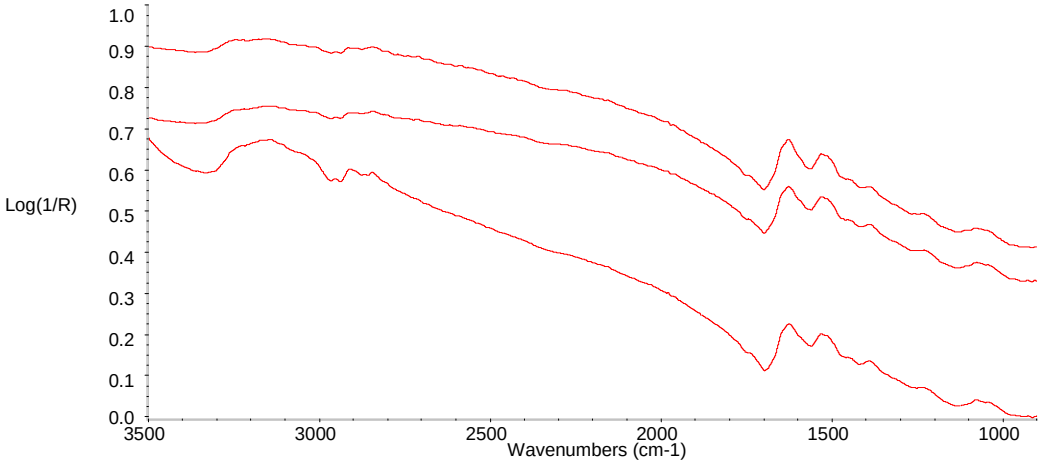

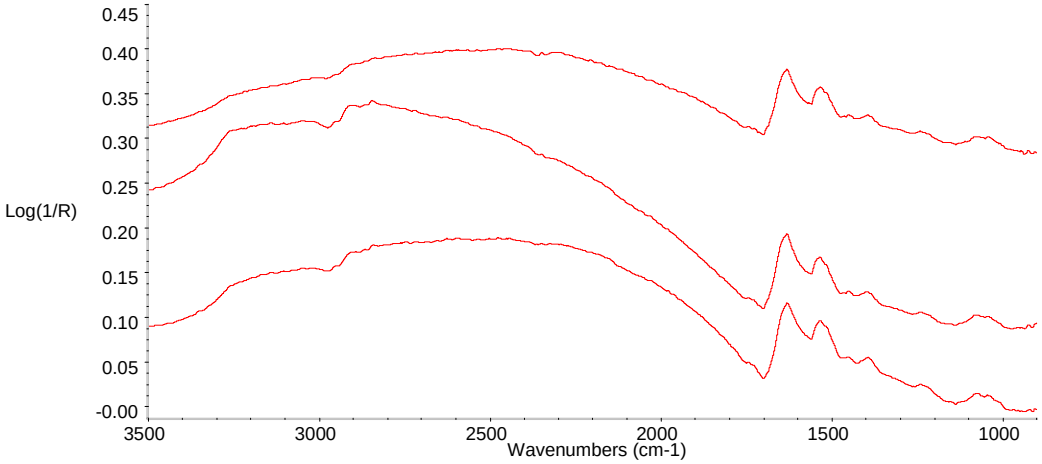
0.45
0.40
0.35
0.30
0.25
0.20
0.15
0.10
0.05
-0.00
Log(1/R)
3500
3000
2500
2000
1500
1000
Wavenumbers (cm-1)

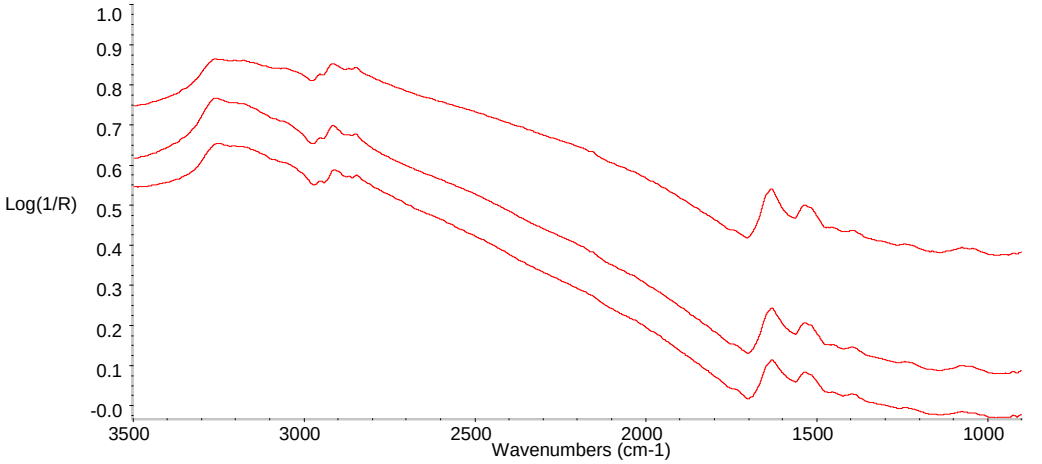
1.0
0.9
0.8
0.7
0.6
0.5
0.4
0.3
0.2
0.1
-0.0
Log(1/R)
3500
3000
2500
2000
1500
1000
Wavenumbers (cm-1)

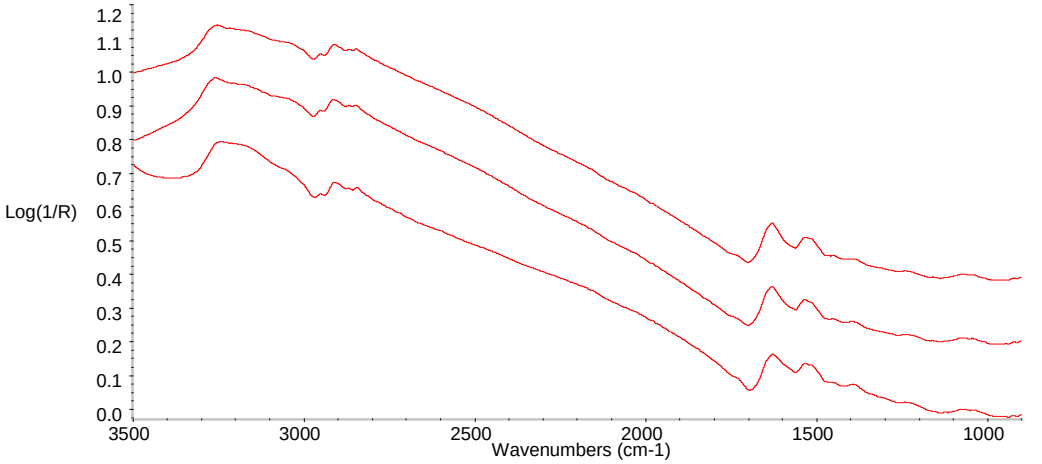
1.2
1.1
1.0
0.9
0.8
0.7
0.6
0.5
0.4
0.3
0.2
0.1
0.0
Log(1/R)
3500
3000
2500
2000
1500
1000
Wavenumbers (cm-1)

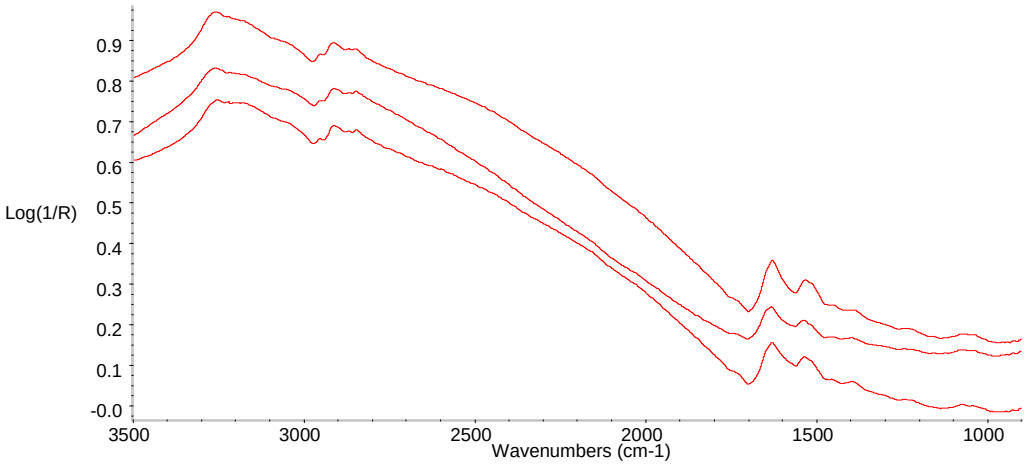

Slide #34 CpATCC 10% PDA

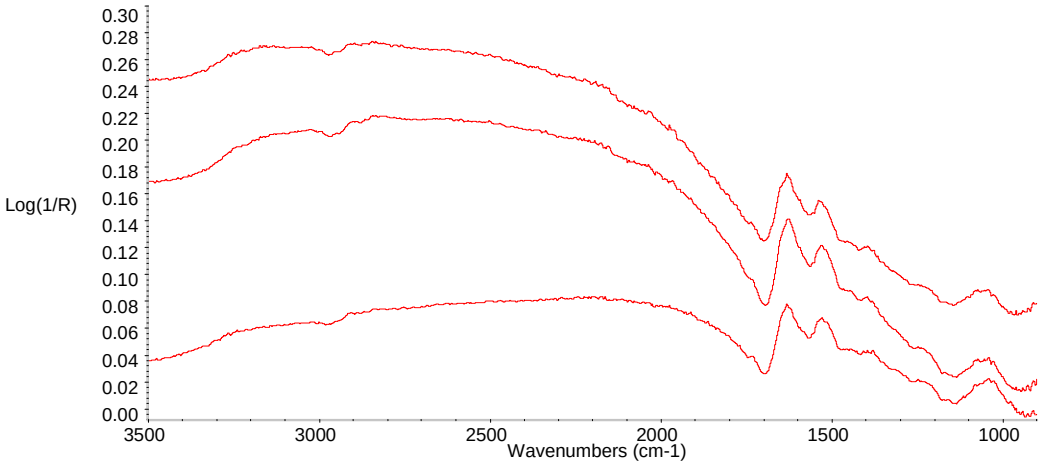

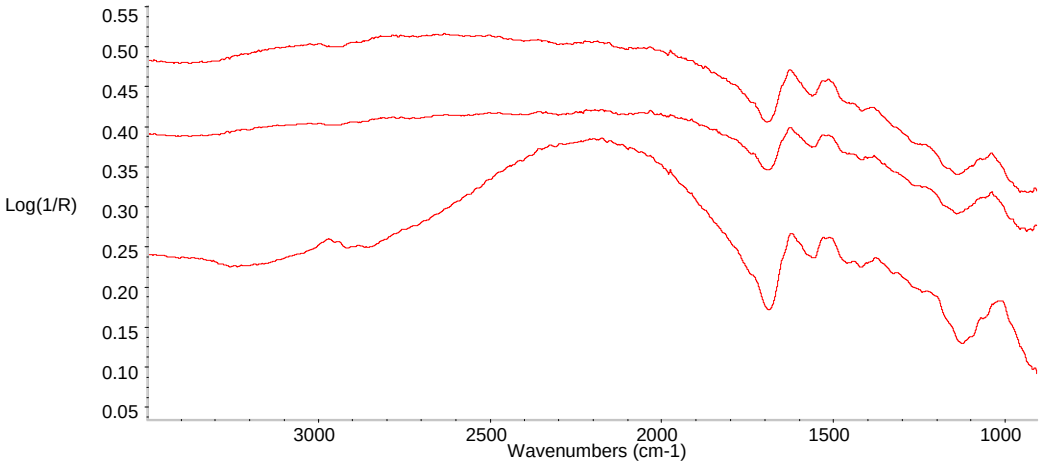

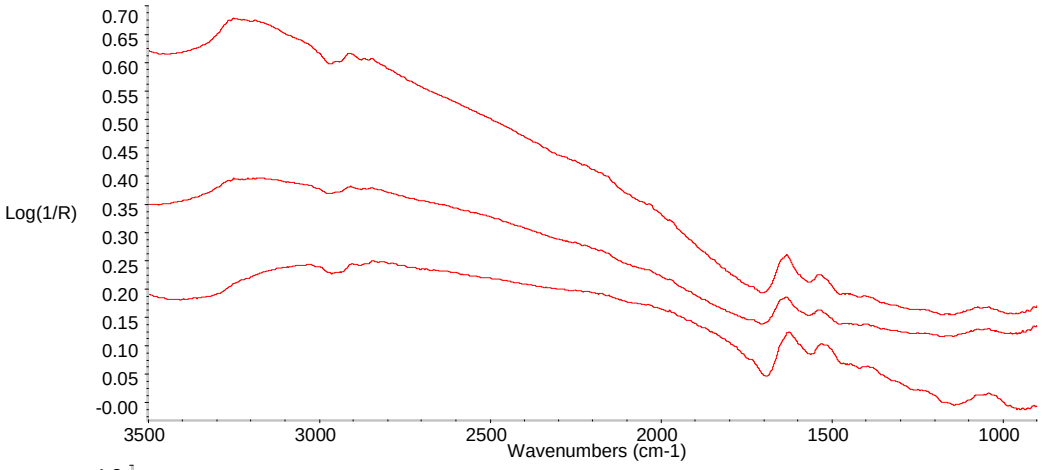
Log(1/R)
0.70
0.65
0.60
0.55
0.50
0.45
0.40
0.35
0.30
0.25
0.20
0.15
0.10
0.05
-0.00
3500
3000
2500
2000
1500
1000
Wavenumbers (cm-1)

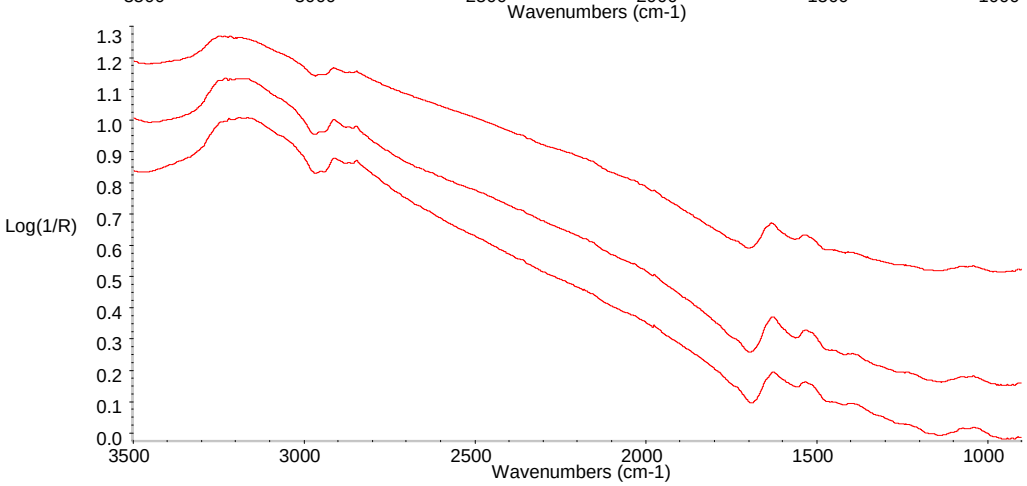
Log(1/R)
1.3
1.2
1.1
1.0
0.9
0.8
0.7
0.6
0.5
0.4
0.3
0.2
0.1
0.0
3500
3000
2500
2000
1500
1000
Wavenumbers (cm-1)

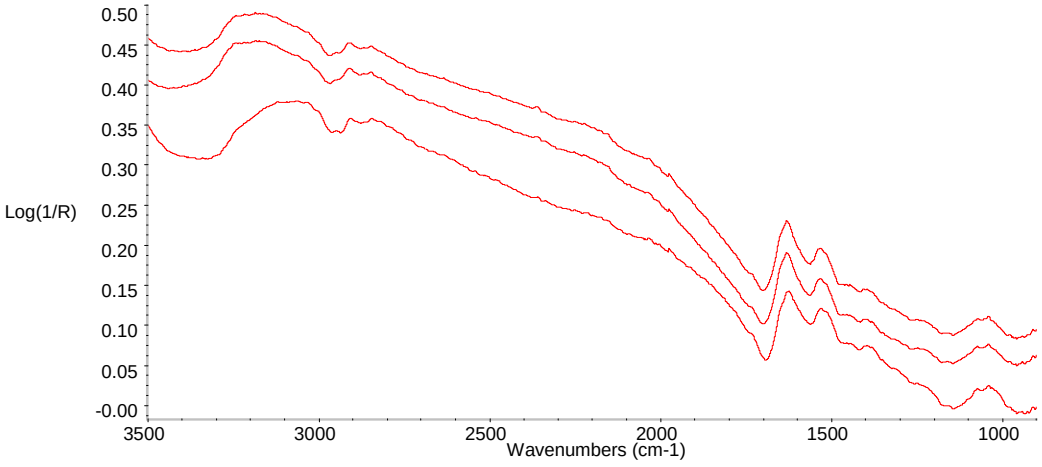
Log(1/R)
0.50
0.45
0.40
0.35
0.30
0.25
0.20
0.15
0.10
0.05
-0.00
3500
3000
2500
2000
1500
1000
Wavenumbers (cm-1)

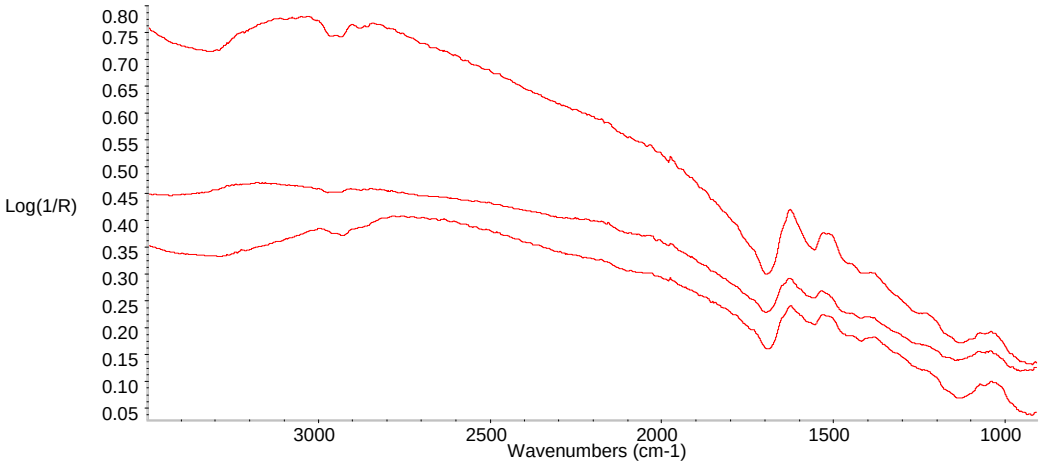

Slide # 37 Cp4666D 100% PDA

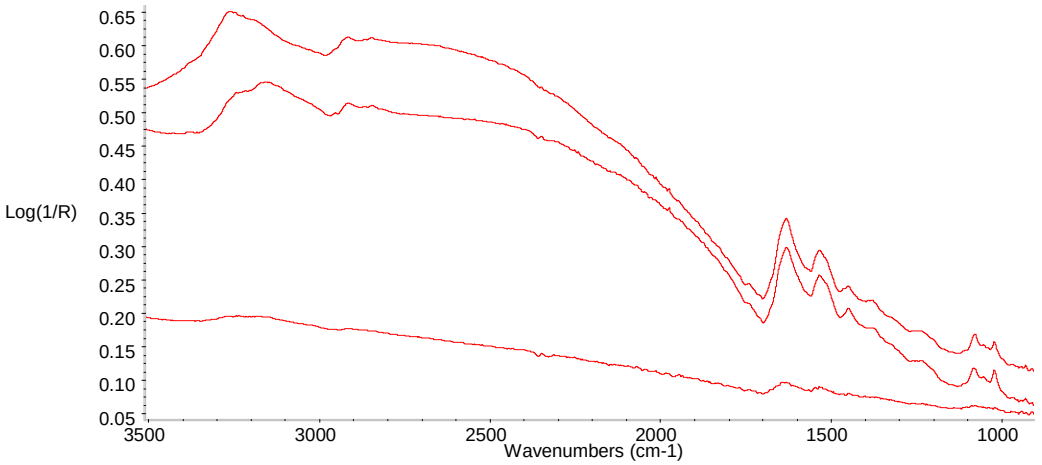

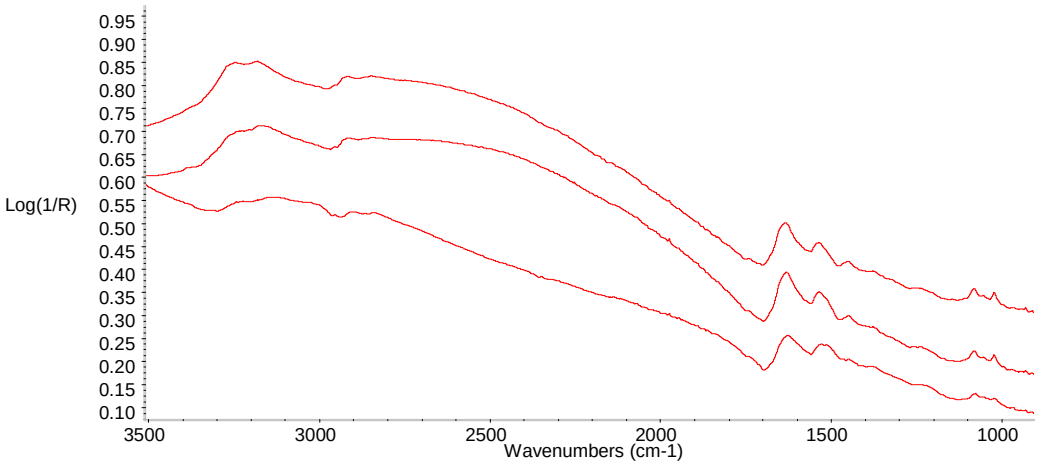

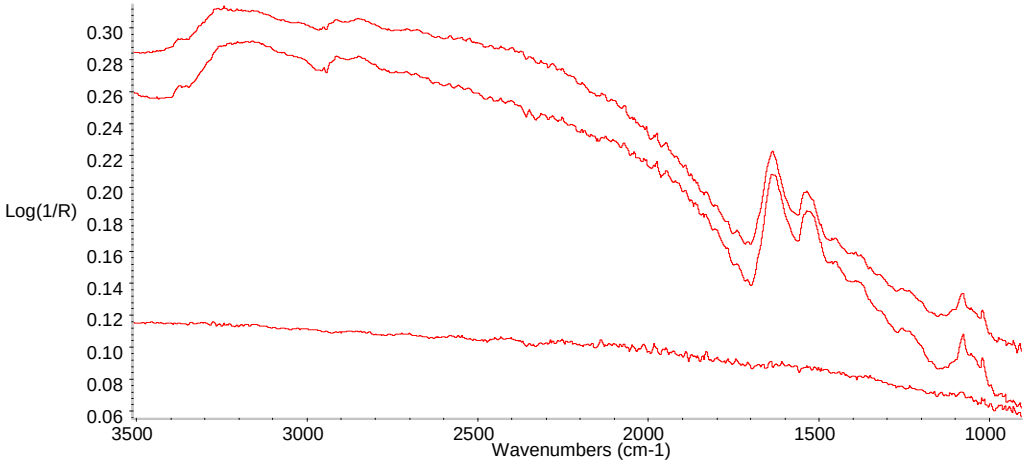

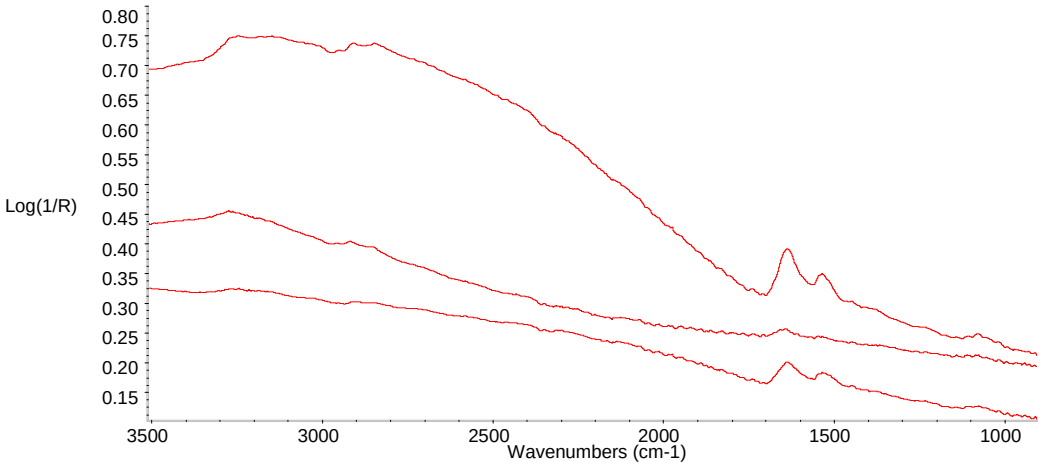

Slide #37 Cp4666D 10% PDA

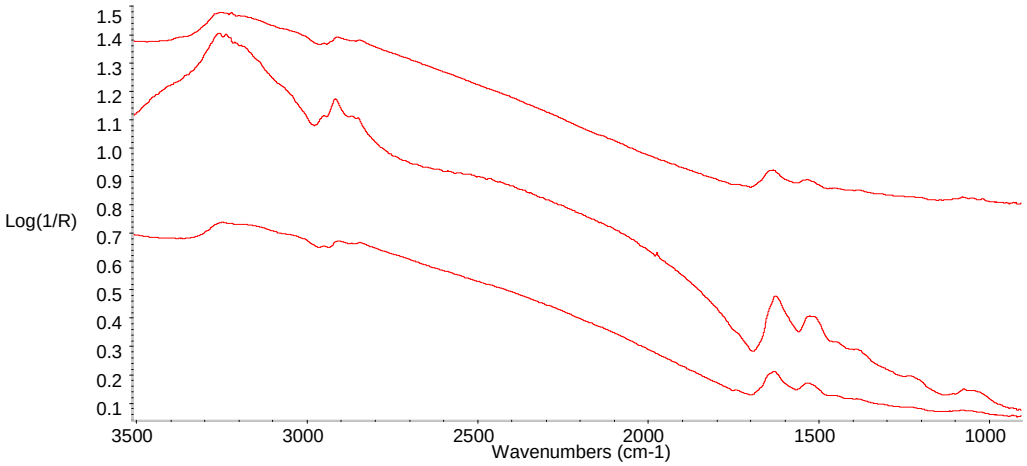

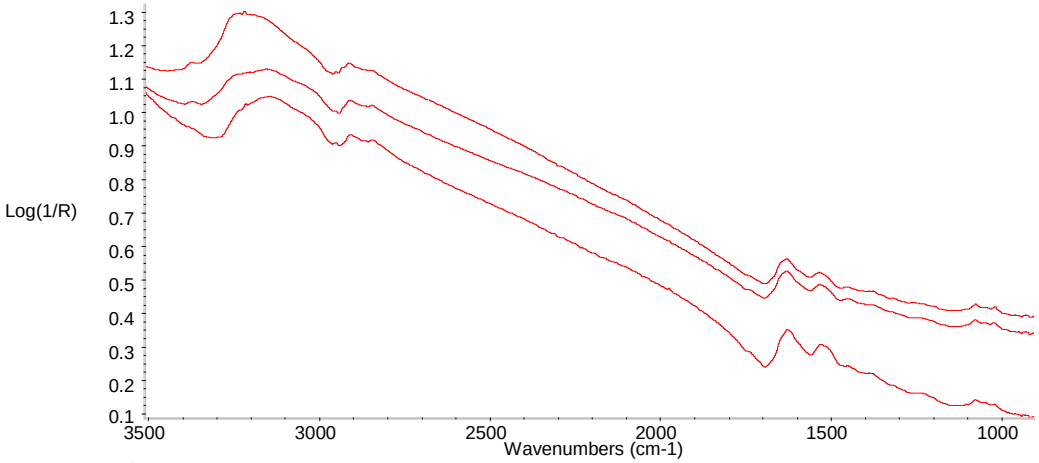
Log(1/R)
1.3
1.2
1.1
1.0
0.9
0.8
0.7
0.6
0.5
0.4
0.3
0.2
0.1
3500
3000
2500
2000
1500
1000
Wavenumbers (cm-1)

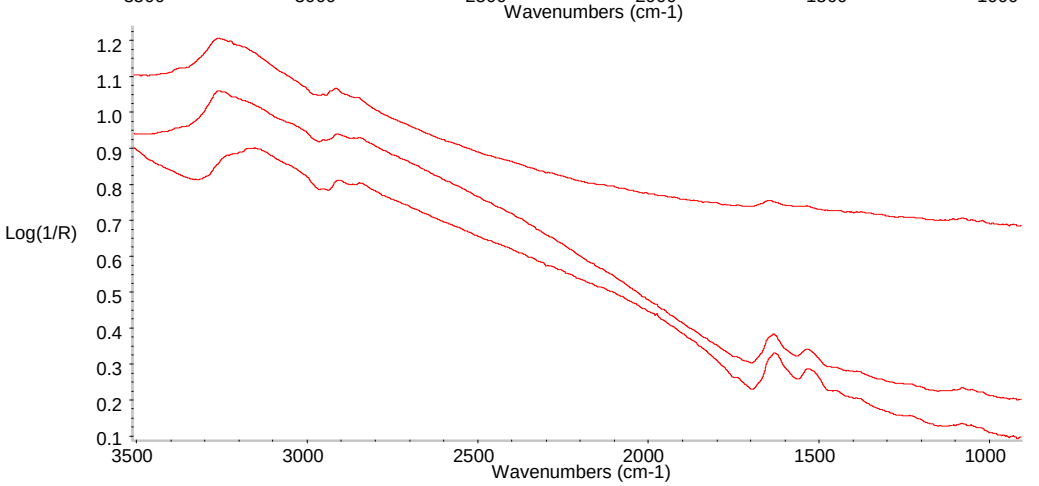
Log(1/R)
1.2
1.1
1.0
0.9
0.8
0.7
0.6
0.5
0.4
0.3
0.2
0.1
3500
3000
2500
2000
1500
1000
Wavenumbers (cm-1)

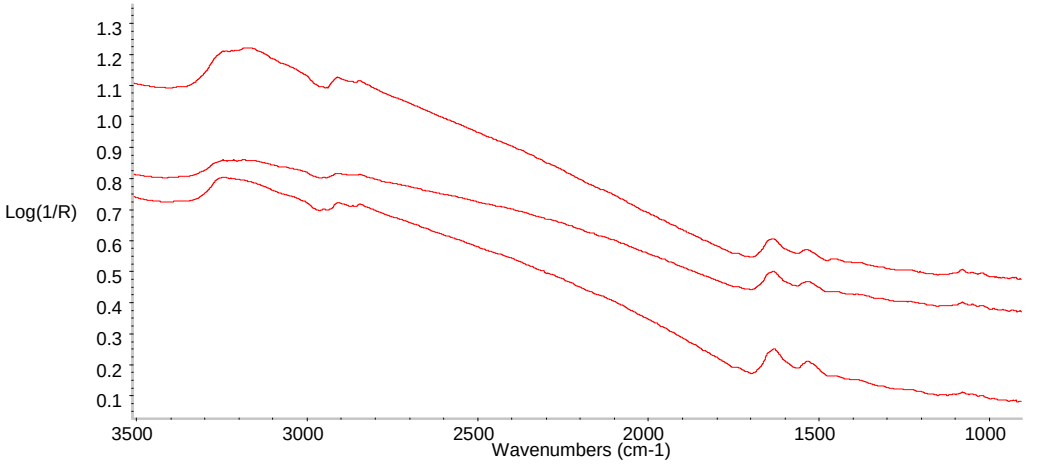
Log(1/R)
1.3
1.2
1.1
1.0
0.9
0.8
0.7
0.6
0.5
0.4
0.3
0.2
0.1
3500
3000
2500
2000
1500
1000
Wavenumbers (cm-1)

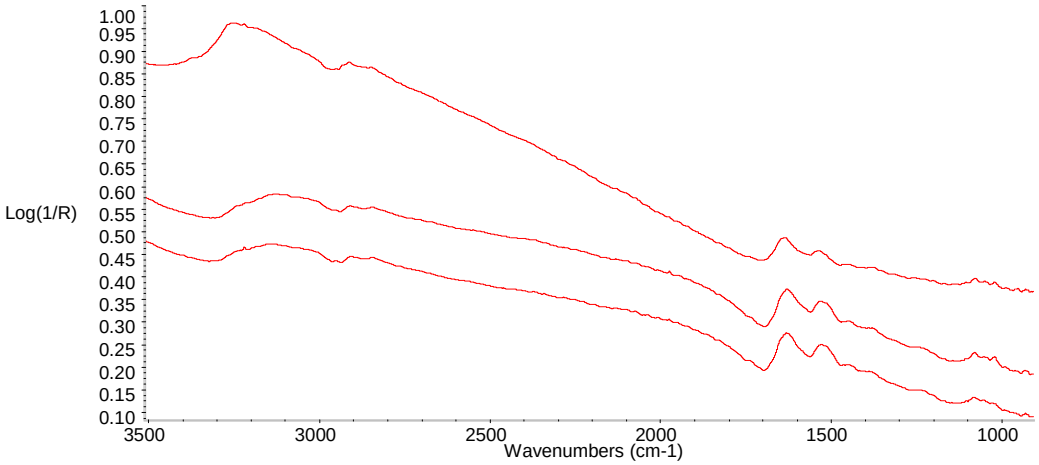

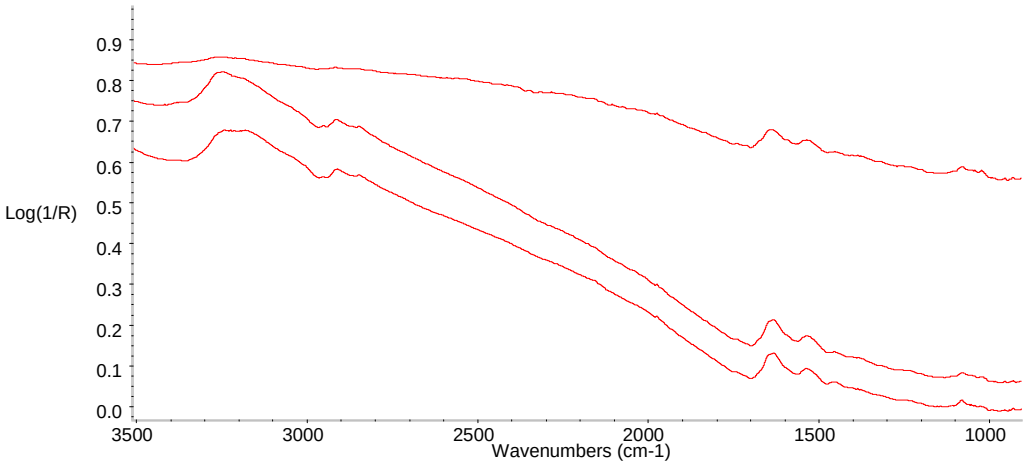

Slide # 38 Fc18 100% PDA

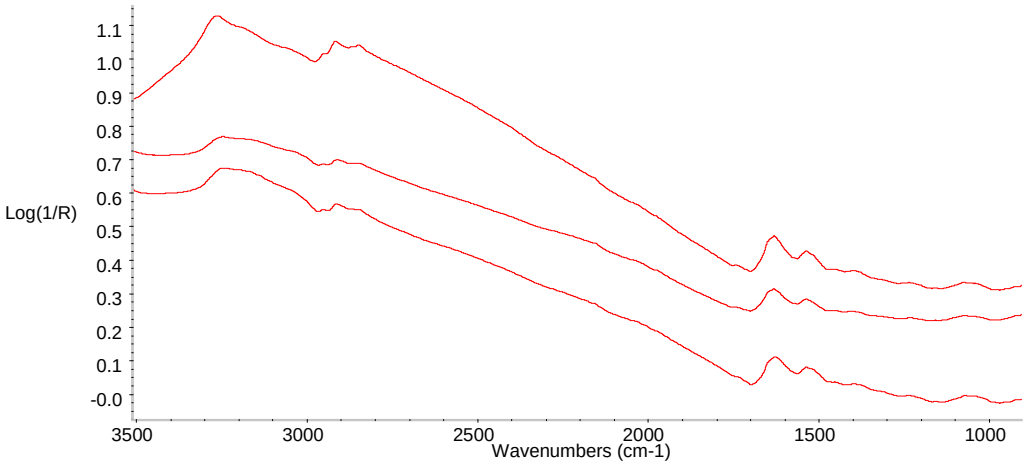

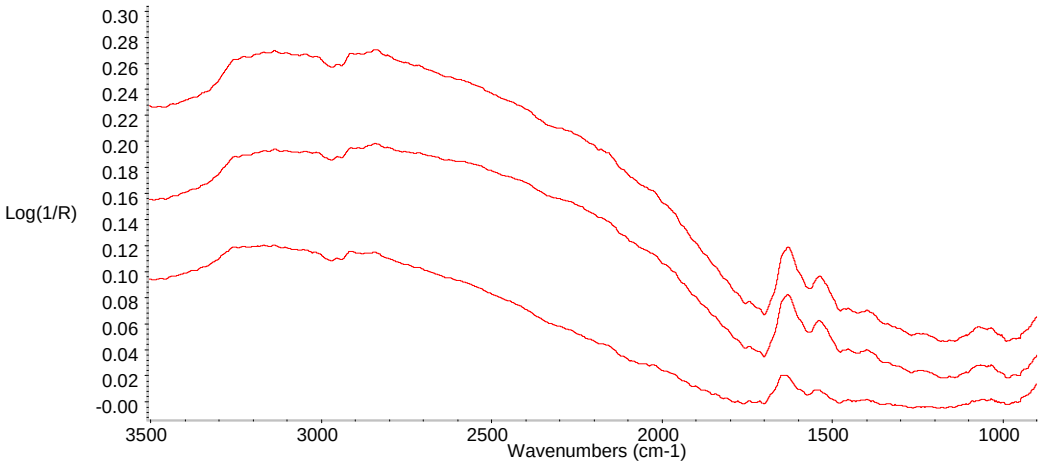
Log(1/R)
0.30
0.28
0.26
0.24
0.22
0.20
0.18
0.16
0.14
0.12
0.10
0.08
0.06
0.04
0.02
-0.00
3500
3000
2500
2000
1500
1000
Wavenumbers (cm-1)

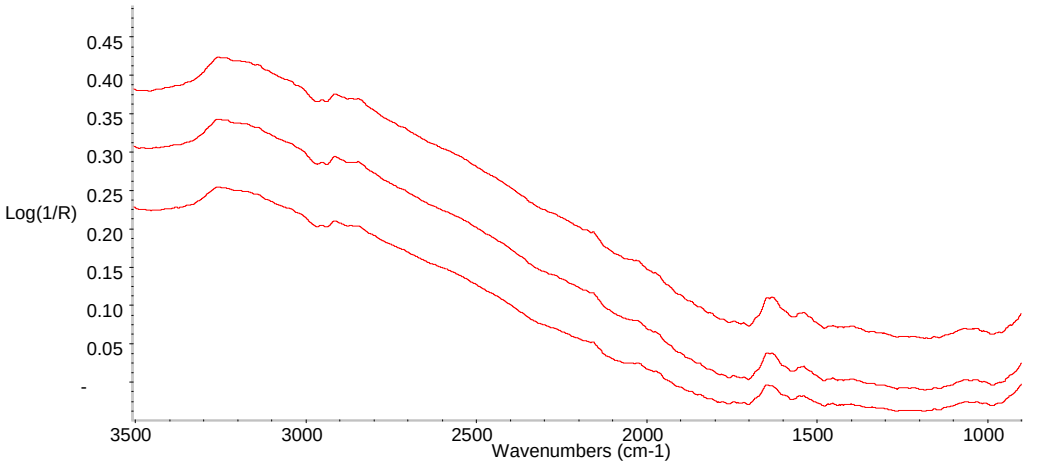
Log(1/R)
0.45
0.40
0.35
0.30
0.25
0.20
0.15
0.10
0.05
-
3500
3000
2500
2000
1500
1000
Wavenumbers (cm-1)

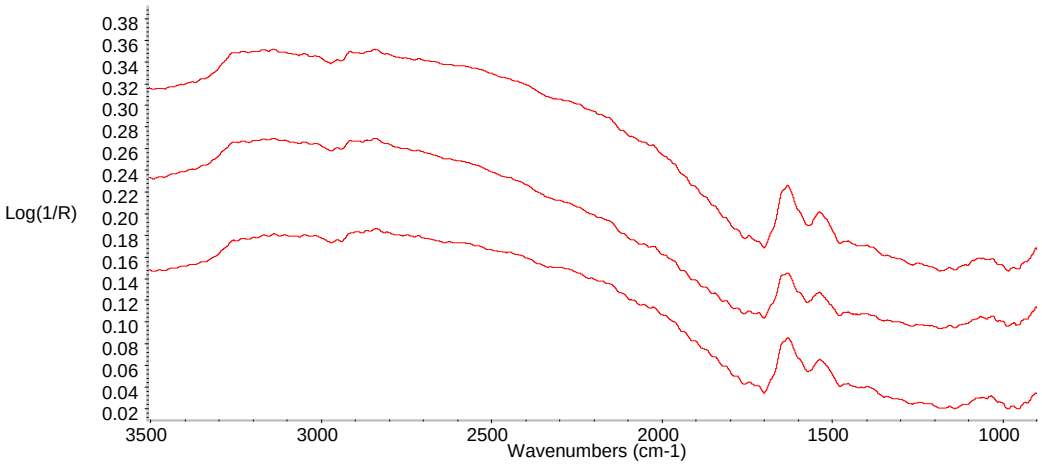
Log(1/R)
0.38
0.36
0.34
0.32
0.30
0.28
0.26
0.24
0.22
0.20
0.18
0.16
0.14
0.12
0.10
0.08
0.06
0.04
0.02
3500
3000
2500
2000
1500
1000
Wavenumbers (cm-1)

Slide #38 Fc18 10% PDA

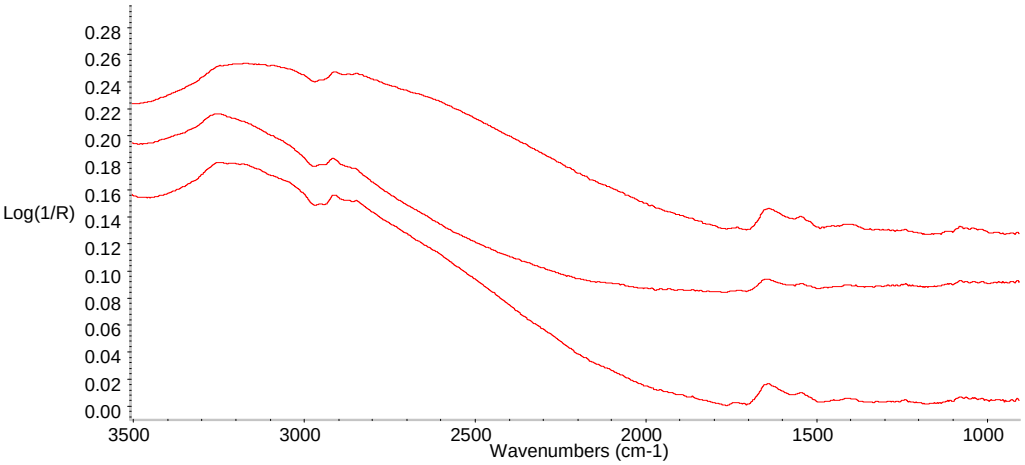

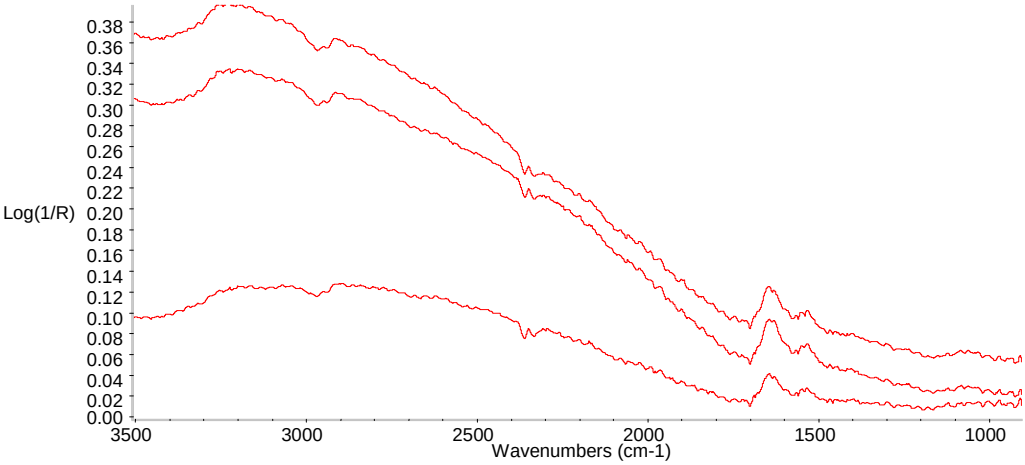

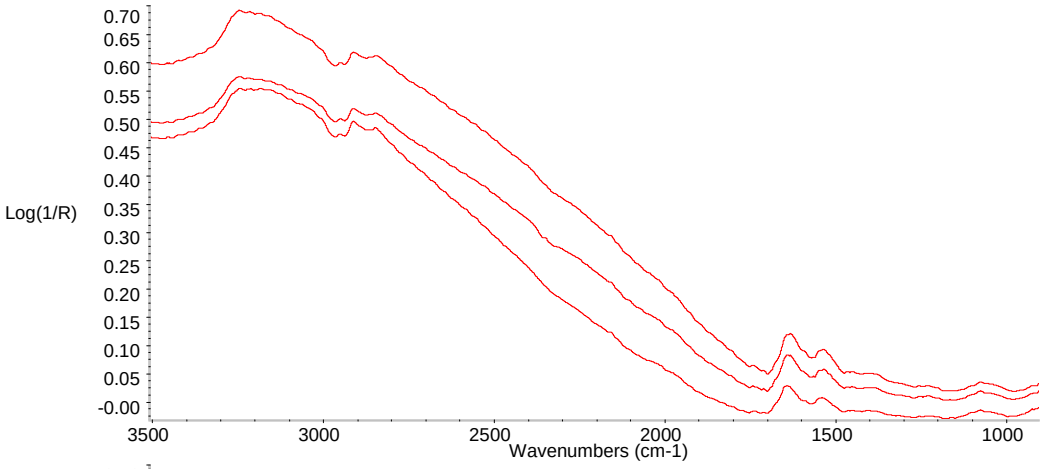

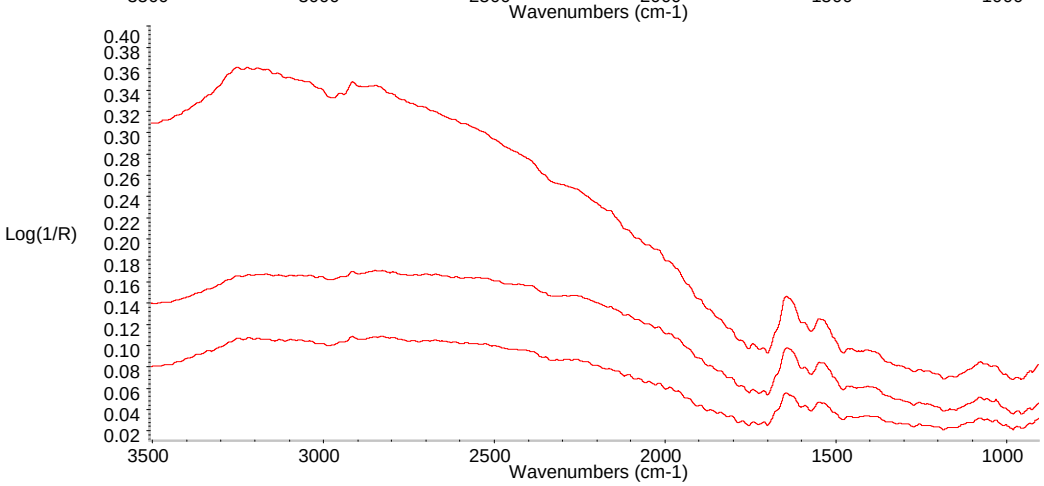

Slide #38 FcRed1 100% PDA

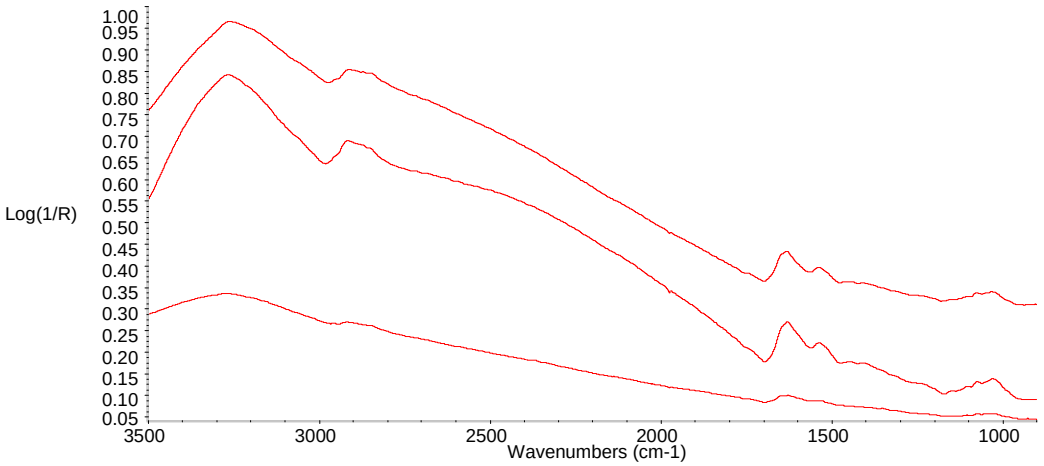

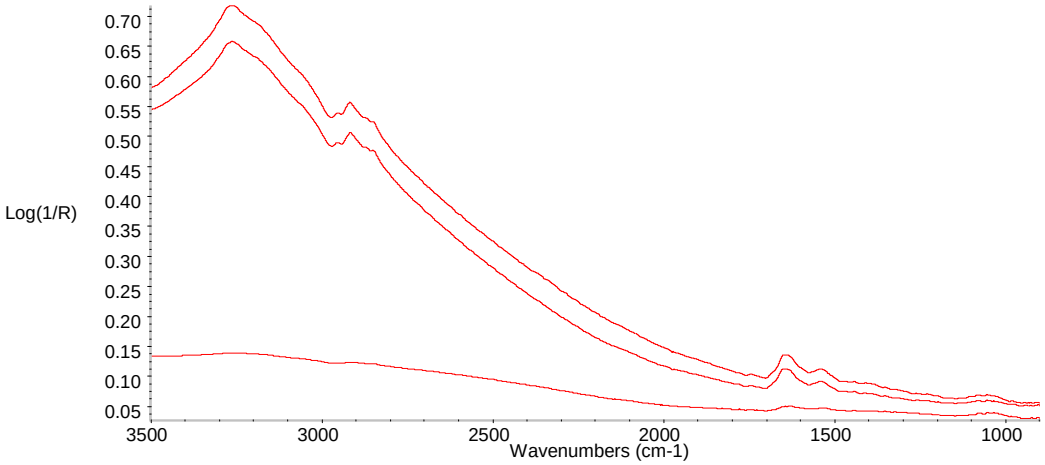
Log(1/R)
0.70
0.65
0.60
0.55
0.50
0.45
0.40
0.35
0.30
0.25
0.20
0.15
0.10
0.05
3500
3000
2500
2000
1500
1000
Wavenumbers (cm-1)


Log(1/R)
0.80
0.75
0.70
0.65
0.60
0.55
0.50
0.45
0.40
0.35
0.30
0.25
0.20
0.15
0.10
0.05
3500
3000
2500
2000
1500
1000
Wavenumbers (cm-1)

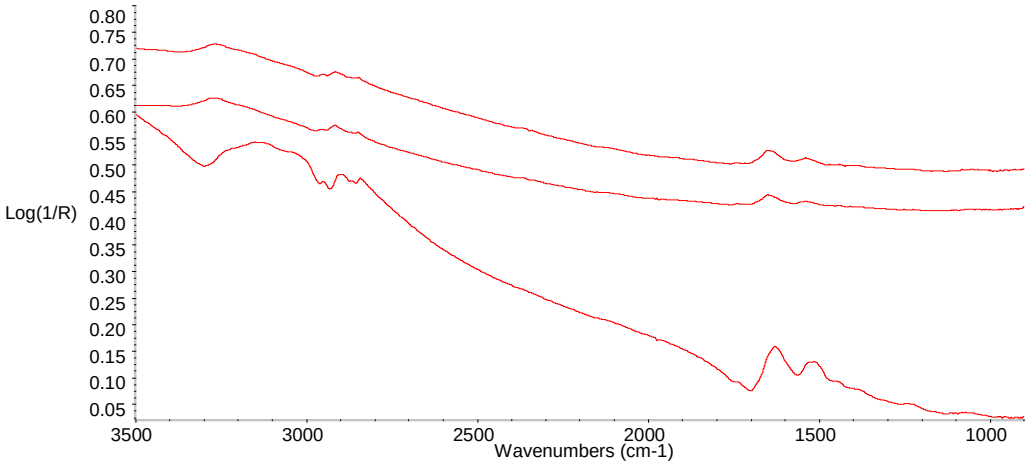
Log(1/R)
0.80
0.75
0.70
0.65
0.60
0.55
0.50
0.45
0.40
0.35
0.30
0.25
0.20
0.15
0.10
0.05
3500
3000
2500
2000
1500
1000
Wavenumbers (cm-1)

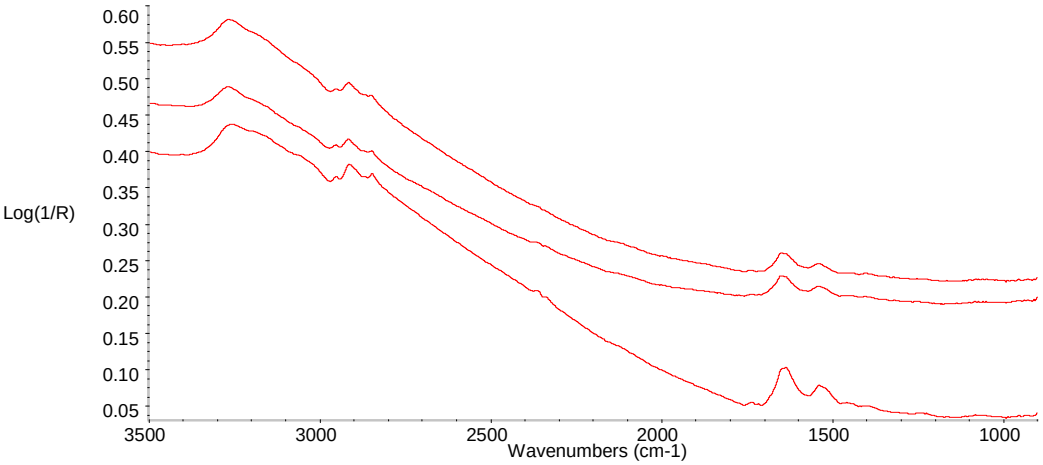

Slide #38 FcRed1 10% PDA

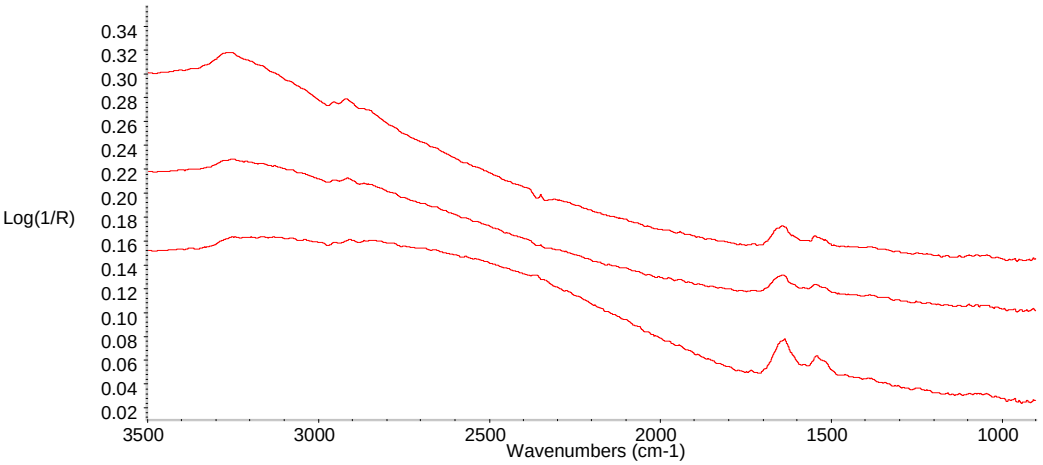

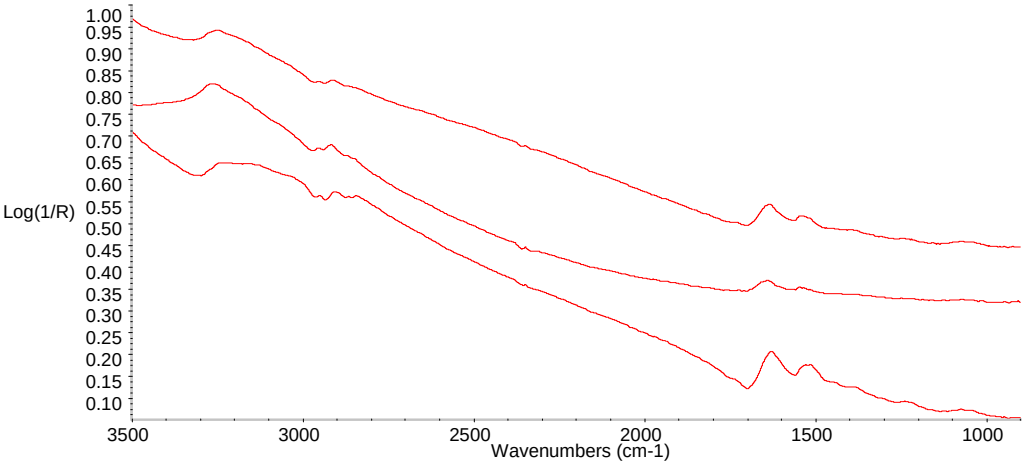

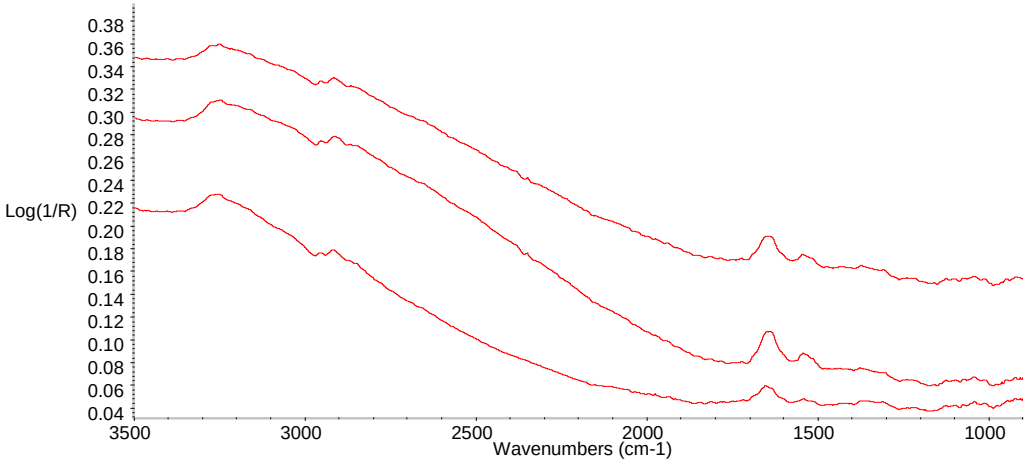

Slide #37L2.5 100% PDA

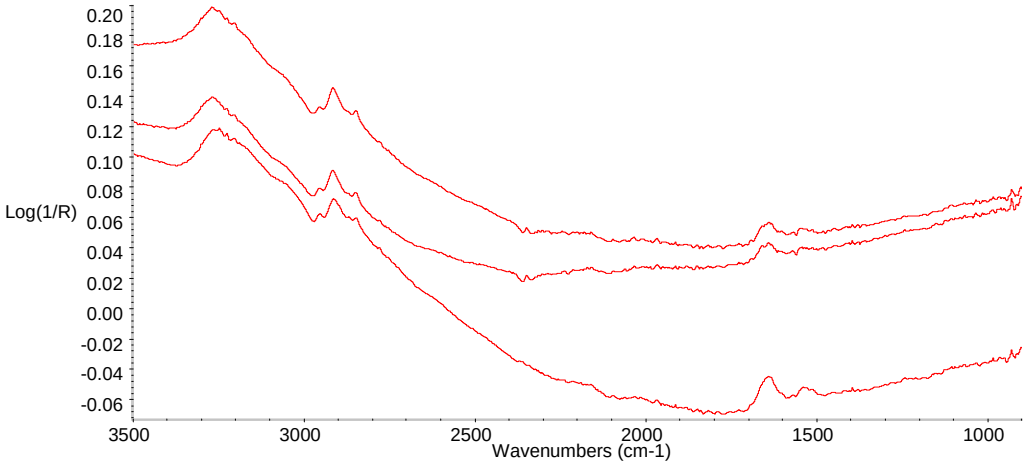

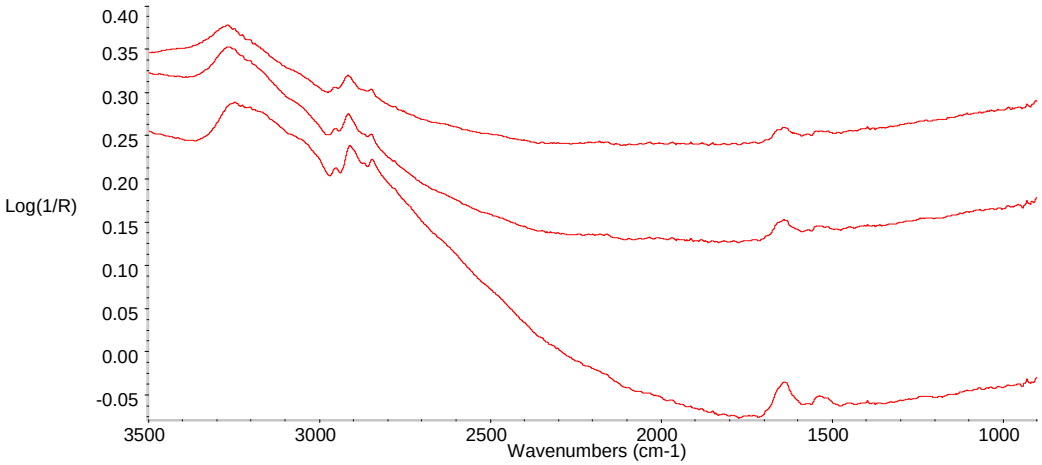
Log(1/R)
0.40
0.35
0.30
0.25
0.20
0.15
0.10
0.05
0.00
-0.05
3500
3000
2500
2000
1500
1000
Wavenumbers (cm-1)

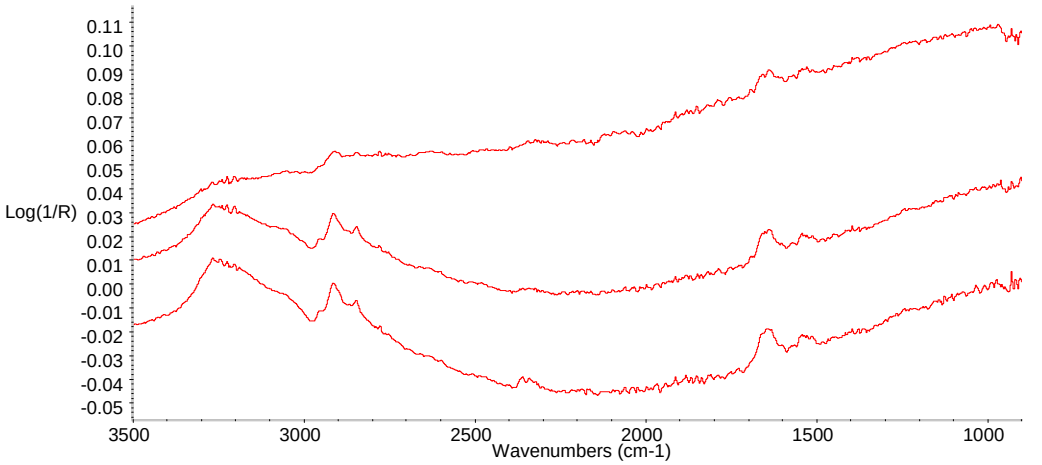
Log(1/R)
0.11
0.10
0.09
0.08
0.07
0.06
0.05
0.04
0.03
0.02
0.01
0.00
-0.01
-0.02
-0.03
-0.04
-0.05
3500
3000
2500
2000
1500
1000
Wavenumbers (cm-1)

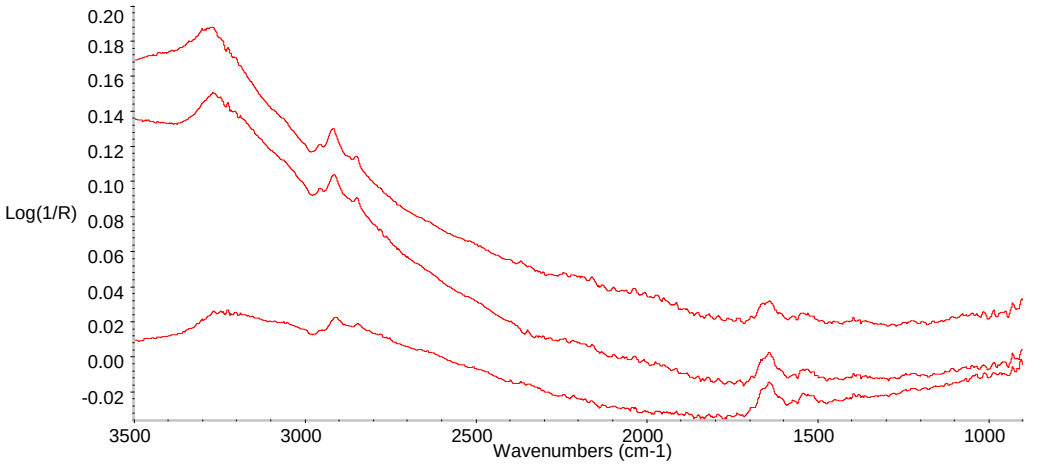
Log(1/R)
0.20
0.18
0.16
0.14
0.12
0.10
0.08
0.06
0.04
0.02
0.00
-0.02
3500
3000
2500
2000
1500
1000
Wavenumbers (cm-1)

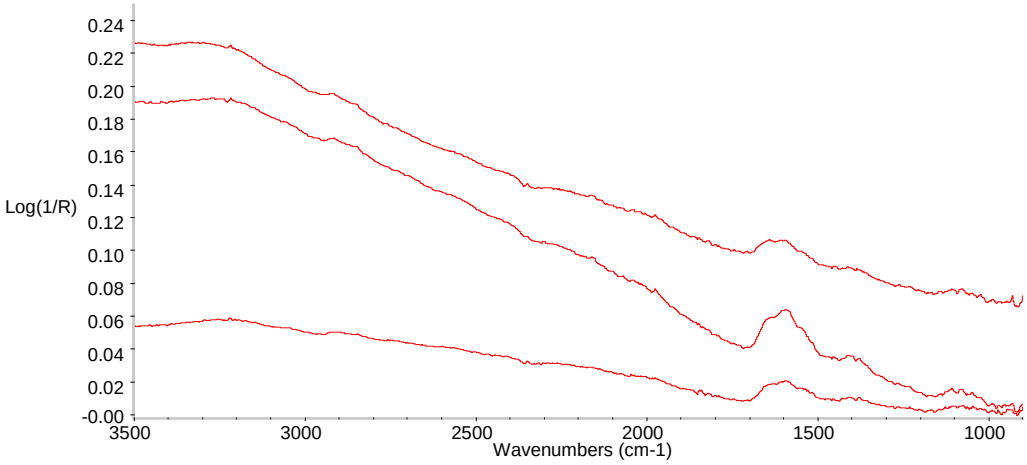
Log(1/R)
0.24
0.22
0.20
0.18
0.16
0.14
0.12
0.10
0.08
0.06
0.04
0.02
-0.00
3500
3000
2500
2000
1500
1000
Wavenumbers (cm-1)


Log(1/R)
0.75
0.70
0.65
0.60
0.55
0.50
0.45
0.40
0.35
0.30
0.25
0.20
0.15
0.10
0.05
0.00
-0.05
-0.10
3500
3000
2500
2000
1500
1000
Wavenumbers (cm-1)


Log(1/R)
0.28
0.26
0.24
0.22
0.20
0.18
0.16
0.14
0.12
0.10
0.08
0.06
0.04
3500
3000
2500
2000
1500
1000
Wavenumbers (cm-1)

Slide #34 CmPath 100% PDA

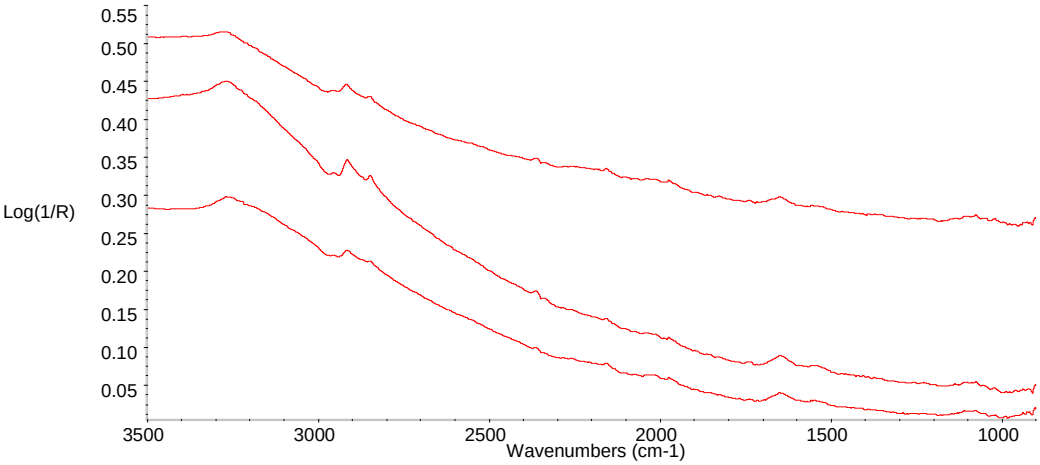

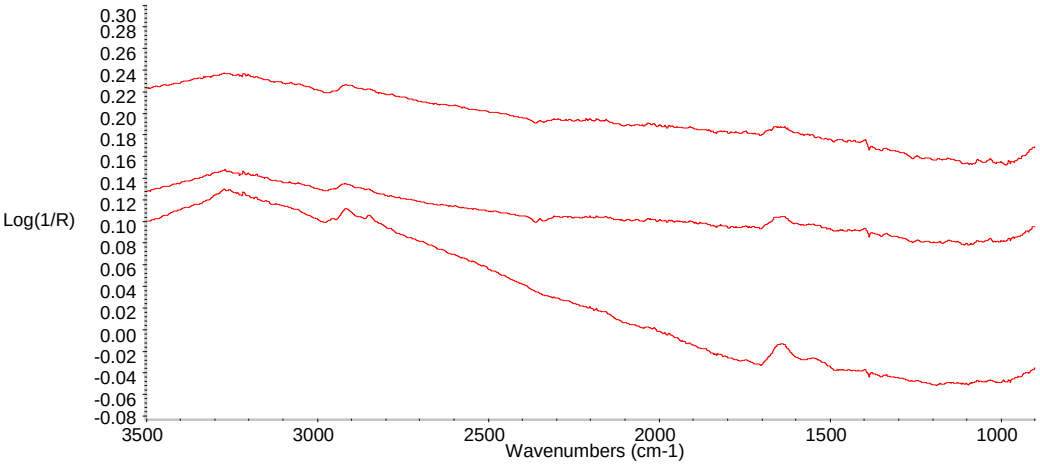

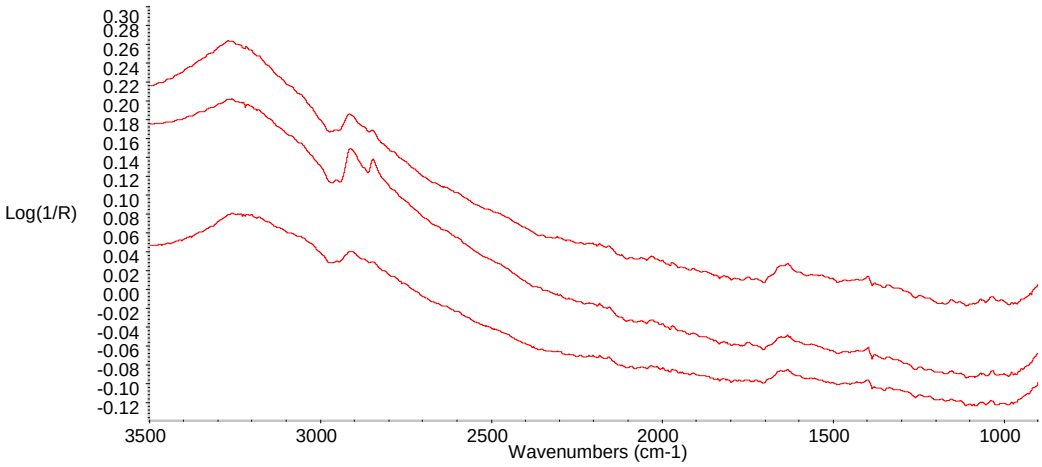
Log(1/R)
0.30
0.28
0.26
0.24
0.22
0.20
0.18
0.16
0.14
0.12
0.10
0.08
0.06
0.04
0.02
0.00
-0.02
-0.04
-0.06
-0.08
-0.10
-0.12
3500
3000
2500
2000
1500
1000
Wavenumbers (cm-1)

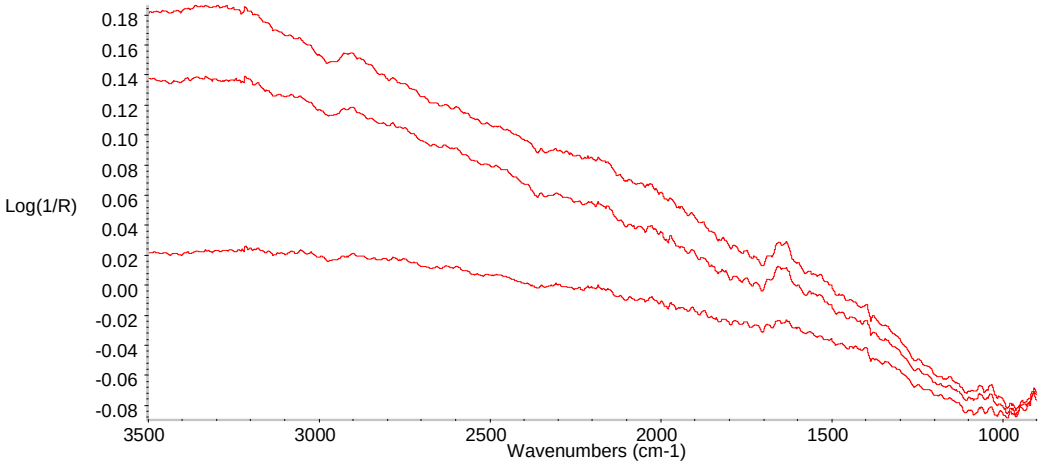
Log(1/R)
0.18
0.16
0.14
0.12
0.10
0.08
0.06
0.04
0.02
0.00
-0.02
-0.04
-0.06
-0.08
3500
3000
2500
2000
1500
1000
Wavenumbers (cm-1)

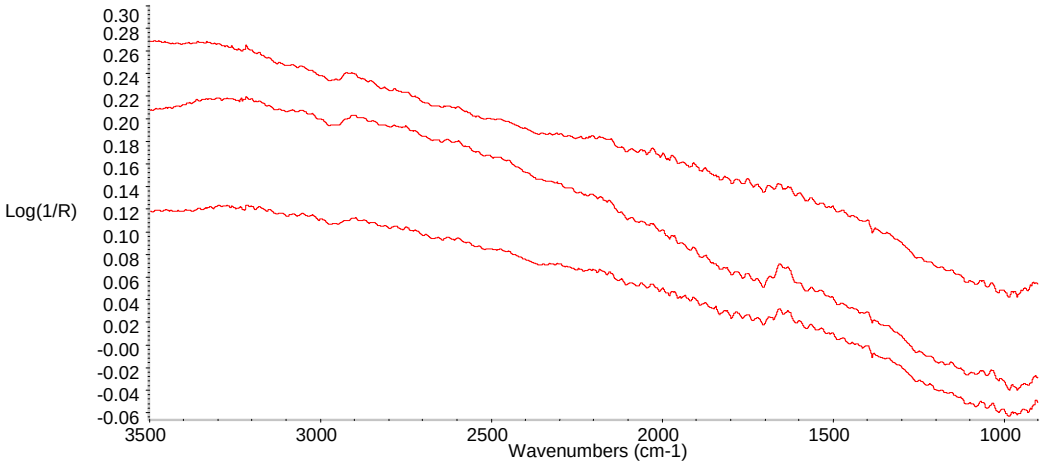
Log(1/R)
0.30
0.28
0.26
0.24
0.22
0.20
0.18
0.16
0.14
0.12
0.10
0.08
0.06
0.04
0.02
0.00
-0.02
-0.04
-0.06
3500
3000
2500
2000
1500
1000
Wavenumbers (cm-1)

SRC April 2008

Slide #34 CpATCC 100% PDA

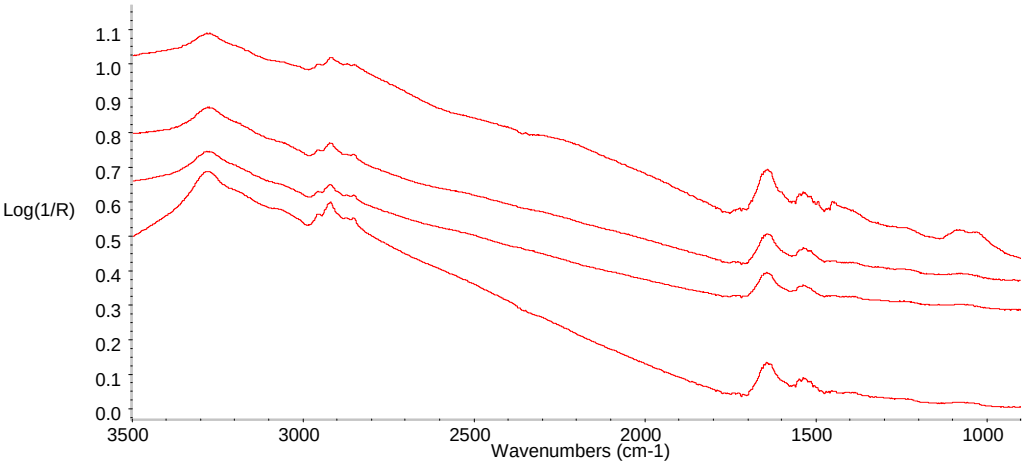

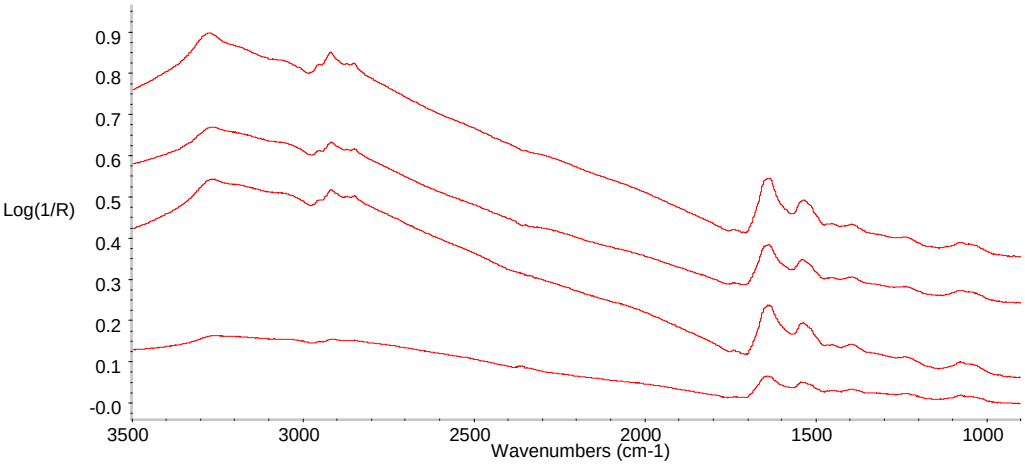

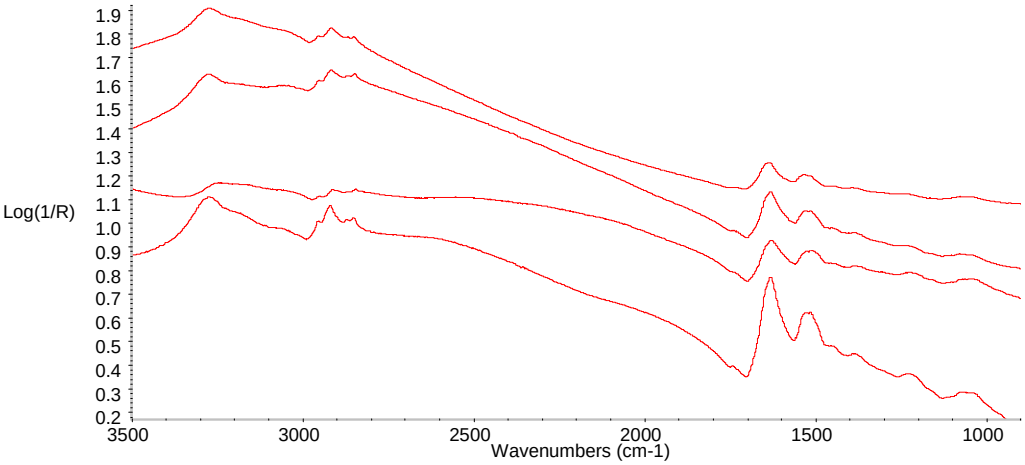

Slide #34 CpATCC 100% PDA

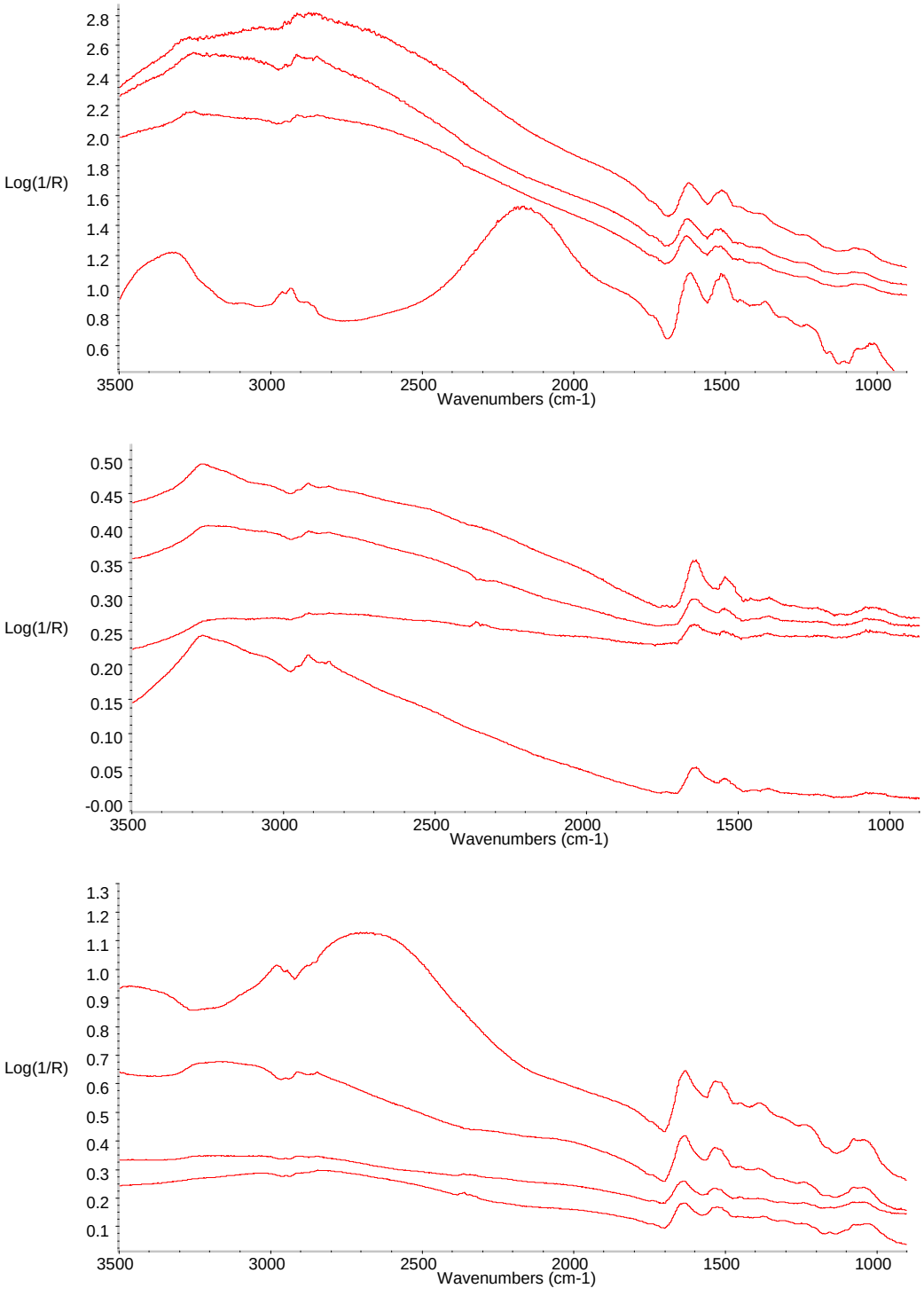

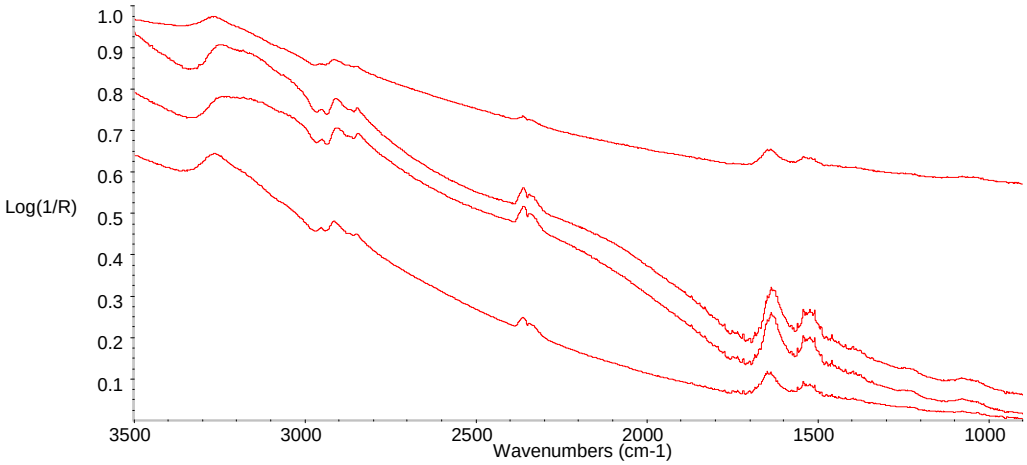
Log(1/R)
1.0
0.9
0.8
0.7
0.6
0.5
0.4
0.3
0.2
0.1
3500
3000
2500
2000
1500
1000
Wavenumbers (cm-1)

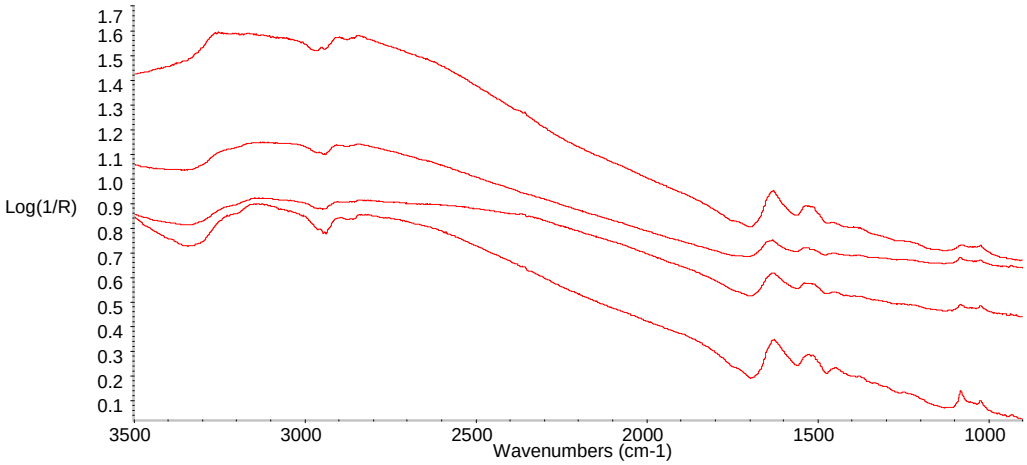
Log(1/R)
1.7
1.6
1.5
1.4
1.3
1.2
1.1
1.0
0.9
0.8
0.7
0.6
0.5
0.4
0.3
0.2
0.1
3500
3000
2500
2000
1500
1000
Wavenumbers (cm-1)


Log(1/R)
1.2
1.1
1.0
0.9
0.8
0.7
0.6
0.5
0.4
0.3
0.2
0.1
3500
3000
2500
2000
1500
1000
Wavenumbers (cm-1)

Slide #37 Cp4666D 10% PDA

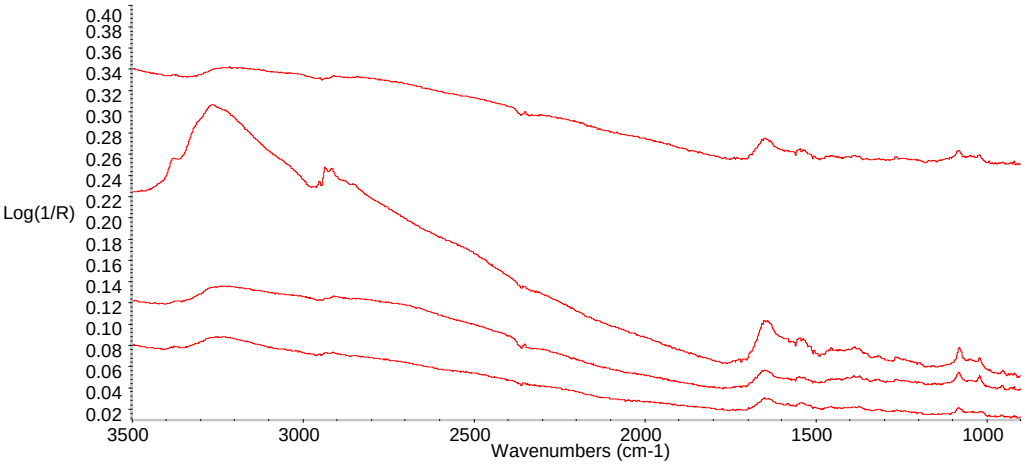

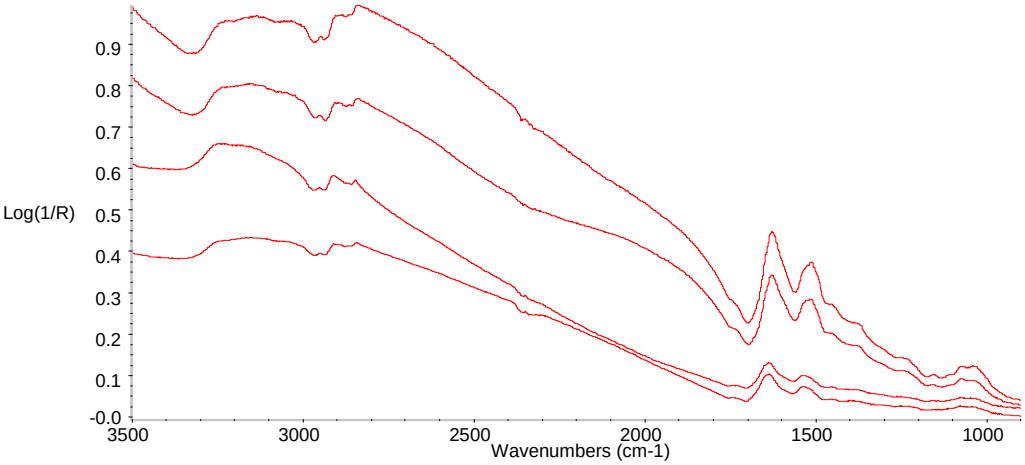

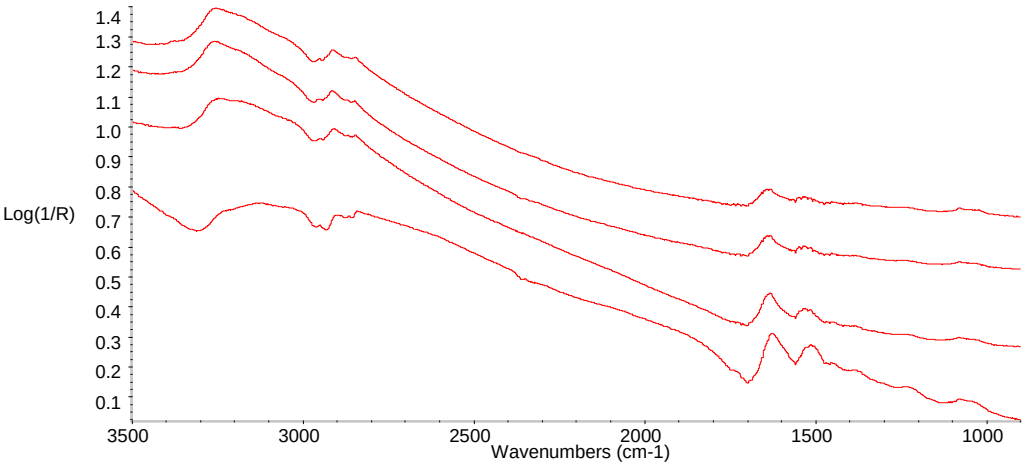

Slide #38 Fc18 100% PDA

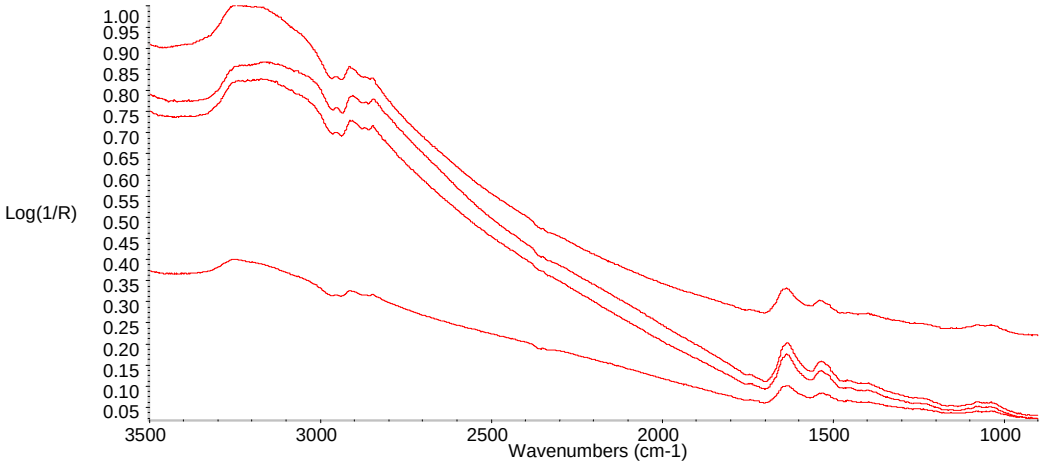

Slide #38 Fc18 10% PDA

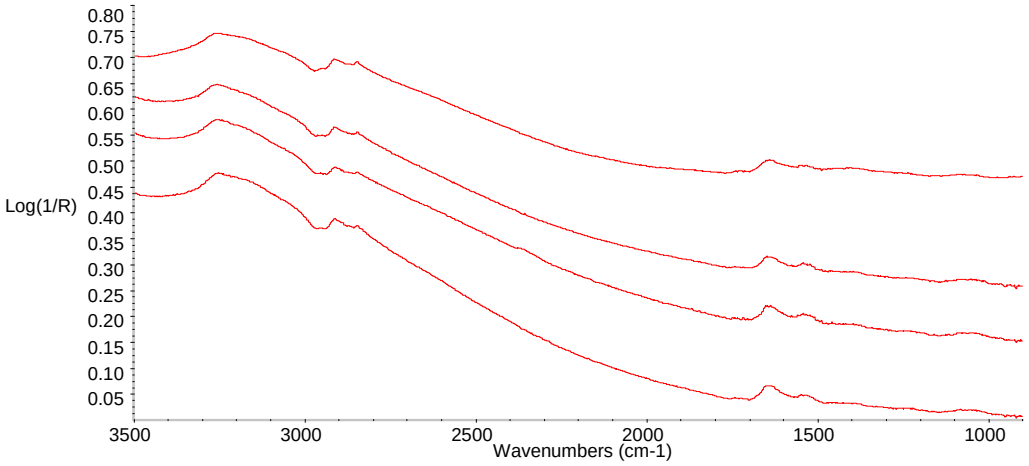

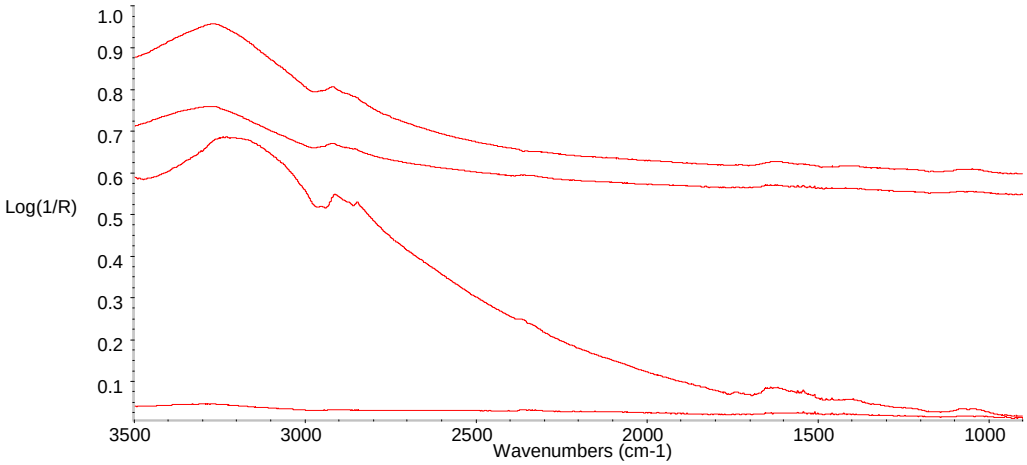

Side #38 FcRed1 100% PDA

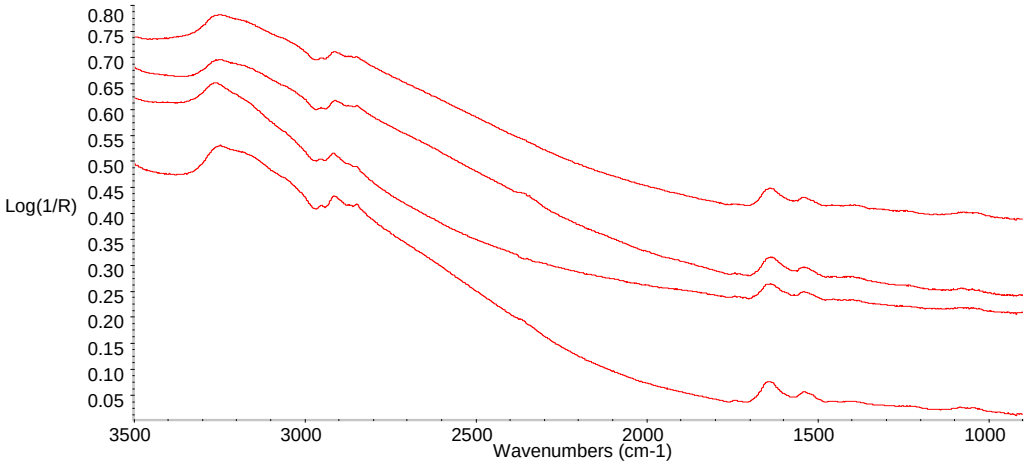

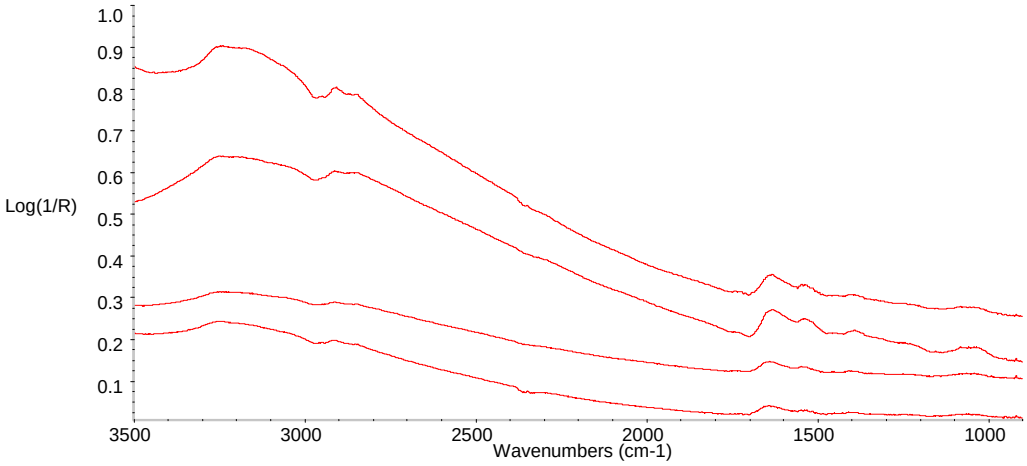

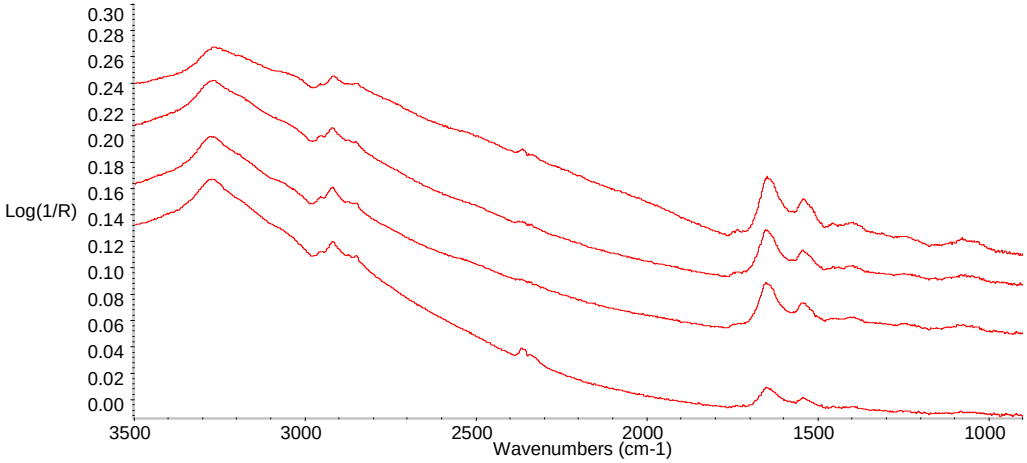

Slide #38 FcRed1 10% PDA

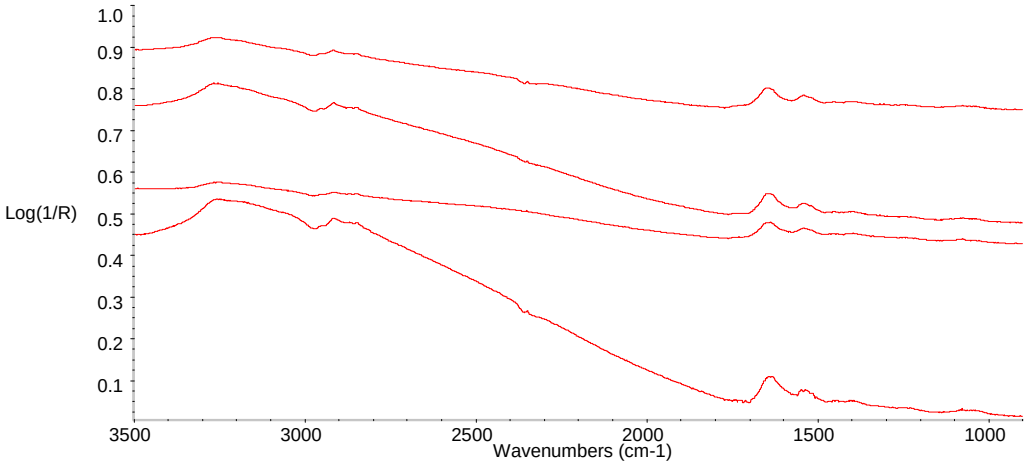

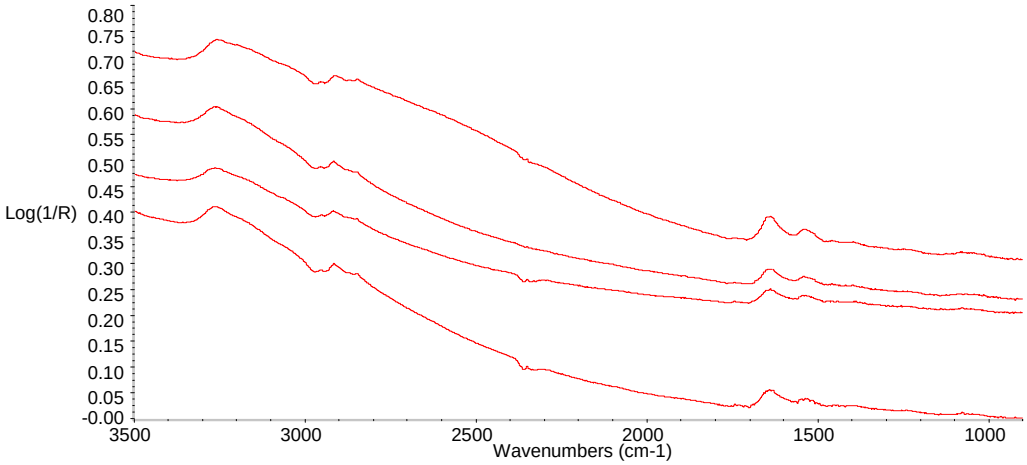

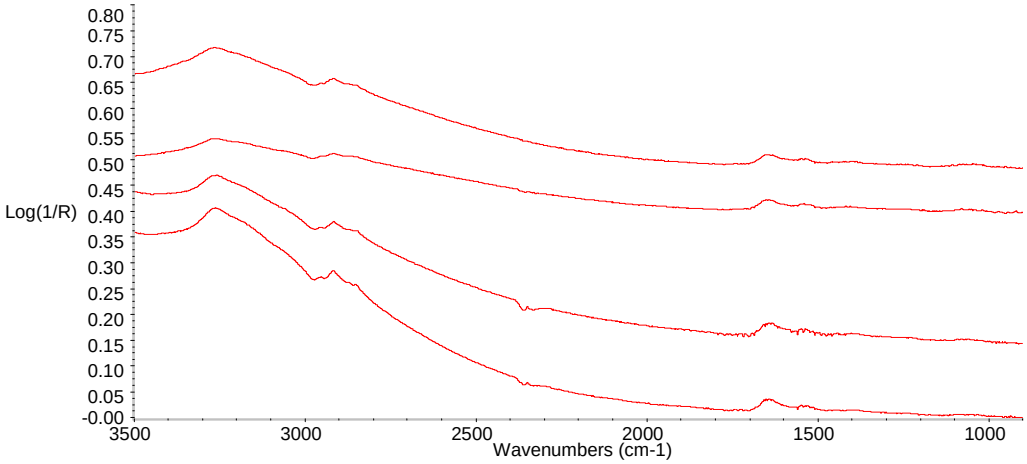

Slide #37 L2.5 100% PDA

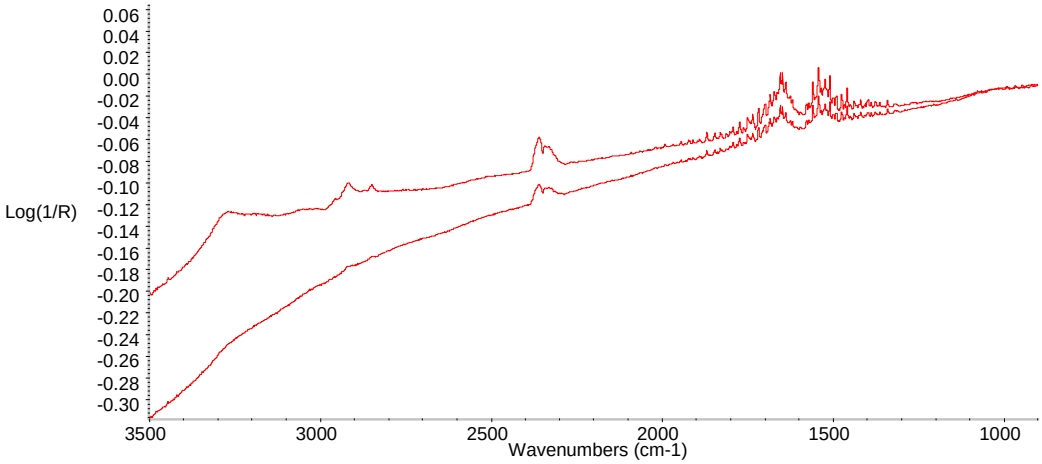

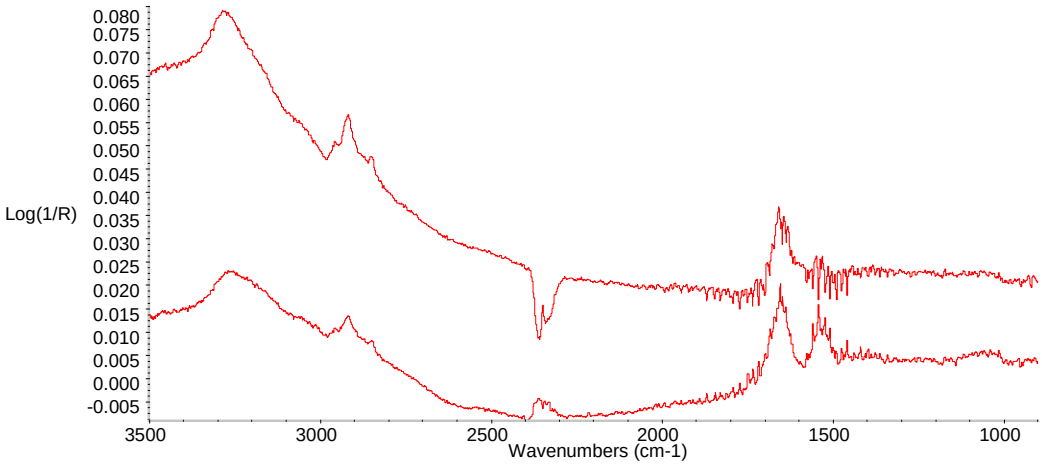

Slide #34 CmPath 100% PDA

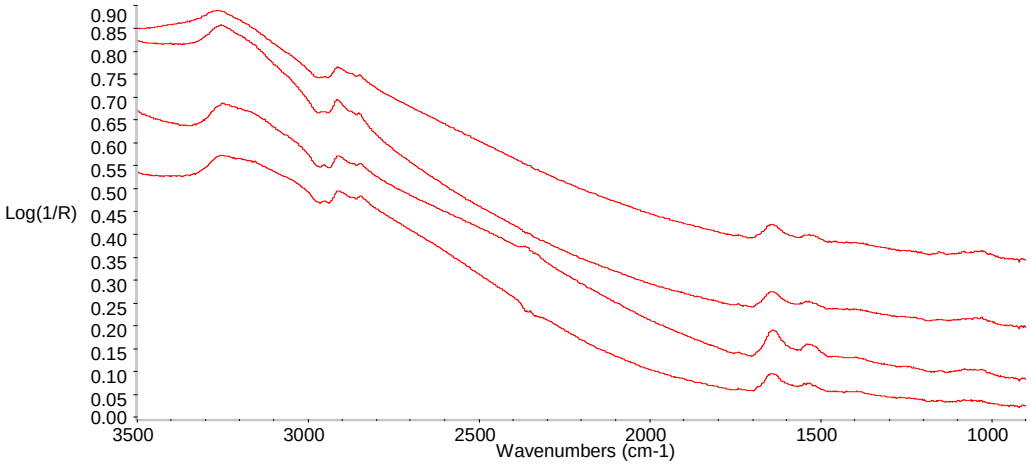

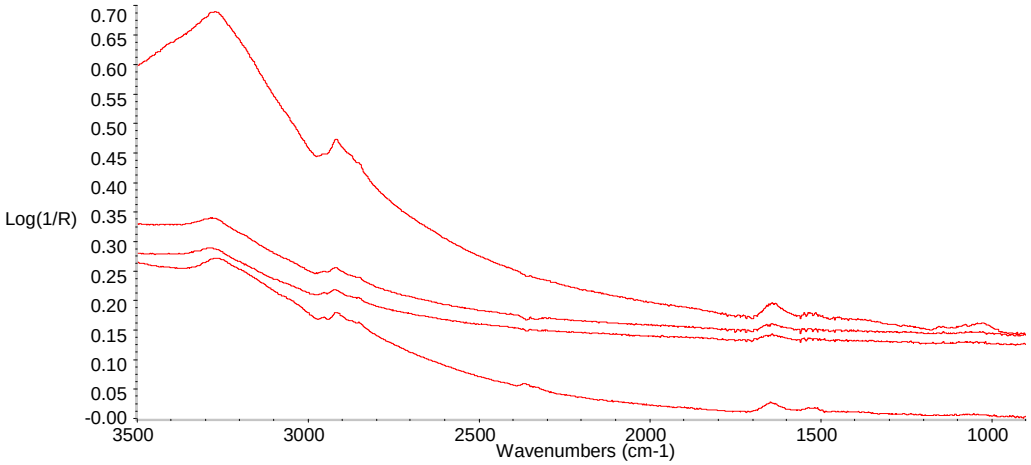

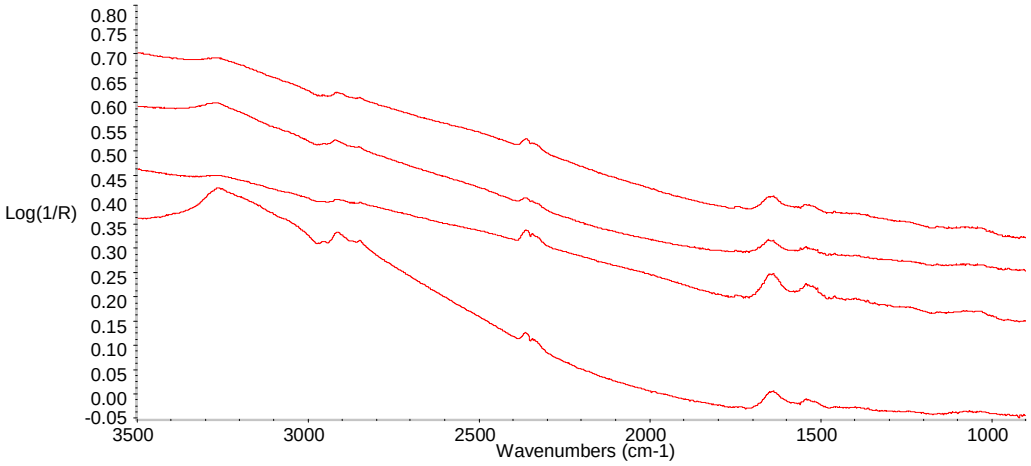

Slide #34 CmPath 10% PDA

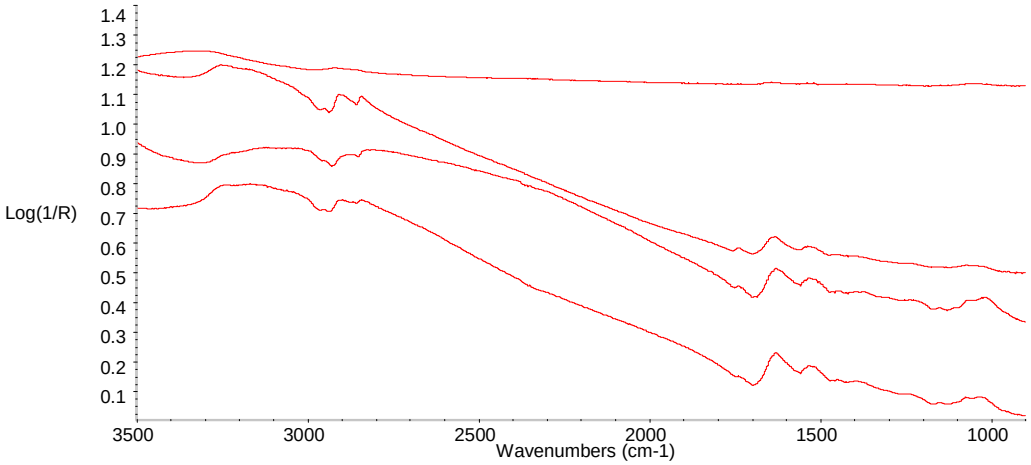

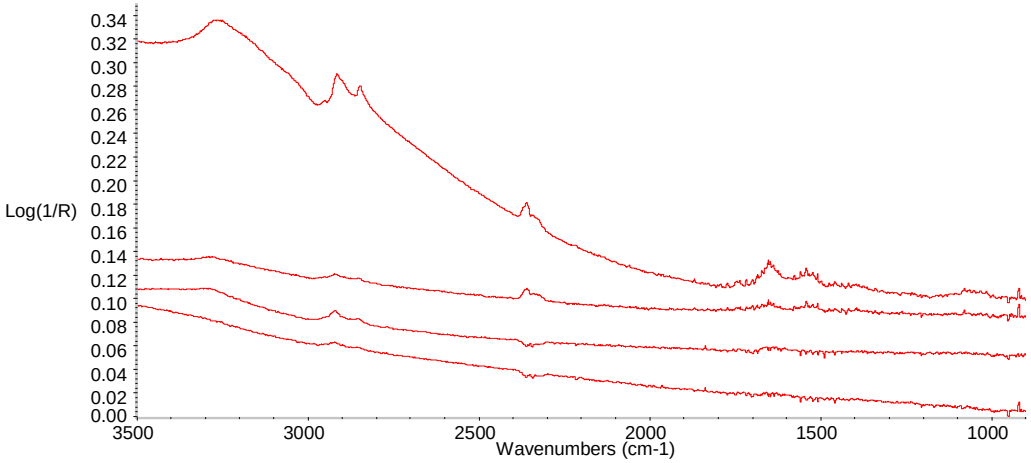

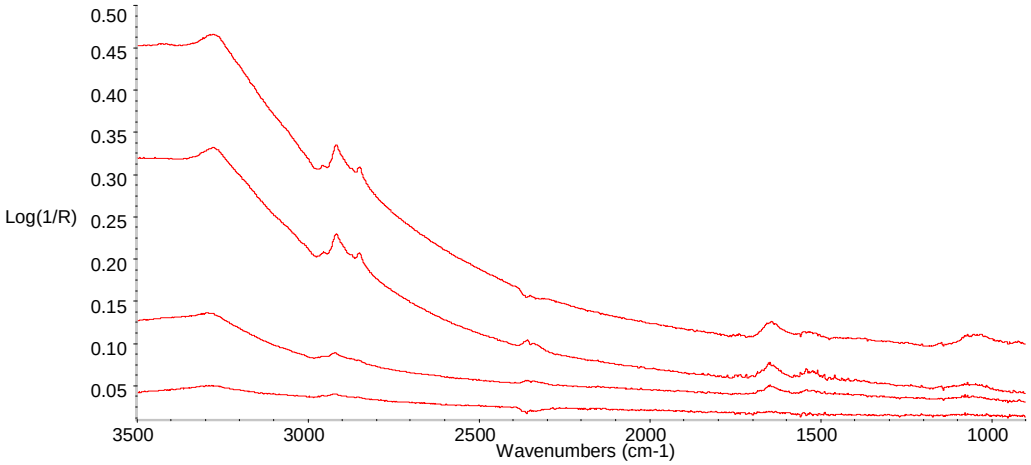

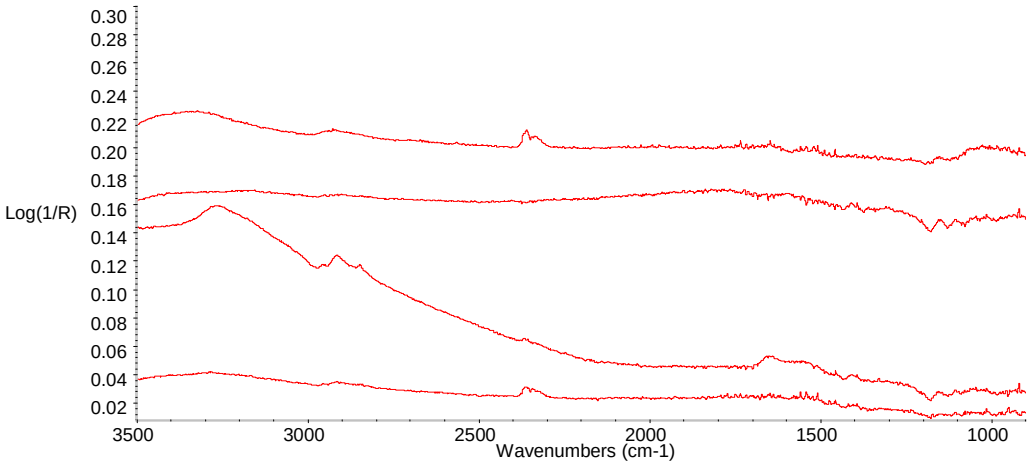
Log(1/R)
0.30
0.28
0.26
0.24
0.22
0.20
0.18
0.16
0.14
0.12
0.10
0.08
0.06
0.04
0.02
3500
3000
2500
2000
1500
1000
Wavenumbers (cm-1)

CLS June 2008

Slide #34 CpATCC 10% PDA

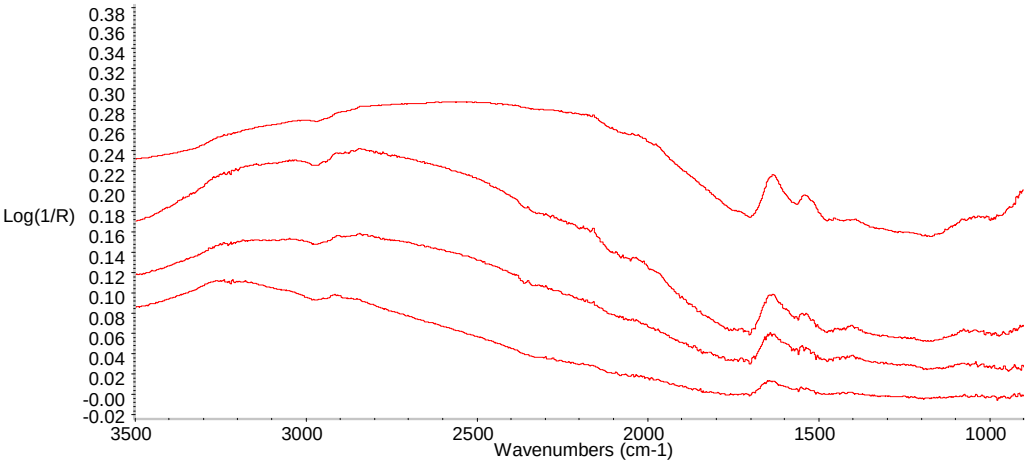

Slide #40 CpATCC 100% PDA

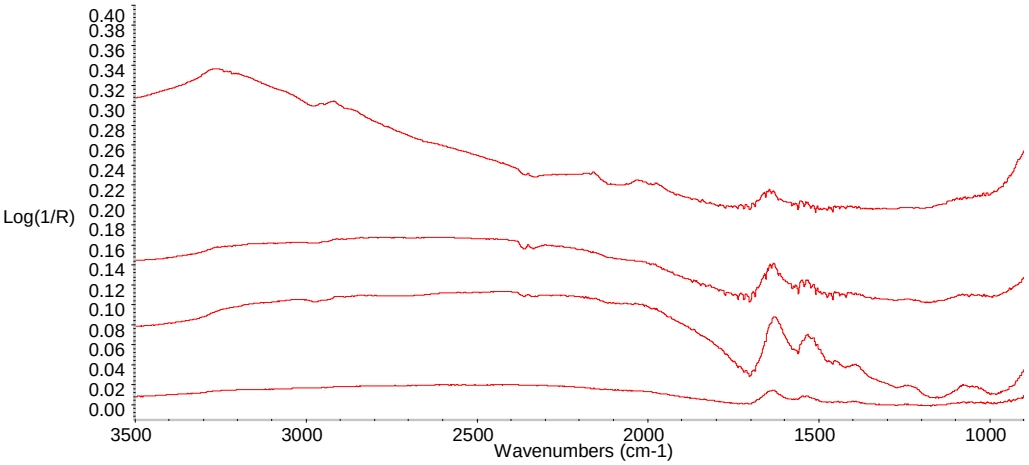

Slide #39 Cp4666D 100% PDA

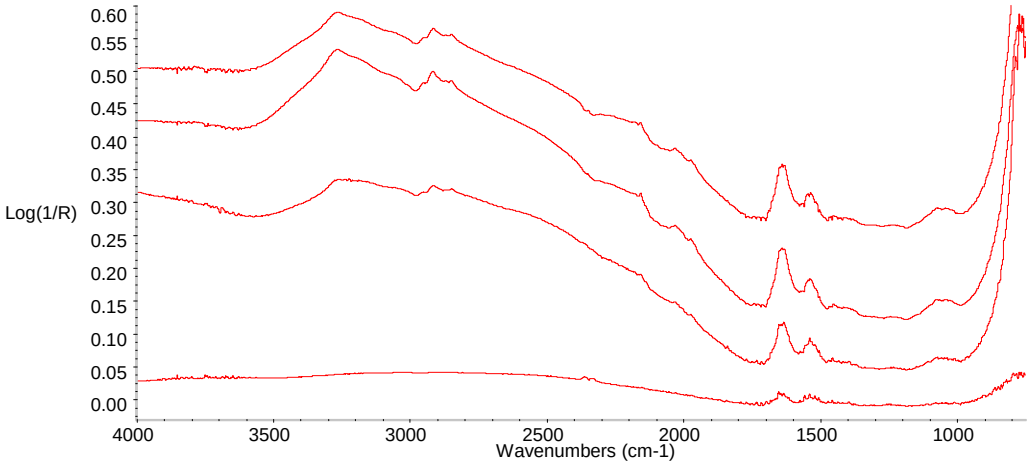

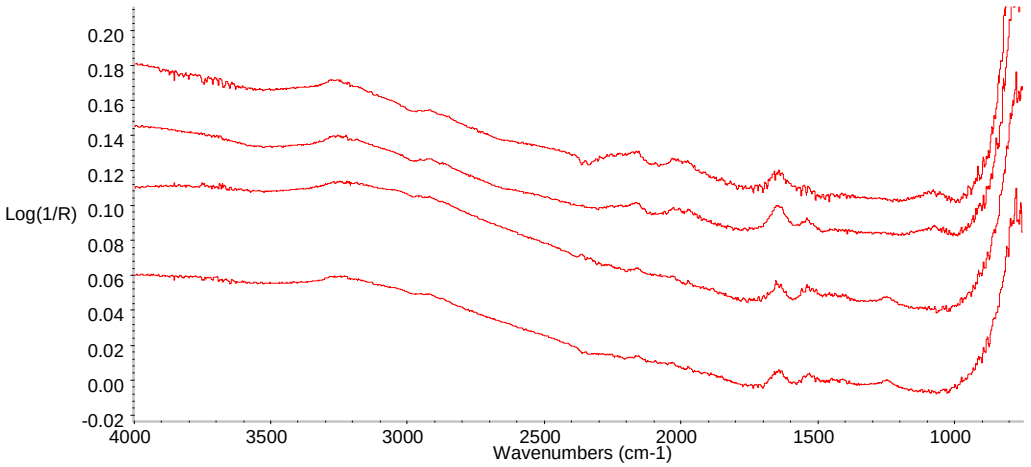

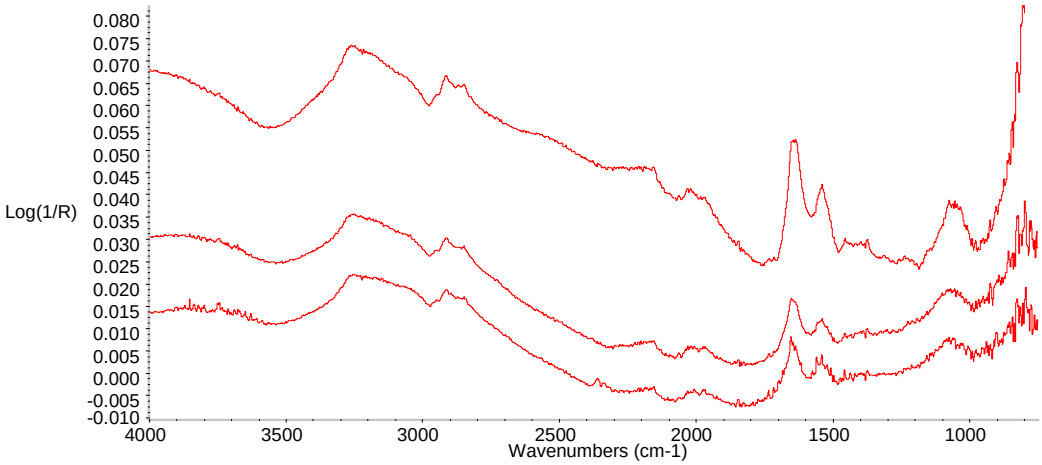

Slide #39 Cp4666D 1% PDA

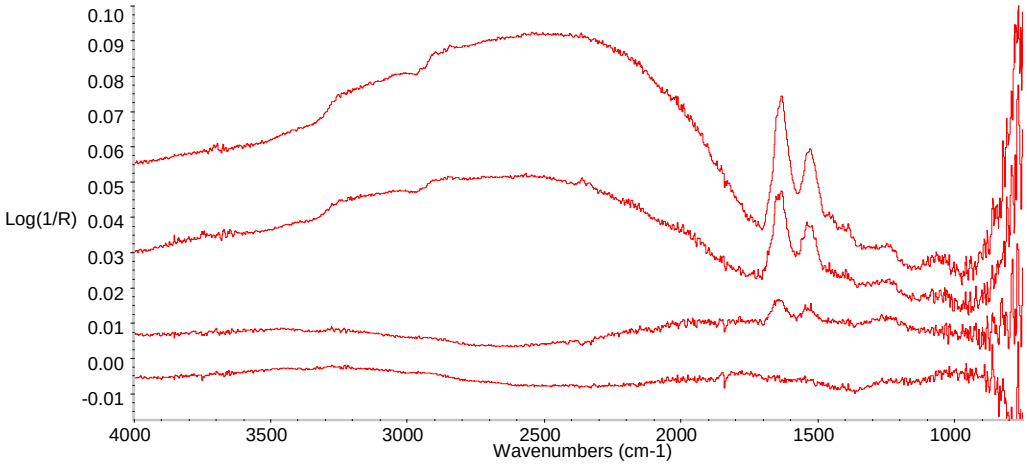

Slide #43 FcRed1 3% PDA

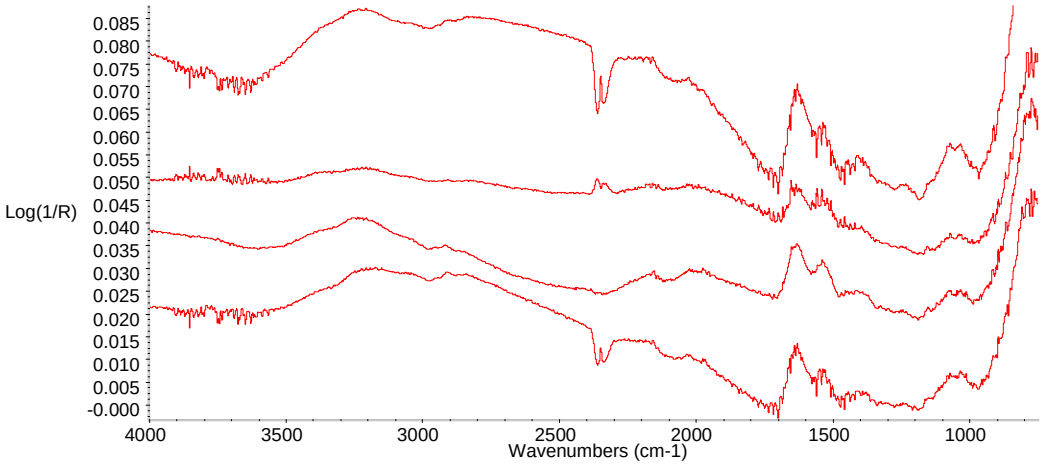

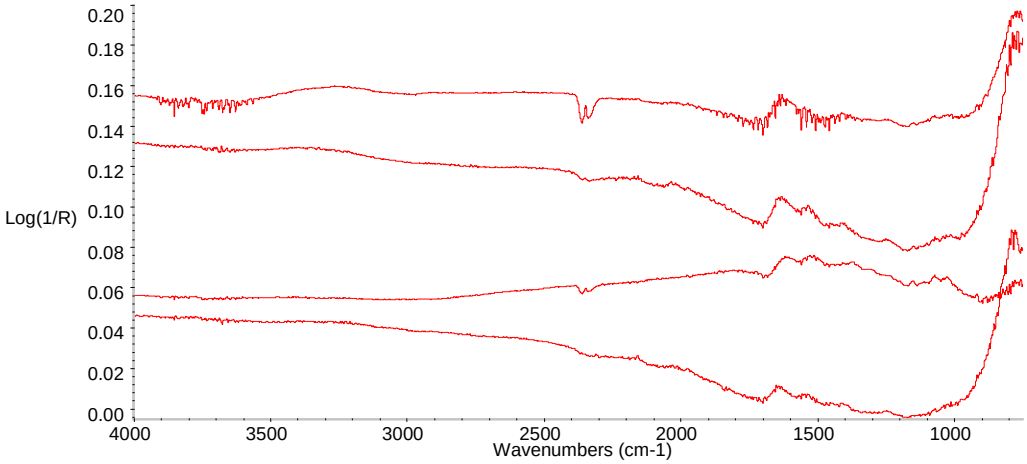

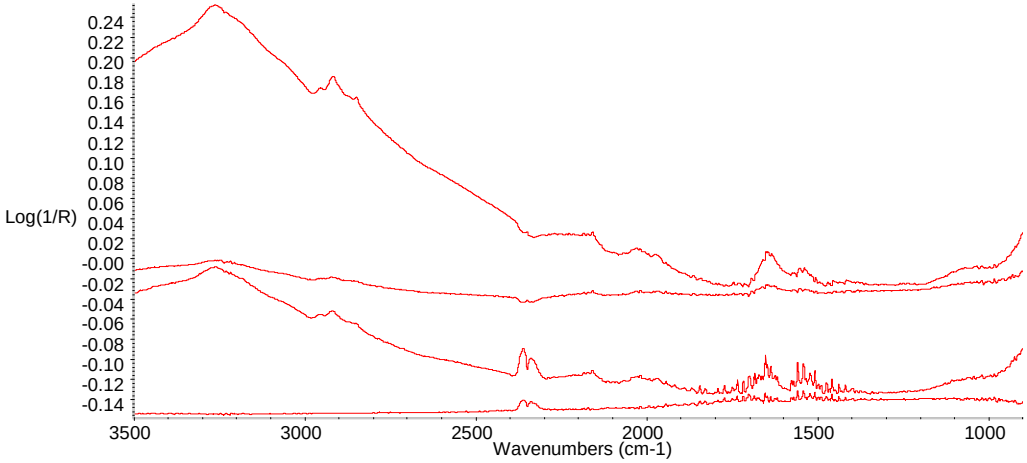

Slide #41 L2.5 10% PDA

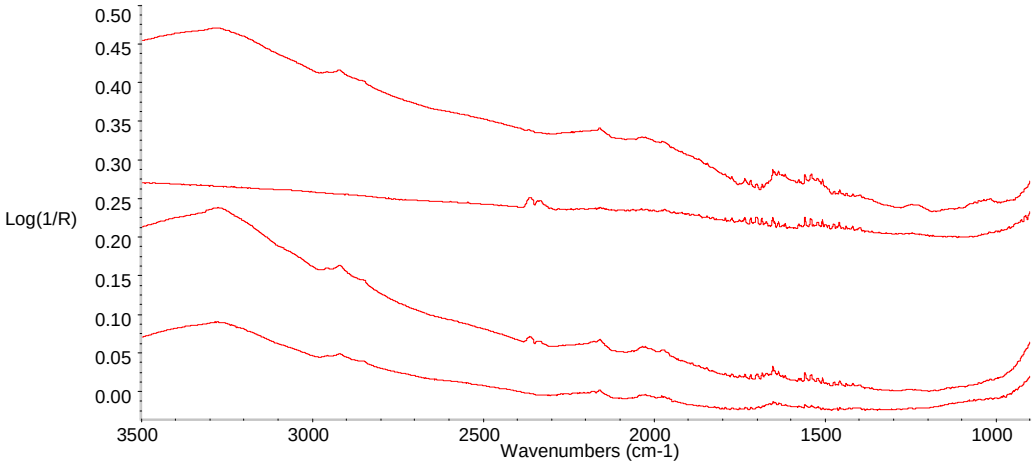

Slide #41 L2.5 1% PDA

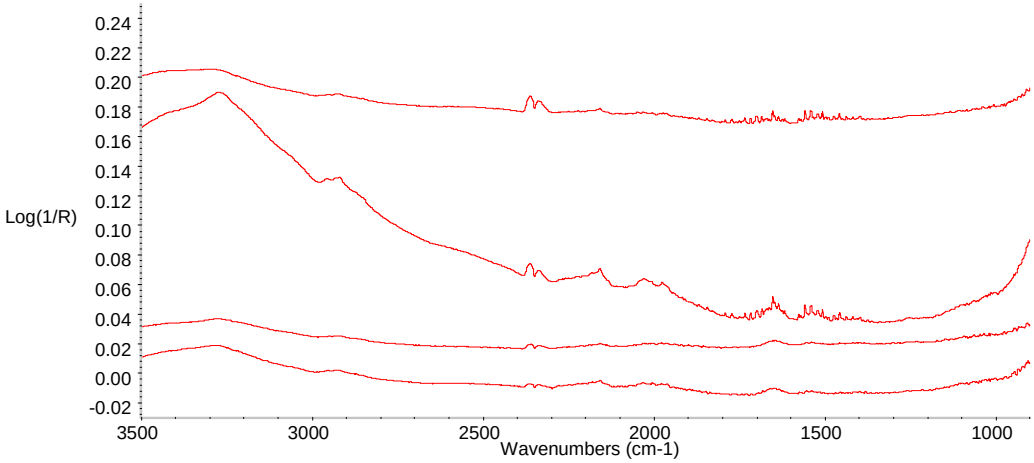

SRC November 2008

Slide #45 CpATCC 100% PDA

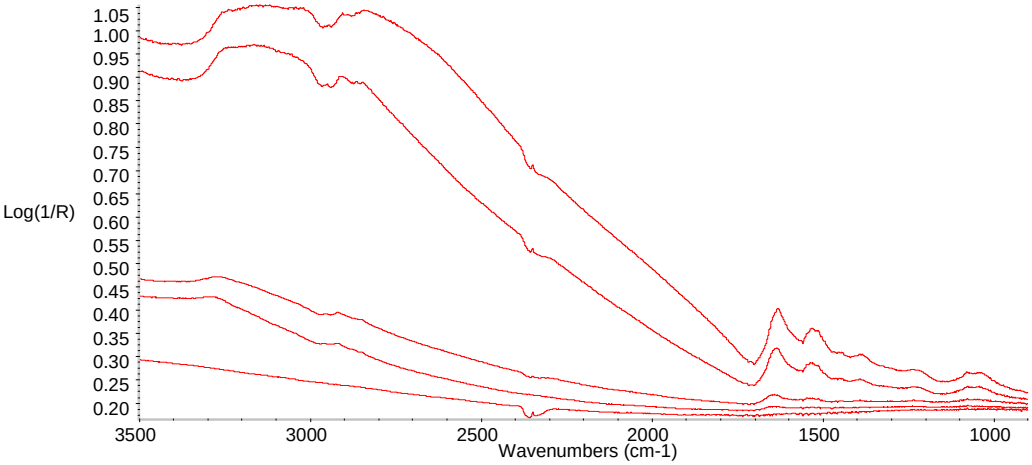

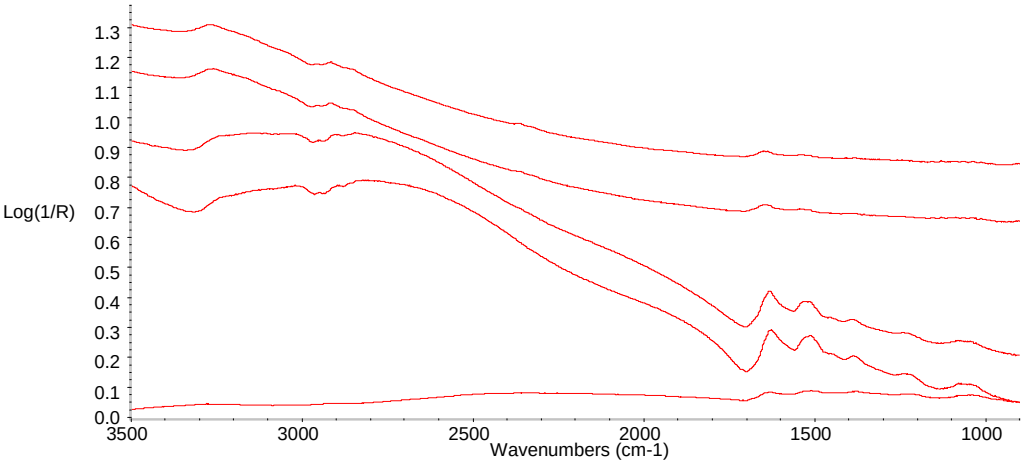

Slide #46 Cp4666D 100% PDA

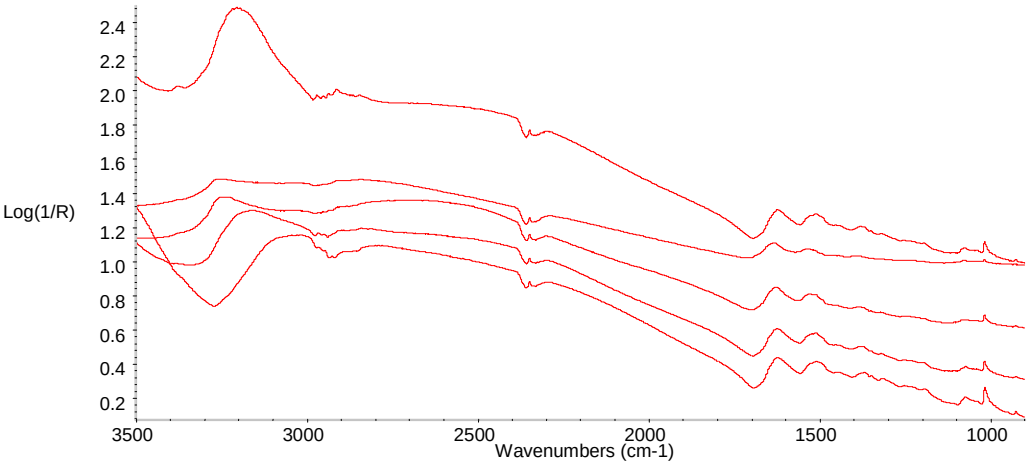

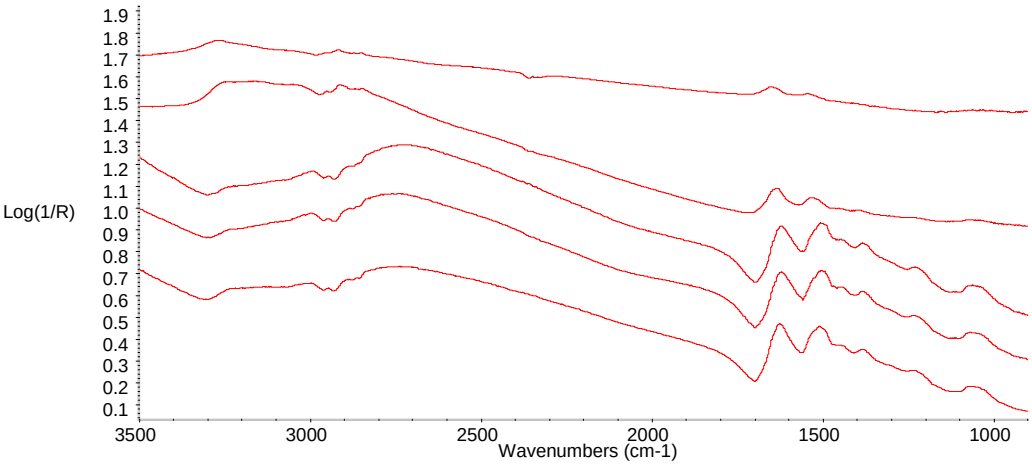

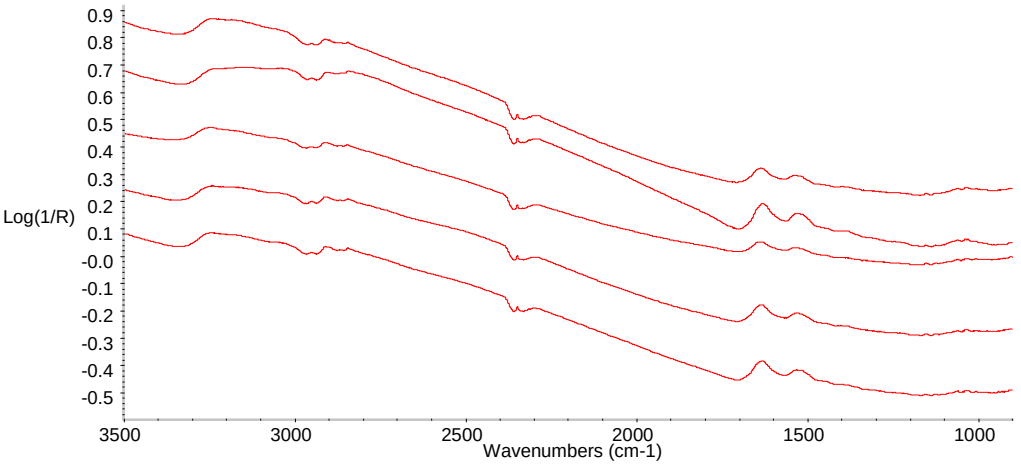

Slide #47 Fc18 100% PDA

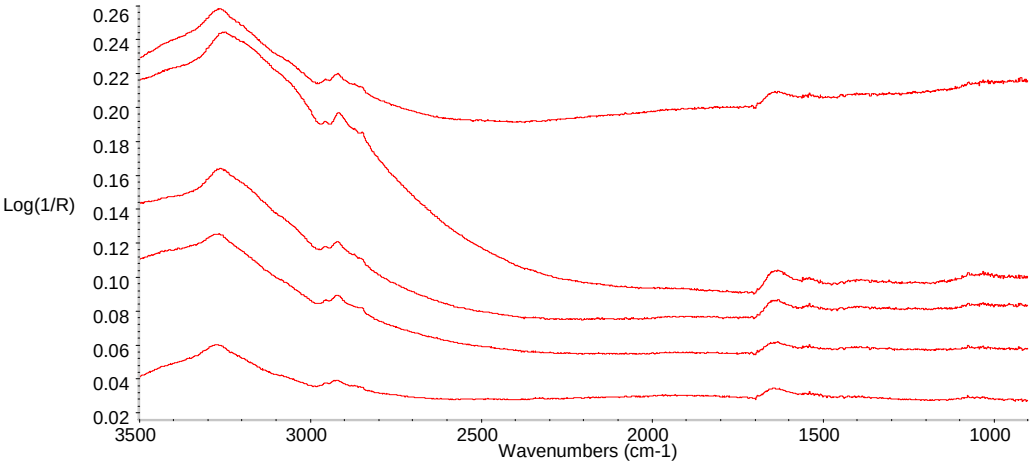

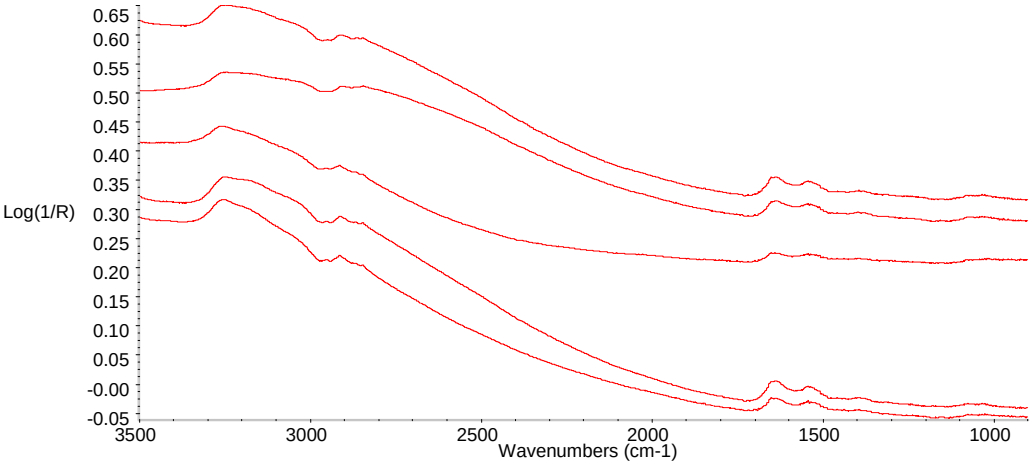

Slide #48 FcRed1 100% PDA

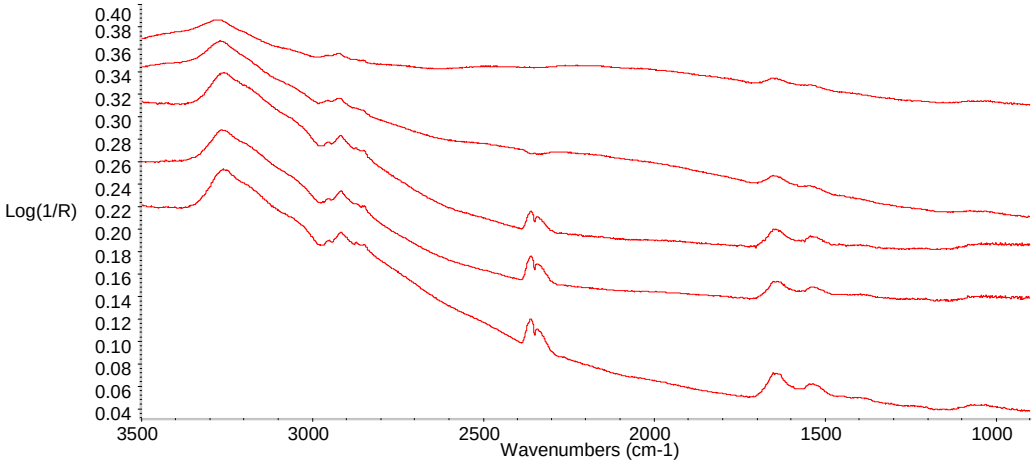
Log(1/R)
0.40
0.38
0.36
0.34
0.32
0.30
0.28
0.26
0.24
0.22
0.20
0.18
0.16
0.14
0.12
0.10
0.08
0.06
0.04
3500
3000
2500
2000
1500
1000
Wavenumbers (cm-1)

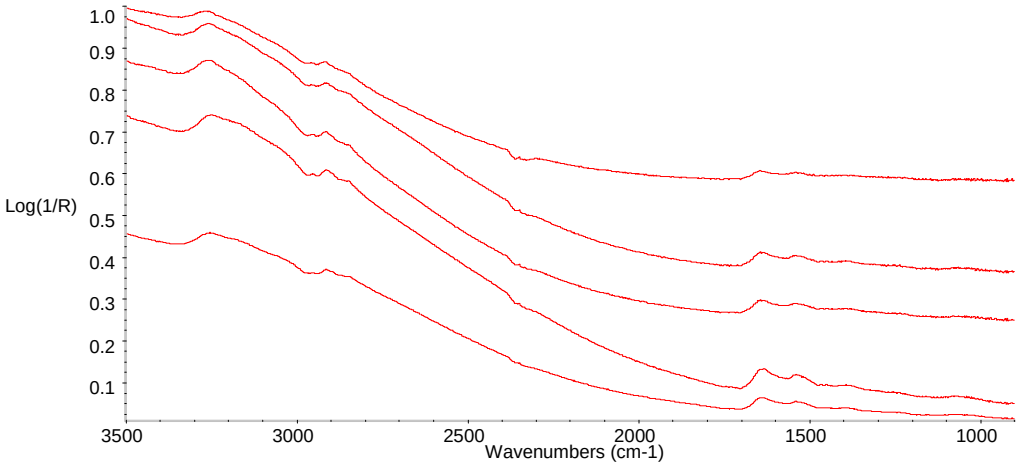
Log(1/R)
1.0
0.9
0.8
0.7
0.6
0.5
0.4
0.3
0.2
0.1
3500
3000
2500
2000
1500
1000
Wavenumbers (cm-1)

CLS December 2008

Slide #46 Cp4666D 100% PDA

collected at tip, 18, 30, 37, 45, 54, 62 µm from tips

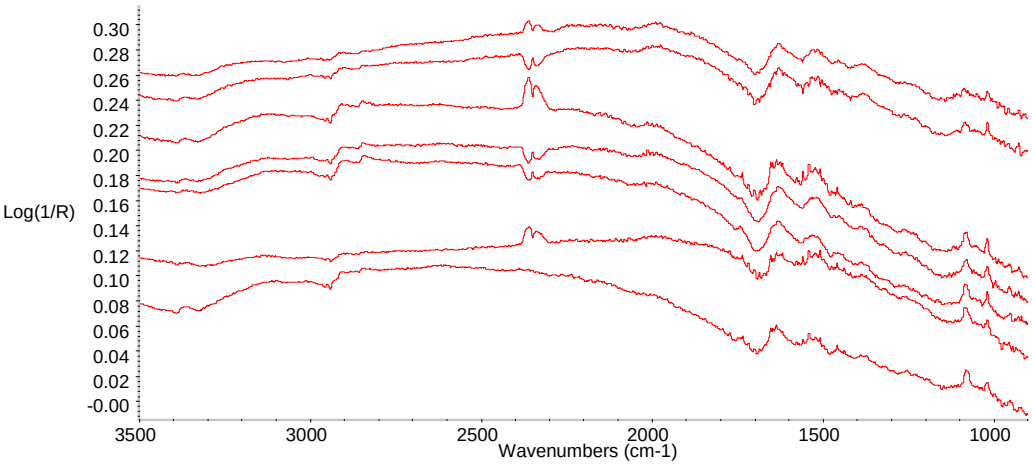

The following groups of spectra collected 30 µm from tips of different hyphae:

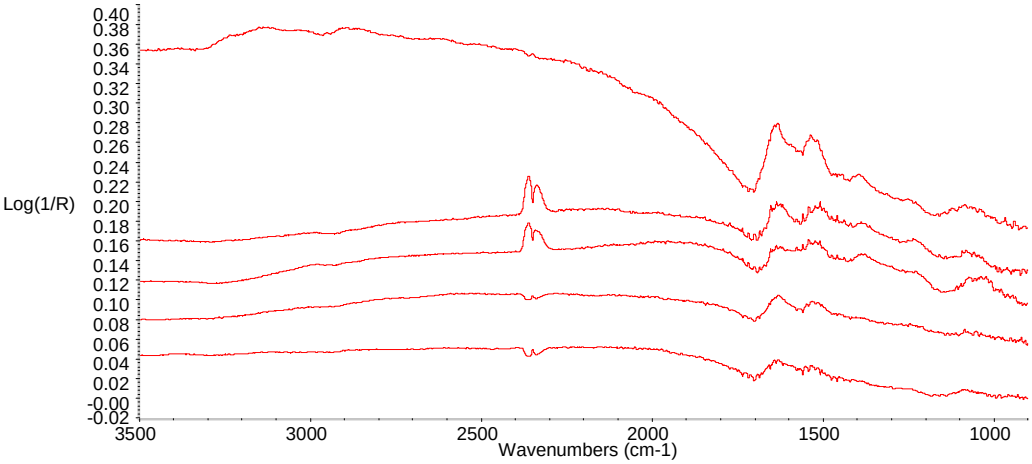

Slide #46 Cp4666D 10% PDA

The following groups of spectra collected 30um from tips of different hyphae and used a 15 x 15 um aperture:

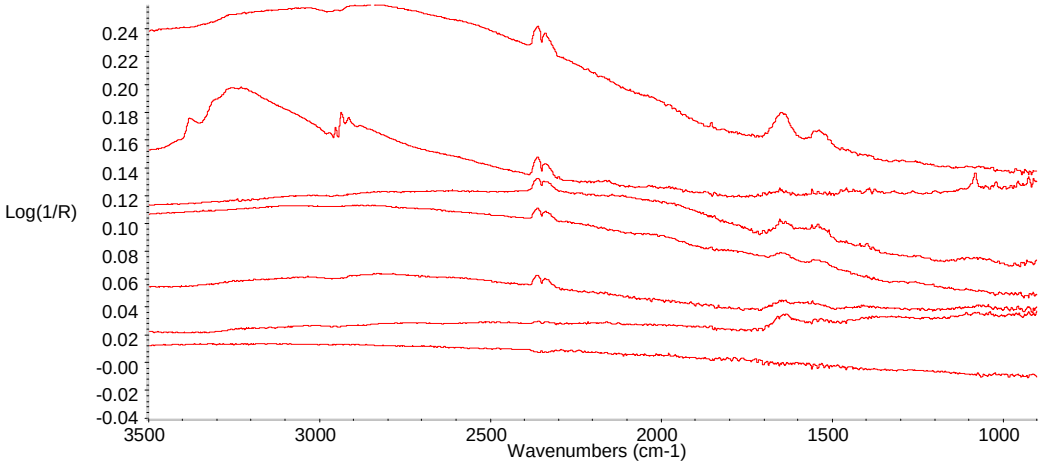

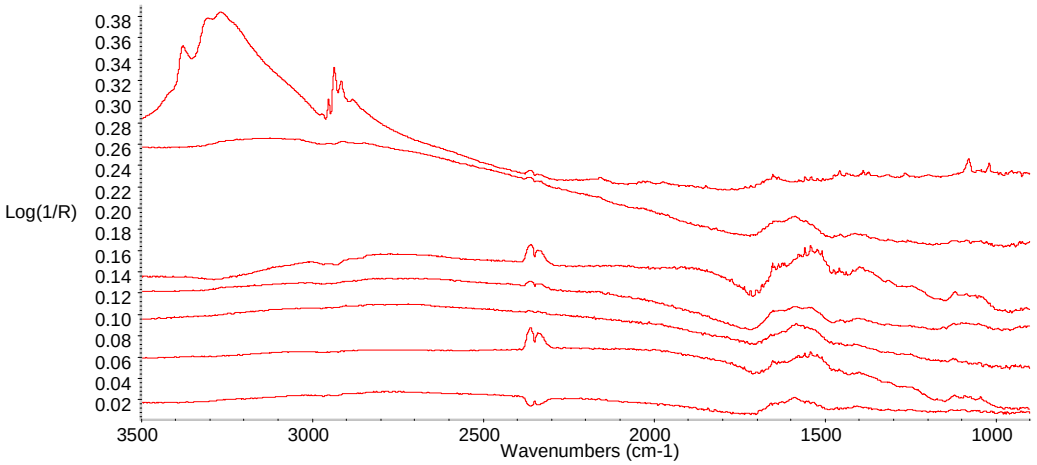

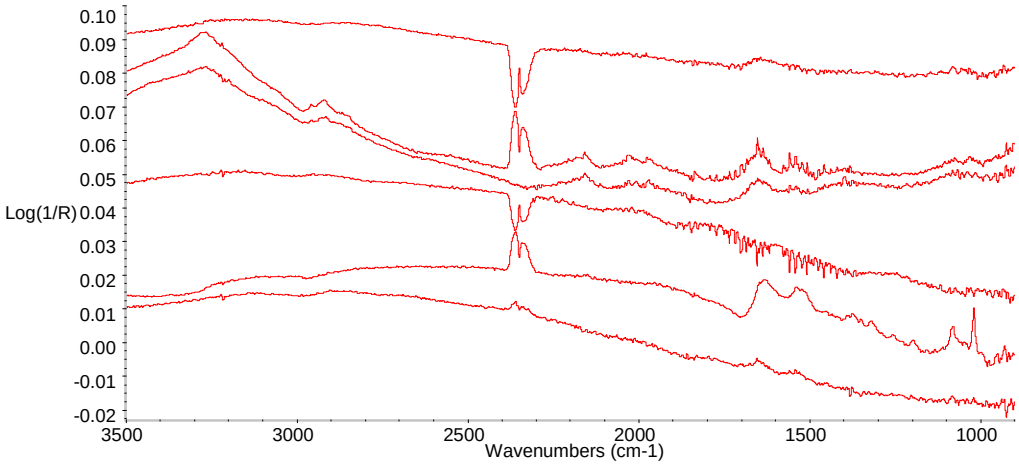

Slide #63 Cp4666D 1x GYE

The following groups of spectra collected 30 μm from tips of different hyphae and used a 15x15 um aperture:

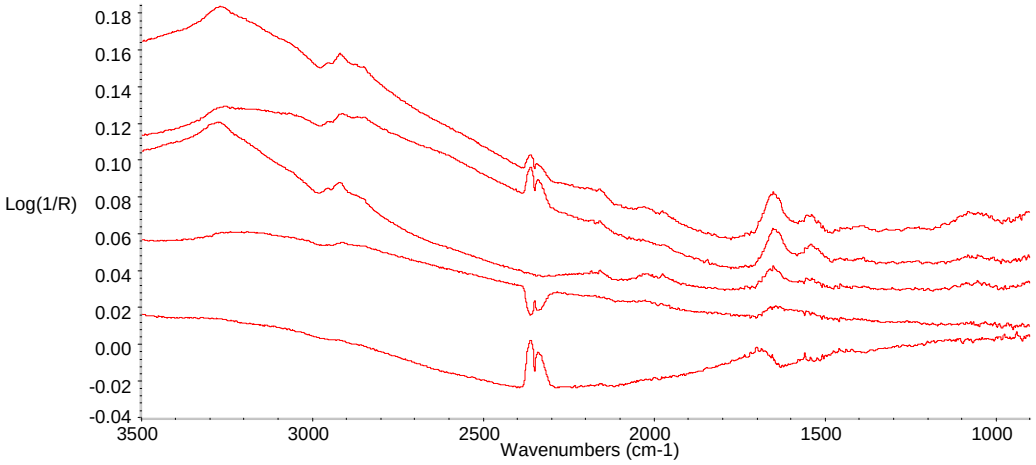

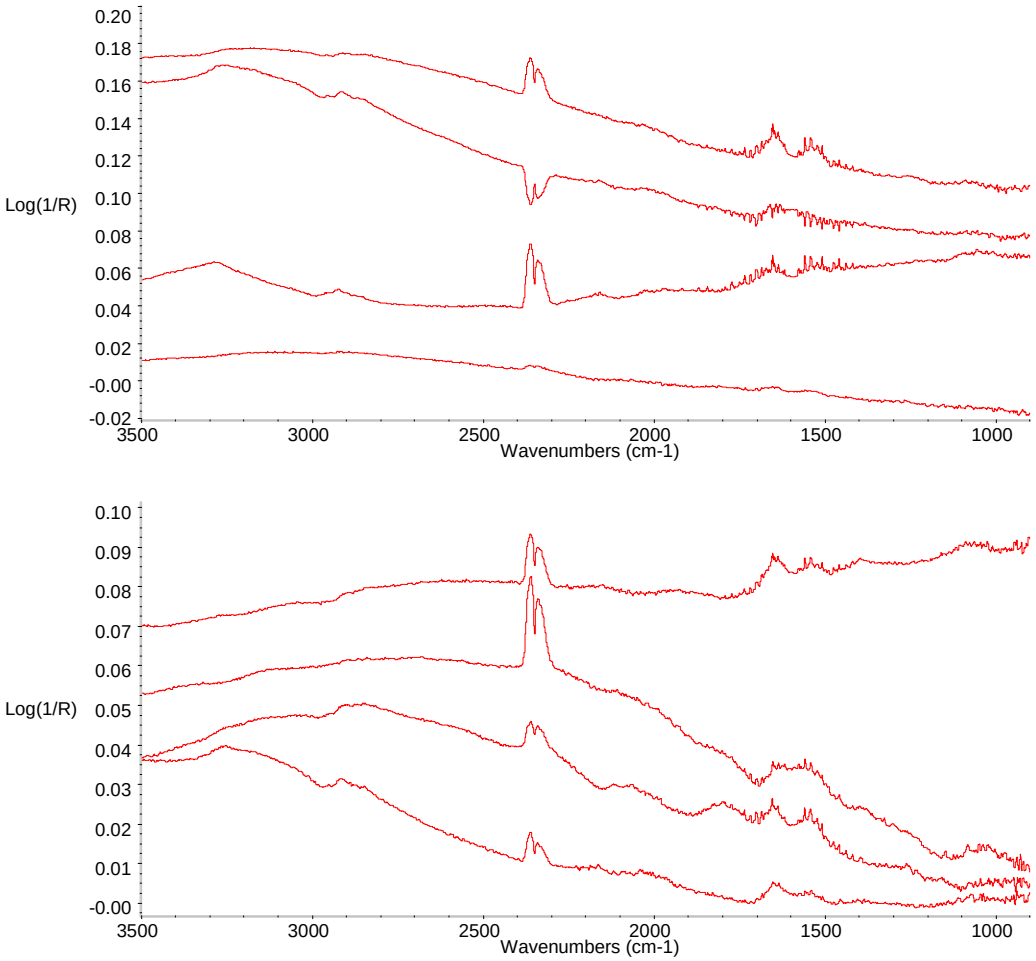
Log(1/R)
0.20
0.18
0.16
0.14
0.12
0.10
0.08
0.06
0.04
0.02
-0.00
-0.02
3500
3000
2500
2000
1500
1000
Wavenumbers (cm-1)
Log(1/R)
0.10
0.09
0.08
0.07
0.06
0.05
0.04
0.03
0.02
0.01
-0.00
3500
3000
2500
2000
1500
1000
Wavenumbers (cm-1)

SRC August 2009

Slide #128 Cp4666D no virus 100% PDA

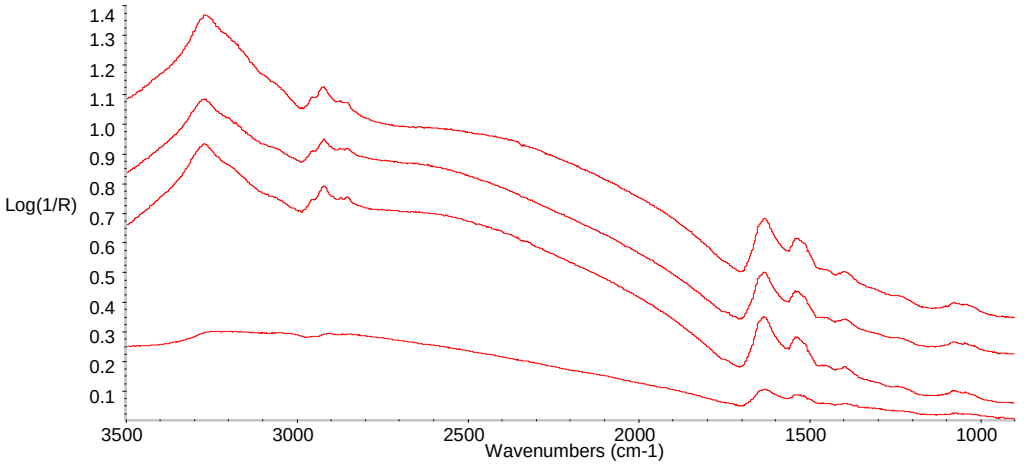

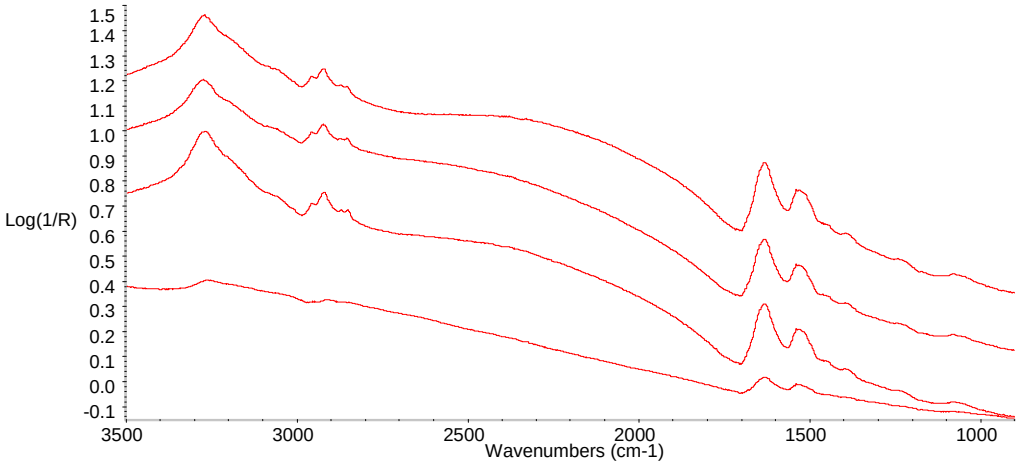

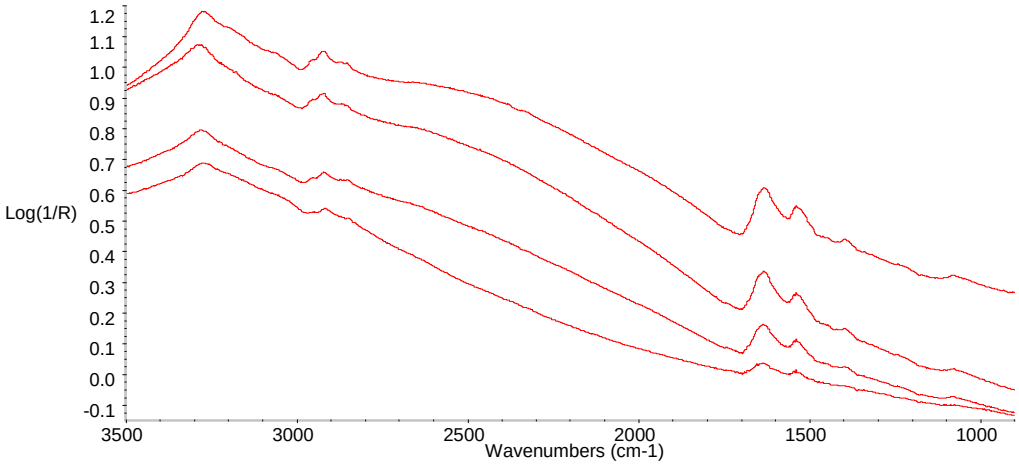
Log(1/R)
1.2
1.1
1.0
0.9
0.8
0.7
0.6
0.5
0.4
0.3
0.2
0.1
0.0
-0.1
3500
3000
2500
2000
1500
1000
Wavenumbers (cm-1)

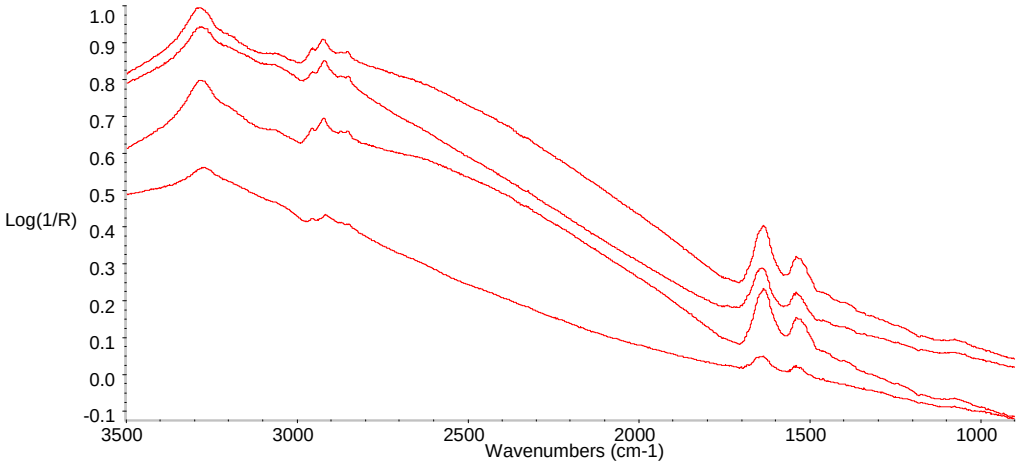
Log(1/R)
1.0
0.9
0.8
0.7
0.6
0.5
0.4
0.3
0.2
0.1
0.0
-0.1
3500
3000
2500
2000
1500
1000
Wavenumbers (cm-1)

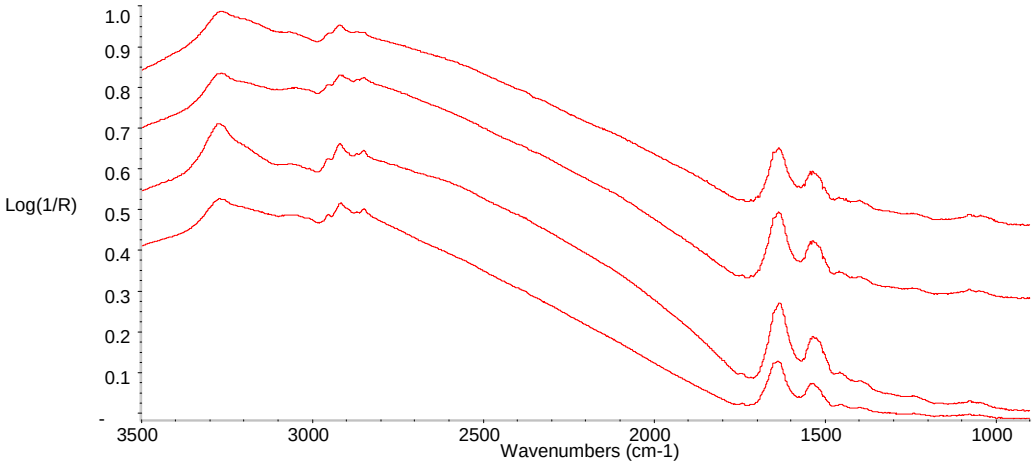
Log(1/R)
1.0
0.9
0.8
0.7
0.6
0.5
0.4
0.3
0.2
0.1
-
3500
3000
2500
2000
1500
1000
Wavenumbers (cm-1)

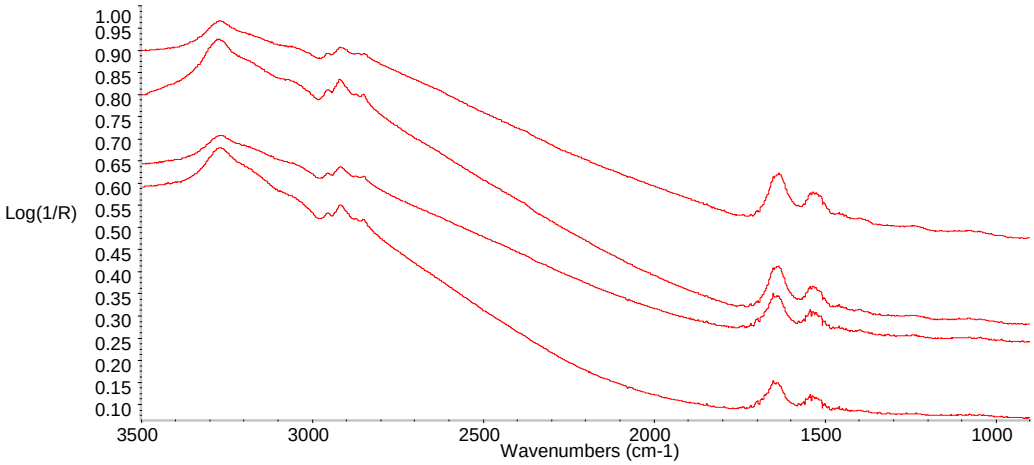

Slide #129 Cp4666D with virus 100% PDA

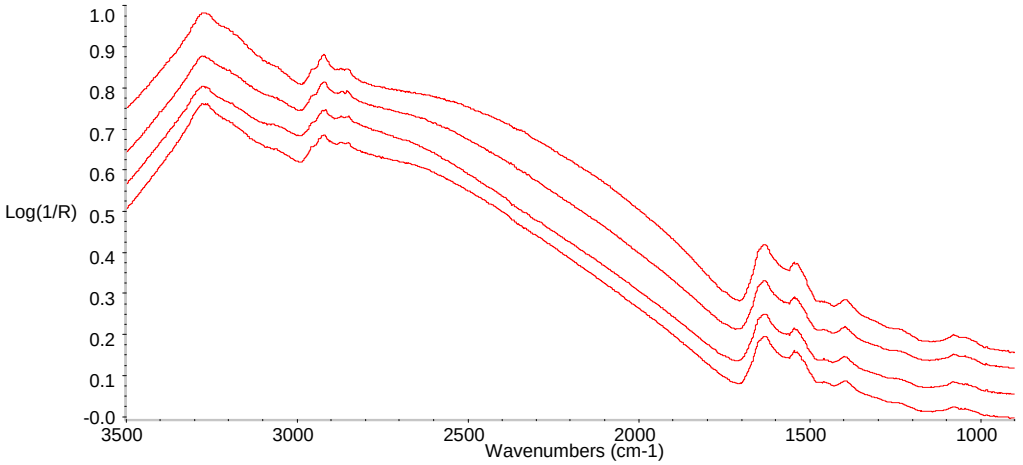

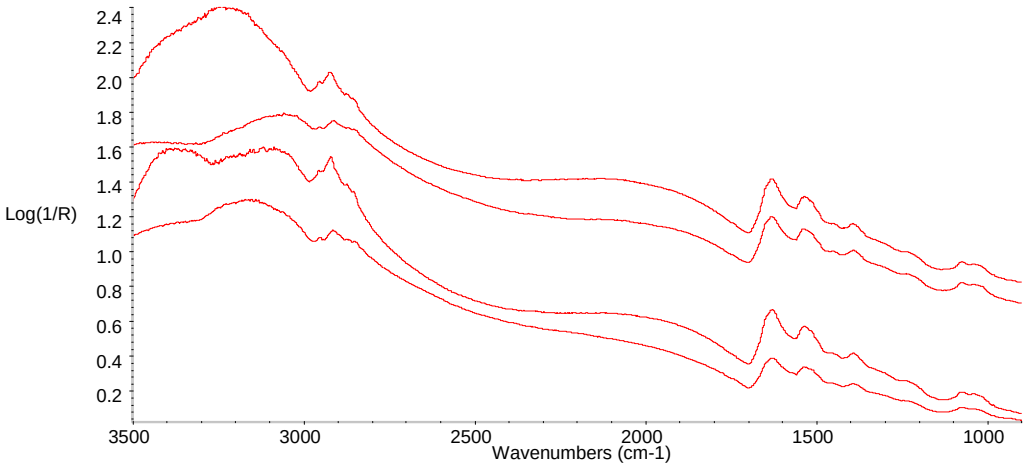

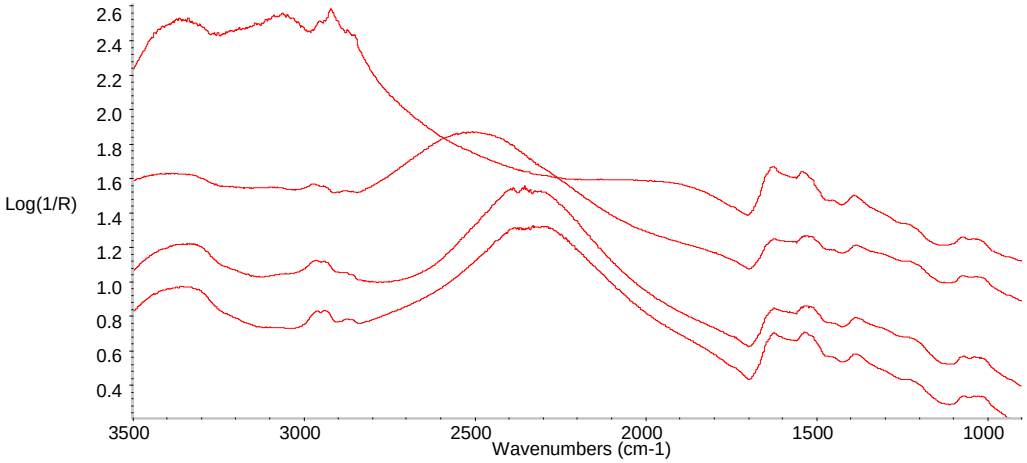
Log(1/R)
2.6
2.4
2.2
2.0
1.8
1.6
1.4
1.2
1.0
0.8
0.6
0.4
3500
3000
2500
2000
1500
1000
Wavenumbers (cm-1)

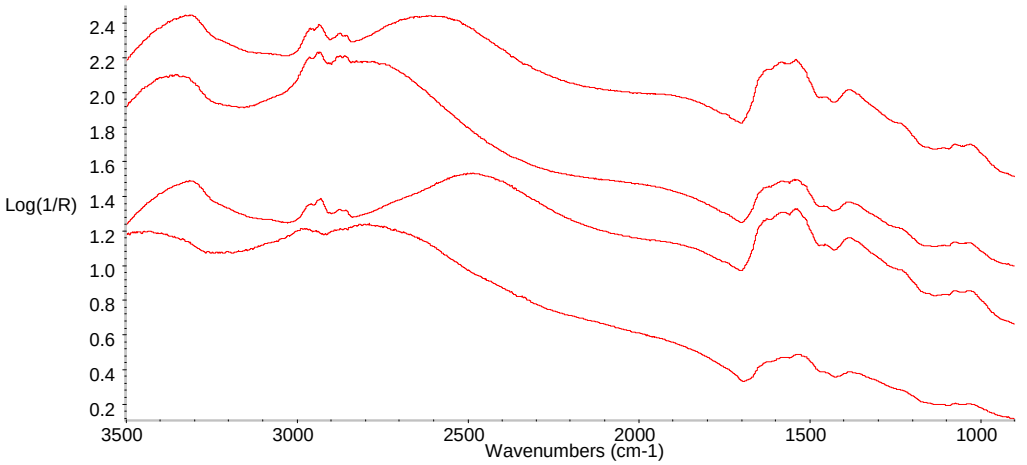
Log(1/R)
2.4
2.2
2.0
1.8
1.6
1.4
1.2
1.0
0.8
0.6
0.4
0.2
3500
3000
2500
2000
1500
1000
Wavenumbers (cm-1)

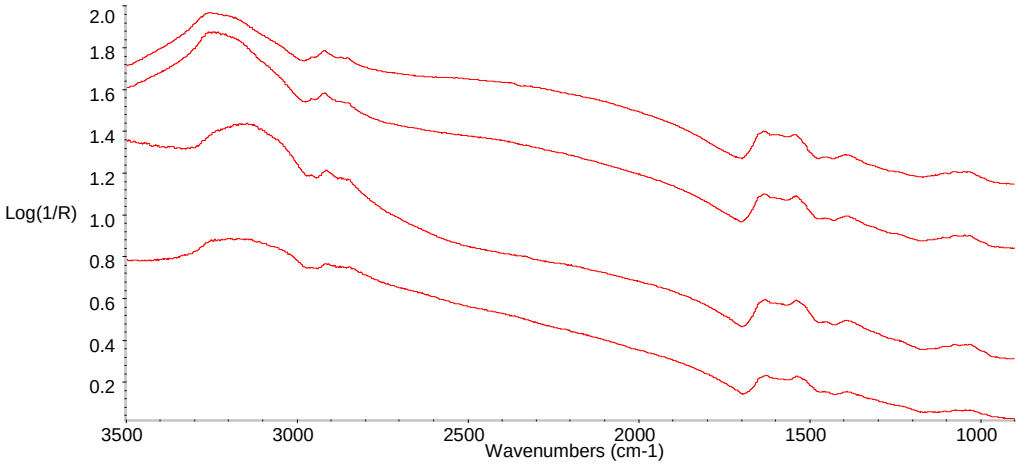
Log(1/R)
2.0
1.8
1.6
1.4
1.2
1.0
0.8
0.6
0.4
0.2
3500
3000
2500
2000
1500
1000
Wavenumbers (cm-1)

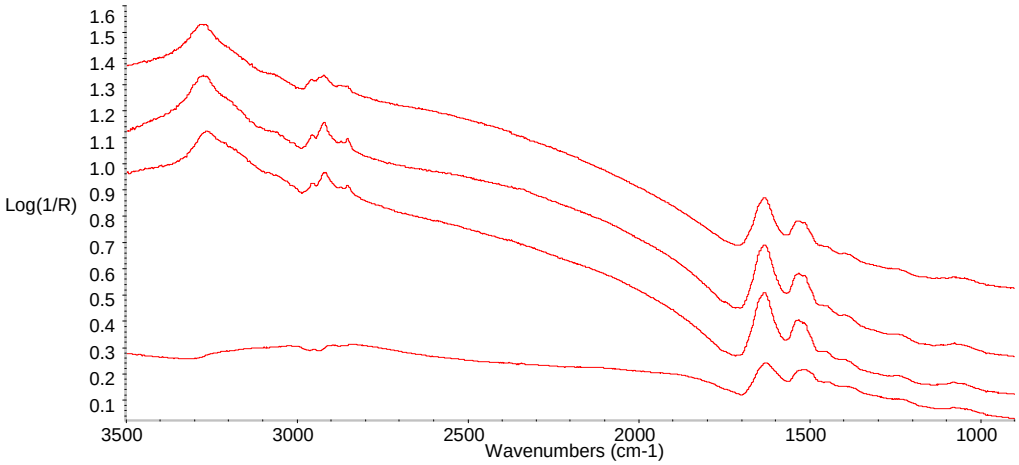
Log(1/R)
1.6
1.5
1.4
1.3
1.2
1.1
1.0
0.9
0.8
0.7
0.6
0.5
0.4
0.3
0.2
0.1
3500
3000
2500
2000
1500
1000
Wavenumbers (cm-1)

Appendix II: FTIR FPA Maps

All maps are processed to show area under the amide I band.

Amide I processing parameters

Left edge: 1666.1
Center: 1635.5
Right edge: 1610.2

Left baseline: 1711.2
Right baseline: 1479.7

Colour intensity is -0.1 (blue) to 4.000 (red), unless otherwise noted.

Any maps containing mannitol are marked (M).

CpATCC

Slide #34 CpATCC 100% PDA

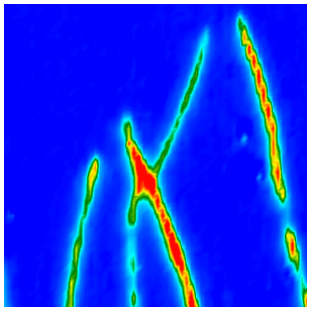
Map 1: M

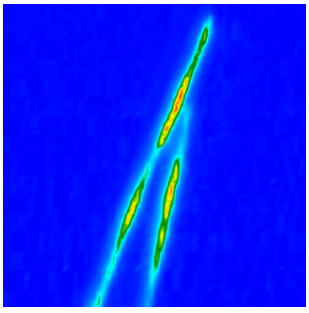
Map 2

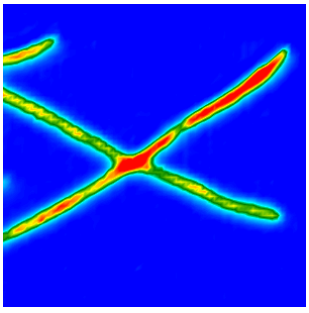
Map 3

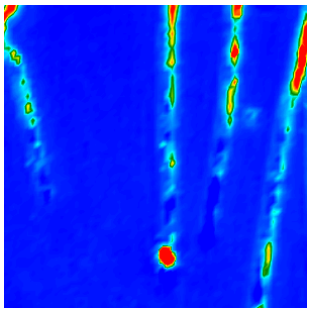

Map 4: M
colour: 0.000 to 0.1123

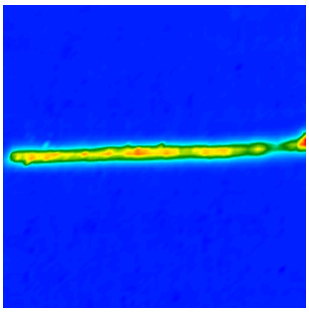

Map 5: M

Slide #34 CpATCC 10% PDA

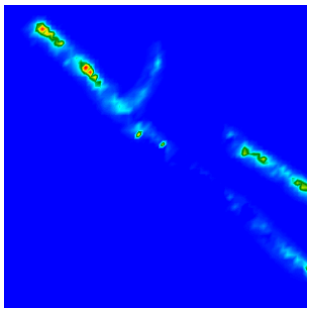

Map 1
colour: 0.0069 to 0.1836

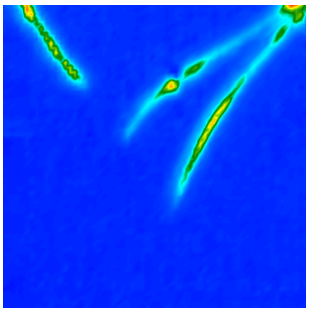

Map 2

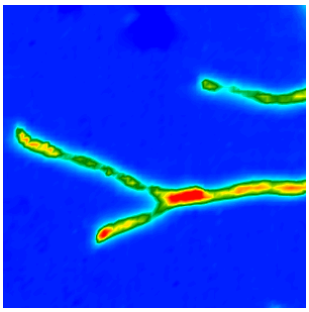

Map 3

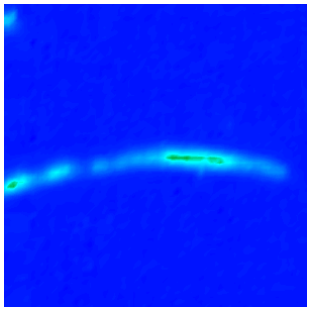

Map 4

Slide #40 CpATCC 10% and 100%

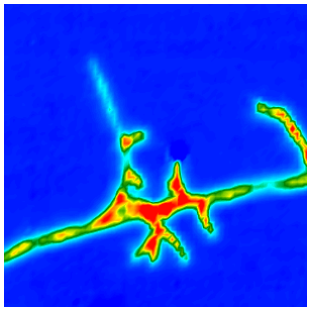

Map 1: M

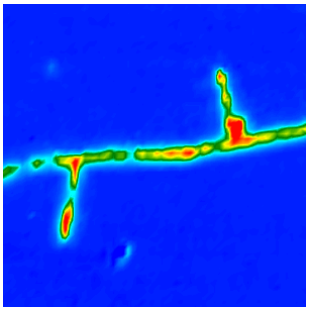

Map 2: M

Slide #45 CpATCC 100% PDA

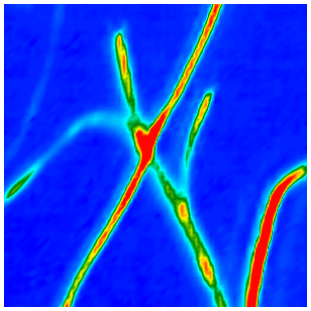

Map 1

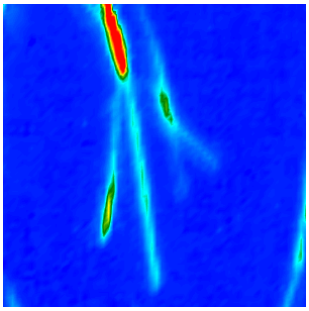

Map2

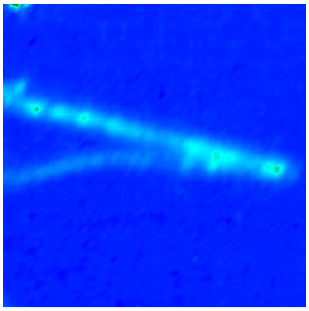

Map 3

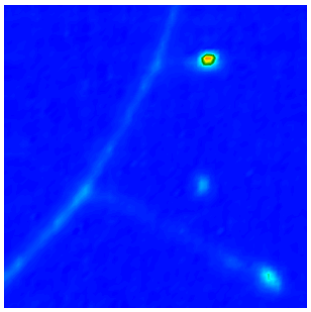

Map 5: M

Slide #45 CpATCC 10% PDA

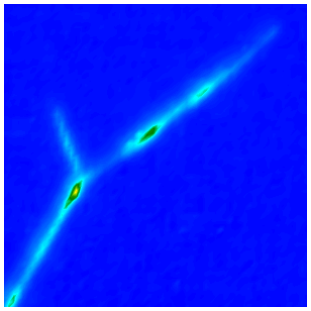

Map 1

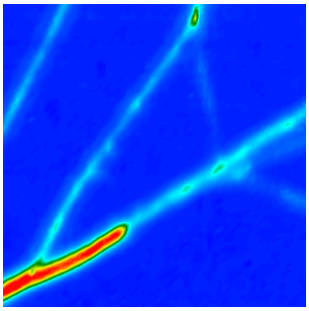

Map2

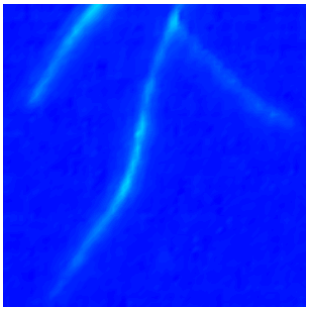

Map 3

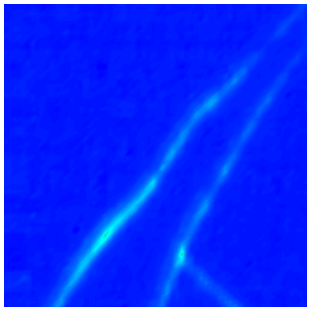

Map 4

Slide #45 CpATCC 3% PDA

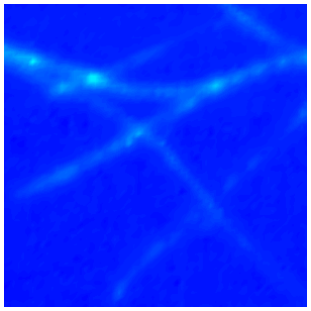

Map 1

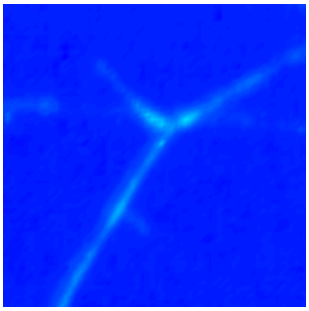

Map 5

Cp4666D

Slide #37 Cp4666D 100% PDA

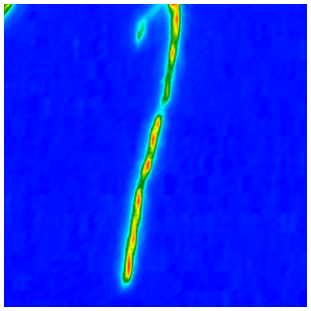
Map 1: M

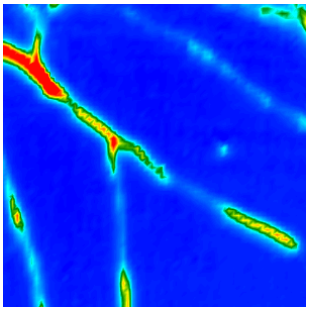
Map2

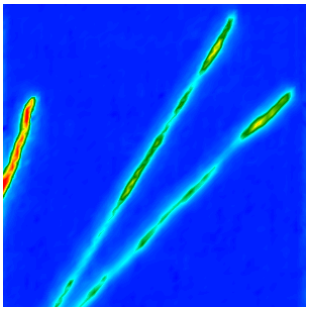
Map 3: M

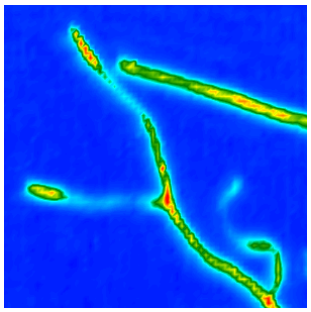
Map 4: M

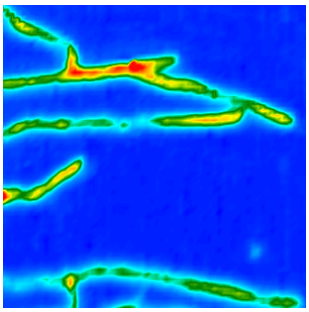
Map 5: M

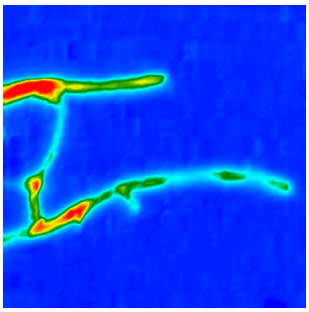
Map 6: M

Slide #37 Cp4666D ON GOLD 100% PDA

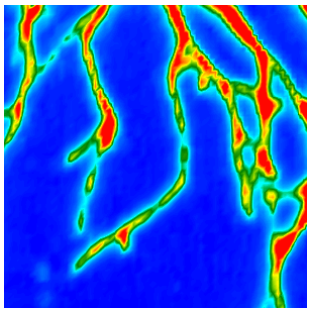
Map 7: M

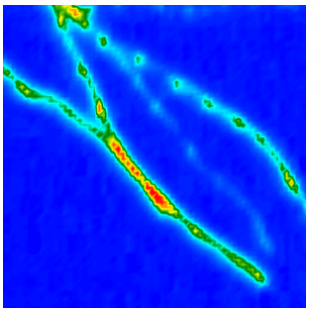
Map8: M

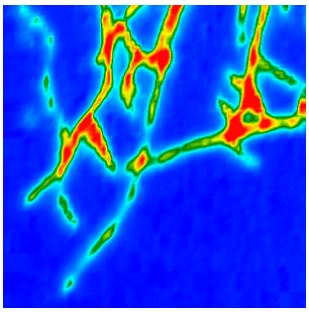
Map 9: M

Slide #37 Cp4666D 10% PDA

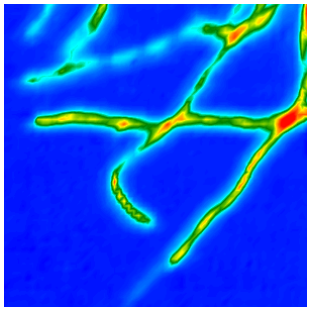

Map 1: M

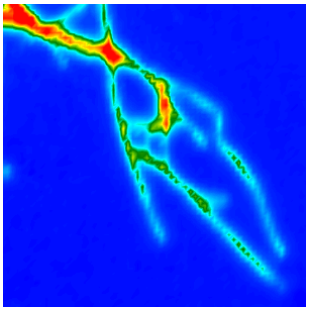

Map 2: M
colour: -0.100 to 8.000

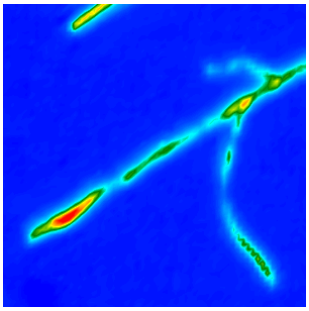

Map 3: M

Slide #39 Cp4666D 100% PDA

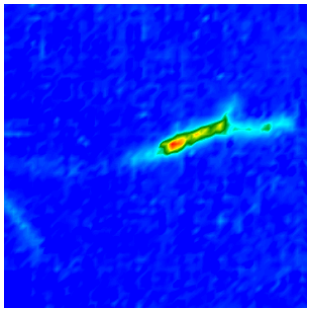

Map 1
colour: 0.0323 to 0.5254

Slide #39 Cp4666D 10% PDA

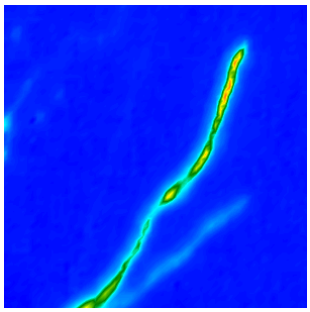

Map 1

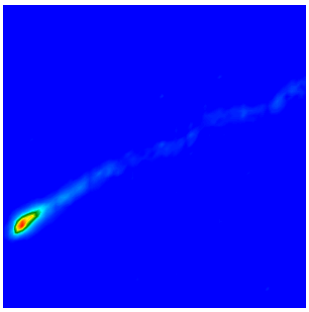

Map 2
colour: 0.1178 to 1.5691

Slide #46 Cp4666D 100% PDA

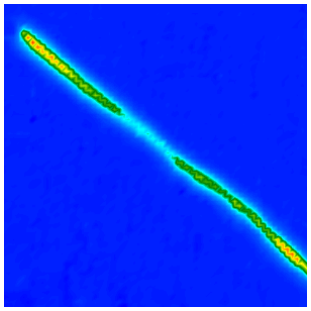

Map 1: M

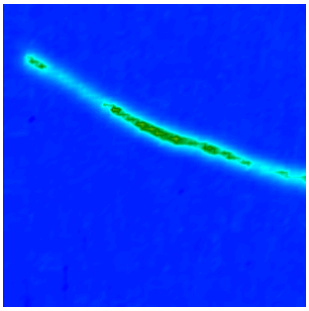

Map 2: M

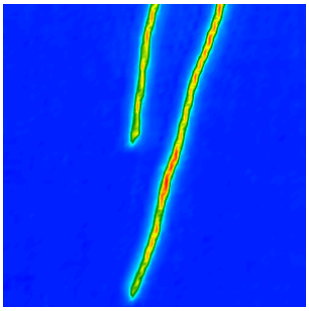

Map 3

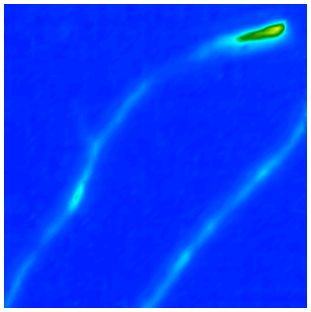

Map 4: M

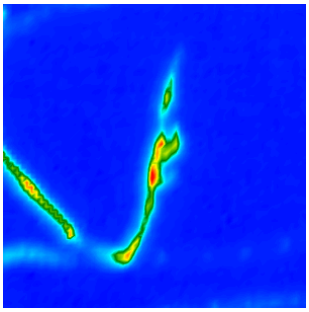

Map 5

Slide #46 Cp4666D 10% PDA

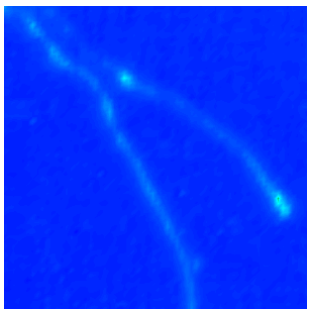

Map 1: M

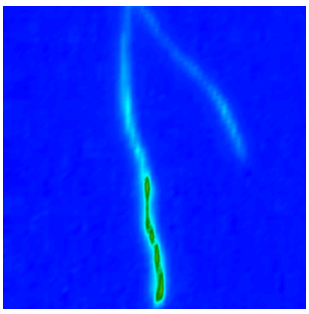

Map 2

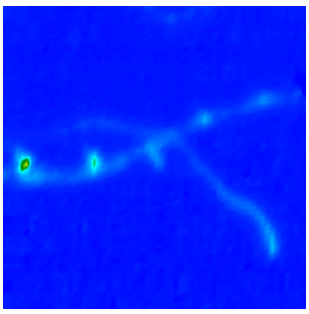

Map 3

Slide #46 Cp4666D 3% PDA

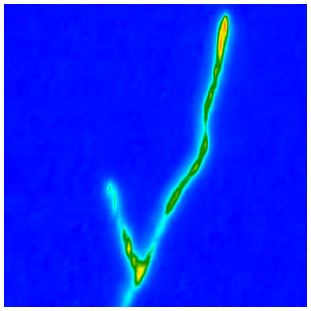

Map 1

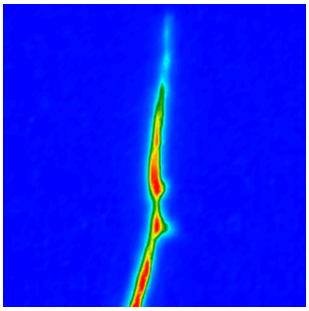

Map 2

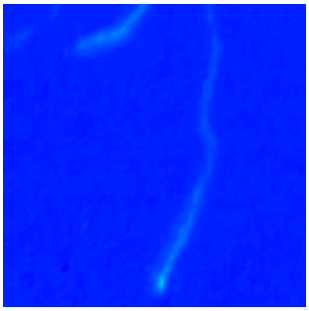

Map 3

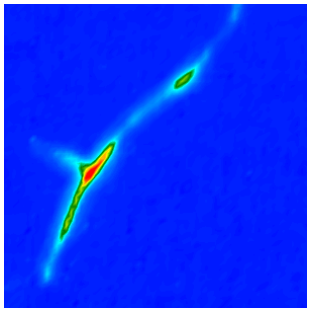

Map 4

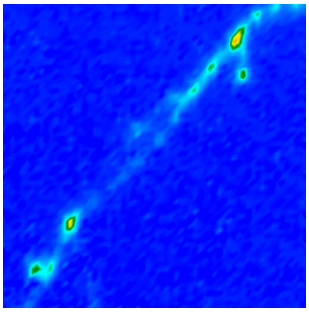

Map 5

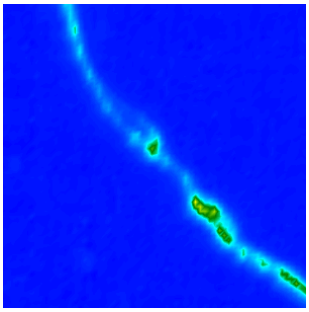

Map 6

Slide #46 Cp4666D 1% PDA

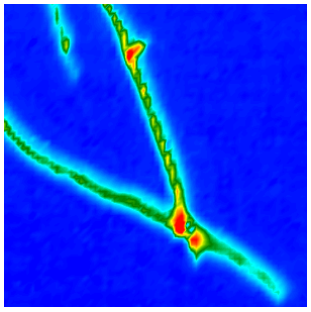

Map 1

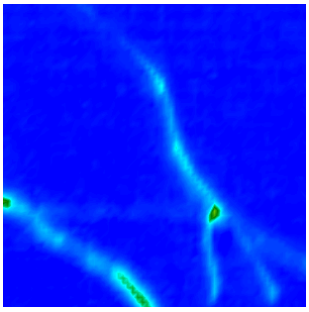

Map 2

Slide #63 Cp4666D 1x GYE

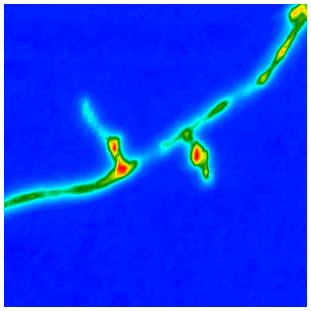

Map 1

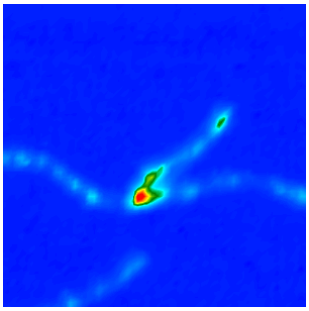

Map 3: M

Slide #63 Cp4666D 0.1x GYE

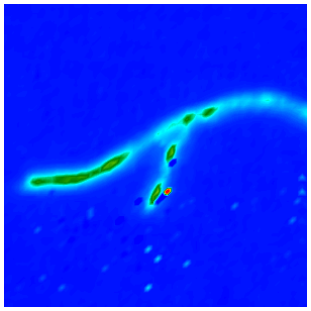

Map 1: M

Slide #135 Cp4666D Block A 100% PDA

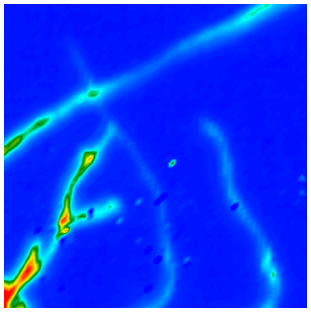

Map 1

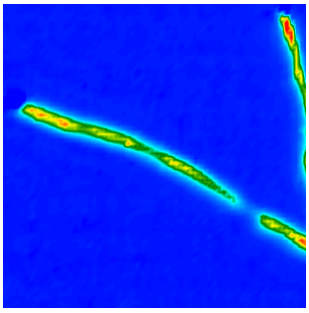

Map 2

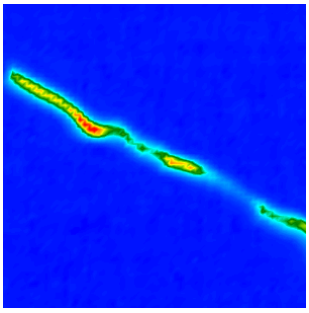

Map 3

Slide #135 Cp4666D Block B 100% PDA

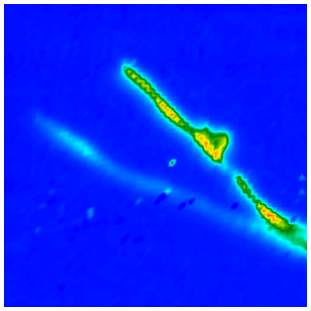
Map 1

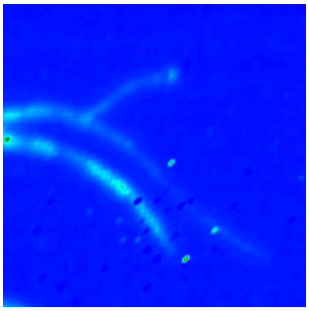
Map 2

Slide #135 CPA Block C 100% PDA

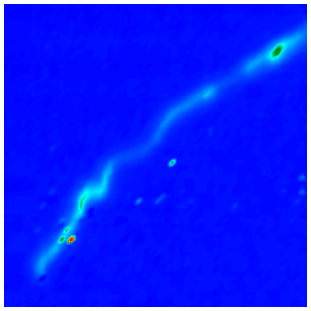
Map 1

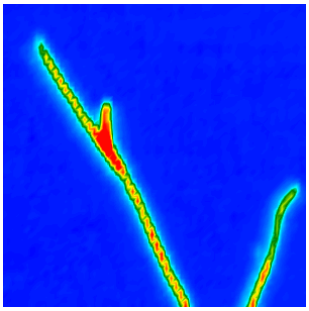
Map 2

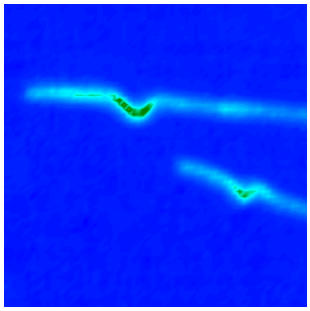
Map 3

Slide #135 CPA Block D 100% PDA

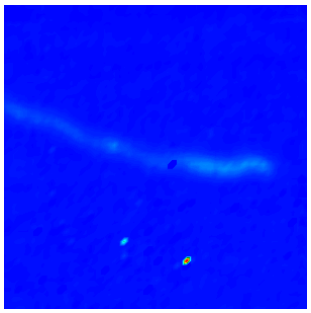
Map 1

Appendix III: Raman Spectra

Spectra are displayed in the following order (on the same scale and offset):

tip, 50 µm, 100 µm (bottom to top)

<u>Cp4666D</u>

Slide #37 Cp4666D 100% PDA

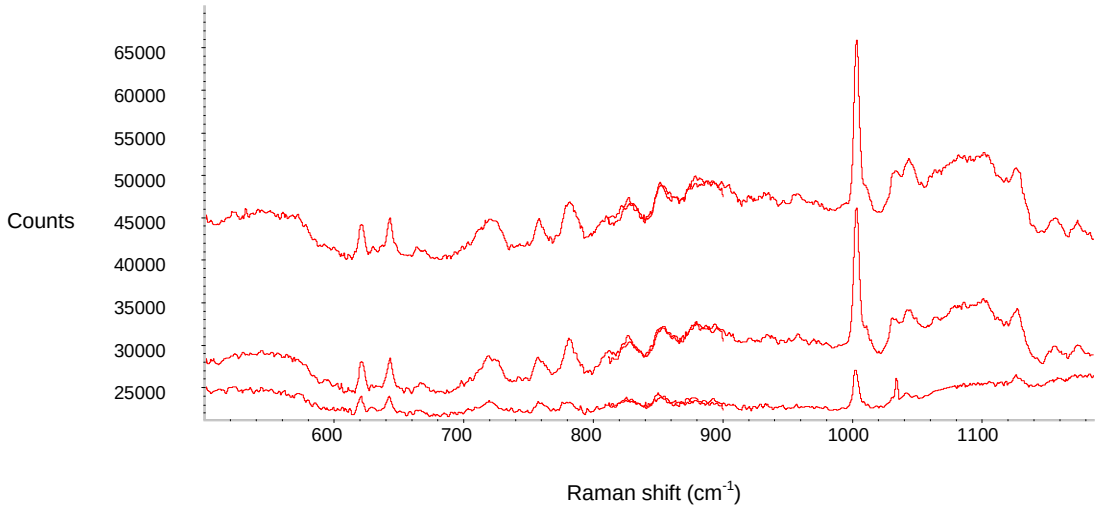

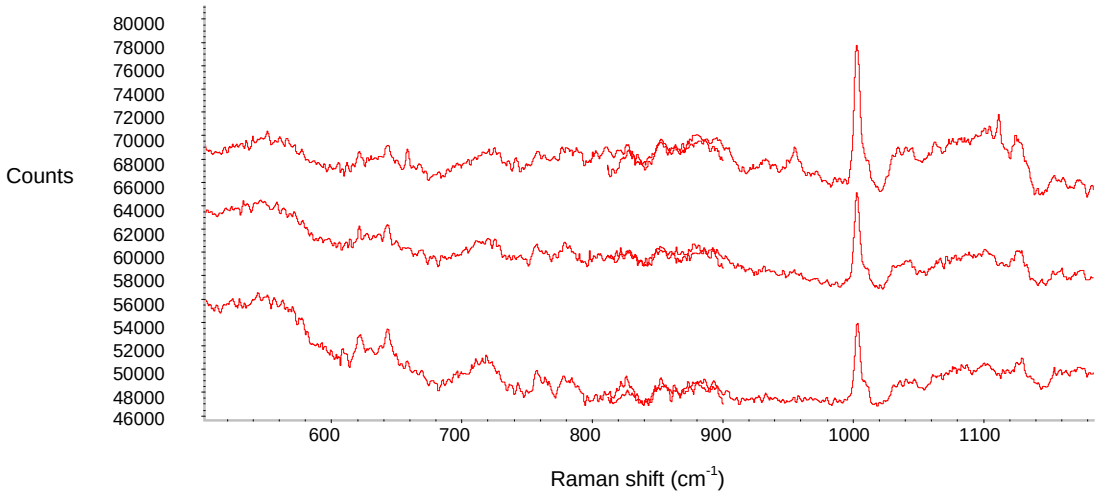
Counts
80000
78000
76000
74000
72000
70000
68000
66000
64000
62000
60000
58000
56000
54000
52000
50000
48000
46000
600
700
800
900
1000
1100
Raman shift (cm-1)

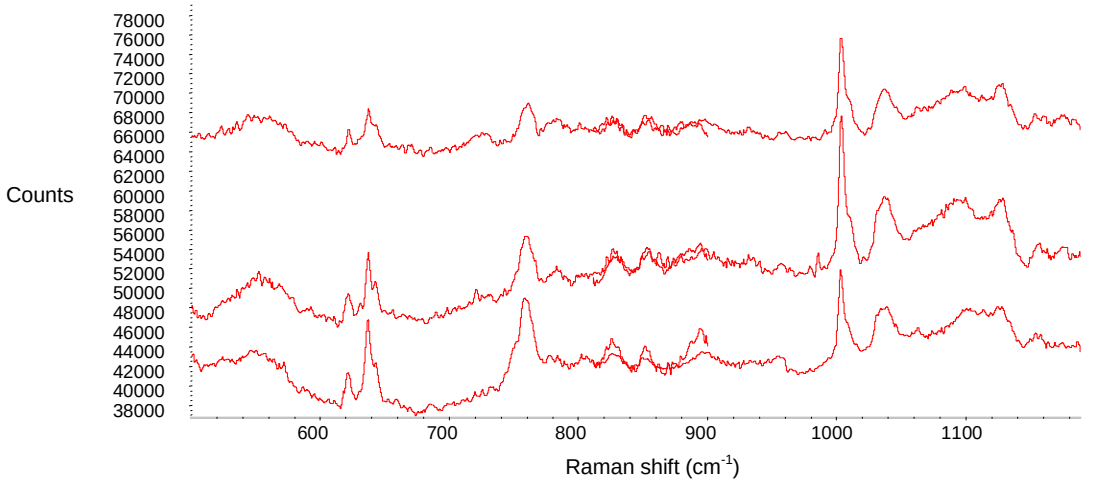
Counts
78000
76000
74000
72000
70000
68000
66000
64000
62000
60000
58000
56000
54000
52000
50000
48000
46000
44000
42000
40000
38000
600
700
800
900
1000
1100
Raman shift (cm-1)

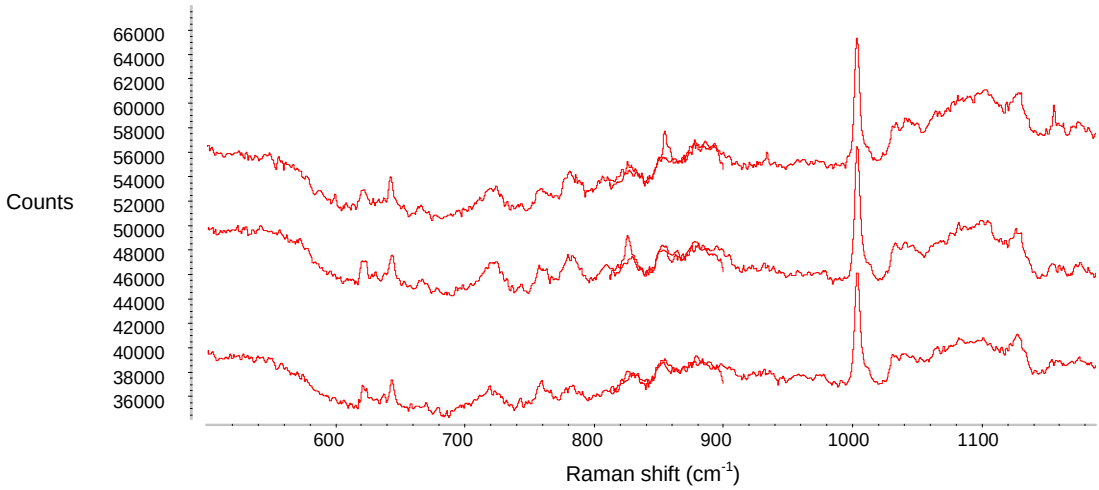
Counts
66000
64000
62000
60000
58000
56000
54000
52000
50000
48000
46000
44000
42000
40000
38000
36000
600
700
800
900
1000
1100
Raman shift (cm-1)

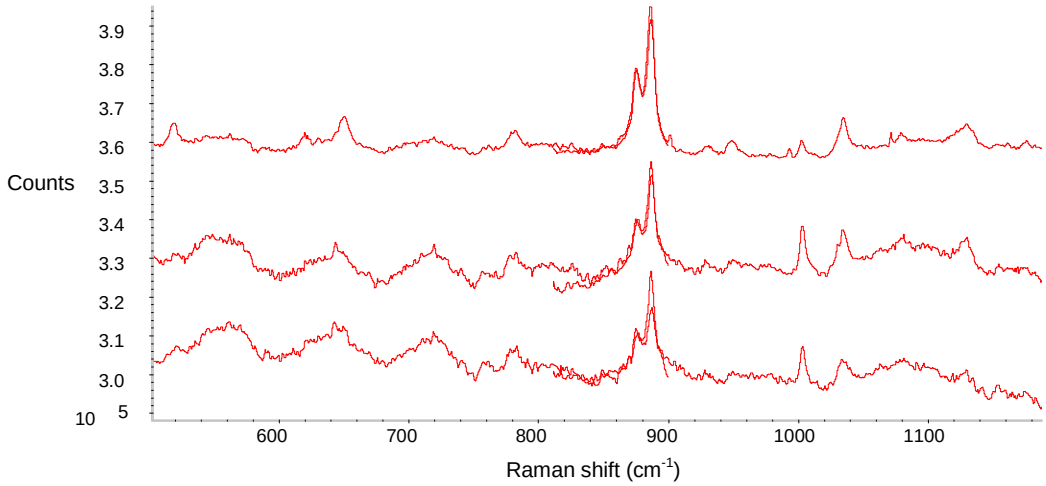
Counts
3.9
3.8
3.7
3.6
3.5
3.4
3.3
3.2
3.1
3.0
10 5
600
700
800
900
1000
1100
Raman shift (cm-1)

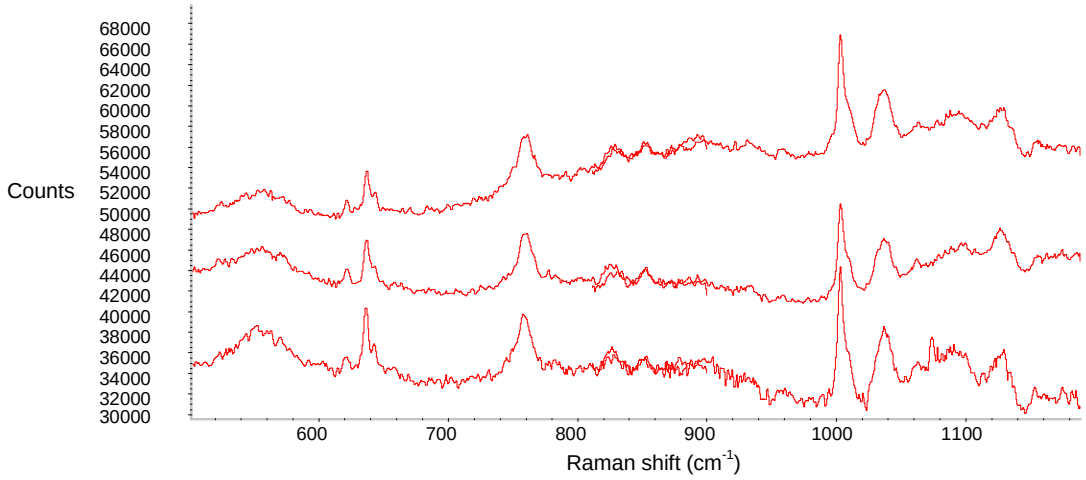
Counts
68000
66000
64000
62000
60000
58000
56000
54000
52000
50000
48000
46000
44000
42000
40000
38000
36000
34000
32000
30000
600
700
800
900
1000
1100
Raman shift (cm-1)

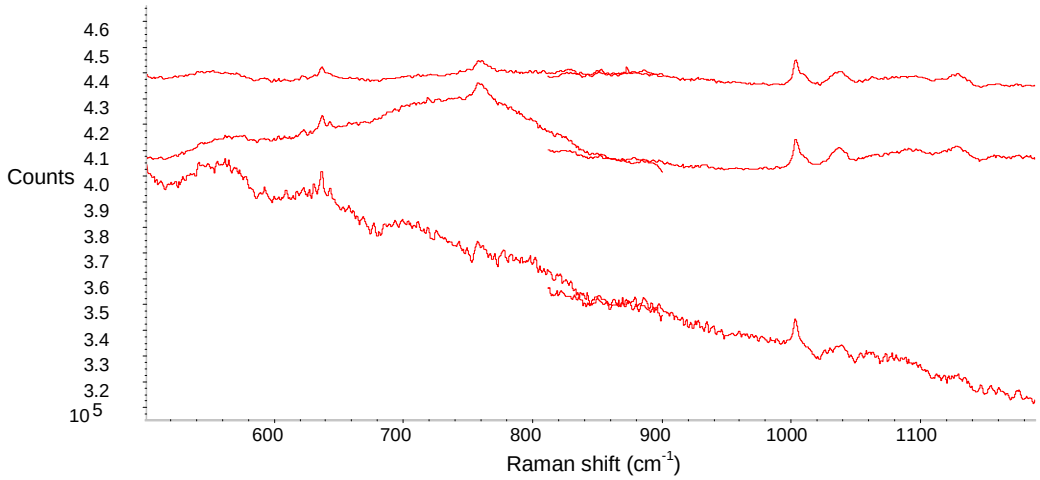
Counts
4.6
4.5
4.4
4.3
4.2
4.1
4.0
3.9
3.8
3.7
3.6
3.5
3.4
3.3
3.2
10 5
600
700
800
900
1000
1100
Raman shift (cm-1)

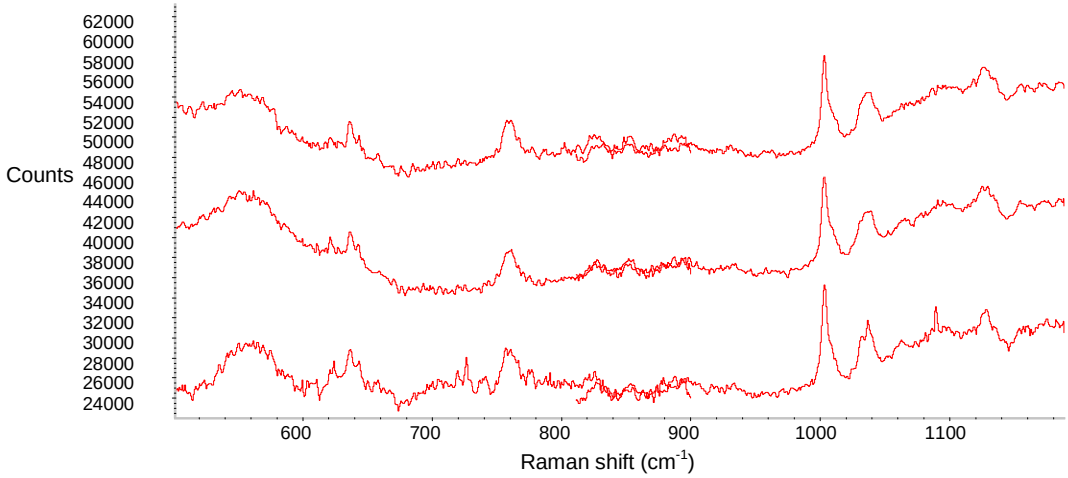
Counts
62000
60000
58000
56000
54000
52000
50000
48000
46000
44000
42000
40000
38000
36000
34000
32000
30000
28000
26000
24000
600
700
800
900
1000
1100
Raman shift (cm-1)

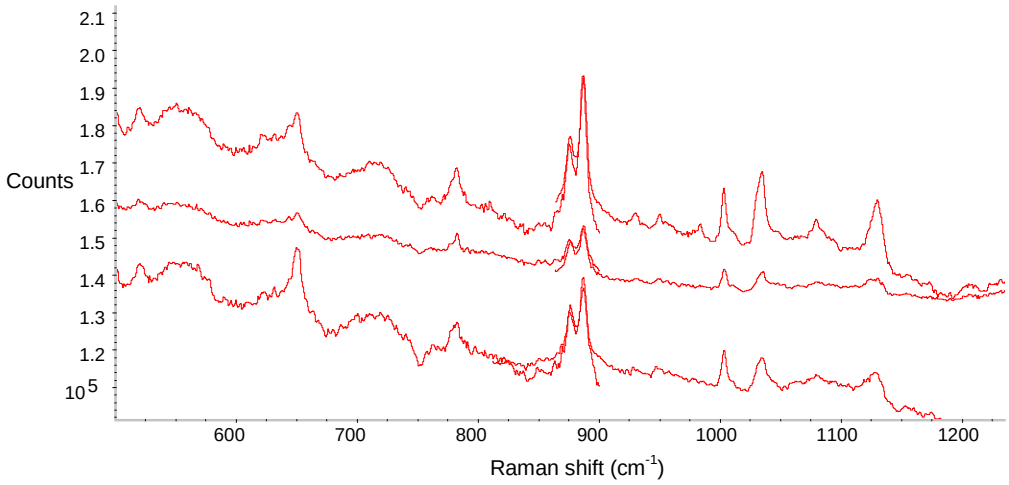
Counts
2.1
2.0
1.9
1.8
1.7
1.6
1.5
1.4
1.3
1.2
10^5
600
700
800
900
1000
1100
1200
Raman shift (cm-1)

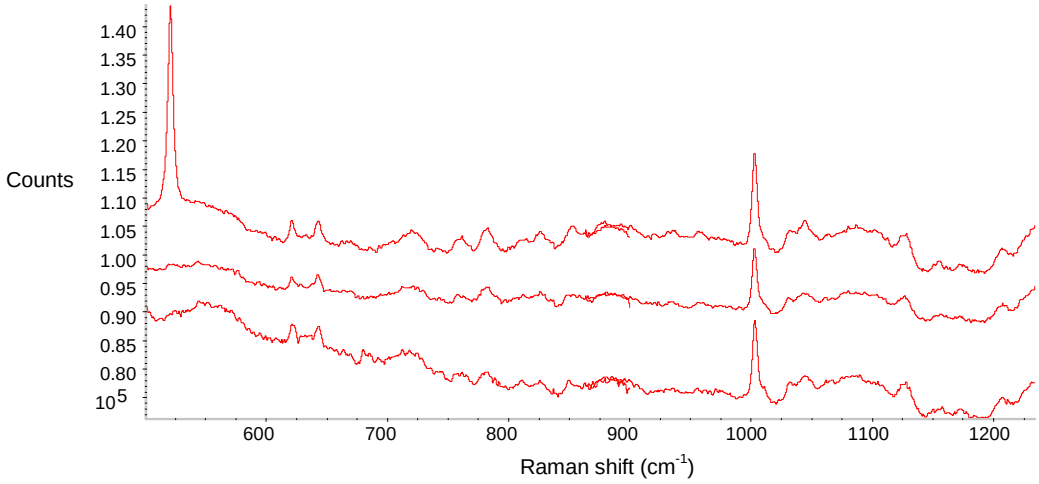
Counts
1.40
1.35
1.30
1.25
1.20
1.15
1.10
1.05
1.00
0.95
0.90
0.85
0.80
10^5
600
700
800
900
1000
1100
1200
Raman shift (cm-1)

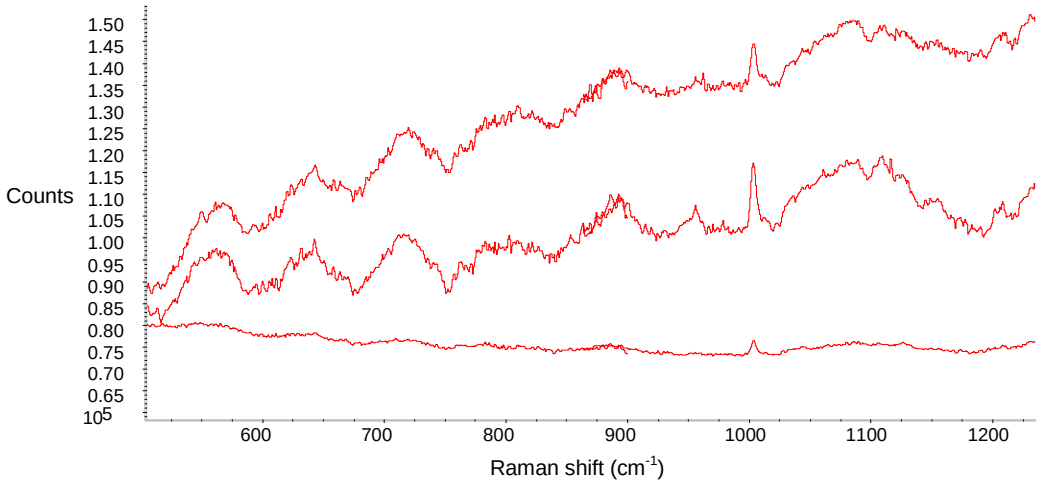
Counts
1.50
1.45
1.40
1.35
1.30
1.25
1.20
1.15
1.10
1.05
1.00
0.95
0.90
0.85
0.80
0.75
0.70
0.65
10^5
600
700
800
900
1000
1100
1200
Raman shift (cm-1)

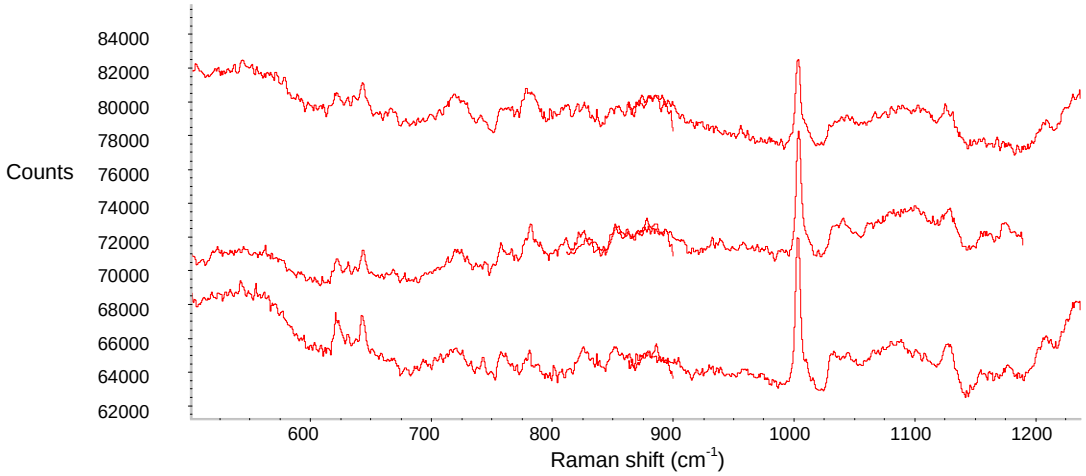
Counts
84000
82000
80000
78000
76000
74000
72000
70000
68000
66000
64000
62000
600
700
800
900
1000
1100
1200
Raman shift (cm-1)

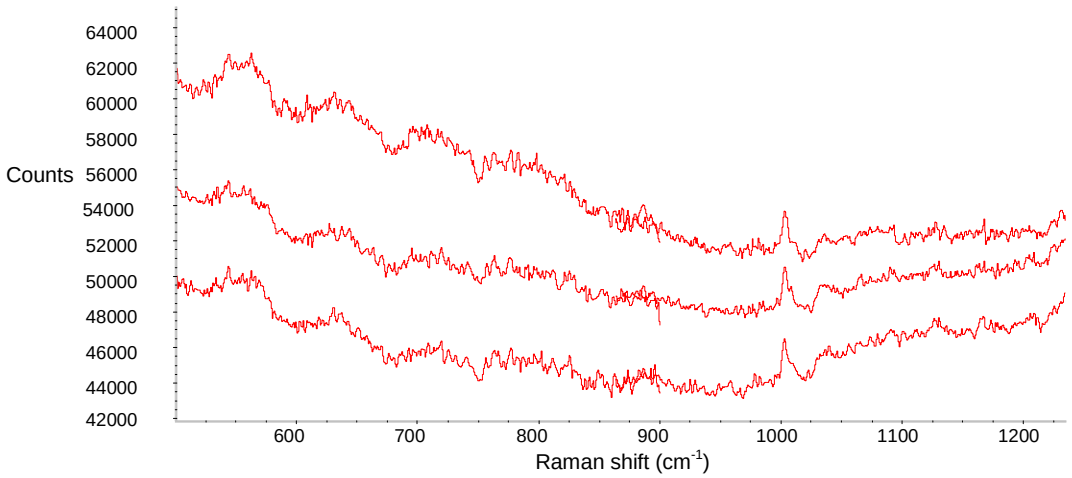
Counts
64000
62000
60000
58000
56000
54000
52000
50000
48000
46000
44000
42000
600
700
800
900
1000
1100
1200
Raman shift (cm-1)

Slide #37 Cp4666D 10% PDA

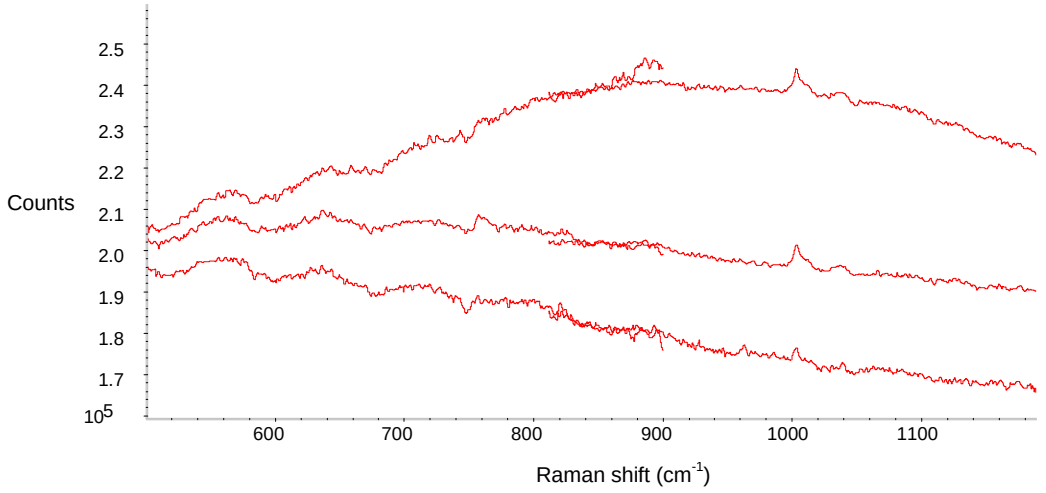

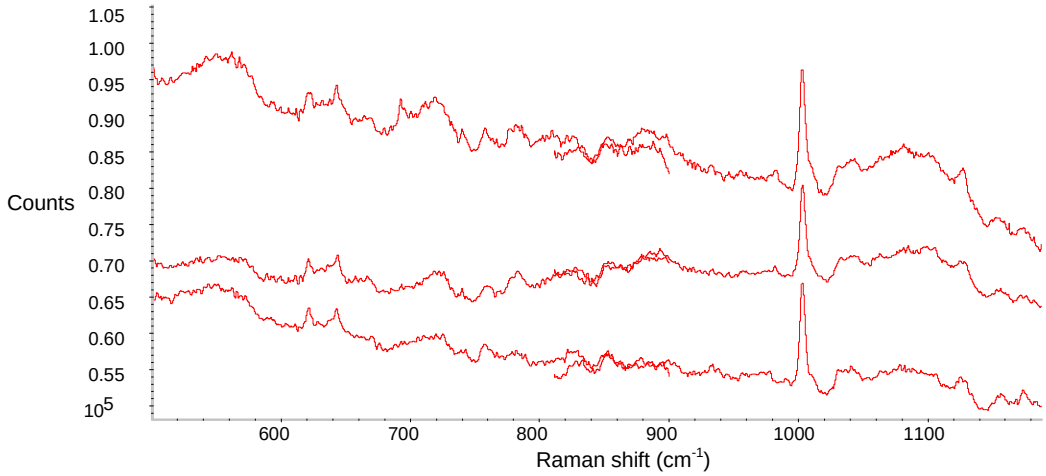

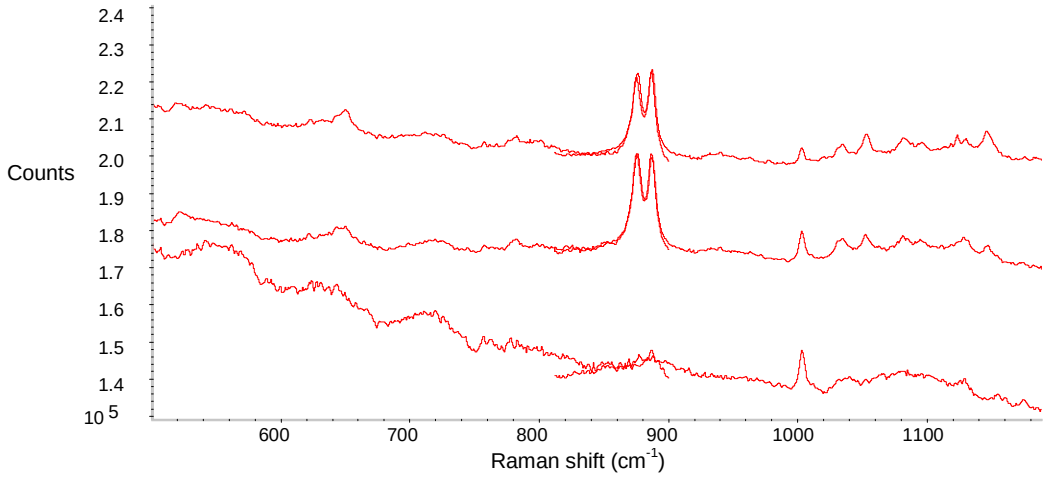

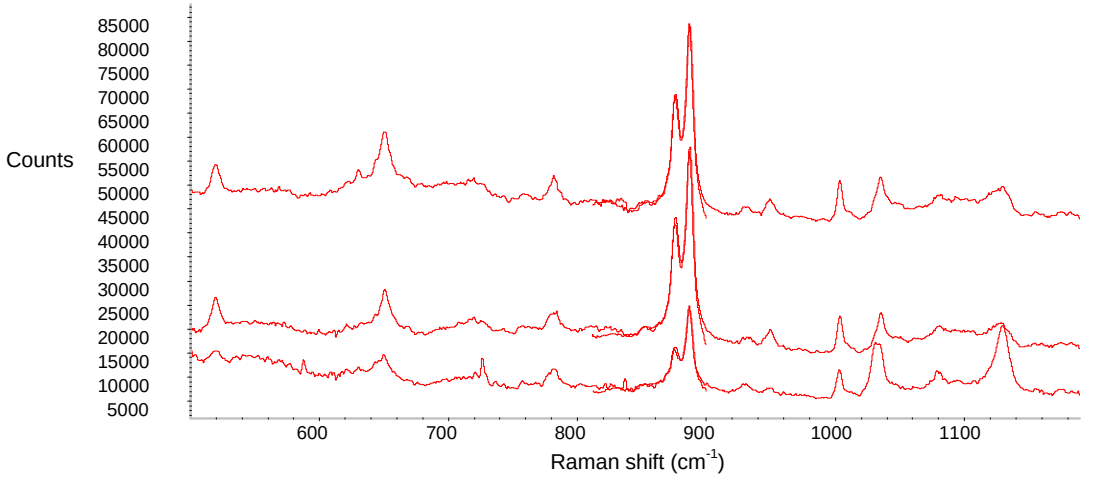
Counts
85000
80000
75000
70000
65000
60000
55000
50000
45000
40000
35000
30000
25000
20000
15000
10000
5000
600
700
800
900
1000
1100
Raman shift (cm-1)

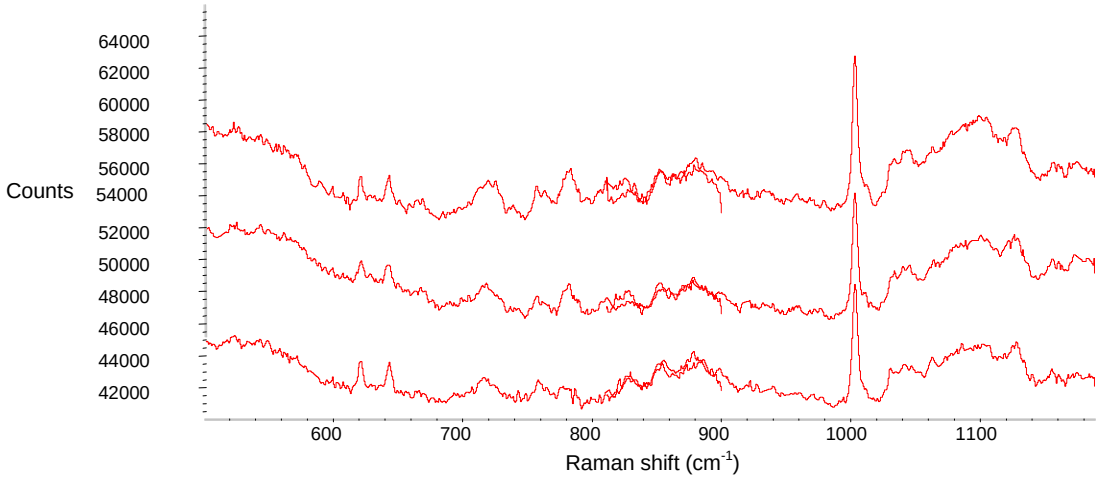
Counts
64000
62000
60000
58000
56000
54000
52000
50000
48000
46000
44000
42000
600
700
800
900
1000
1100
Raman shift (cm-1)

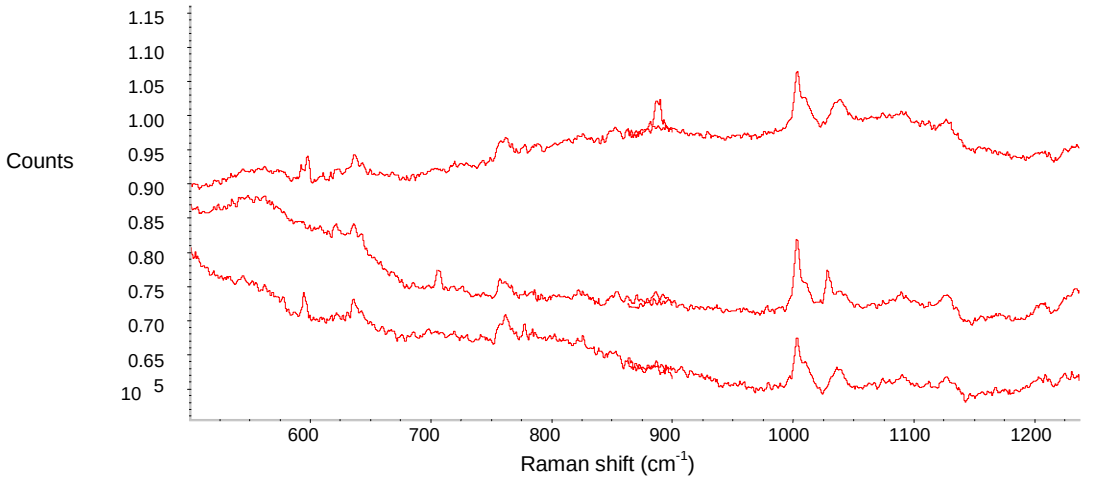
Counts
1.15
1.10
1.05
1.00
0.95
0.90
0.85
0.80
0.75
0.70
0.65
10 5
600
700
800
900
1000
1100
1200
Raman shift (cm-1)

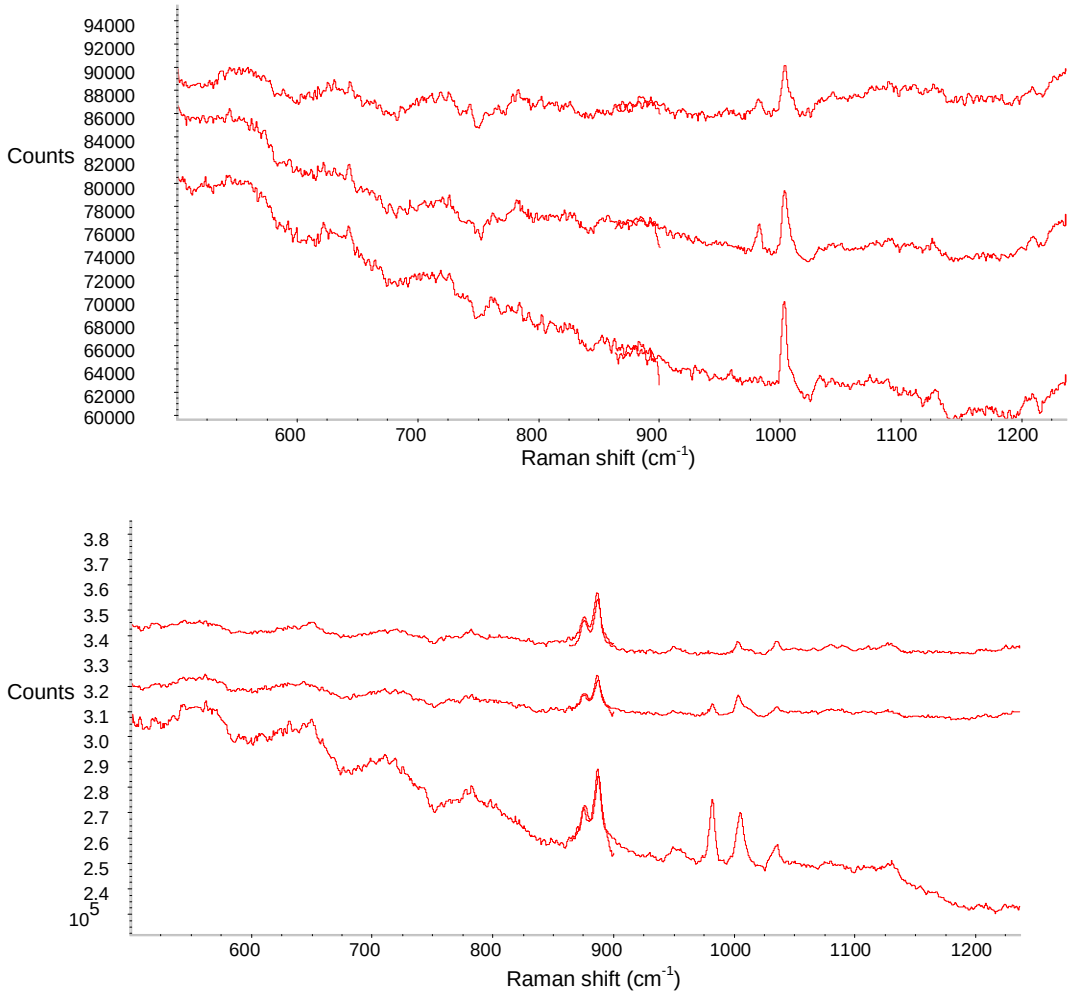

Slide #133 Cp4666D no virus 100% PDA

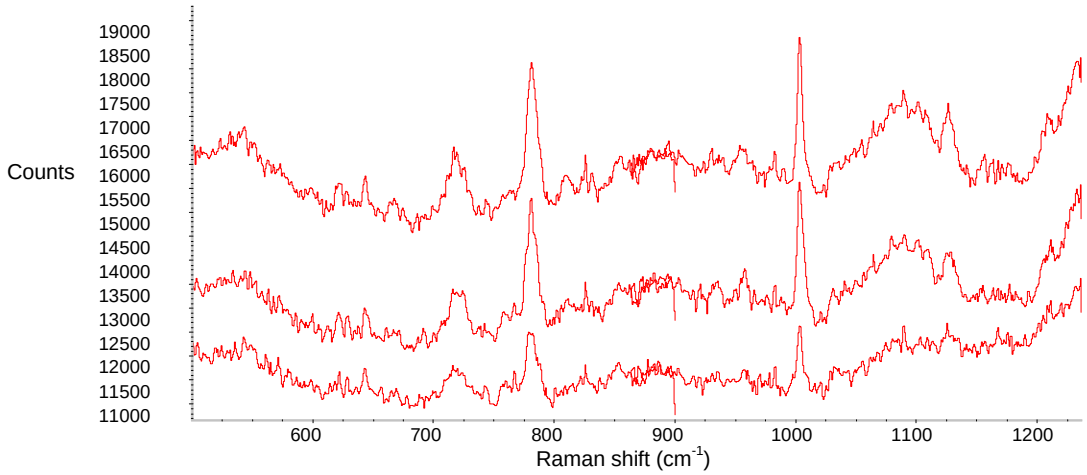

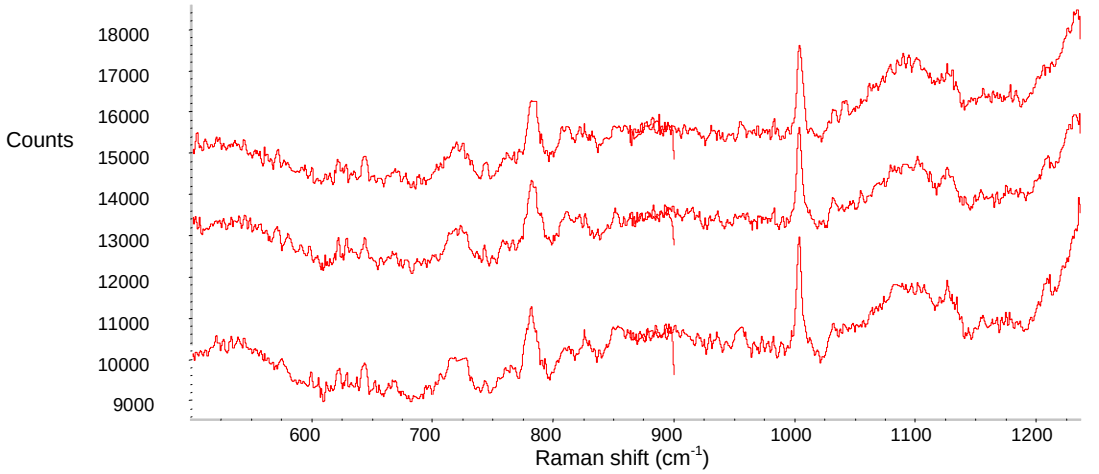
Counts
18000
17000
16000
15000
14000
13000
12000
11000
10000
9000
600
700
800
900
1000
1100
1200
Raman shift (cm-1)

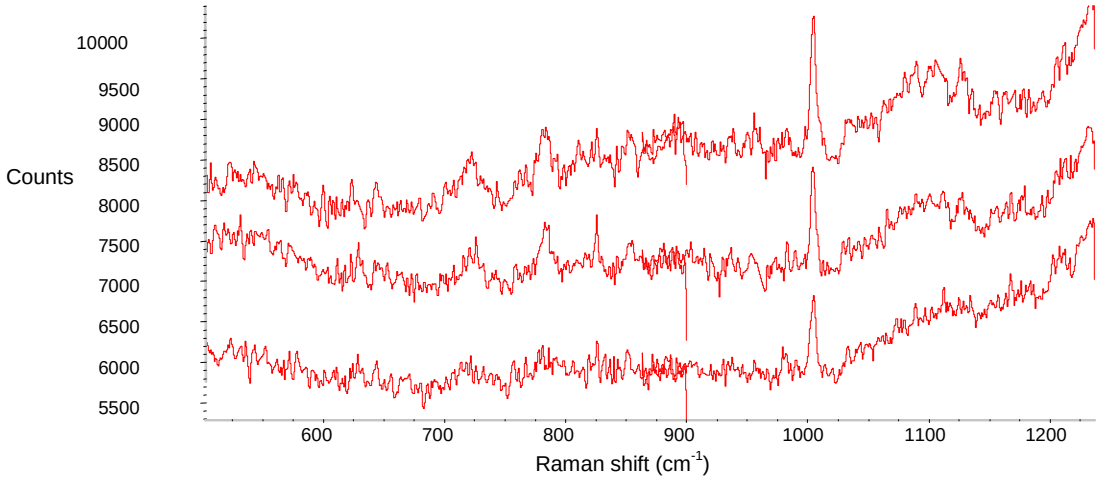
Counts
10000
9500
9000
8500
8000
7500
7000
6500
6000
5500
600
700
800
900
1000
1100
1200
Raman shift (cm-1)

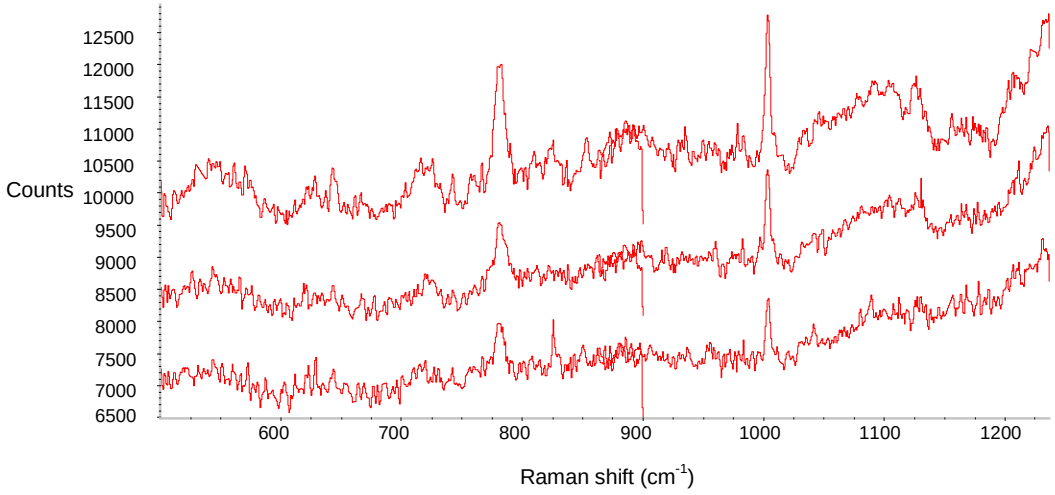
Counts
12500
12000
11500
11000
10500
10000
9500
9000
8500
8000
7500
7000
6500
600
700
800
900
1000
1100
1200
Raman shift (cm-1)

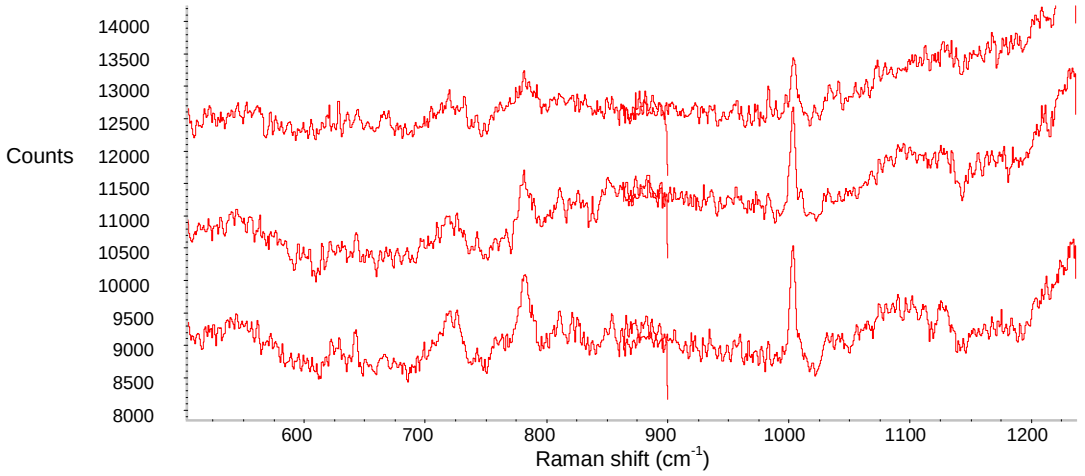
Counts
14000
13500
13000
12500
12000
11500
11000
10500
10000
9500
9000
8500
8000
600
700
800
900
1000
1100
1200
Raman shift (cm-1)

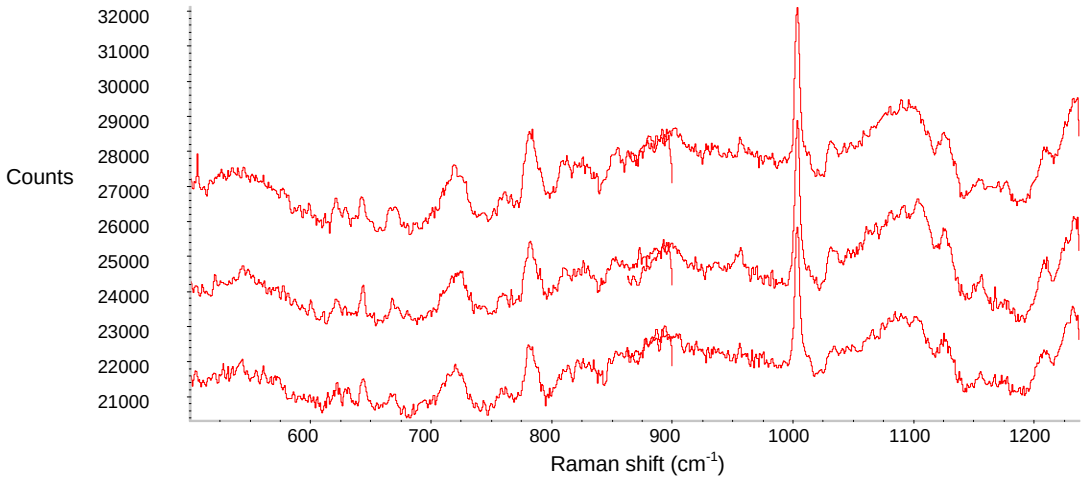
Counts
32000
31000
30000
29000
28000
27000
26000
25000
24000
23000
22000
21000
600
700
800
900
1000
1100
1200
Raman shift (cm-1)

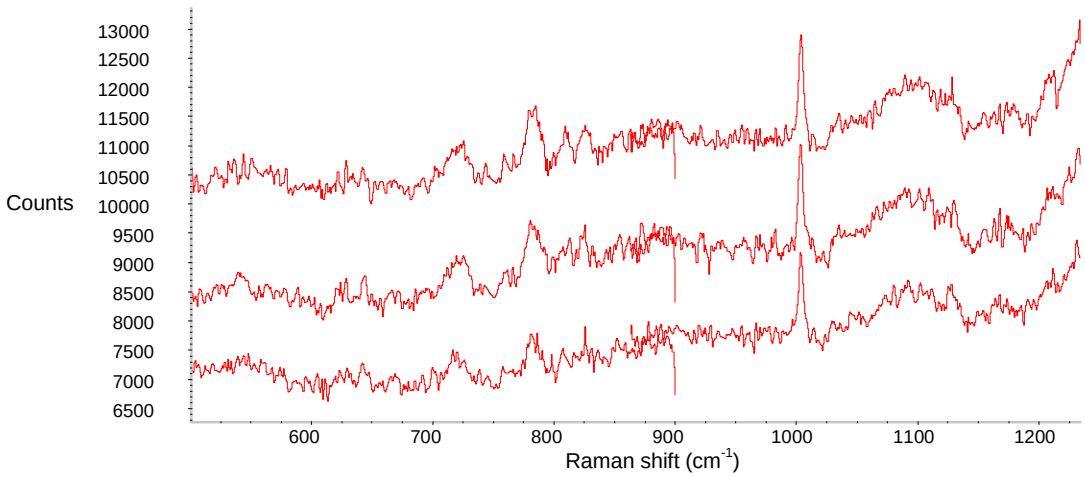
Counts
13000
12500
12000
11500
11000
10500
10000
9500
9000
8500
8000
7500
7000
6500
600
700
800
900
1000
1100
1200
Raman shift (cm-1)

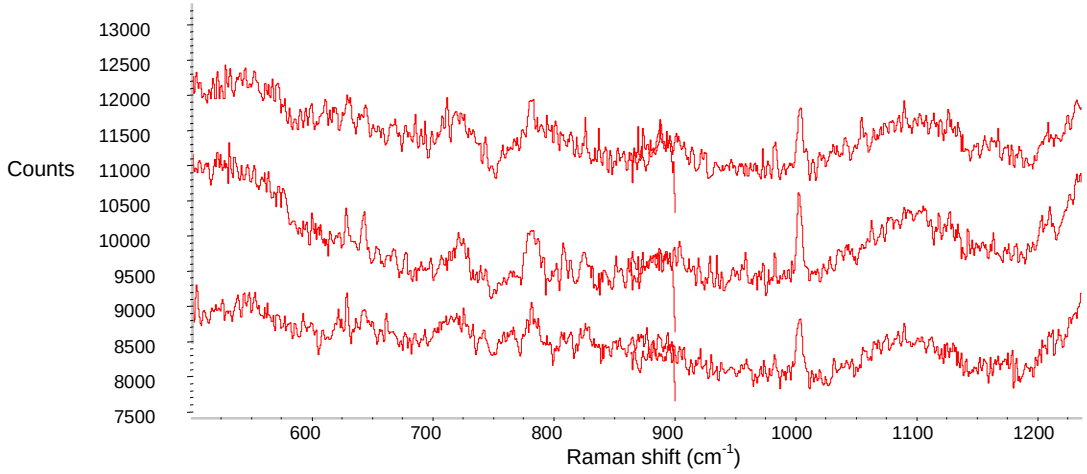

Slide #134 Cp4666D with virus 100% PDA

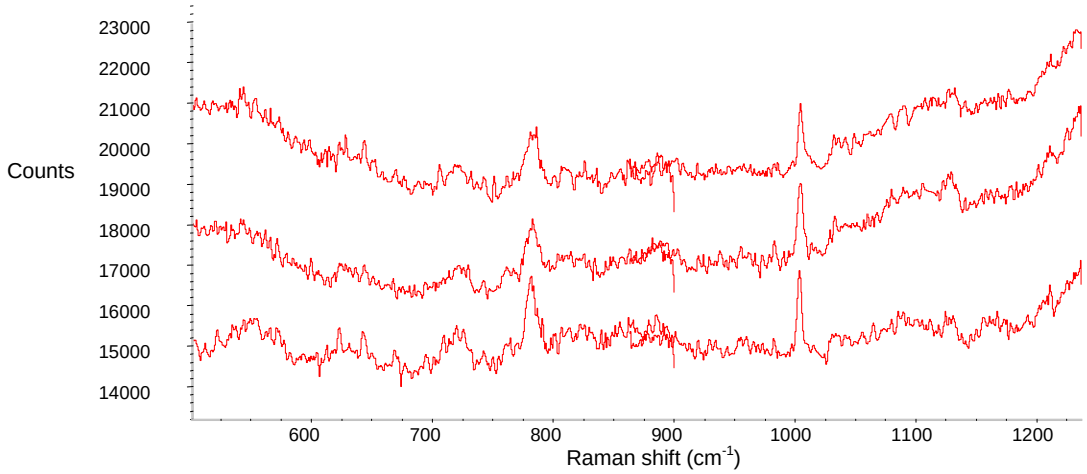

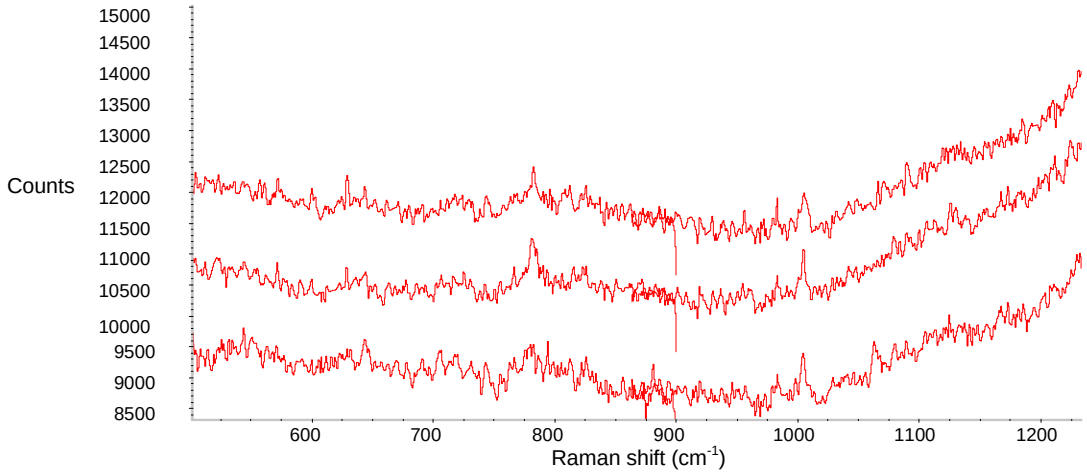

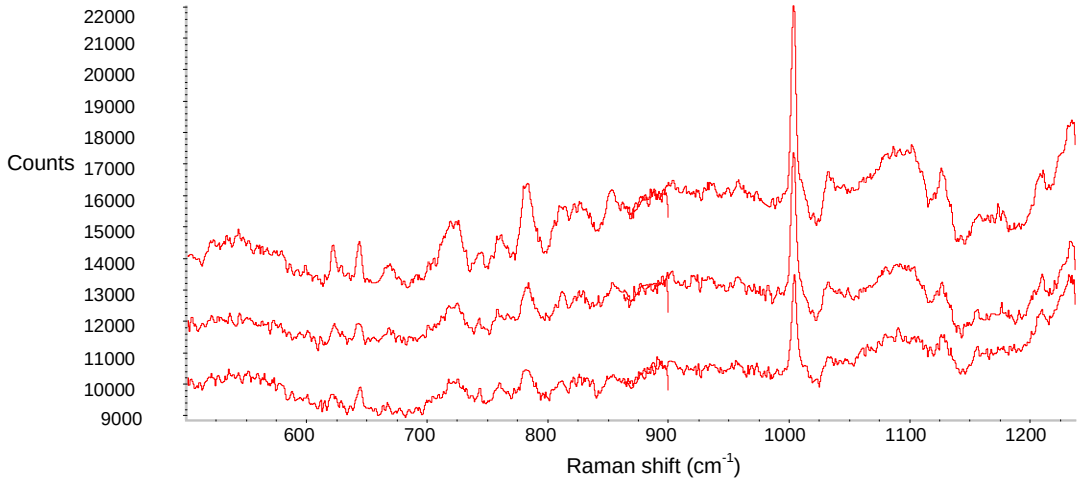

Slide #38 Fc18 100% PDA

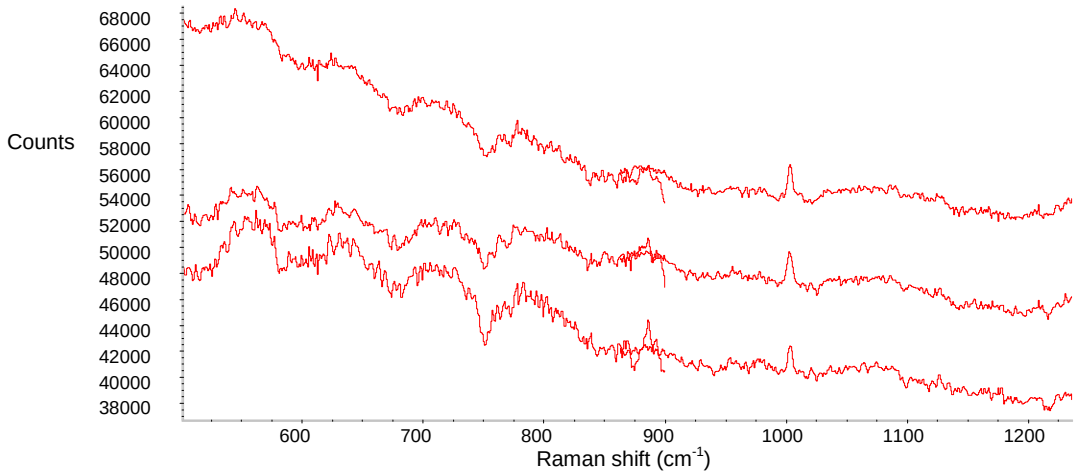

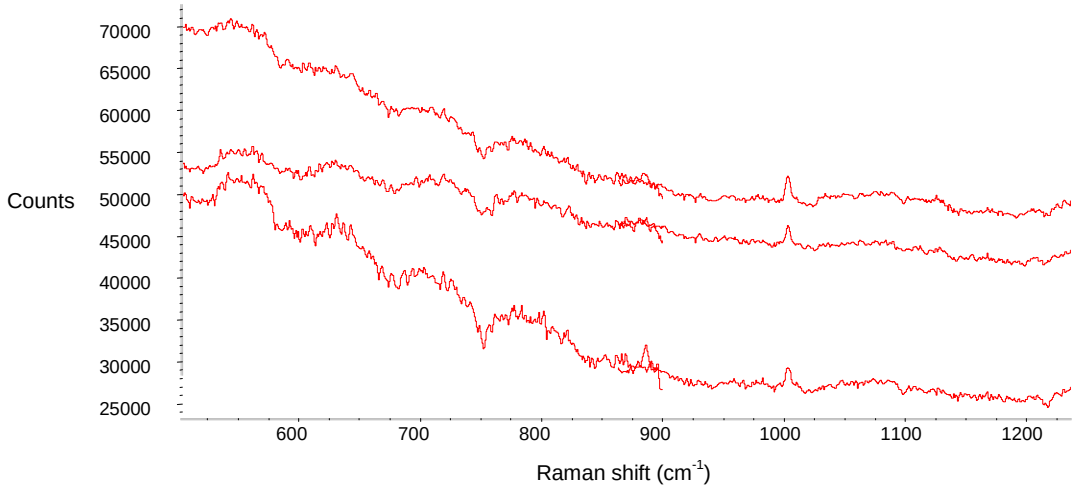

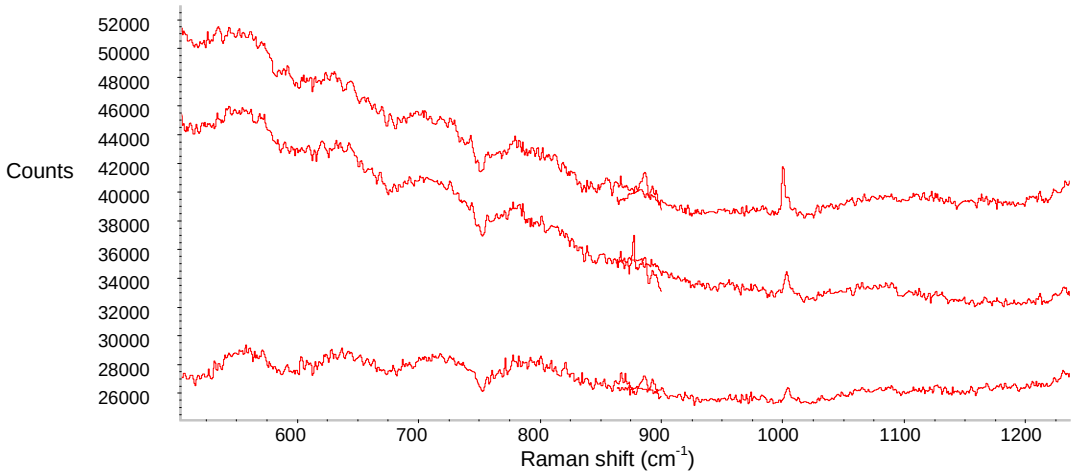
Counts
52000
50000
48000
46000
44000
42000
40000
38000
36000
34000
32000
30000
28000
26000
600
700
800
900
1000
1100
1200
Raman shift (cm-1)

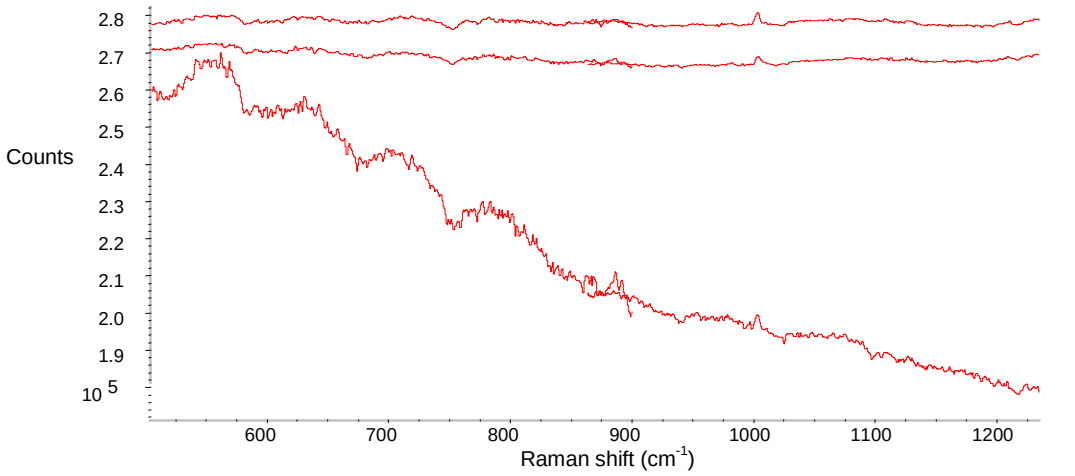
Counts
2.8
2.7
2.6
2.5
2.4
2.3
2.2
2.1
2.0
1.9
10 5
600
700
800
900
1000
1100
1200
Raman shift (cm-1)

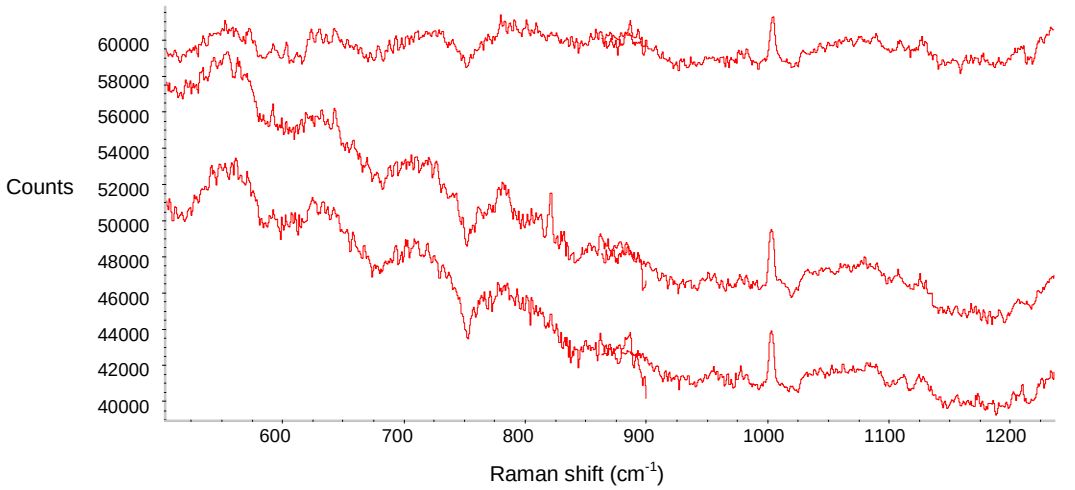
Counts
60000
58000
56000
54000
52000
50000
48000
46000
44000
42000
40000
600
700
800
900
1000
1100
1200
Raman shift (cm-1)

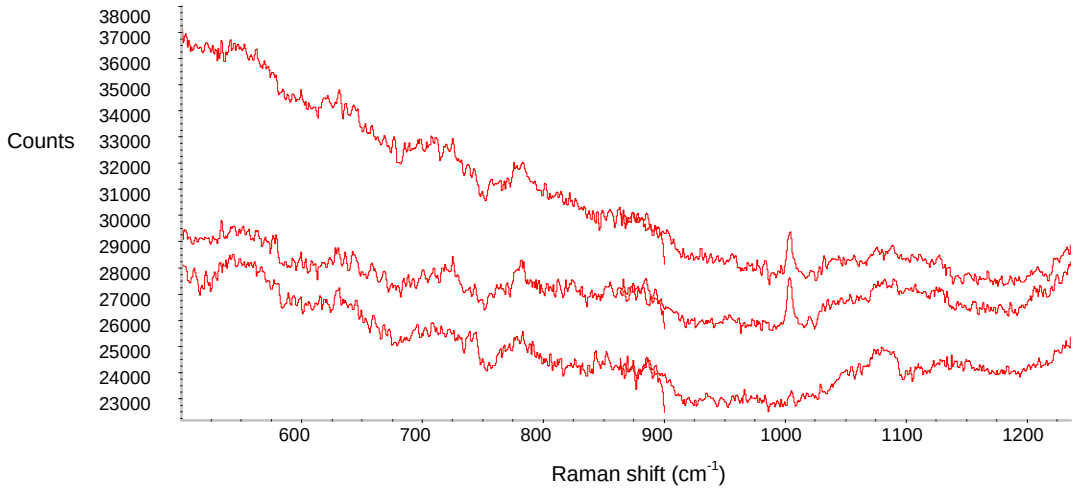

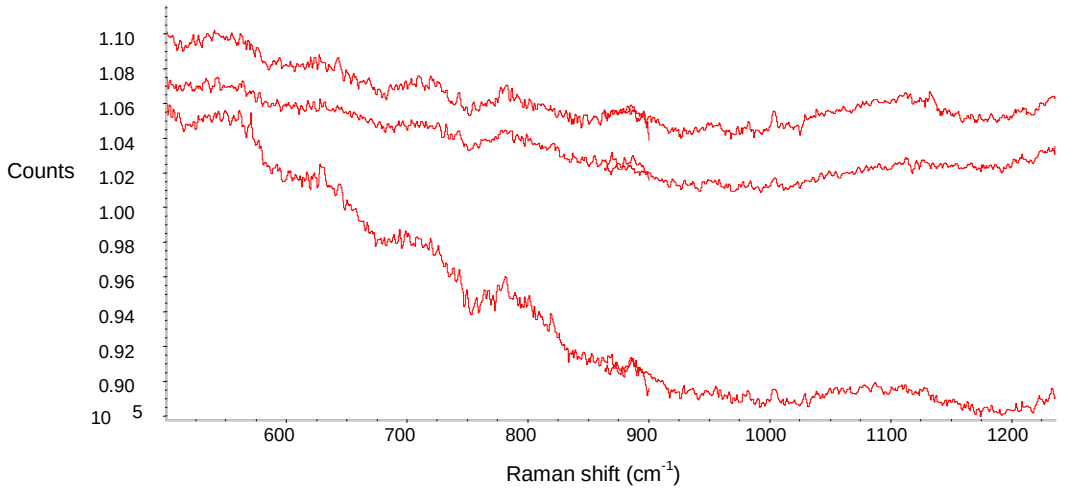

Slide #38 FcRed1 100% PDA

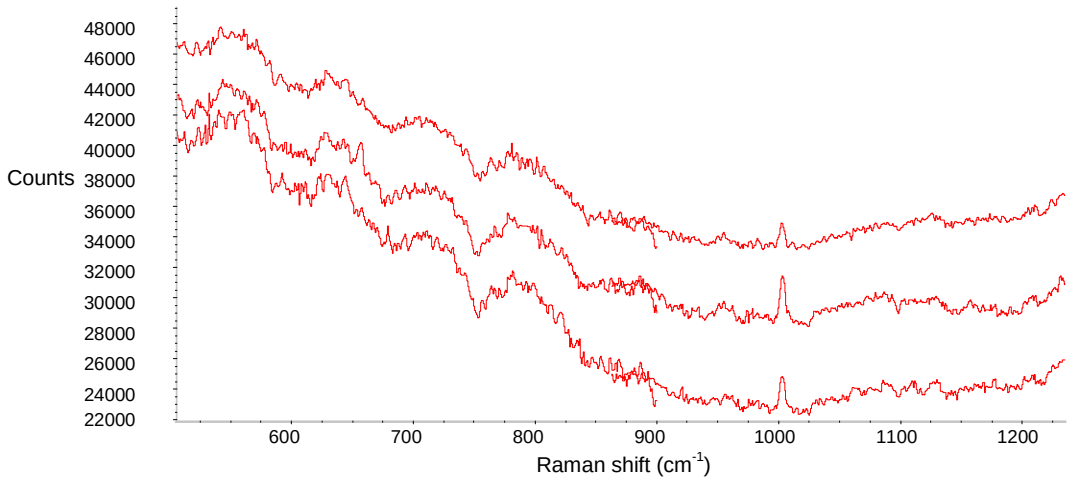

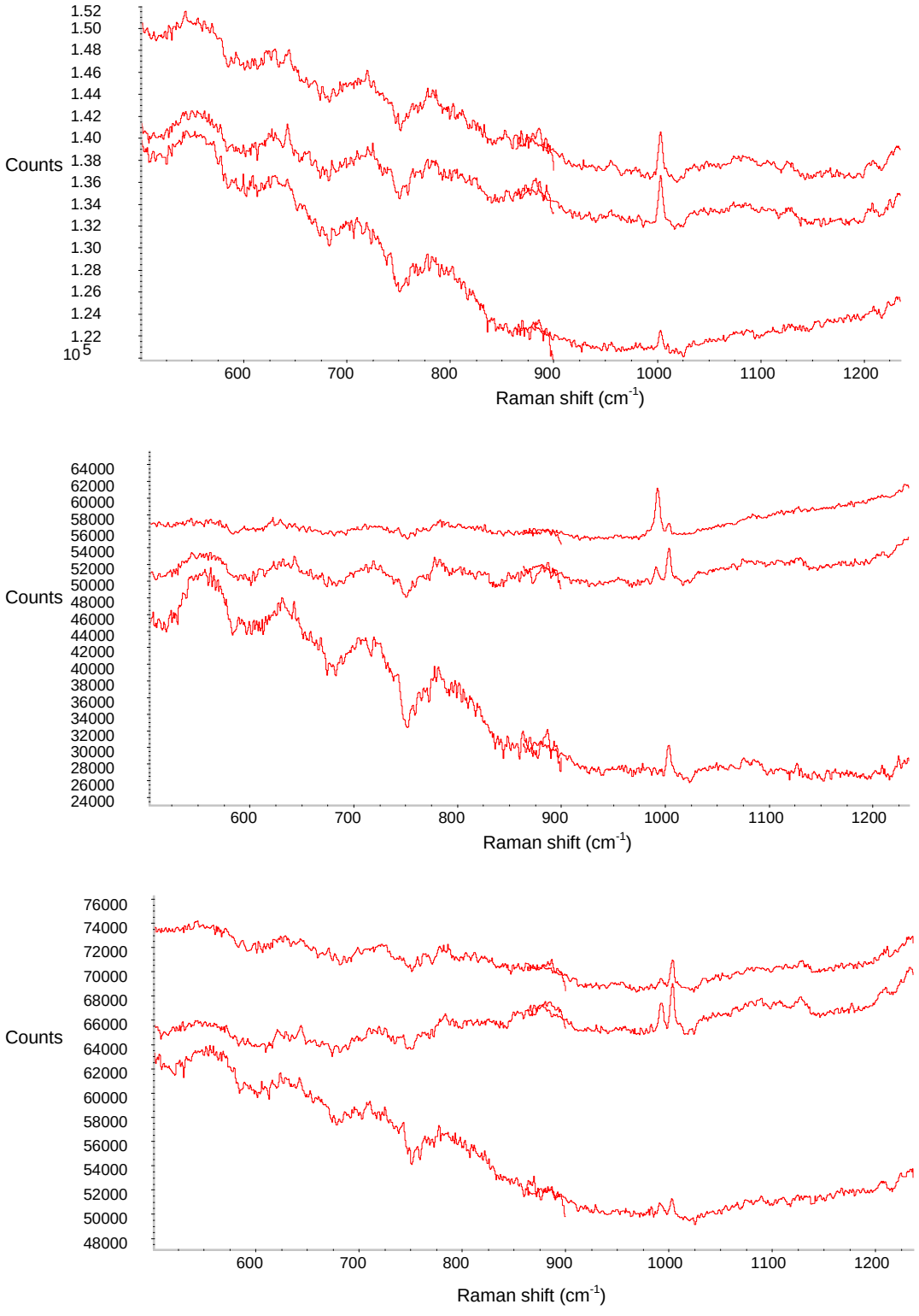
Counts
1.52
1.50
1.48
1.46
1.44
1.42
1.40
1.38
1.36
1.34
1.32
1.30
1.28
1.26
1.24
1.22
10^5
600
700
800
900
1000
1100
1200
Raman shift (cm-1)
Counts
64000
62000
60000
58000
56000
54000
52000
50000
48000
46000
44000
42000
40000
38000
36000
34000
32000
30000
28000
26000
24000
600
700
800
900
1000
1100
1200
Raman shift (cm-1)
Counts
76000
74000
72000
70000
68000
66000
64000
62000
60000
58000
56000
54000
52000
50000
48000
600
700
800
900
1000
1100
1200
Raman shift (cm-1)

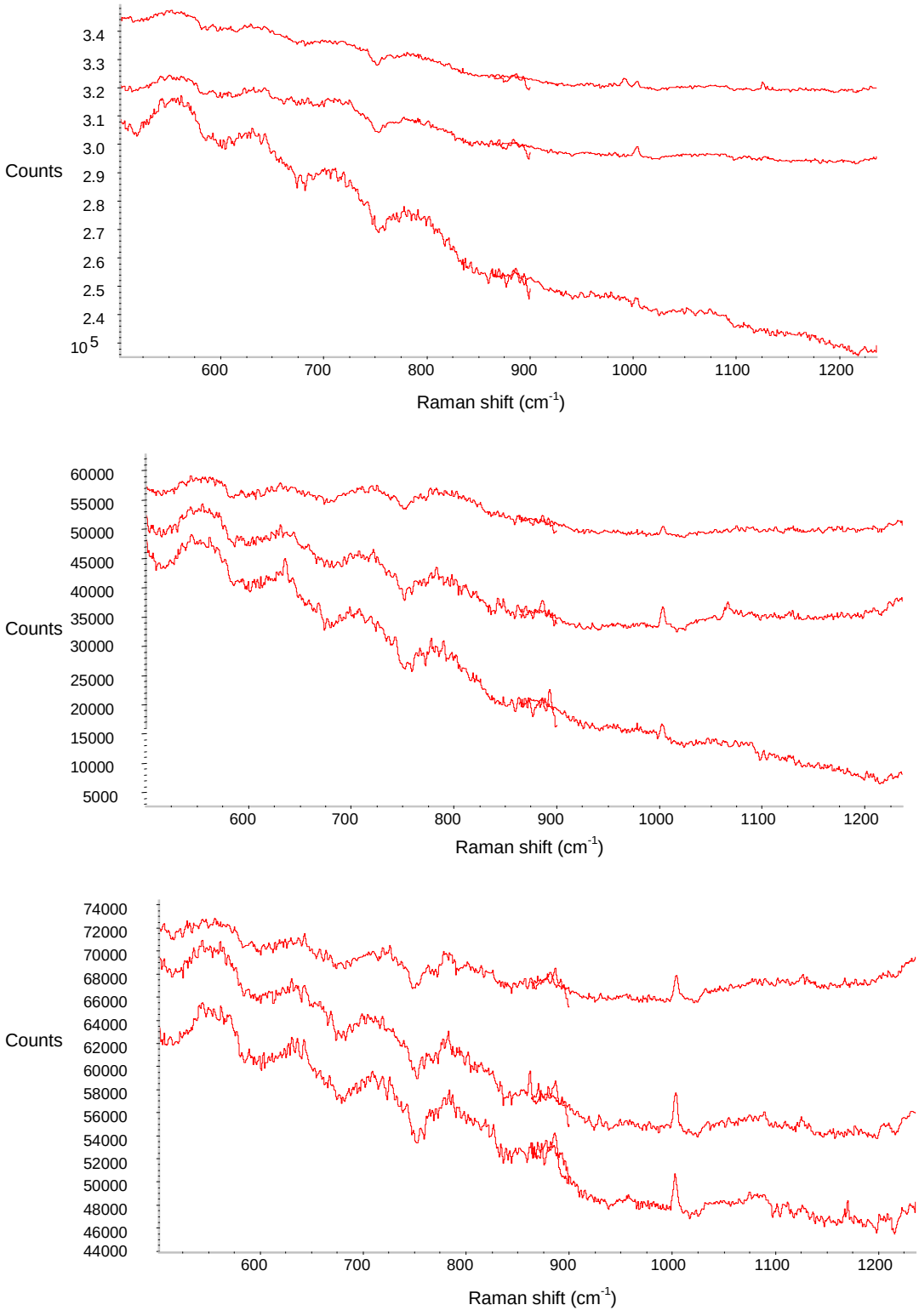
Counts
3.4
3.3
3.2
3.1
3.0
2.9
2.8
2.7
2.6
2.5
2.4
10 5
600
700
800
900
1000
1100
1200
Raman shift (cm-1)
Counts
60000
55000
50000
45000
40000
35000
30000
25000
20000
15000
10000
5000
600
700
800
900
1000
1100
1200
Raman shift (cm-1)
Counts
74000
72000
70000
68000
66000
64000
62000
60000
58000
56000
54000
52000
50000
48000
46000
44000
600
700
800
900
1000
1100
1200
Raman shift (cm-1)

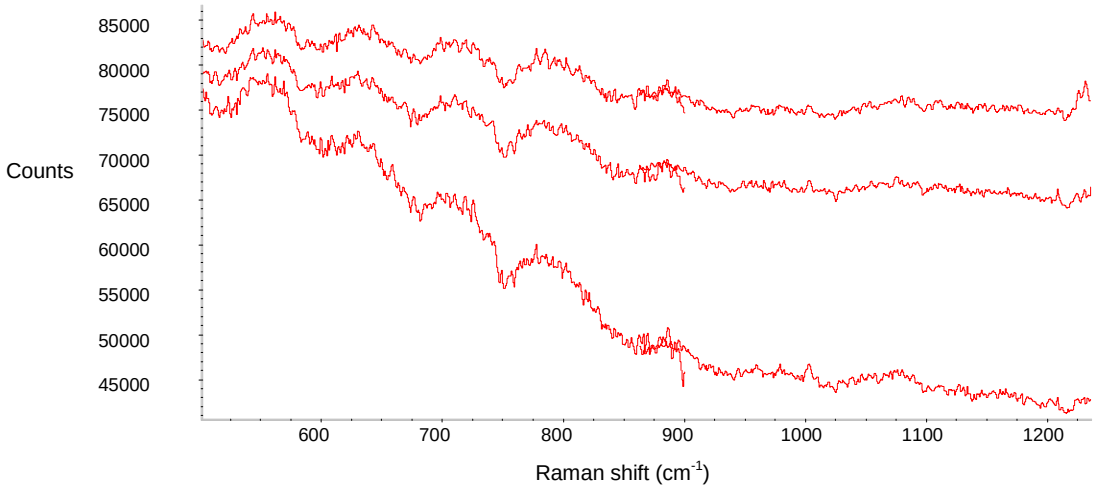
Counts
85000
80000
75000
70000
65000
60000
55000
50000
45000
600
700
800
900
1000
1100
1200
Raman shift (cm-1)

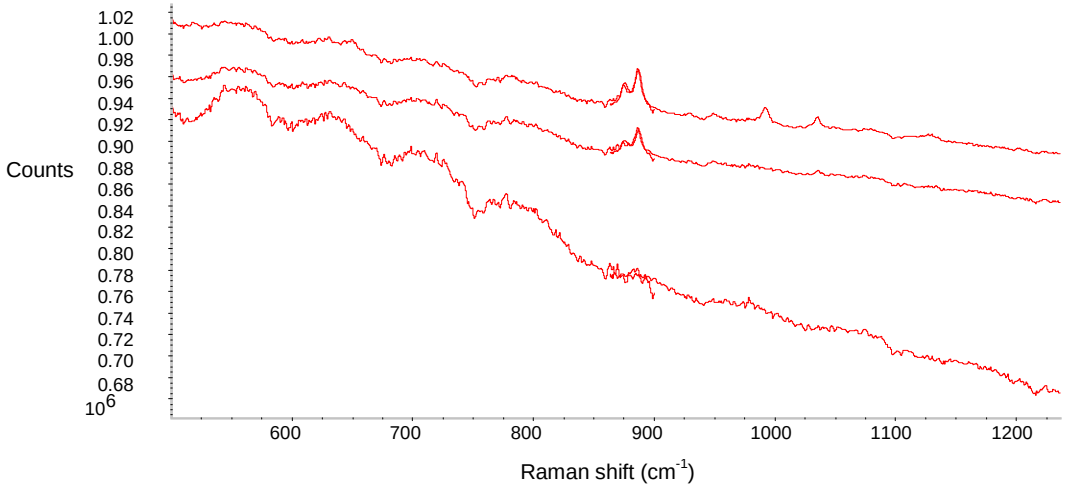
Counts
1.02
1.00
0.98
0.96
0.94
0.92
0.90
0.88
0.86
0.84
0.82
0.80
0.78
0.76
0.74
0.72
0.70
0.68
10^6
600
700
800
900
1000
1100
1200
Raman shift (cm-1)

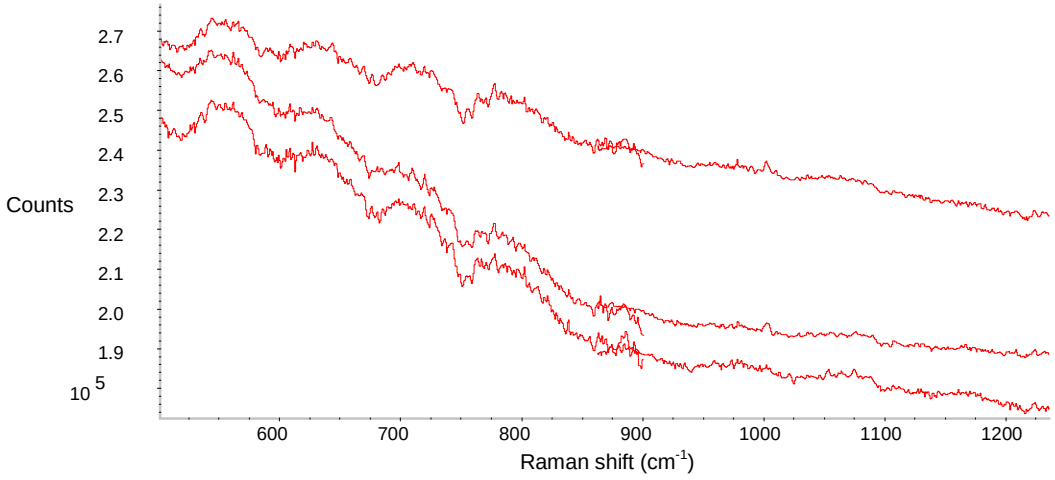
Counts
2.7
2.6
2.5
2.4
2.3
2.2
2.1
2.0
1.9
10^5
600
700
800
900
1000
1100
1200
Raman shift (cm-1)

Slide #38 FcRed1 10% PDA

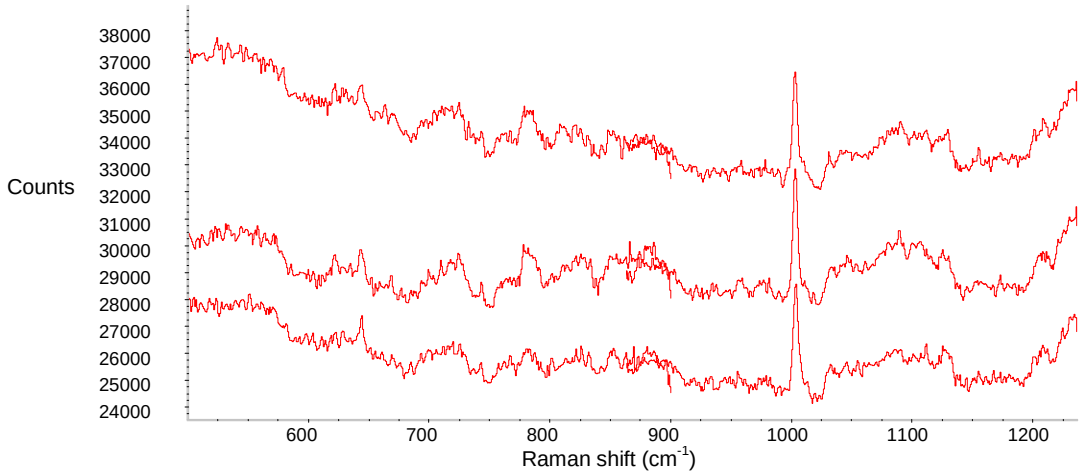

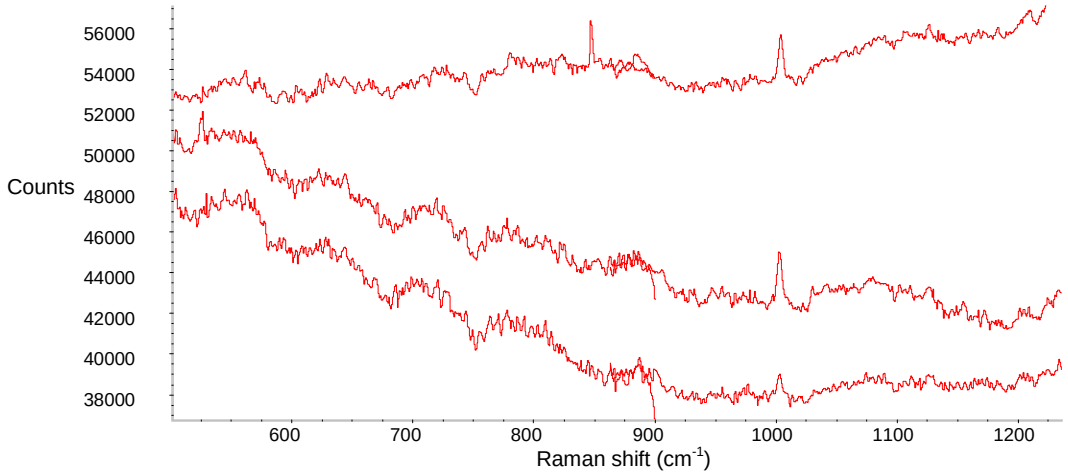

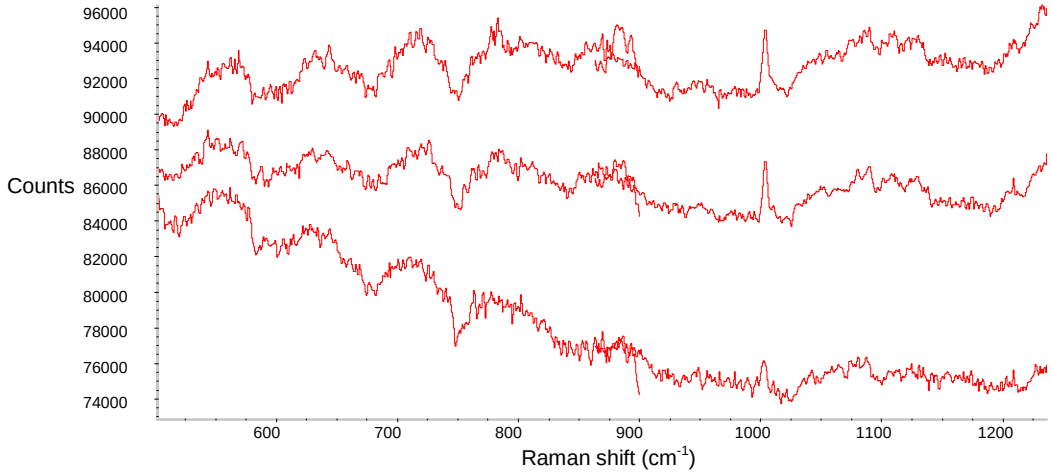

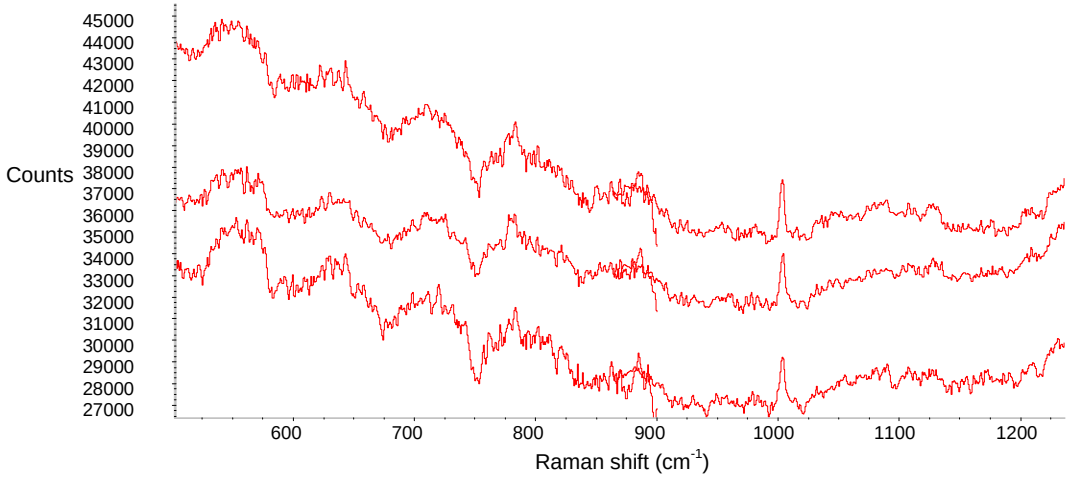
Counts
45000
44000
43000
42000
41000
40000
39000
38000
37000
36000
35000
34000
33000
32000
31000
30000
29000
28000
27000
600
700
800
900
1000
1100
1200
Raman shift (cm-1)

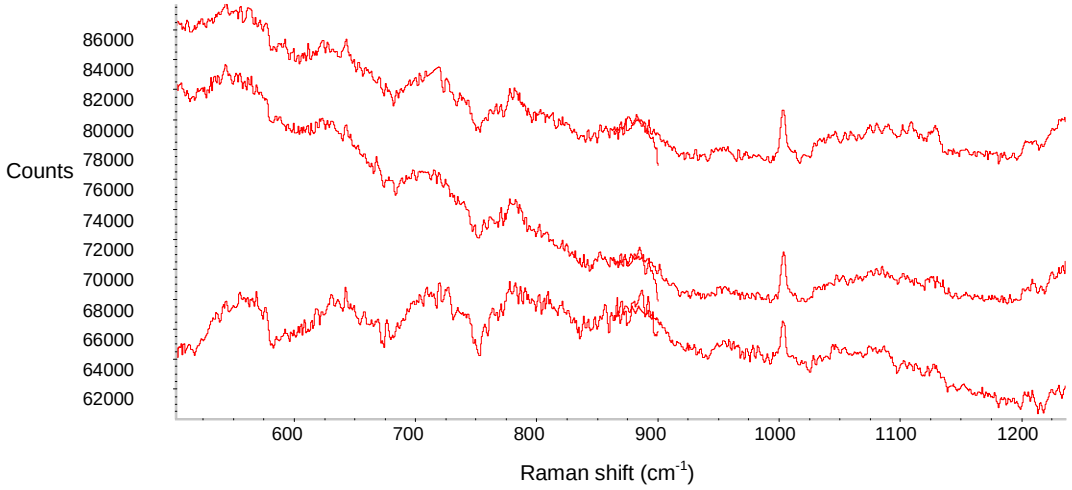
Counts
86000
84000
82000
80000
78000
76000
74000
72000
70000
68000
66000
64000
62000
600
700
800
900
1000
1100
1200
Raman shift (cm-1)

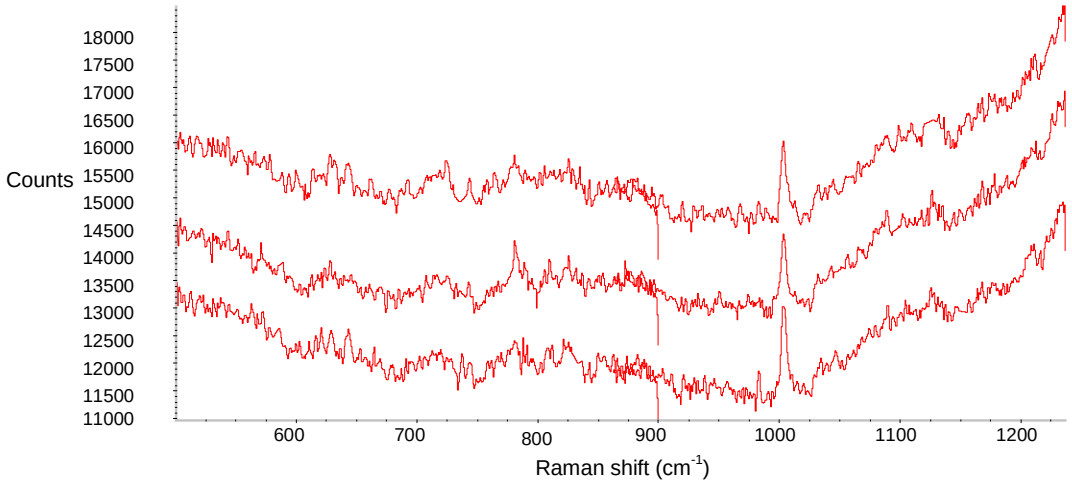
Counts
18000
17500
17000
16500
16000
15500
15000
14500
14000
13500
13000
12500
12000
11500
11000
600
700
800
900
1000
1100
1200
Raman shift (cm-1)

After the defense of this thesis, it was determined that the Raman spectrum of mannitol also depends on the polarization of the source.

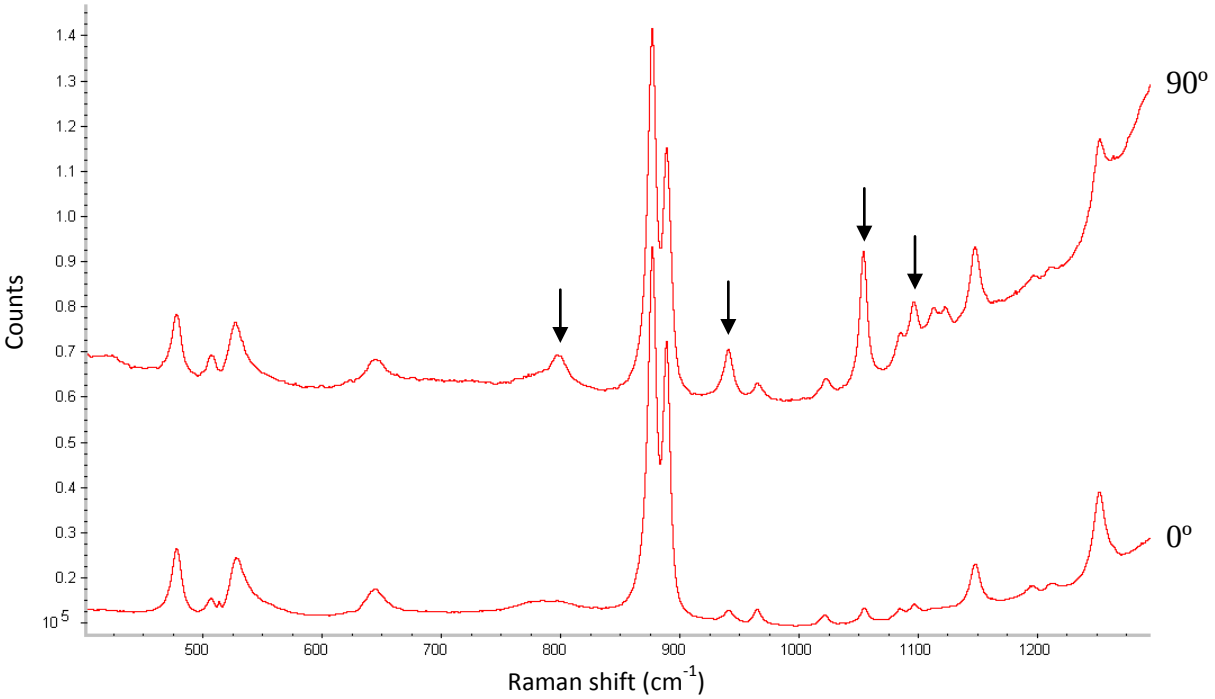

Figure A. Raman spectra of crystalline mannitol collected with a 785 nm laser. The polarization of the source was changed for each acquisition with the use of a polarizer. Bands that experience the greatest change in relative intensity are indicated by arrows.